University of Alberta

INVESTIGATION OF THE INTERNAL DYNAMICS OF AMMONIA IN VAN DER WAALS COMPLEXES WITH RARE GAS ATOMS: FOURIER TRANSFORM MICROWAVE SPECTRA AND *AB INITIO* CALCULATIONS

by

Jennifer Anne van Wijngaarden ©

A thesis submitted to the Faculty of Graduate Studies and Research in partial fulfillment of the requirements of the degree Doctor of Philosophy

Department of Chemistry

Edmonton, Alberta

Spring 2002

National Library of Canada
Acquisitions and Bibliographic Services
395 Wellington Street
Ottawa ON K1A 0N4
Canada

Bibliothèque nationale du Canada
Acquisitions et services bibliographiques
395, rue Wellington
Ottawa ON K1A 0N4
Canada

Your file Votre référence

Our file Notre référence

The author has granted a non-exclusive licence allowing the National Library of Canada to reproduce, loan, distribute or sell copies of this thesis in microform, paper or electronic formats.

L'auteur a accordé une licence non exclusive permettant à la Bibliothèque nationale du Canada de reproduire, prêter, distribuer ou vendre des copies de cette thèse sous la forme de microfiche/film, de reproduction sur papier ou sur format électronique.

The author retains ownership of the copyright in this thesis. Neither the thesis nor substantial extracts from it may be printed or otherwise reproduced without the author's permission.

L'auteur conserve la propriété du droit d'auteur qui protège cette thèse. Ni la thèse ni des extraits substantiels de celle-ci ne doivent être imprimés ou autrement reproduits sans son autorisation.

0-612-68634-5

Canada

University of Alberta

Library Release Form

Name of Author: Jennifer van Wijngaarden

Title of Thesis: Investigation of the internal dynamics of ammonia in van der Waals complexes with rare gas atoms: Fourier transform microwave spectra and *ab initio* calculations

Degree: Doctor of Philosophy

Year this Degree Granted: 2002

Permission is hereby granted to the University of Alberta Library to reproduce single copies of this thesis and to lend or sell such copies for private, scholarly, or scientific research purposes only.

The author reserves all other publication and other rights in association with the copyright in this thesis, and except as herein before provided, neither the thesis nor any substantial portion thereof may be printed or otherwise reproduced in any material form whatever without the author's prior written permission.

4119 113 St.
Edmonton, AB
T6J 1L2
Canada

Date: 4 April, 2002

University of Alberta

Faculty of Graduate Studies and Research

The undersigned certify that they have read, and recommend to the Faculty of Graduate Studies and Research for acceptance, a thesis entitled: **"Investigation of the internal dynamics of ammonia in van der Waals complexes with rare gas atoms: Fourier transform microwave spectra and *ab initio* calculations"**, submitted by **Jennifer van Wijngaarden** in partial fulfillment of the requirements for the degree of Doctor of Philosophy.

Dr. W. Jäger (*Supervisor*)

Dr. R. E. D. McClung (*Chair*)

Dr. M. Klobukowski

Dr. A. Mar

Dr. J. Tuszynski

Dr. R. P. Steer (*University of Saskatchewan*)

Date: 27. March 2002

ABSTRACT

Microwave rotational spectra of seven different van der Waals complexes consisting of one, two, or three rare gas (Rg) atoms bound to one NH_3 molecule were measured using a pulsed molecular beam Fourier transform microwave spectrometer. The rotational spectrum of each complex is complicated by the internal rotation and inversion motions of the NH_3 subunit. Due to the large amplitudes of these motions, the NH_3 moiety can essentially be regarded as a sphere during the rotational analysis of each species.

The rotational transitions of the Rg-NH_3 (Rg = Ne, Ar, Kr) dimers follow the pattern of a diatomic molecule. The Ne_2-NH_3 ($^{20}Ne_2$-, $^{22}Ne_2$-) and Ar_2-NH_3 trimers are asymmetric tops and their spectra consist of *a*-type and *b*-type transitions, respectively. The $^{20}Ne^{22}Ne$-NH_3 isotopomer is also an asymmetric top but both *a*- and *b*-type transitions are allowed due to the reduced symmetry of the complex. The Ar_3-NH_3 and Ne_3-NH_3 ($^{20}Ne_3$-, $^{22}Ne_3$-) tetramers are oblate and prolate symmetric tops, respectively. The mixed isotopomers, $^{20}Ne_2{}^{22}Ne$-NH_3 and $^{20}Ne^{22}Ne_2$-NH_3, are asymmetric tops and their spectra contain *a*- and *b*-type and *a*- and *c*-type transitions, respectively. The rotational constants obtained from fitting the spectra of the various Rg_n-NH_3 (n = 1, 2, 3) complexes were used to estimate the Rg-Rg and Rg-NH_3 bond lengths in each species. The ^{14}N nuclear quadrupole hyperfine structures of the rotational transitions were resolved for each complex and analyzed in terms of the orientation and dynamics of the NH_3 moiety within the clusters. Additional splittings due to the inversion of ammonia were resolved

for each deuterated isotopomer and compared as general indicators of the relative energy differences between the two inversion states of each cluster.

The experimental results were complemented by the construction of *ab initio* potential energy surfaces for the Ne_n-NH_3 (n = 1, 2, 3) complexes using fourth order Møller-Plessett (MP4) perturbation theory and coupled cluster [CCSD(T)] theory. Three surfaces were constructed for each cluster based on different umbrella angles of the NH_3 monomer to simulate the inversion motion. The topologies of the potential energy surfaces were compared for the three Ne containing complexes and were related to experimentally derived parameters for each system.

PREFACE

This thesis is based on the research I have done at the University of Alberta between September 1997 and February 2002. Some of the projects described in this work have been published. I have chosen not to include these in the references of each chapter since I refer to the same projects throughout my thesis. For the sake of completeness, I provide here the references for work that appears in print at this time.

Chapter 3:

Jennifer van Wijngaarden and Wolfgang Jäger, "*Microwave spectra of the Ar-ND_3 van der Waals complex and its partially deuterated isotopomers*", Journal of Chemical Physics. **114**, 3968-3976 (2001).

Jennifer van Wijngaarden and Wolfgang Jäger "*Microwave rotational spectra of the Kr-NH_3 van der Waals complex*", Molecular Physics. **99**, 1215-1228 (2001).

Jennifer van Wijngaarden and Wolfgang Jäger, "*Investigation of the Ne-NH_3 van der Waals complex: Rotational spectrum and ab initio calculations*", Journal of Chemical Physics. **115**, 6504-6512 (2001).

Chapter 5:

Jennifer van Wijngaarden and Wolfgang Jäger, "*Microwave rotational spectra of the Ar_3-NH_3 van der Waals tetramer*", Journal of Chemical Physics. **116**, 2379-2387 (2002).

Jennifer van Wijngaarden

ACKNOWLEDGMENTS

I wish to express my thanks to my supervisor Wolfgang Jäger for his support and guidance over the past 4.5 years. He has given me many opportunities to learn and grow as a scientist and for this, I am extremely grateful.

I also want to thank my colleagues in the Jäger group, both past and present, for fostering many useful discussions over the years. In particular, I would like to acknowledge Dr. Yunjie Xu for her invaluable advice during the course of my research. A special note of thanks goes to Kai Brendel from Universität Kiel for providing computer support during the last stages of my *ab initio* calculations and for his friendship over the past year.

The course of my research was greatly enhanced by the support of several people outside of the Jäger group. In this respect, I would like to thank Dr. P. N. Roy for sharing his computational resources for my preliminary *ab initio* calculations and Dr. R. Wasylishen for providing me with office space while I wrote my thesis. I also wish to thank Dr. M. C. L. Gerry from the University of British Columbia for lending the group a microwave synthesizer that I used for double resonance experiments.

Finally, I wish to acknowledge the people that have made my time in Edmonton an unforgettable experience. I am leaving with many wonderful memories of my days with Dr. Grace Greidanus-Strom, Lesley Liu, Jennifer Doubt, and Peggy Daley. I am extremely grateful to each of them for their support and friendship.

TABLE OF CONTENTS

Chapter 1. Introduction 1

References 11

Chapter 2. Experimental 15

2.1 Overview of FTMW spectroscopy 15

2.2 Theoretical considerations 17

2.3 FTMW spectrometer design 22

References 32

Chapter 3. Investigation of the Rg-NH_3 van der Waals dimers: Rotational spectra and *ab initio* calculations 33

3.1 Introduction 33

3.2 Experimental method 37

3.3 Spectral search and assignment 39

3.3.1 Molecular symmetry group theory 40

a) Rg-NH_3 and Rg-$^{15}NH_3$ 40

b) Rg-ND_3 42

c) Rg-ND_2H 42

d) Rg-NDH_2 42

3.3.2 Isotopomers of Kr-NH_3 43

a) Kr-NH_3 and Kr-$^{15}NH_3$ 43

b) Kr-ND_3 47

c) Kr-ND_2H 50

d) Kr-NDH_2 51

3.3.3 Deuterated isotopomers of Ar-NH_3 51

a) Ar-ND_3 51

b) Ar-ND_2H 55

c) Ar-NDH_2 56

3.3.4 Isotopomers of Ne-NH_3 56

a) Ne-NH_3 and Ne-$^{15}NH_3$ 56

b) Ne-ND_3 58

c) Ne-ND_2H 60

d) Ne-NDH_2 60

3.4 *Ab initio* calculations for Ne-NH_3 61

3.5 Discussion 63

3.5.1 Spectroscopic constants and derived molecular parameters ... 63
3.5.2 The $\Sigma 1_1$ excited internal rotor state ... 67
3.5.3 Inversion tunnelling ... 71
3.5.4 *Ab initio* potential energy surfaces of Ne-NH_3 ... 73
3.6 Concluding remarks ... 79
References ... 81

Chapter 4. Investigation of the Rg_2-NH_3 van der Waals trimers: Rotational spectra and *ab initio* calculations 85

4.1 Introduction ... 85
4.2 Experimental method ... 86
4.3 Spectral search and assignment ... 87
4.3.1 Isotopomers of Ar_2-NH_3 ... 88
a) Ar_2-NH_3 and Ar_2-$^{15}NH_3$ 89
b) Ar_2-ND_3 93
c) Ar_2-ND_2H 95
d) Ar_2-NDH_2 96
4.3.2 Isotopomers of Ne_2-NH_3 ... 97
a) $^{20}Ne^{22}Ne$-NH_3 and $^{20}Ne^{22}Ne$-$^{15}NH_3$ 97
b) $^{20}Ne_2$-NH_3, $^{20}Ne_2$-$^{15}NH_3$, and $^{22}Ne_2$-NH_3 1023
c) $^{20}Ne_2$-ND_3 107
d) $^{20}Ne_2$-ND_2H 109
e) $^{20}Ne_2$-NDH_2 110
4.4 *Ab initio* calculations for Ne_2-NH_3 ... 111
4.5 Discussion ... 113
4.5.1 Spectroscopic constants and derived molecular parameters ... 113
4.5.2 Inversion tunnelling ... 117
4.5.3 *Ab initio* potential energy surfaces of Ne_2-NH_3 ... 120
4.6 Concluding remarks ... 128
References ... 130

Chapter 5. Investigation of the Rg_3-NH_3 van der Waals tetramers: Rotational spectra and *ab initio* calculations 133

5.1 Introduction ... 133
5.2 Experimental method ... 134

5.3 Spectral search and assignment 135

5.3.1 Isotopomers of Ar_3-NH_3 135

a) Ar_3-NH_3 and Ar_3-$^{15}NH_3$ 137
b) Ar_3-ND_3 142
c) Ar_3-ND_2H 144
d) Ar_3-NDH_2 145

5.3.2 Isotopomers of Ne_3-NH_3 147

a) $^{20}Ne_3$-NH_3, $^{22}Ne_3$-NH_3, $^{20}Ne_3$-$^{15}NH_3$, and $^{22}Ne_3$-$^{15}NH_3$ 149
b) $^{20}Ne_3$-ND_3 152
c) $^{20}Ne_3$-ND_2H 153
d) $^{20}Ne_3$-NDH_2 154
e) $^{20}Ne_2{}^{22}Ne$-NH_3 and $^{20}Ne_2{}^{22}Ne$-$^{15}NH_3$ 155
f) $^{20}Ne^{22}Ne_2$-NH_3 and $^{20}Ne^{22}Ne_2$-$^{15}NH_3$ 159

5.4 *Ab initio* calculations for Ne_3-NH_3 161

5.5 Discussion 163

5.5.1 Spectroscopic constants and derived molecular parameters.... 163

5.5.2 Inversion tunnelling 167

5.5.3 *Ab initio* potential energy surfaces of Ne_3-NH_3 170

5.6 Concluding remarks 175

References 178

Chapter 6. General conclusions **180**

References 185

Appendix 1. Molecular symmetry group tables 186

Appendix 2. Tables of microwave transition frequencies measured for the Rg-NH_3 dimers 190

Appendix 3. Tables of *ab initio* data for the Ne-NH_3 dimer..... 200

Appendix 4. Tables of microwave transition frequencies measured for the Rg_2-NH_3 trimers 215

Appendix 5. Tables of *ab initio* data for the Ne_2-NH_3 trimer..... 227

Appendix 6. Tables of microwave transition frequencies measured for the Rg_3-NH_3 tetramers 238

Appendix 7. Tables of *ab initio* data for the Ne_3-NH_3 tetramer..... 248

LIST OF TABLES

Table

3.1 Summary of the molecular symmetry group theory analysis for the metastable states of the Rg-NH_3 isotopomers. 41

3.2 Spectroscopic constants and derived molecular parameters for Kr-NH_3. 44

3.3 Spectroscopic constants and derived molecular parameters for Kr-$^{15}NH_3$. 46

3.4 Spectroscopic constants and derived molecular parameters for Kr-ND_3, Kr-ND_2H, and Kr-NDH_2. 49

3.5 Spectroscopic constants and derived molecular parameters for Ar-ND_3, Ar-ND_2H, and Ar-NDH_2. 54

3.6 Spectroscopic constants and derived molecular parameters for Ne-NH_3 and Ne-$^{15}NH_3$. 57

3.7 Spectroscopic constants and derived molecular parameters for Ne-ND_3, Ne-ND_2H, and Ne-NDH_2. 59

3.8 Estimated orientation of ammonia in the Kr-NH_3, Ar-NH_3, and Ne-NH_3 dimers. 65

4.1 Summary of the molecular symmetry group theory analysis for the metastable states of the Ar_2-NH_3 isotopomers. 90

4.2 Spectroscopic constants for Ar_2-NH_3 and Ar_2-$^{15}NH_3$. 92

4.3 Spectroscopic constants for Ar_2-ND_3, Ar_2-ND_2H, and Ar_2-NDH_2. 94

4.4 Summary of the molecular symmetry group theory analysis for the metastable states of the Ne_2-NH_3 isotopomers. 99

4.5 Spectroscopic constants for $^{22}Ne^{20}Ne$-NH_3 and $^{22}Ne^{20}Ne$-$^{15}NH_3$. 103

4.6 Spectroscopic constants for Ne_2-NH_3 and Ne_2-$^{15}NH_3$. 106

4.7 Spectroscopic constants for $^{20}Ne_2$-ND_3, $^{20}Ne_2$-ND_2H, and $^{20}Ne_2$-NDH_2. 108

4.8 Estimated orientation of ammonia in the Ar_2-NH_3 and Ne_2-NH_3 trimers. 114

4.9 Comparison of the bond lengths (Å) for various van der Waals dimers and trimers. 117

5.1 Summary of the molecular symmetry group theory analysis for the metastable states of the Rg_3-NH_3 isotopomers. 137

5.2 Spectroscopic constants for Ar_3-NH_3 and Ar_3-$^{15}NH_3$. 141

5.3 Spectroscopic constants for Ar_3-ND_3, Ar_3-ND_2H, and Ar_3-NDH_2. 143

5.4 Spectroscopic constants for Ne_3-NH_3 and Ne_3-$^{15}NH_3$. 151

5.5 Spectroscopic constants for Ne_3-ND_3, Ne_3-ND_2H, and Ne_3-NDH_2. 153

5.6 Summary of the molecular symmetry group theory analysis for the metastable states of the $^{20}Ne_2{}^{22}Ne$-NH_3 and $^{20}Ne^{22}Ne_2$-NH_3 isotopomers. 156

5.7 Spectroscopic constants for $^{20}Ne_2{}^{22}Ne$-NH_3 and $^{20}Ne^{22}Ne_2$-NH_3. 159

5.8 Estimated orientation of ammonia in the Ar_3-NH_3 and Ne_3-NH_3 tetramers. 165

5.9 Comparison of the bond lengths (Å) for various van der Waals dimers, trimers, and tetramers. 167

5.10 Comparison of the inversion tunnelling splittings (kHz) for the Rg-NH_3, Rg_2-NH_3, and Rg_3-NH_3 complexes. 169

A1.1 The D_{3h} molecular symmetry group. 187

A1.2 The C_{2v} molecular symmetry group. 187

A1.3 The G_{24} molecular symmetry group. 188

A1.4 The G_8 molecular symmetry group. 188

A1.5 The G_{36} molecular symmetry group. 189

A1.6 The G_{12} molecular symmetry group. 189

A2.1 Measured transition frequencies (MHz) for the $\Sigma 0_{0a}$ state of Kr-NH_3. 191

A2.2 Measured transition frequencies (MHz) for the $\Sigma 0_{0a}$ states of ^{83}Kr-NH_3 and ^{83}Kr-$^{15}NH_3$. 192

A2.3 Measured transition frequencies (MHz) for the $\Sigma 0_{0a}$ state of Kr-$^{15}NH_3$. 192

A2.4 Measured transition frequencies (MHz) for the $\Sigma 0_0$ states of Kr-ND_3. 193

A2.5 Measured transition frequencies (MHz) for the $\Sigma 1_1$ states of Kr-ND_3. 193

A2.6 Measured transition frequencies (MHz) for the $\Sigma 0_{00}$ states of Kr-ND_2H. 194

A2.7 Measured transition frequencies (MHz) for the $\Sigma 0_{00}$ states of Kr-NDH_2. 195

A2.8 Measured transition frequencies (MHz) for the $\Sigma 0_0/\Sigma 1_1$ states of Ar-ND_3. 196

A2.9 Measured transition frequencies (MHz) for the $\Sigma 0_{00}$ states of Ar-ND_2H and Ar-NDH_2. 197

A2.10 Measured transition frequencies (MHz) for the $\Sigma 0_{0a}$ state of Ne-NH_3. 197

A2.11 Measured transition frequencies (MHz) for the $\Sigma 0_{0a}$ state of Ne-$^{15}NH_3$. 198

A2.12 Measured transition frequencies (MHz) for the $\Sigma 0_0$ states of Ne-ND_3. 198

A2.13 Measured transition frequencies (MHz) for the $\Sigma 0_{00}$ states of $Ne\text{-}ND_2H$. 199

A2.14 Measured transition frequencies (MHz) for the $\Sigma 0_{00}$ states of $Ne\text{-}NDH_2$. 199

A3.1 Interaction energies (μE_h) of $Ne\text{-}NH_3$ calculated at the MP4 level for the equilibrium geometry of NH_3 (>HNH=106.67°). 201

A3.2 Interaction energies (μE_h) of $Ne\text{-}NH_3$ calculated at the MP4 level for the intermediate geometry of NH_3 (>HNH=113.34°). 203

A3.3 Interaction energies (μE_h) of $Ne\text{-}NH_3$ calculated at the MP4 level for the planar geometry of NH_3 (>HNH=120.00°). 205

A3.4 Finer scan interaction energies (μE_h) of $Ne\text{-}NH_3$ calculated at the MP4 level for the equilibrium geometry of NH_3 (>HNH=106.67°). 206

A3.5 Finer scan interaction energies (μE_h) of $Ne\text{-}NH_3$ calculated at the MP4 level for the intermediate geometry of NH_3 (>HNH=113.34°). 207

A3.6 Finer scan interaction energies (μE_h) of $Ne\text{-}NH_3$ calculated at the MP4 level for the planar geometry of NH_3 (>HNH=120.00°). 208

A3.7 Interaction energies (μE_h) of $Ne\text{-}NH_3$ calculated at the CCSD(T) level for the equilibrium geometry of NH_3 (>HNH=106.67°). 209

A3.8 Interaction energies (μE_h) of $Ne\text{-}NH_3$ calculated at the CCSD(T) level for the intermediate geometry of NH_3 (>HNH=113.34°). 210

A3.9 Interaction energies (μE_h) of $Ne\text{-}NH_3$ calculated at the CCSD(T) level for the planar geometry of NH_3 (>HNH=120.00°). 211

A3.10 Interaction energies (μE_h) of $Ne\text{-}NH_3$ calculated at the CCSD(T) level for the equilibrium geometry of NH_3 (>HNH=106.67°) using the aug-cc-pVDZ basis set for Ne. 212

A3.11 Interaction energies (μE_h) of $Ne\text{-}NH_3$ calculated at the CCSD(T) level for the intermediate geometry of NH_3 (>HNH=113.34°) using the aug-cc-pVDZ basis set for Ne. 213

A3.12 Interaction energies (μE_h) of $Ne\text{-}NH_3$ calculated at the CCSD(T) level for the planar geometry of NH_3 (>HNH=120.00°) using the aug-cc-pVDZ basis set for Ne. 214

A4.1 Measured transition frequencies (MHz) for the $\Sigma 0_{0a}$ state of $Ar_2\text{-}NH_3$. 216

A4.2 Measured transition frequencies (MHz) for the $\Sigma 0_{0a}$ state of $Ar_2\text{-}^{15}NH_3$. 217

A4.3 Measured transition frequencies (MHz) for the $\Sigma 0_0$ states of $Ar_2\text{-}ND_3$. 218

A4.4 Measured transition frequencies (MHz) for the $\Sigma 0_{00}$ states of $Ar_2\text{-}ND_2H$. 219

A4.5 Measured transition frequencies (MHz) for the $\Sigma 0_{00}$ states of Ar_2-NDH_2. 220

A4.6 Measured transition frequencies (MHz) for the $\Sigma 0_{0a}$ state of $^{20}Ne^{22}Ne$-NH_3. 221

A4.7 Measured transition frequencies (MHz) for the $\Sigma 0_{0a}$ state of $^{20}Ne^{22}Ne$-$^{15}NH_3$. 222

A4.8 Measured transition frequencies (MHz) for the $\Sigma 0_{0a}$ states of $^{20}Ne_2$-NH_3 and $^{22}Ne_2$-NH_3. 223

A4.9 Measured transition frequencies (MHz) for the $\Sigma 0_{0a}$ state of $^{20}Ne_2$-$^{15}NH_3$. 223

A4.10 Measured transition frequencies (MHz) for the $\Sigma 0_0$ states of $^{20}Ne_2$-ND_3. 224

A4.11 Measured transition frequencies (MHz) for the $\Sigma 0_{00}$ states of $^{20}Ne_2$-ND_2H. 225

A4.12 Measured transition frequencies (MHz) for the $\Sigma 0_{00}$ states of $^{20}Ne_2$-NDH_2. 226

A5.1 Interaction energies (μE_h) of Ne_2-NH_3 calculated at the CCSD(T) level for the equilibrium geometry of NH_3 (>HNH=106.67°) at β=90°. 228

A5.2 Interaction energies (μE_h) of Ne_2-NH_3 calculated at the CCSD(T) level for the intermediate geometry of NH_3 (>HNH=113.34°) at β=90°. 229

A5.3 Interaction energies (μE_h) of Ne_2-NH_3 calculated at the CCSD(T) level for the planar geometry of NH_3 (>HNH=120.00°) at β=90°. 230

A5.4 Interaction energies (μE_h) of Ne_2-NH_3 calculated at the CCSD(T) level for the equilibrium geometry of NH_3 (>HNH=106.67°) at β=90°. 231

A5.5 Interaction energies (μE_h) of Ne_2-NH_3 calculated at the CCSD(T) level for the intermediate geometry of NH_3 (>HNH=113.34°) at β=90°. 232

A5.6 Interaction energies (μE_h) of Ne_2-NH_3 calculated at the CCSD(T) level for the planar geometry of NH_3 (>HNH=120.00°) at β=90°. 234

A5.7 Interaction energies (μE_h) of Ne_2-NH_3 calculated at the CCSD(T) level for the equilibrium geometry of NH_3 (>HNH=106.67°) at β=90° using the aug-cc-pVDZ basis set for Ne. 235

A5.8 Interaction energies (μE_h) of Ne_2-NH_3 calculated at the CCSD(T) level for the intermediate geometry of NH_3 (>HNH=113.34°) at β=90° using the aug-cc-pVDZ basis set for Ne. 236

A5.9 Interaction energies (μE_h) of Ne_2-NH_3 calculated at the CCSD(T) level for the planar geometry of NH_3 (>HNH=120.00°) at β=90° using the aug-cc-pVDZ basis set for Ne. 237

A6.1 Measured transition frequencies (MHz) for the $\Sigma 0_{0a}$ state of Ar_3-NH_3. 239

A6.2 Measured transition frequencies (MHz) for the $\Sigma 0_{0a}$ state of Ar_3-$^{15}NH_3$. 239

A6.3 Measured transition frequencies (MHz) for the $\Sigma 0_0$ states of Ar_3-ND_3. 240

A6.4 Measured transition frequencies (MHz) for the $\Sigma 0_{00}$ states of Ar_3-ND_2H. 241

A6.5 Measured transition frequencies (MHz) for the $\Sigma 0_{00}$ states of Ar_3-NDH_2. 242

A6.6 Measured transition frequencies (MHz) for the $\Sigma 0_{0a}$ states of $^{20}Ne_3$-NH_3 and $^{22}Ne_3$-NH_3. 243

A6.7 Measured transition frequencies (MHz) for the $\Sigma 0_{0a}$ states of $^{20}Ne_3$-$^{15}NH_3$ and $^{22}Ne_3$-$^{15}NH_3$. 243

A6.8 Measured transition frequencies (MHz) for the $\Sigma 0_0$ states of $^{20}Ne_3$-ND_3. 244

A6.9 Measured transition frequencies (MHz) for the $\Sigma 0_{00}$ states of $^{20}Ne_3$-ND_2H. 244

A6.10 Measured transition frequencies (MHz) for the $\Sigma 0_{00}$ states of $^{20}Ne_3$-NDH_2. 245

A6.11 Measured transition frequencies (MHz) for the $\Sigma 0_{00a}$ state of $^{20}Ne_2{}^{22}Ne$-NH_3. 245

A6.12 Measured transition frequencies (MHz) for the $\Sigma 0_{00a}$ state of $^{20}Ne_2{}^{22}Ne$-$^{15}NH_3$. 246

A6.13 Measured transition frequencies (MHz) for the $\Sigma 0_{00a}$ state of $^{20}Ne{}^{22}Ne_2$-NH_3. 246

A6.14 Measured transition frequencies (MHz) for the $\Sigma 0_{00a}$ state of $^{20}Ne{}^{22}Ne_2$-$^{15}NH_3$. 247

A7.1 Interaction energies (μE_h) of Ne_3-NH_3 calculated at the CCSD(T) level for the equilibrium geometry of NH_3 (>HNH=106.67°). 249

A7.2 Interaction energies (μE_h) of Ne_3-NH_3 calculated at the CCSD(T) level for the intermediate geometry of NH_3 (>HNH=113.34°). 250

A7.3 Interaction energies (μE_h) of Ne_3-NH_3 calculated at the CCSD(T) level for the planar geometry of NH_3 (>HNH=120.00°). 251

LIST OF FIGURES

Figure

2.1 Bloch vector diagram depicting the $\pi/2$ condition in a rotating reference frame. 21

2.2 Schematic of the mechanical parts of the FTMW spectrometer. 23

2.3 The microwave circuit. 27

2.4 Pulse sequence for a single FTMW experiment. 30

3.1 Coordinate system of the Rg-NH_3 dimers. 35

3.2 Spectrum of the J=1-0 rotational transition of ^{83}Kr-NH_3 for the $\Sigma 0_{0a}$ state. 45

3.3 Spectrum of the J=1-0 rotational transition of Ar-ND_3 for the $\Sigma 0_{0s}$ and $\Sigma 0_{0a}$ inversion states. 53

3.4 Minimum energy (MP4) path of Ne-NH_3 from $\theta=0^o$ to $\theta=180^o$ when NH_3 is in it experimental equilibrium conformation. 75

3.5 Comparison of the minimum energy (MP4) paths of Ne-NH_3 for the three different NH_3 monomer geometries. 76

3.6 Comparison of the interaction energy (MP4) for the three different NH_3 geometries as a function of the van der Waals bond length R and the orientation ϕ. 78

4.1 Geometry of the Ar_2-NH_3 trimer in the principal inertial axis system. 88

4.2 Predicted energy level diagram for the Ar_2-NH_3 asymmetric top. 91

4.3 Geometries of the Ne_2-NH_3 trimers in the principal inertial axis system. 98

4.4 Spectra comparing the relative intensities of *a*-type and *b*-type transitions observed for the $^{20}Ne^{22}Ne$-NH_3 isotopomer. 101

4.5 Predicted energy level diagram for the $^{20}Ne_2$ and $^{22}Ne_2$ containing isotopomers of the Ne_2-NH_3 asymmetric top. 104

4.6 Coordinate system of Ne_2-NH_3 used for the *ab initio* calculations. 112

4.7 Comparison of the minimum energy [CCSD(T)] paths of the Ne-NH_3 dimer and Ne_2-NH_3 trimer as a function of the θ coordinate. 122

4.8 Comparison of the minimum energy [CCSD(T)] paths of Ne_2-NH_3 as a function of the θ coordinate for $\phi=60^o$, $\beta=90^o$. 123

4.9 Comparison of the interaction energy [CCSD(T)] of Ne_2-NH_3 as a function of the R coordinate for three different umbrella angles of NH_3. 125

4.10 Comparison of the interaction energy [CCSD(T)] of Ne_2-NH_3 as a function of the R coordinate for two different ϕ orientations. 127

5.1 Geometry of the Ar_3-NH_3 oblate symmetric top in the principal inertial axis system. 136

5.2 Predicted energy level diagram for the Ar_3-NH_3 oblate symmetric top. 140

5.3 Spectrum of the $J_K=4_03_0$ and $J_K=4_3$-3_3 transitions of Ar_3-ND_2H. 146

5.4 Geometries of the Ne_3-NH_3 isotopomers in the principal inertial axis system. 148

5.5 Predicted energy level diagram for the $^{20}Ne_3$-NH_3 and $^{22}Ne_3$-NH_3 prolate symmetric tops. 150

5.6 Predicted energy level diagram for the $^{20}Ne_2{}^{22}Ne$-NH_3 and $^{20}Ne^{22}Ne_2$-NH_3 asymmetric tops. 157

5.7 Spectra comparing the relative intensities of *a*-type and *b*-type transitions observed for $^{20}Ne_2{}^{22}Ne$-NH_3. 158

5.8 Coordinate system of Ne_3-NH_3 used for the *ab initio* calculations. 162

5.9 Comparison of the minimum energy [CCSD(T)] paths of the Ne-NH_3 dimer, Ne_2-NH_3 trimer, and Ne_3-NH_3 tetramer as a function of the θ coordinate. 171

5.10 Comparison of the minimum energy [CCSD(T)] paths of the Ne_3-NH_3 tetramer as a function of the the θ coordinate for $\phi=0^\circ$ with the C_3 axis of NH_3 lying in the *ac*-plane of the tetramer. 173

CHAPTER 1

Introduction

The notion of forces between molecules dates back to the late 19th century with the pioneering work of Johannes Diderik van der Waals.[1] Van der Waals won the Nobel Prize in Physics in 1910, in part, for his development of the theory of corresponding states which established an equation of state for the relationship between the pressures, volumes, and temperatures of gases and liquids. The early contributions of van der Waals have had a lasting impact in chemistry as demonstrated by the common reference in textbooks that all attractive forces between molecules are 'van der Waals' interactions.[2,3,4] His work, in essence, laid the foundation for realizing the fundamental connection between the properties of bulk matter and intermolecular forces.

Since the time of van der Waals, our understanding of intermolecular interactions has continued to evolve. Crucial advances[5,6,7] were made at the beginning of the 20th century and after the work of London[8] in the 1930s, it was established that the interaction energy between molecules was composed of four distinct components, termed the electrostatic, induction, dispersion, and exchange energies. The origins of the first three components are rooted in the physical properties of the individual substituents, that is, the permanent multipole moments and polarizabilities of the molecules involved in the interaction. For neutral species, the electrostatic, induction, and dispersion energies can be thought of as arising from multipole-multipole, multipole-induced multipole, and induced multipole-induced multipole interactions, respectively. The fourth component is

quantum mechanical in origin and is a result of the Pauli exclusion principle which forbids two electrons with the same spin from penetrating the same region of space. These four components form the core of the classical theory of intermolecular interactions and when combined in a pairwise additive manner, can often, but not always, provide a qualitative explanation of bulk phase properties. A well-cited exception is the inadequacy of the pairwise additive approach for the prediction of the crystal structures of rare gases (Rg). Under the assumption of pairwise additivity, a hexagonal close-packed structure is expected for all Rg atom solids except helium, while X-ray diffraction experiments prove that the actual structures are face-centered cubic.[9] Furthermore, the experimentally determined crystal binding energies deviate from the theoretical values by about 10%.

Since intermolecular interactions are not strictly additive, a rigorous, quantitative description of condensed phases requires knowledge of the contributions made by many body forces. Thus, to achieve molecular level understanding of condensed phases, it is necessary to accurately characterize the nature of both the additive and the nonadditive contributions to intermolecular interaction energies. The primary goal is therefore to construct potential energy surfaces that capture each component of the interaction energy between molecules and to relate these to intrinsic, physical properties of the substituents involved. Typically, interaction potentials are derived using one of two methods: a) by fitting experimental data to mathematical expressions or b) via direct *ab initio* quantum mechanical calculations.[10] In general, the nonadditive contributions to potential energy surfaces are not well understood. The key to achieving an accurate picture of intermolecular interactions on the microscopic level thus lies in the parallel pursuit of

experimental methods that identify nonadditive effects and the derivation of functional forms that describe them.

Historically, experimental attempts to elucidate the role of nonadditive contributions to intermolecular interaction energies were made via measurements of gas imperfections[11] and molecular beam scattering techniques.[12,13] The successes of these experiments were limited by their sensitivity and accuracy. A more recent approach which overcomes these problems involves the measurement of high resolution spectra of weakly bound complexes that are formed in molecular beam expansions. These complexes are held together mainly by dispersion interactions and are commonly called van der Waals molecules. During the formation of these species in a molecular beam, low vibrational and rotational temperatures are achieved and as a result, only the lowest energy levels are populated. This reduces the spectral congestion. Furthermore, since van der Waals complexes are studied in a collision-free environment, the experimental data are not obscured by structural disorder or spatial and temporal inhomogeneities which plague bulk phase measurements.[14] This allows the determination of spectroscopic constants with great precision and these parameters are, in turn, intrinsically sensitive to the fine details of the potential energy surface that describes the weak interaction. Evidence of three body and higher order effects is obtained through comparison of the spectra of van der Waals dimers with the spectra of larger van der Waals clusters. If the appropriate binary potentials are accurately known, the nonadditive contributions to the interaction energy can, in principle, be isolated for van der Waals complexes composed of three or more substituents. Once the nonadditive effects are identified, various models of

the nonadditivity can be tested for their ability to reproduce the spectral deviation from pairwise additive predictions.

Van der Waals molecules are particularly attractive candidates for studying nonadditive effects because the size of the weakly bound cluster can be increased in a stepwise fashion. In general, Rg_n-molecule systems are prototypes for investigating solvation on the molecular level.[14] Rare gas atoms are the ideal choice of solvent since they serve as structureless probes of the weak interaction with the molecule of interest. These complexes are readily produced in a molecular beam expansion and several Rg-Rg and Rg-molecule potentials are well-determined. This allows accurate identification of nonadditive contributions to the interaction energies of the larger clusters. In principle, higher order nonadditive effects can be isolated as Rg atoms are added to the cluster in a stepwise fashion provided that the lower order terms are well-characterized from the analysis of the smaller clusters. Since van der Waals complexes are held together by weak forces, they often exhibit large amplitude bending and stretching modes with frequencies on the order of tens or hundreds of GHz.[15] These motions depend directly and sensitively on the intermolecular potential energy surface. The experimental information extracted from the measurement of van der Waals vibrations and excited vibrational states may be used to build and test theoretical models that describe how to couple the intermolecular and intramolecular modes in weakly bound complexes. The ability to produce a range of different sizes of Rg_n-molecule complexes via molecular beam techniques thus affords the opportunity to observe, on the microscopic scale, how both the structural and dynamical properties of weakly bound systems evolve as successive Rg atoms are added.

Furthermore, the molecule of interest can be spectroscopically probed in cryogenic Rg matrices which provides a definition of the bulk limit that the Rg_n-molecule clusters approach.[16] In this respect, van der Waals clusters have the potential to bridge the gap between isolated molecules and condensed phases.

The current work describes a series of experimental and *ab initio* computational investigations of van der Waals complexes containing one, two, and three Rg atoms paired with NH_3. The desire to understand the physical and chemical properties of NH_3 on the microscopic level arises from its critical role in a variety of processes. Since the reactivity of NH_3 depends on interactions between NH_3 and other molecules, a precise knowledge of weak interactions with NH_3 is integral to the understanding of these processes on the molecular level. The primary use of NH_3 is agricultural. It is commonly used as a fertilizer, either by direct application or in the form of ammonium salts (nitrates, sulfates, and phosphates).[17] Industrial uses of NH_3 include: petroleum refining, metallurgical processes, semiconductor manufacturing, rubber processing, welding, and as a solvent for scrubbing fossil fuel combustion streams. Ammonia is used commercially as a refrigerant and as a reagent for making explosives, sulfuric acid, nitric acid, acetaminophen, resins, dyes, insecticides, household cleaning agents, and synthetic fibres such as rayon and nylon. In the laboratory, NH_3 is known for its ability to solvate electrons. Alkali metals dissolve in NH_3 to form a blue solution which conducts electricity and is a good reducing agent. In this capacity, NH_3 is a necessary solvent for certain synthetic routes such as the Birch reduction in which aromatic rings are reduced to nonconjugated dienes. Ammonia has been of interest to astronomers and astrophysicists

for over 30 years. In fact, NH_3 was the first polyatomic molecule[18] detected in space and has since been found to be abundant in the interstellar medium, stars, comets, meteorites, as well as in the atmospheres of Jupiter, Saturn, Uranus, and Neptune through radioastronomical methods. Recent astrophysical observations have attempted to link the abundance of deuterated forms of NH_3 with the level of surface chemistry activity in various interstellar regions.[19,20]

The spectroscopy of NH_3 is complicated by the presence of a soft inversion coordinate. The nitrogen atom can move from its position at the apex of the pyramidally shaped molecule through the plane of the three hydrogen atoms to the other side of the plane. This is characterized by a double well potential and quantum mechanical tunnelling through the barrier between the two potential minima leads to a splitting of the vibrational energy levels into two tunnelling states. The transition between the two inversion tunnelling components of the ground vibrational state of NH_3 falls in the microwave region (~1.25 cm^{-1}) of the electromagnetic spectrum.[21] The inversion spectrum of NH_3 was measured by Cleeton and Williams in 1934 and was, in fact, the first microwave spectrum ever reported.[22] Townes and co-workers successfully devised a way to invert the population of the two states which ultimately led to the development of the maser.[23] The fact that the inversion splitting of NH_3 falls in the microwave region was elementary to the discovery of the maser since spontaneous emission is proportional to the cube of the transition frequency and is therefore very weak in this region. Masers, and the lasers that followed, have had a large impact in communications, navigation, medicine, and a host of other fields.

Since NH_3 is integral to many processes and has a rich spectroscopic history, it is not surprising that NH_3 containing van der Waals dimers have been the subject of a number of spectroscopic studies over the past 20 years. Some examples are: $(NH_3)_2$,[24,25] NH_3-H_2O,[26,27] NH_3-CO_2,[25,28] NH_3-CO,[29] NH_3-OCS,[25] NH_3-N_2O,[25,30] NH_3-SO_3,[31,32] NH_3-H_2S,[27,33] NH_3-CF_3H,[34] NH_3-CH_3OH,[35] NH_3-C_6H_5OH,[36] NH_3-HCN,[25] NH_3-HCCH,[25,37] NH_3-HCN,[38] and NH_3-HNO_3.[39] In gas phase binary complexes, NH_3 acts solely as a hydrogen acceptor or Lewis base in contrast to H_2O which exhibits amphoteric behaviour. High resolution spectra provide the necessary information for the construction of accurate potentials to characterize these weak interactions and explain such anomalous behaviour. In addition to the large volume of work on NH_3-molecule complexes, spectroscopic studies of the Ar-NH_3 dimer have been reported in the microwave,[25,40,41] submillimeter,[41,42] and infrared[43,44,45,46,47] regions. These investigations have shown that the NH_3 subunit undergoes large amplitude internal rotation and inversion motions while bound to the Ar atom. This leads to the observation of multiple internal rotor and inversion tunnelling states in the spectrum of the Ar-NH_3 dimer. The desire to understand these complicated internal dynamics on the molecular level has led to numerous theoretical studies of Ar-NH_3 in recent years.[48,49,50,51,52,53] Of the previously reported NH_3 containing van der Waals dimers, Ar-NH_3 is the simplest starting point for investigating the dynamics of weak interactions with NH_3. This arises from the fact that the dimensionality of the required model is reduced when the binding partner is a spherical Rg atom instead of a molecule. In general, the Ar-NH_3 dimer is viewed as a model system for studying the coupling of intermolecular and intramolecular modes in weakly bound

complexes. Furthermore, Ar-NH_3 is a prototype for modelling a 'symmetric top and ball' interaction potential in the same way that the Ar-HCl complex was adopted as a 'rod and ball' model.[54,55,56,57]

Despite extensive studies of Ar-NH_3, there have been no previous spectroscopic investigations of other Rg-NH_3 dimers. High resolution spectra of the other dimers in this series promise to reveal how the size and polarizability of the Rg binding partner influences the internal rotation and inversion dynamics of NH_3. Information about the internal rotation of NH_3 can be extracted from the spectra of excited internal rotor tunnelling states as well as through analysis of the nuclear quadrupole hyperfine structure arising from the presence of the quadrupolar ^{14}N nucleus. The observation of inversion tunnelling splittings in the spectra of the deuterated isotopomers can provide information about the inversion of ammonia in the ground state of the van der Waals dimers. This information is not available from the spectra of the NH_3 containing isotopomers since one inversion tunnelling component of the ground internal rotor state is missing due to the requirements of nuclear spin statistics. The spectroscopic studies can also be extended to larger van der Waals clusters such as the Rg_2-NH_3 trimers and Rg_3-NH_3 tetramers to determine the effect of multiple Rg atom binding partners on the internal dynamics of NH_3. Microwave investigations of the trimers and tetramers also offer the opportunity to study the nonadditive contributions to the interaction energies of NH_3 containing van der Waals complexes. The argon containing trimers and tetramers are of particular interest in this respect since the Ar-NH_3[51] and Ar-Ar[58,59,60] potentials are well-determined. The spectra may be complemented by *ab initio* calculations which provide qualitative

information about the topologies of the intermolecular potential energy surfaces of the Rg_n-NH_3 (n=1, 2, 3) complexes. For example, a comparison of the *ab initio* derived barriers to the internal rotation of NH_3 in the Rg_n-NH_3 (n=1, 2, 3) clusters can assist in the interpretation of the experimentally determined ^{14}N nuclear quadrupole coupling constants which are sensitive to the orientation and internal rotation dynamics of NH_3 within the complexes.

The remainder of this thesis is divided into five chapters. Chapter 2 outlines the principles of Fourier transform microwave spectroscopy and describes the technical details of the instrument used to record the rotational spectra of the Rg_n-NH_3 (n=1, 2, 3) complexes. Chapter 3 is devoted to the spectroscopic investigations of the Rg-NH_3 (Rg=Kr, Ar, Ne) dimers. The structures and dynamics of the dimers are detailed through analysis of the rotational constants, the ^{14}N nuclear quadrupole hyperfine structure, and the inversion tunnelling splittings. Furthermore, three *ab initio* potential energy surfaces for the Ne-NH_3 dimer are presented and the topologies are discussed in terms of the related spectroscopic observations. Chapter 4 describes the rotational spectra of the Rg_2-NH_3 (Rg=Ar, Ne) trimers and *ab initio* calculations for Ne_2-NH_3. Comparisons are made between the experimentally and theoretically derived results of the van der Waals dimers and trimers. In Chapter 5, the microwave studies are extended to include the Rg_3-NH_3 (Rg=Ar, Ne) tetramers. *Ab initio* calculations for the Ne_3-NH_3 complex are presented and compared with the measured rotational spectra and with the potential energy surfaces constructed for the two smaller Ne containing clusters. A summary of the experimental and theoretical results obtained for the Rg_n-NH_3 (n=1, 2, 3) van der Waals complexes is

given in Chapter 6 along with several considerations for future research in the field.

References

1. J. D. van der Waals, *On the Continuity of the Gaseous and Liquid states*, North Holland, Amsterdam (1988).

2. P. Atkins, *Physical Chemistry*, 5th edition, W. H. Freeman and Co., New York (1994).

3. J. McMurray and R. C. Fay, *Chemistry,* Prentice Hall, Englewood Cliffs (1995).

4. J. C. Kotz and P. Treichel, *Chemistry and Chemical Reactivity*, 3rd edition, Saunders College Publishing, Fort Worth (1996).

5. P. Debye, *Physik. Z.* **21**, 178 (1920).

6. W. H. Keeson, *Physik. Z.* **22**, 129 (1921).

7. J. C. Slater, *Phys. Rev.* **32**, 349 (1928).

8. F. London, *Trans. Faraday Soc.* **33**, 8 (1937).

9. M. L. Klein and J. A. Venables, *Rare Gas Solids,* Vol. I, Academic Press, London (1976).

10. M. J. Elrod and R. J. Saykally, *Chem. Rev.* **94**, 1975 (1994).

11. A. Michels, J. C. Abels, C. A. ten Seldam, and W. de Graaf, *Physica.* **26**, 381 (1960).

12. D. H. Everett, *Discuss. Faraday Soc.* **40**, 17 (1965).

13. R. Wolfe, J. R. Sams, *J. Chem. Phys.* **44**, 2181 (1966).

14. Z Bačić, "*Structures, Vibrational Frequency Shifts and Photodissociation Dynamics of Ar_nHF van der Waals Clusters*" in *Theory of Atomic and Molecular Clusters*, Editor J. Jellinek, Springer Verlag, Berlin (1999).

15. P. E. S. Wormer and A. van der Avoird, *Chem. Rev.* **100**, 4109 (2000).

16. L. Abouaf-Marguin, M. E. Jacox, and D. E. Milligan, *J. Molec. Spectrosc.* **67**, 24 (1977).

17. M. C. Sneed and J. L. Maynard, *General Inorganic Chemistry*, D. van Nostrand Co. Inc., Toronto (1942).

18. G. Herzberg, *Molecular Spectra and Molecular Structure,* Vol. II, 2nd edition, Kreiger Publishing Co., Malabar (1991).

19. Y. Peng, S. N. Vogel, and J. E. Carlstrom, *Astrophys. J.* **418**, 255 (1993).

20. E. Roueff, S. Tine, L. H. Coudert, G. Pineau des Forets, E. Falgraone, and M. Gerin, *Astron. Astrophys.* **354**, L63 (2000).

21. M. W. P. Strandberg, *Microwave Spectroscopy*, Methuen and Co. Ltd., New York (1954).

22. C. E. Cleeton and N. H. Williams, *Phys. Rev.* **45**, 234 (1934).

23. A. Lytel, *Lasers and Masers*, Howard W. Sams & Co., Indianapolis (1964).

24. E. N. Karyakin, G. T. Fraser, J. G. Loeser, and R. J. Saykally, *J. Chem. Phys.* **110**, 9555 (1999); and references therein.

25. G. T. Fraser, D. D. Nelson Jr., A. Charo, and W. Klemperer, *J. Chem. Phys.* **82**, 2535 (1985).

26. G. T. Fraser and R. D. Suenram, *J. Chem. Phys.* **96**, 7287 (1992); and references therein.

27. P. Herbine, T. A. Hu, G. Johnson, and T. R. Dyke, *J. Chem. Phys.* **93**, 5485 (1990).

28. G. T. Fraser, K. R. Leopold, and W. Klemperer, *J. Chem. Phys.* **81**, 2577 (1984).

29. G. T. Fraser, D. D. Nelson Jr., K. I. Peterson, and W. Klemperer, *J. Chem. Phys.* **84**, 2472 (1986).

30. G. T. Fraser, D. D. Nelson Jr. G. J. Gerfen, and W. Klemperer, *J. Chem. Phys.* **83**, 5442 (1985).

31. M. Canagaratna, J. A. Phillips, H. Goodfriend, and K. R. Leopold, *J. Am. Chem. Soc.* **118**, 5290 (1996).

32. M. Canagaratna, M. E. Ott, and K. R. Leopold, *Chem. Phys. Lett.* **281**, 63 (1997).

33. G. Hilpert, G. T. Fraser, R. D. Suenram, and E. N. Karyakin, *J. Chem. Phys.* **102**, 4321 (1995).

34. G. T. Fraser, F. J. Lovas, R. D. Suenram, D. D. Nelson Jr., and W. Klemperer, *J. Chem. Phys.* **84**, 5983 (1986).

35. G. T. Fraser, R. D. Suenram, F. J. Lovas, and W. J. Stevens, *Chem. Phys.* **125**, 35 (1988).

36. A. Schiefke, C. Deusen, C. Jacoby, M. Gerhards, M. Schmitt, and K. Kleinermanns, *J. Chem. Phys.* **102**, 9197 (1995).

37. G. T. Fraser, K. R. Leopold, and W. Klemperer, *J. Chem. Phys.* **80**, 1423 (1984).

38. G. T. Fraser, K. R. Leopold, D. D. Nelson Jr., A. Tung, and W. Klemperer, *J. Chem. Phys.* **80**, 3073 (1984).

39. M. E. Ott and K. R. Leopold, *J. Chem. Phys. A.* **103**, 1322 (1999).

40. D. D. Nelson Jr., G. T. Fraser, K. I. Peterson, K. Zhao, and W. Klemperer, *J. Chem. Phys.* **85**, 5512 (1986).

41. E. Zwart, H. Linnartz, W. L. Meerts, G. T. Fraser, D. D. Nelson Jr., and W. Klemperer, *J. Chem. Phys.* **95**, 793 (1991).

42. E. Zwart and W. L. Meerts, *Chem. Phys.* **151**, 407 (1991).

43. A. Bizzari, B. Heijmen, S. Stolte, and J. Reuss, *Z. Phys. D.* **10**, 291 (1988).

44. C. A. Schmuttenmaer, R. C. Cohen, J. G. Loeser, and R. J. Saykally, *J. Chem. Phys.* **95**, 9 (1991).

45. G. T. Fraser, A. S. Pine, and W. A. Kreiner, *J. Chem. Phys.* **94**, 9061 (1991).

46. A. Grushow, W. A. Burns, S. W. Reeve, M. A. Dvorak, and K. R. Leopold, *J. Chem. Phys.* **100**, 2413 (1994).

47. C. A. Schmuttenmaer, J. G. Loeser, and R. J. Saykally, *J. Chem. Phys.* **101**, 139 (1994).

48. G. Chałasiński, S. M. Cybulski, M. M. Szczęśniak, and S. Scheiner, *J. Chem. Phys.* **91**, 7809 (1989).

49. M. Bulski, P. E. S. Wormer, and A. van der Avoird, *J. Chem. Phys.* **94**, 491 (1991).

50. J. W. I. van Bladel, A. van der Avoird, P. E. S. Wormer, *J. Chem. Phys.* **94**, 501 (1991); *J. Phys. Chem.* **95**, 5414 (1991); *Chem. Phys.* **165**, 47 (1992).

51. C. A. Schmuttenmaer, R. C. Cohen, and R. J. Saykally, *J. Chem. Phys.* **101**, 146 (1994).

52. F. -M. Tao and W. Klemperer, *J. Chem. Phys.* **101**, 1129 (1994).

53. J. Milan, N. Halberstadt, G. van der Sanden, and A. van der Avoird, *J. Chem. Phys.* **106**, 9141 (1997).

54. J. M. Hutson, *J. Chem. Phys.* **89**, 4550 (1988).

55. G. Chałasiński, M. M. Szczęśniak, and B. Kukawska-Tarnawska, *J. Chem. Phys.* **94**, 6677 (1991).

56. M. M. Szczęśniak, R. A. Kendall, and G. Chałasiński, *J. Chem. Phys.* **95**, 5169 (1991).

57. J. M. Hutson, *J. Phys. Chem.* **96**, 4237 (1992).

58. E. A. Colbourn and A. E. Douglas, *J. Chem. Phys.* **65**, 1741 (1976).

59. P. R. Herman, P. E. LaRocque, and B. P. Stoicheff, *J. Chem. Phys.* **89**, 4535 (1988).

60. R. Aziz, *J. Chem. Phys.* **99**, 4518 (1993).

CHAPTER 2

Experimental

The rotational spectra of the $Rg_{1,2,3}$-NH_3 complexes have been recorded using a pulsed molecular beam Fourier transform microwave (FTMW) spectrometer. Before presenting these studies in detail, it is instructive to provide an overview of FTMW spectroscopy and a description of the spectrometer used for this research. The current chapter is divided into three parts. The first section provides a general explanation of the underlying principles of FTMW spectroscopy and explains the advantages of this technique over waveguide-based microwave experiments. Secondly, the theoretical basis of FTMW is briefly described. The most important mathematical expressions are provided and related to key experimental requirements. The final section provides a more detailed description of the mechanical and electronic components of the FTMW spectrometer employed in this work and outlines the general procedure for measuring the rotational spectra of van der Waals complexes.

2.1 Overview of FTMW spectroscopy

In FTMW spectroscopy, a microwave cavity is formed by two spherical mirrors which are installed inside a vacuum chamber. The cavity can be tuned by changing the separation of the mirrors so that it is in resonance with a desired microwave frequency. A gaseous sample is introduced into the chamber through a pulsed nozzle and the supersonic jet expansion propagates along the microwave cavity axis. A microwave pulse

is applied and if the sample has a rotational transition within the bandwidth of the microwave cavity, the dipole moments of the individual molecules align in the electric field and the molecules rotate in phase with each other as a result of the coherence property of the external microwave radiation. This is detected as a macroscopic polarization of the molecular ensemble that oscillates with the rotational transition frequency of the molecules. The coherent signal emitted as a consequence of the oscillating macroscopic dipole moment is recorded as a function of time as the molecules travel the length of the cavity and decays as the molecules collide with the back mirror. The digitized time domain signal is then Fourier transformed to obtain a frequency spectrum (and ultimately a power spectrum) and the entire sequence can be repeated and the signals averaged.

The principal advantages that FTMW spectroscopy offers over traditional waveguide-based microwave techniques are an increased sensitivity and resolution. The heightened sensitivity of FTMW allows the measurement of rotational spectra of molecules that possess low dipole moments and has two main origins. The first is inherent to the FT procedure itself since each pulse cycle of the experiment provides time domain data which includes spectral information over a range of frequencies. The second arises from the use of a molecular beam expansion in the FTMW experiment. In the molecular beam, the motion of the molecules is nearly restricted to a translational motion along the direction of the beam propagation. Through efficient cooling, very low rotational temperatures (< 1 K) are achieved and only the lowest energy rotational levels of the sample molecules are populated. Furthermore, the low rotational temperatures

create large population differences between adjacent energy levels. This enhances the sensitivity with which the lowest energy rotational transitions can be measured. The incorporation of a molecular beam also provides the opportunity to study unstable molecules, such as van der Waals complexes and radicals, since the sample in the microwave cavity essentially experiences a collision-free environment. These species cannot be studied using static gas samples as in waveguide-based spectroscopy. The increased resolution of FTMW spectroscopy allows the measurement of spectral hyperfine features such as tunnelling splittings for molecules that undergo internal motions and nuclear quadrupole hyperfine structure for species that contain quadrupolar nuclei. High resolution is achieved because the traditional sources of line broadening in static gas samples, such as pressure broadening and Doppler broadening, are removed by the use of a molecular beam. Typically, the line widths of our FTMW spectra are on the order of 7 kHz and the transition frequencies are recorded with a precision of ±1 kHz.

2.2 Theoretical considerations

The theoretical basis of FTMW spectroscopy is rooted in the Bloch equations which were originally developed for NMR spectroscopy. The electric field analogues of the Bloch equations have been previously derived.[1,2,3] These describe the interaction between the electric dipole moments of the sample molecules and the electromagnetic field that is pulsed into the microwave cavity. In the derivation, the molecular sample is treated as an ensemble of N two-level systems. The two energy levels, 'a' and 'b', are separated in energy by $\hbar\omega_o$ where ω_o is the angular transition frequency. Each two level-

system is described by a wavefunction that is a superposition of the stationary wavefunctions of the two states, $|a\rangle$ and $|b\rangle$, with each term multiplied by a time dependent coefficient, a(t) and b(t), respectively. Interactions between the N systems are neglected and thus each system is described by the same Hamiltonian, $\hat{H}$, which is the sum of a zeroth order term, $\hat{H}_o$, and a perturbation term, $\hat{H}_{int} = -\hat{\mu}\,\varepsilon_o\cos(\omega t)$. The latter defines the interaction between the electric dipole moment (μ) of the molecular system and the applied electromagnetic radiation with angular frequency ω. In the density matrix formalism, the ensemble average of the dipole moment, $\langle\overline{\mu}\rangle$, is given by the following equation:

$$\langle\overline{\mu}\rangle = \frac{1}{N}\sum_{j=1}^{N}\langle\overline{\mu}\rangle_j = \mathrm{Tr}\{\overline{\rho}\cdot\overline{\mu}\}. \qquad (2.1)$$

The 2 x 2 density matrix, $\overline{\rho}$, contains the time dependent matrix elements ρ_{aa}, ρ_{ab}, ρ_{ba}, and ρ_{bb}. The diagonal elements, ρ_{aa} and ρ_{bb}, are the population probabilities of energy levels 'a' and 'b', respectively. The off-diagonal elements, ρ_{ab} and ρ_{ba}, are the coherence terms which define the phase relations between the wavefunctions of the two energy levels. The density matrix elements are defined as:

$$\rho_{aa} = \frac{1}{N}\sum_{j=1}^{N} a_j(t)a_j(t)^*,\quad \rho_{bb} = \frac{1}{N}\sum_{j=1}^{N} b_j(t)b_j(t)^*,$$
$$\rho_{ab} = \frac{1}{N}\sum_{j=1}^{N} a_j(t)b_j(t)^*,\quad \rho_{ba} = \frac{1}{N}\sum_{j=1}^{N} b_j(t)a_j(t)^*. \qquad (2.2)$$

In the 2 x 2 transition dipole moment matrix, $\overline{\mu}$, the diagonal matrix elements are zero and $\mu_{ab} = \mu_{ba}$.

$$\overline{\mu} = \begin{bmatrix} 0 & \mu_{ab} \\ \mu_{ba} & 0 \end{bmatrix} \tag{2.3}$$

Thus, from equation (2.1),

$$\langle \overline{\mu} \rangle = \mu_{ab}\{\rho_{ab(t)} - \rho_{ba(t)}\}. \tag{2.4}$$

The macroscopic polarization, P(t), of the molecular ensemble is defined by multiplying equation (2.4) by the number density (^{1}N) of the two-level systems. The density matrix evolves with time according to the time-dependent Schrödinger equation. In density matrix notation:

$$i\hbar \frac{\partial \rho}{\partial t} = [\overline{H}, \overline{\rho}]. \tag{2.5}$$

Substitution of the Hamiltonian and density matrix representations into equation (2.5) yields a set of coupled differential equations which define the first derivatives of the density matrix elements with respect to time. These are simplified by transformation into a reference frame that rotates with the frequency of the external radiation, ω, and by invoking the rotating wave approximation which neglects the high frequency terms.[3] These equations can be expressed in terms of the real, physical variables: u(t), v(t), w(t), and s, which are linear combinations of the density matrix elements in the new reference frame.

$$
\begin{aligned}
u(t) &= \rho_{ab}(t)e^{-i\omega t} + \rho_{ba}(t)e^{i\omega t}, \\
v(t) &= i[\rho_{ba}(t)e^{i\omega t} + \rho_{ab}(t)e^{-i\omega t}], \\
w(t) &= \rho_{aa}(t) - \rho_{bb}(t), \\
s(t) &= \rho_{aa}(t) + \rho_{bb}(t).
\end{aligned}
\tag{2.6}
$$

The first two variables, u(t) and v(t), are coherence terms which are related to the real and imaginary portions of the macroscopic polarization of the molecular ensemble, respectively and w(t) is the population difference of the two energy levels. The sum of the populations in the two energy levels, s, is time independent. The coupled linear differential equations in terms of the new variables are known collectively as the Bloch equations:

$$
\begin{aligned}
\dot{u} &= \Delta\omega \cdot v, \\
\dot{v} &= \Delta\omega \cdot u - x \cdot w, \\
\dot{w} &= x \cdot v, \\
\dot{s} &= 0,
\end{aligned}
\tag{2.7}
$$

where $\Delta\omega = \omega_o - \omega$ is the off-resonance of the external microwave radiation from the transition frequency and $x = \mu_{ab}\,\varepsilon/\hbar$ is the Rabi frequency which depends on the transition dipole moment of the molecules, μ_{ab}, and the amplitude, ε, of the applied electromagnetic field. Relaxation effects can be added phenomenologically to the Bloch equations.

The macroscopic polarization of the ensemble is induced by interaction with a pulse of microwave radiation. If a "hard" microwave pulse, defined by $x >> \Delta\omega$, is applied, the off-resonance factor $\Delta\omega$ can be neglected. With $\Delta\omega = 0$, $x \neq 0$, and the initial conditions: $u(0) = v(0)$, $w(0) = w_o$, the Bloch equations (2.7) can be solved to obtain:

$$
\begin{aligned}
u(t) &= 0; \\
v(t) &= -w_o \sin(xt_p), \\
w(t) &= w_o \cos(xt_p).
\end{aligned}
\tag{2.8}
$$

Maximum polarization of the ensemble is therefore achieved when $xt_p = \pi/2$ or $(2n+1)\pi/2$ where n = 0, 1, 2, ... etc. This is called the $\pi/2$-condition. After a pulse of duration $t_p = \pi/2x$, the initial population difference, w_o, is converted into a macroscopic polarization of the molecular ensemble since $v(\pi/2x) = -w_o$ from equation (2.8). This is schematically represented using a Bloch vector diagram as shown in Figure 2.1. Thus, to achieve the maximum polarization of the sample, the microwave excitation pulse must be carefully optimized at the beginning of the experiment to ensure that the $\pi/2$-condition is met. The macroscopic polarization, P(t), of the molecular ensemble is given by the expression:

$$P(t) = {}^{1}N\mu_{ab}\{u(t)\cos(\omega t) - v(t)\sin(\omega t)\}. \qquad (2.9)$$

Figure 2.1 Bloch vector diagram depicting the $\pi/2$-condition in a rotating reference frame. The initial population difference, w_o, between the two energy levels is converted into a macroscopic polarization along v, after application of a $\pi/2$ pulse of microwave radiation that is resonant with a molecular transition frequency.

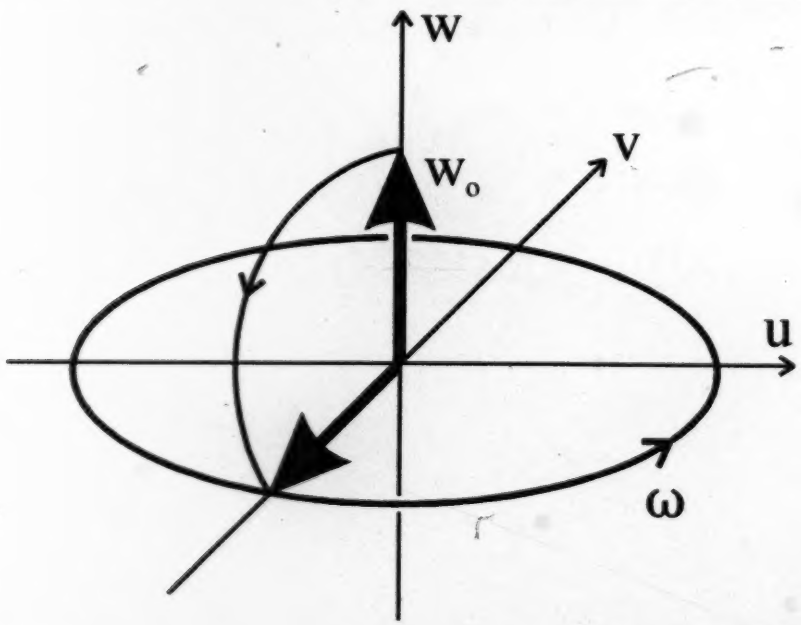

After the polarizing microwave pulse, x = 0 and the transient emission signal is recorded. Using the initial condition $t = t_p$, the Bloch equations can be solved at time t' after the microwave pulse to obtain:

$$\begin{aligned} u(t') &= w_o \sin(\Delta\omega t'), \\ v(t') &= -w_o \cos(\Delta\omega t'), \\ w(t') &= 0. \end{aligned} \qquad (2.10)$$

Substitution in equation (2.9) yields:

$$P(t') = {}^{1}N\mu_{ab} \sin(\omega_o t'). \qquad (2.11)$$

Thus, the induced macroscopic polarization oscillates with the transition frequency, ω_o. The transient signal emitted by the molecular ensemble is proportional to the polarization and is recorded as a function of time and then Fourier transformed to obtain the frequency (and power) spectrum.

2.3 FTMW spectrometer design

The rotational spectra described in the following chapters were recorded using a pulsed molecular beam FTMW spectrometer that has been described previously.[4] The design follows that of Balle and Flygare[5] with some later modifications.[6] The basic features are summarized below and the mechanical parts of the spectrometer are shown schematically in Figure 2.2. A Fabry-Perot cavity is formed by two spherical aluminum mirrors that are 260 mm in diameter with a radius of curvature of 380 mm. The separation between the two mirrors can be adjusted from approximately 200 mm to 400

Figure 2.2 Schematic of the mechanical parts of the FTMW spectrometer. 1) Stainless steel vacuum chamber. 2) Diffusion pump (30 cm diameter) to evacuate the vacuum chamber. 3) Mechanical pump for backing the diffusion pump. 4) Spherical aluminum mirror mounted on one flange of the vacuum chamber. 5) Movable spherical aluminum mirror mounted on two rails. 6) Pulsed nozzle that introduces the gas sample into the vacuum chamber. 7) Wire hook antenna used to couple the microwave radiation into the chamber and to couple the emission signal for superheterodyne detection out of the chamber. 8) A second wire hook antenna couples the microwave radiation out of the chamber for tuning the microwave cavity into resonance. 9) Computer controlled Motor Mike to adjust the position of the movable mirror. 10) Motor Mike controller for remote control of the mirror separation. 11) Personal computer that controls the experiment. 12) Microwave diode detector used for monitoring the cavity throughput. 13) Microwave detector amplifier. 14) Oscilloscope for observing the analog signal from the microwave detector after amplification. 15) TTL pulse generator that allows phase coherent control of the experiment. 16) Pulsed nozzle driver that opens and closes the nozzle. 17) Butterfly valve to isolate the vacuum chamber from the diffusion pump. 18) Valve that vents the chamber to the atmosphere. 19) Connects the sample mixing system to the diffusion pump for evacuation. 20) Connects the sample mixing system to the mechanical pump for rough evacuation. 21) Flexible vacuum tubing with stainless steel coil reinforcement that helps to isolate the instrument from vibrations of the mechanical pump. 22) Exhaust fumes from the mechanical pump are bypassed to a fumehood.

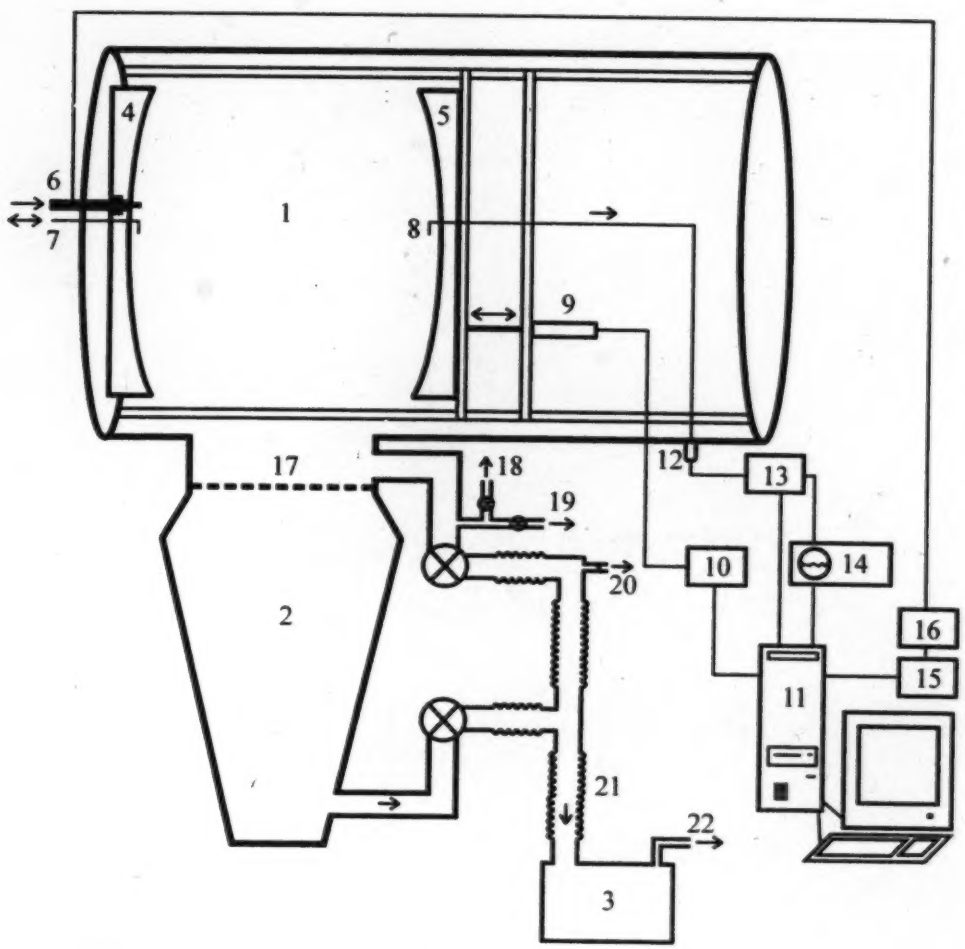
4
5
6
7
1
8
9
17
18
19
12
13
10
14
20
2
16
15
11
21
22
3

mm. The microwave cavity is stationed inside a vacuum chamber that is pumped at a speed of 2000 L s^{-1} by a diffusion pump that is 30 cm in diameter. The diffusion pump is backed by a mechanical pump. One mirror is mounted on a flange of the vacuum chamber and the other mirror can slide on two high precision linear rails. The position of the second mirror can be adjusted remotely to tune the cavity into resonance with the desired microwave frequency. The microwave source is a Hewlett-Packard synthesizer (model HP 83711 A) that generates cw radiation between 1 GHz and 20 GHz. The microwave radiation is coupled into the vacuum chamber via a wire hook antenna that is installed at the center of the stationary mirror. This same antenna is used to couple the coherent microwave molecular emission of the sample out of the chamber to a sensitive detection system. The sample is prepared at room temperature by combining the appropriate gases in a sample mixing system and is then introduced into the microwave cavity via a pulsed nozzle with an orifice diameter of 0.8 mm that is mounted near the center of the stationary mirror. The van der Waals complexes are formed by collisions of the gas molecules as they exit the nozzle in the supersonic jet expansion. To maximize the production of trimer and tetramer complexes, a high backing pressure must be maintained in the sample containment system. Since the molecular beam propagates parallel to the microwave cavity axis, each transition is detected as a Doppler doublet. The transition frequency is taken as the average of the two Doppler components.

The signal emitted by the molecular ensemble is often weak and as a result, a very sensitive detection method is required. In this case, a double superheterodyne mixing scheme is employed for detection purposes. The microwave circuit is schematically

shown in Figure 2.3. The microwave synthesizer is set to frequency, ν_m. This radiation is divided into two components of equal power. The excitation branch is fed through an isolator and then mixed with a 20 MHz reference frequency to produce two sidebands, ν_m+20 MHz and ν_m−20 MHz. The microwave cavity is tuned to the latter frequency. The microwave excitation radiation may be amplified if more power is required or attenuated to provide less power in the polarizing radiation. Two *p-i-n* diode switches are used to generate a microwave pulse which is coupled into the cavity through a circulator which limits the flow of the microwave radiation to one direction. If the molecules in the supersonic jet expansion have transitions within the bandwidth of the excitation pulse and within the bandwidth of the microwave cavity, their dipole moments align and, under the proper excitation conditions, a macroscopic polarization of the sample ensues. The microwave molecular emission signal has a frequency of ν_m−20 MHz+$\Delta\nu$ where $\Delta\nu$ is the difference between the microwave excitation frequency and the molecular transition frequency. The transient emission signal is coupled out of the cavity via the circulator and amplified. At this point, the microwave signal is mixed down to a radiofrequency (RF) using the second branch of microwave radiation (ν_m) from the synthesizer. The resulting RF signal, −20 MHz+$\Delta\nu$, is amplified and passed through a 20 MHz bandpass filter. The signal is then downconverted to 15 MHz+$\Delta\nu$, using a second mixer that couples in a 35 MHz reference frequency. After passing through a 15 MHz bandpass filter, the RF signal (15 MHz+$\Delta\nu$) is amplified and coupled into a transient recorder that contains an analog-to-digital convertor. From there, the digitized time domain data is sent into a personal computer and Fourier transformed to obtain the spectrum from which the microwave

Figure 2.3 The microwave circuit. 1) Microwave synthesizer with a built-in 10 MHz reference crystal. The crystal provides a reference frequency for the pulse generator and is multiplied to obtain the necessary mixing frequencies for the superheterodyne detection scheme. 2) Power divider splits the microwave radiation. One branch is used for molecular excitation in the microwave cavity and the other branch is used to later downconvert the detected emission signal. 3) Isolator prevents radiation from propagating backward and damaging the synthesizer. 4) Microwave *p-i-n* diode switch. 5) Double balanced mixer. 6) Microwave signal amplifier. 7) Microwave *p-i-n* diode switch. A microwave pulse is generated when 4) and 7) are opened. 8) Circulator for coupling excitation radiation into the cavity and coupling the molecular emission signal out of the cavity. 9) Microwave *p-i-n* diode switch isolates the detection circuit during the microwave excitation pulse. 10) Low noise microwave signal amplifier. 11) Image rejection mixer. The signal is mixed down to the radiofrequency (RF) range using the second brach of radiation from the synthesizer. 12) RF signal amplifier. 13) 20 MHz bandpass filter. 14) Mixer to downconvert the emission signal a second time to around 15 MHz. 15) 15 MHz bandpass filter. 16) RF amplifier. 17) Transient recorder with a built-in A/D converter digitizes the RF signal. 18) Personal computer receives and analyzes digitized time domain signal. 19) TTL pulse generator that enables phase coherent control of the experiment. It controls a) the pulsed nozzle, b) c) the *p-i-n* diode switches, and d) the transient recorder.

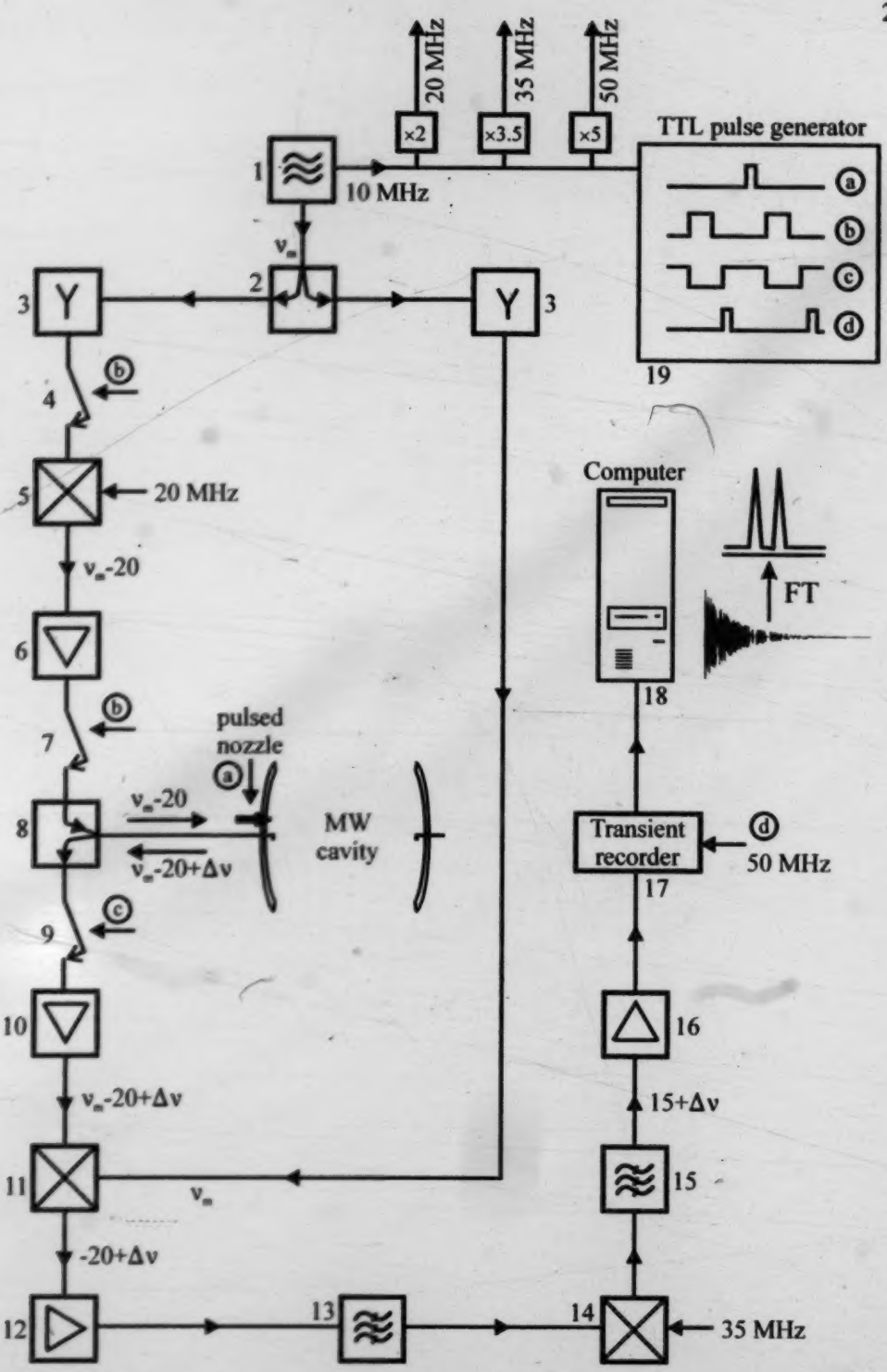
20 MHz
35 MHz
50 MHz
×2
×3.5
×5
TTL pulse generator
1
10 MHz
ν_m
2
3
Y
Y
3
19
4
b
5
20 MHz
ν_m-20
6
7
b
pulsed nozzle
a
8
ν_m-20
ν_m-20+Δν
MW cavity
9
c
10
ν_m-20+Δν
11
ν_m
-20+Δν
12
13
14
35 MHz
Computer
FT
18
Transient recorder
d
50 MHz
17
16
15+Δν
15

transition frequencies are read.

The timing of the FTMW experiment must be carefully controlled since the molecular emission signal is often weak and must be phase coherently averaged. The key events that must be synchronized are: a) the molecular pulse from the nozzle, b) the microwave excitation pulse, c) the opening and closing of the switch protecting the detection system, and d) the triggering of the transient recorder for detection. Figure 2.4 shows the sequence of pulses used in a single FTMW experiment. The pulses to the nozzle driver, switches, and transient recorder are produced by a TTL signal generator that is clocked by the 10 MHz reference crystal that is built into the microwave source. The entire pulse sequence can be repeated and the signal averaged until a satisfactory signal-to-noise ratio is achieved in the spectrum.

At the outset of studying a new van der Waals complex, the rotational spectrum is predicted according to an estimated structure. Normally, the most intense transitions are sought first. Since this may require scanning over a large frequency range, it is necessary to estimate several experimental parameters that will affect the emission signal detected in the FTMW experiment. If complexes of similar composition have been previously reported, the experimental conditions are optimized for a known van der Waals complex before searching for the new species. An important parameter to consider is the composition of the sample mixture. The ratios of gases included in the sample mixture and the total backing pressure are optimized by trial and error according to the strength of the signal each sample produces. The amount of sample injected into the vacuum chamber is adjusted by manually altering the voltage of the pulsed nozzle driver. The

Figure 2.4 Pulse sequence for a single FTMW experiment. a) A microwave pulse of duration ~ 0.2 - 10 μs is generated while b) the protective switch to the detection circuit is closed. After allowing time for the excitation radiation to dissipate in the cavity, the protective switch is opened. c) Data acquisition is triggered and a background signal is recorded. d) The nozzle is opened for a short time (~ 1 ms) allowing gas molecules into the chamber and after a suitable delay (0.7 ms), e) a second pulse of microwave radiation is coupled into the cavity while f) the protective switch is closed. g) A second trigger begins data acquisition and the molecular signal can be isolated after subtraction of the background signal. The entire pulse sequence can be repeated and the signals averaged.

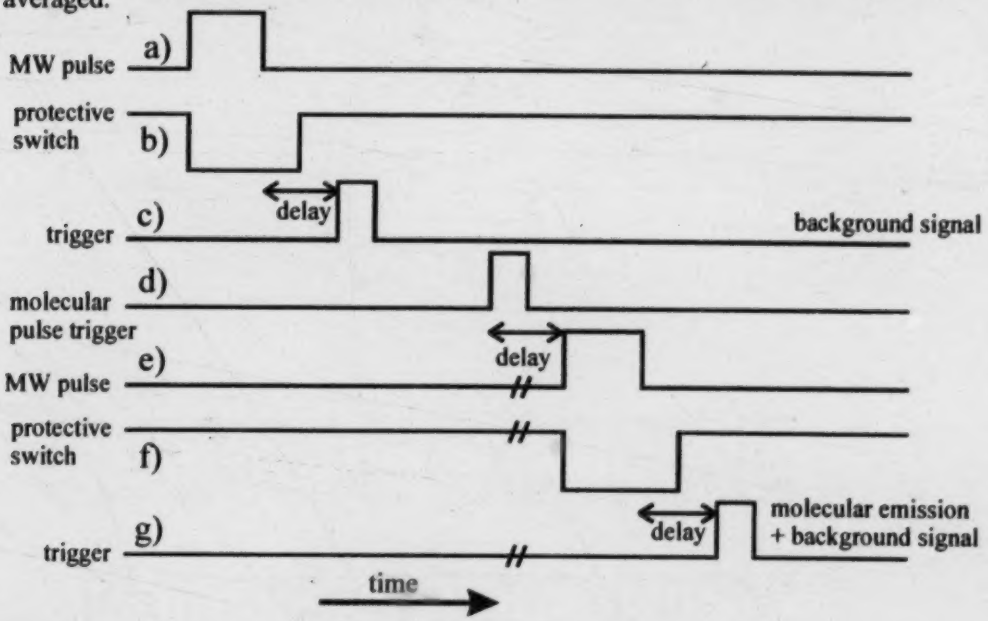

lengths of the wire antennas in the microwave cavity must be changed depending on the frequency of the desired search range. To generate the maximum polarization of the molecular sample for detection purposes, the microwave power and the microwave pulse length must be optimized. This requires consideration of the magnitude of the dipole moment expected for the species under study. The power of the excitation radiation can be increased by addition of a solid state microwave amplifier to the microwave circuit as shown in Figure 2.3. This is particularly crucial when probing complexes with small

dipole moments to ensure that the $\pi/2$-condition is met. The microwave power can also be decreased if necessary by including attenuators in the excitation branch. The length of the microwave pulse is computer controlled as are the lengths of the delays between the molecular and microwave pulses and the microwave pulse and data acquisition trigger (Figure 2.4). After careful adjustment of the aforementioned parameters, a chosen frequency range is scanned automatically, usually in steps of 0.2 MHz, until a molecular emission signal is detected. Once a rotational transition is found that may be assigned to the complex of interest, the experimental parameters are carefully re-optimized for the new transition. This improves the experimental conditions of the scans for additional rotational transitions that may be less intense and whose frequencies may not be well-predicted.

References

1. J. C. McGurk, T. G. Schmalz, and W. H. Flygare, *Advances in Chemical Physics*, Vol. XXV, John Wiley and Sons, New York (1974).

2. R. L. Shoemaker, *Laser and Coherence Spectroscopy*, Editor J. I. Steinfeld, Plenum Press, New York (1978).

3. H. Dreizler, *Mol. Phys.* **59**, 1 (1986).

4. Y. Xu and W. Jäger, *J. Chem. Phys.* **106**, 7968 (1997).

5. T. J. Balle and W. H Flygare, *Rev. Sci. Instrum.* **52**, 33 (1981).

6. J. -U. Grabow and W. Stahl, *Z. Naturforsch. A: Phys. Sci.* **45**, 1043 (1990).

CHAPTER 3

Investigation of the Rg-NH_3 van der Waals dimers: Rotational spectra and *ab initio* calculations

3.1 Introduction

High resolution spectra of NH_3 containing van der Waals dimers provide invaluable information for the construction of accurate binary potentials that characterize weak interactions with NH_3. Since NH_3 has a soft inversion coordinate, modeling weak interactions with NH_3 provides an additional challenge. To construct potentials that accurately describe the highly dynamic nature of NH_3 containing van der Waals complexes, a detailed knowledge of how various intermolecular and intramolecular degrees of freedom couple together in weakly bound systems is required. The desire to understand these phenomena on the microscopic level has led to the adoption of the Ar-NH_3 complex as a model system by both spectroscopists and theoreticians.

Microwave spectra of Ar-NH_3 were first reported by Klemperer and co-workers.[1,2] They concluded that the NH_3 subunit undergoes nearly free internal rotation within the dimer complex. The measured transitions were assigned to the ground internal rotor state, associated with an *ortho* nuclear spin function for the three hydrogens. For this state, only one of the inversion components has a nonzero spin statistical weight. Zwart *et al.*[3] used microwave and submillimeter wave spectroscopy to measure and assign the spectra of the lowest energy *para* states of the Ar-NH_3 dimer which were complicated by Coriolis perturbation. In the *para* states, both inversion components have nonzero spin weights.

The spectra revealed that the inversion of NH_3 in the complex is nearly free in some states while effectively quenched in others. Submillimeter[4] and far infrared[5,6,7,8] studies of Ar-NH_3 have measured excited van der Waals bending and stretching modes while infrared[1,9,10] experiments have probed the ν_2 umbrella mode of NH_3 within the van der Waals dimer. Spectroscopic studies of van der Waals and monomer vibrations are particularly crucial for modeling the coupling of inter- and intramolecular modes in weakly interacting systems since they provide information that is sensitive to a larger region of the intermolecular potential energy surface.

Schmuttenmaer *et al.*[11] did a least squares fit of microwave, submillimeter, and far infrared transitions to obtain a three dimensional potential energy surface for the Ar-NH_3 interaction. The global minimum of 149.6 cm^{-1} corresponds to a structure in which the C_3 axis of NH_3 is almost perpendicular to the van der Waals axis ($\theta = 96.6°$) with the Ar atom situated between two hydrogen atoms ($\phi = 60°$) and a van der Waals bond length of 3.57 Å. The structural coordinates are defined in Figure 3.1. At least three *ab initio* potential energy surfaces have been reported for Ar-NH_3. The first, by Chałasiński *et al.*[12], used second order Møller-Plessett (MP2) perturbation theory and found a global minimum of 115 cm^{-1} at R = 3.75 Å, $\theta = 100°$, $\phi = 60°$. A more recent calculation by Tao and Klemperer[13] was conducted at the MP4 level with the addition of bond functions and reported a minimum of 130.1 cm^{-1} at R = 3.628 Å, $\theta = 90°$, $\phi = 60°$. Bulski *et al.*[14] constructed potential energy surfaces for four different umbrella angles of NH_3 within the Ar-NH_3 complex. For the equilibrium geometry of NH_3, the global minimum is 134.23cm^{-1} at R = 3.59 Å, $\theta = 105°$, $\phi = 60°$. In general, the *ab initio* calculations are

Figure 3.1 Coordinate system of the Rg-NH_3 dimers. R is the van der Waals bond length and is defined as the distance between the Rg atom and the center of mass of the NH_3 subunit. The angles θ and ϕ describe the orientation of the NH_3 subunit within the complex. The C_3 axis of NH_3 is along the van der Waals bond with the hydrogen atoms pointing towards the Rg atom when $\theta = 0°$. When $\theta = 90°$ and $\phi = 60°$, the C_3 axis is perpendicular to R and the Rg atom sits between two hydrogen atoms.

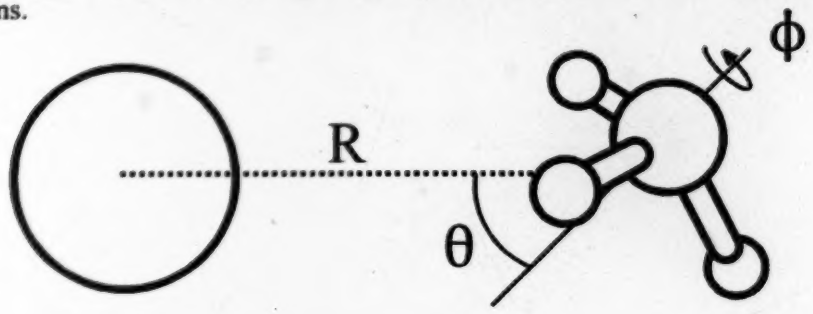

qualitatively consistent with the empirical potential of Schmuttenmaer *et al.*[11] All predicted a minimum energy structure with the C_3 axis of NH_3 nearly perpendicular to the intermolecular axis with the Ar atom in the plane between two hydrogen atoms. The anisotropy at the radial minimum as a function of the angular coordinates was well reproduced by Tao and Klemperer's surface while the other *ab initio* calculations predicted significantly higher anisotropy, particularly in the ϕ coordinate. The potential energy surfaces generated by Bulski *et al.*[14] were used to calculate the bound rovibrational states of the Ar-NH_3 dimer in a series of papers by van Bladel *et al.*[15,16,17] Their latest calculation[17] explicitly included the inversion coordinate of the NH_3 monomer. They calculated the ground state rotational constant, B, to be 2973 MHz for the inversion state that has a nonzero spin weight. This is almost 100 MHz larger than the experimentally determined value of 2876.848 MHz.[2]

Despite the extensive interest in NH_3 containing complexes, few van der Waals

complexes containing ND_3 have been measured, with exceptions such as $(ND_3)_2$,[18,19,20] ND_3-H_2O,[21] and ND_3-CO.[22] A high resolution spectroscopic study of the Ar-ND_3 complex can provide experimental information regarding the inversion of the bound ammonia monomer that is unavailable from all of the previously reported studies of Ar-NH_3. In Ar-NH_3, one inversion tunnelling state is missing due to spin statistics for each of the *ortho* nuclear spin states. This makes it impossible to obtain direct information about the inversion tunnelling for these states. The nuclear spin statistics are different for Ar-ND_3, consisting of three identical bosons (D) instead of fermions (H), and as a result, all of the inversion states have a nonzero spin statistical weight. A comparison of the inversion splitting in different internal rotor states of the Ar-ND_3 complex would provide an interesting test of the existing empirical Ar-NH_3 potential by Schmuttenmaer *et al.*[11] Although the Ar-NH_3 complex has been extensively studied, there have been no spectroscopic investigations of other Rg-NH_3 dimers. Microwave investigations of Kr-NH_3 and Ne-NH_3 provide the opportunity to study the effect of the Rg atom size and polarizability on the internal rotation and inversion of the NH_3 molecule within the weakly bound complex. In addition, Ne-NH_3 is well suited for *ab initio* calculations since the basis sets for Ne, nitrogen, and hydrogen are more computationally manageable than those for larger atoms such as Kr. This allows the use of a higher level of theory as well as the calculation of more points on the potential energy surface since the computational costs are lower.

This chapter describes the first high resolution, microwave spectroscopic investigation of the Kr-NH_3 and Ne-NH_3 van der Waals complexes. In total, 14

isotopomers of Kr-NH_3 and 10 isotopomers of Ne-NH_3 were measured including the deuterium containing species. In addition, the results of the first microwave study of Ar-ND_3 and its partially deuterated isotopomers are presented and compared with the previously reported microwave studies of Ar-NH_3.[2,3] The observed spectra correspond to the ground internal rotor states of the various dimer complexes as well as the first excited internal rotor states of the Ar-ND_3 and Kr-ND_3 complexes. The spectra reveal the presence of large amplitude internal motions of the NH_3 moiety within the dimers. The ^{14}N nuclear quadrupole hyperfine structure is analyzed in terms of the internal dynamics of NH_3. For each of the deuterated isotopomers, a tunnelling splitting is observed due to the inversion of the NH_3 subunit within the complex. Furthermore, three *ab initio* potential energy surfaces have been constructed for the Ne-NH_3 complex using MP4 and coupled cluster [CCSD(T)] theories. The topological features are discussed with respect to the spectroscopic observations and are compared with the previous theoretical studies of Ar-NH_3.[13]

3.2 Experimental Method

The rotational spectra of the Rg-NH_3 (Rg = Ne, Ar, Kr) van der Waals complexes were recorded between 4 GHz and 24 GHz using a pulsed molecular beam Fourier transform microwave spectrometer of the Balle-Flygare type[23] as described in Chapter 2. The relatively small dipole moments of the dimer complexes made it necessary to include a solid state microwave amplifier for the excitation pulses to achieve maximum polarization. The widths of single isolated lines were ~7 kHz (full width at half height);

the accuracy of the measured frequencies was estimated to be ±1 kHz.

The complexes were generated in a molecular beam expansion of a gas mixture through a pulsed nozzle with an orifice diameter of 0.8 mm (General Valve Corp., Series 9) mounted near the center of one of the cavity mirrors. The molecular expansion travelled parallel to the microwave cavity axis, and all of the observed transitions were doubled due to the Doppler effect. The rotational temperature was estimated to be less than 1 K in the expansion. The sample gas mixture was prepared at room temperature. To record the spectra of Kr-NH_3, the sample contained 0.5 % NH_3 gas and 2 % Kr with Ne as a backing gas to maintain pressures of approximately 7 atm. For Ar-NH_3, a similar mixture was prepared with 5 % Ar replacing the krypton gas and for the Ne-NH_3 studies, the mixture contained 0.5 % NH_3 in Ne. Isotopically enriched samples were used to record the spectra of the $^{15}NH_3$ (Cambridge Isotope Laboratories, 98 % ^{15}N) and ND_3 (Cambridge Isotope Laboratories, 99 % D) containing complexes. The spectra of the Rg-ND_2H and Rg-NDH_2 isotopomers were recorded using the gas mixture containing ND_3. The intensities of the Rg-ND_2H and Rg-NDH_2 transitions increased significantly once the ND_3 gas mixture was left in the sample system for several hours.

The spectroscopic assignment of transitions within the excited internal rotor states of Ar-ND_3 and Kr-ND_3 was verified using a microwave-microwave double resonance technique. For these experiments, a second microwave synthesizer was incorporated into the existing spectrometer setup. The microwave radiation from the second synthesizer was coupled into the vacuum chamber perpendicular to the microwave cavity axis using a horn antenna. The radiation from the second synthesizer was used to excite a pump

transition. The intensity of a signal transition was monitored while the second synthesizer was on resonance with the pump transition. The frequency of the second synthesizer was then moved off resonance and the intensity of the signal transition was checked a second time. An increase in the signal intensity when the pump transition was excited was taken as an indication that the pump and signal transitions shared a common energy level.

3.3 Spectral search and assignment

Previous spectroscopic studies of the Ar-NH_3 complex revealed that the rotation of the NH_3 moiety within the complex leads to the observation of several internal rotor states. An additional tunnelling splitting due to the inversion of the NH_3 subunit was observed for excited internal rotor states associated with a *para* nuclear spin function.[3,11] This splitting was not observed for the ground state or any other state associated with an *ortho* nuclear spin function. For these states, one inversion component has a nuclear spin statistical weight of zero. It can be shown by molecular symmetry group theoretical analysis[24] that upon deuterium substitution, both inversion components of the ground state have nonzero spin statistical weights.

In the molecular beam expansion, the complexes are characterized by a low rotational temperature of about 0.5 K. At this temperature, only low energy internal rotor states and those associated with a unique nuclear spin function are sufficiently populated for spectroscopic study. The tunnelling states of the Rg-NH_3, Rg-$^{15}NH_3$, and Rg-ND_3 isotopomers are differentiated by labelling them with the appropriate symmetric top rotational quantum numbers of free ammonia (j_k). For the ND_2H and NDH_2 containing

complexes, asymmetric rotor labels are used ($j_{k_a k_c}$). An additional label, K, is used to define the projection of j onto the van der Waals bond axis and is given as Σ for K = 0 and Π for K = 1. To distinguish between inversion tunnelling components, a subscript 's' or 'a' is included to denote the symmetry of the inversion wavefunction, either symmetric or antisymmetric, respectively. The nuclear spin statistical weights of the rotational energy levels of the Rg-NH_3 dimers can be determined using molecular symmetry group theory. The analysis is outlined below for the NH_3 and $^{15}NH_3$ containing isotopomers and a summary of the results for all of the isotopomers is given in Table 3.1.

3.3.1 Molecular symmetry group theory

a) Rg-NH_3 and Rg-$^{15}NH_3$

Including the inversion motion of the NH_3 monomer, the Rg-NH_3 dimers belong to the D_{3h} molecular symmetry group (Appendix 1, Table A1.1). According to Fermi-Dirac statistics, the total wavefunction of the system must be antisymmetric with respect to the interchange of any two protons and thus, the symmetry of the total wavefunction must be A_2' or A_2''. The spins of the three hydrogen nuclei combine to give eight possible nuclear spin functions which span the representation: $4A_1' \oplus 2E'$. The symmetry of the rovibronic part of the wavefunction, including the A_1' and A_2'' symmetries of the 's' and 'a' inversion components, alternates as A_1'/A_1'' (even J/odd J) for the $\Sigma 0_{0s}$ state, A_2''/A_2' for the $\Sigma 0_{0a}$ state, and E'/E'' for the $\Sigma 1_{1s}$ state. To obtain the required total wavefunction symmetry, the $\Sigma 0_{0a}$ state combines with the A_1' nuclear spin function and the $\Sigma 1_{1s}$ state combines with the E' spin function resulting in nuclear spin statistical weights of 4 and 2,

Table 3.1 Summary of molecular symmetry group theory analysis for the metastable states of the Rg-NH_3 isotopomers.

	Rg-NH_3	Rg-ND_3	Rg-ND_2H	Rg-NDH_2
Molecular symmetry group	D_{3h}	D_{3h}	C_{2v}	C_{2v}
Total symmetry required[a]	A_2'/A_2''	A_1'/A_1''	A_1/A_2	B_1/B_2
Nuclear spin symmetry[b]	$4A_1'\oplus 2E'$	$10A_1'\oplus A_2'\oplus 8E'$	$6A_1\oplus 3B_2$	$3A_1\oplus B_2$
Rotational symmetry		even J/odd J		
	A_1'/A_1''	A_1'/A_1''	A_1/A_2	A_1/A_2
NH_3 inversion symmetry		symmetric/antisymmetric		
	A_1'/A_2''	A_1'/A_2''	A_1/B_1	A_1/B_1
NH_3 internal rotation symmetry		ground state/first excited state		
	A_1'/E'	A_1'/E'	n/a	n/a
Rovibrational symmetry[c]		even J/odd J		
$\Sigma 0_{0s}$	A_1'/A_1''	A_1'/A_1''	A_1/A_2	A_1/A_2
$\Sigma 0_{0a}$	A_2''/A_2'	A_2''/A_2'	B_1/B_2	B_1/B_2
$\Sigma 1_{1s}$	E'/E''	E'/E''	n/a	n/a
Predicted nuclear spin statistical weights	$\Sigma 0_{0s}:\Sigma 0_{0a}:\Sigma 1_{1s}$		$\Sigma 0_{0s}:\Sigma 0_{0a}$	
	0:4:2	10:1:8	6:3	1:3

[a] refers to the symmetry of the total wavefunction upon exchange of identical fermions or bosons.

[b] refers to the symmetry of the nuclear spin function of the identical hydrogen or deuterium nuclei only.

[c] includes the NH_3 inversion and NH_3 internal rotation symmetries.

respectively. There is no nuclear spin function with the correct symmetry to combine with the $\Sigma 0_{0s}$ rovibronic wavefunction and consequently, the nuclear spin weight of the $\Sigma 0_{0s}$ state is zero. Thus, for the Rg-NH_3 and Rg-$^{15}NH_3$ complexes, there are two metastable internal rotor states, $\Sigma 0_{0a}$ and $\Sigma 1_{1s}$. Inversion tunnelling of NH_3 may be observed in the $\Sigma 1_1$ state depending on the Boltzmann population of the higher energy $\Sigma 1_{1a}$ state in the molecular beam expansion.

b) Rg-ND_3

The Rg-ND_3 dimers also belong to the D_{3h} molecular symmetry group (Table A1.1), but in contrast to the Rg-NH_3 dimers, the total wavefunction must be symmetric upon exchange of two deuterium nuclei since Bose-Einstein statistics applies. Due to their different nuclear spin symmetries, the $\Sigma 0_{0s}$, $\Sigma 0_{0a}$, and $\Sigma 1_{1s}$ states are all metastable in the jet expansion. Consequently, for the ND_3 containing dimers, an inversion tunnelling splitting is expected in the ground internal rotor state. As with the NH_3 containing isotopomers, inversion tunnelling splitting may be observed in the $\Sigma 1_1$ state if the higher energy $\Sigma 1_{1a}$ state has sufficient population for spectroscopic study.

c) Rg-ND_2H

The Rg-ND_2H complexes belong to the C_{2v} molecular symmetry group (Table A1.2). For the interchange of the two identical bosons, the total wavefunction must be symmetric. An inversion tunnelling splitting is expected in the ground internal rotor state and the nuclear spin statistical weights are 6 and 3 of the $\Sigma 0_{00s}$ and $\Sigma 0_{00a}$ states, respectively. There are no feasible internal motions of ND_2H in the complex that interchange the two deuterium atoms and therefore only the two inversion components of the ground internal rotor state are expected to be sufficiently populated in the molecular beam expansion.

d) Rg-NDH_2

The Rg-NDH_2 dimers also belong to the C_{2v} molecular symmetry group (Table A1.2). In this case, however, the equivalent nuclei are fermions and the total wavefunction must be antisymmetric with respect to the interchange of the two protons.

The nuclear spin statistical weights of the $\Sigma 0_{00s}$ and $\Sigma 0_{00a}$ states are 1 and 3, respectively. As described for the Rg-ND_2H complex, there is no tunnelling motion of the NDH_2 subunit that interchanges the two hydrogen atoms in this complex. Consequently, only the $\Sigma 0_{00s}$ and $\Sigma 0_{00a}$ states are expected to be observed in the spectroscopic study.

3.3.2 Isotopomers of Kr-NH_3

a) Kr-NH_3 and Kr-$^{15}NH_3$

The microwave spectrum of the $\Sigma 0_{0a}$ state of Kr-NH_3 was predicted by treating the complex as a diatomic molecule composed of a Kr atom and a spherical NH_3 moiety. The B rotational constant was estimated by scaling that reported for Ar-NH_3 by the ratio of the reduced masses of the two complexes.[2] Previous studies of Kr and Ar containing complexes, such as Ar-,[25] Kr-H_2O,[26] and Ar-,[27] Kr-CO_2,[28] revealed that the van der Waals bond lengthens by approximately 3 % upon Kr substitution. Taking this into consideration, the B rotational constant for the $\Sigma 0_{0a}$ state was predicted within 92 MHz of the value determined in this work. An advantage of working with Kr is that there are several isotopes with well separated spectra that can be observed in natural abundance: ^{86}Kr (17.37 %), ^{84}Kr (56.90 %), ^{83}Kr (11.55 %), ^{82}Kr (11.56 %), and ^{80}Kr (2.27 %).[29] Furthermore, the ^{83}Kr nucleus has a nuclear spin with quantum number I = 9/2 and an associated nuclear quadrupole moment which leads to the observation of nuclear quadrupole hyperfine structure in the rotational transitions. The analysis of this hyperfine splitting, in addition to that caused by the presence of the ^{14}N (I = 1) nucleus, provides additional information about the van der Waals interaction.

The transition frequencies assigned to the $\Sigma 0_{0a}$ state of Kr-NH_3 are listed in Appendix 2 (Table A2.1) for the ^{86}Kr, ^{84}Kr, ^{82}Kr, and ^{80}Kr containing isotopomers. The spacing between consecutive rotational transitions is relatively constant as expected under the pseudodiatomic molecule model (2B). The rotational and ^{14}N hyperfine analyses were done simultaneously using Pickett's global fitting program[30] and the spectroscopic constants obtained using an expression for linear molecules are listed in Table 3.2. For the ^{83}Kr-NH_3 isotopomer, only the hyperfine components for the J = 1-0 rotational transition were assigned due to the complicated hyperfine pattern arising from the two quadrupolar nuclei, ^{83}Kr (I = 9/2) and ^{14}N (I = 1). The measured transition frequencies are listed in Table A2.2 and a spectrum of the J = 1-0 transition is shown in Figure 3.2 as an example of the sensitivity and the resolution achieved. The nuclear quadrupole coupling constants obtained from the fit of the hyperfine structure of this transition are $\chi_{aa}(^{83}Kr)$ = -1.960(6) MHz and $\chi_{aa}(^{14}N)$ = 0.241(1) MHz, with a standard deviation of 2.3 kHz. The

Table 3.2 Spectroscopic constants and derived molecular parameters for Kr-NH_3.

$\Sigma 0_{0a}$	^{86}Kr-NH_3	^{84}Kr-NH_3	^{82}Kr-NH_3	^{80}Kr-NH_3
Rotational constant /MHz				
B	2312.2304(1)	2321.1770(1)	2330.5543(1)	2340.3937(2)
Centrifugal distortion constant /MHz				
D_J	0.0450(1)	0.0454(1)	0.0457(1)	0.0462(1)
^{14}N quadrupole hyperfine constant /MHz				
χ_{aa}	0.2459(12)	0.2485(12)	0.2483(13)	0.2449(13)
Standard deviation /kHz				
σ	2.7	2.5	3.1	2.1
R (Å)	3.9218	3.9220	3.9221	3.9223
ν_s (cm^{-1})	35.0	35.0	35.1	35.1
k_s (mdyn/Å)	0.0102	0.0102	0.0102	0.0102

Figure 3.2 Spectrum of the J = 1-0 rotational transition of ^{83}Kr-NH$_3$ for the $\Sigma 0_a$ state. The spectrum is a composite of four different spectra, each recorded with 2000 averaging cycles and a sampling interval of 120 ns. The hyperfine structure is due to the quadrupolar ^{83}Kr (I = 9/2) and ^{14}N nuclei (I = 1) for which the χ_{aa} values were determined to be −1.960(6) MHz and 0.241(1) MHz, respectively.

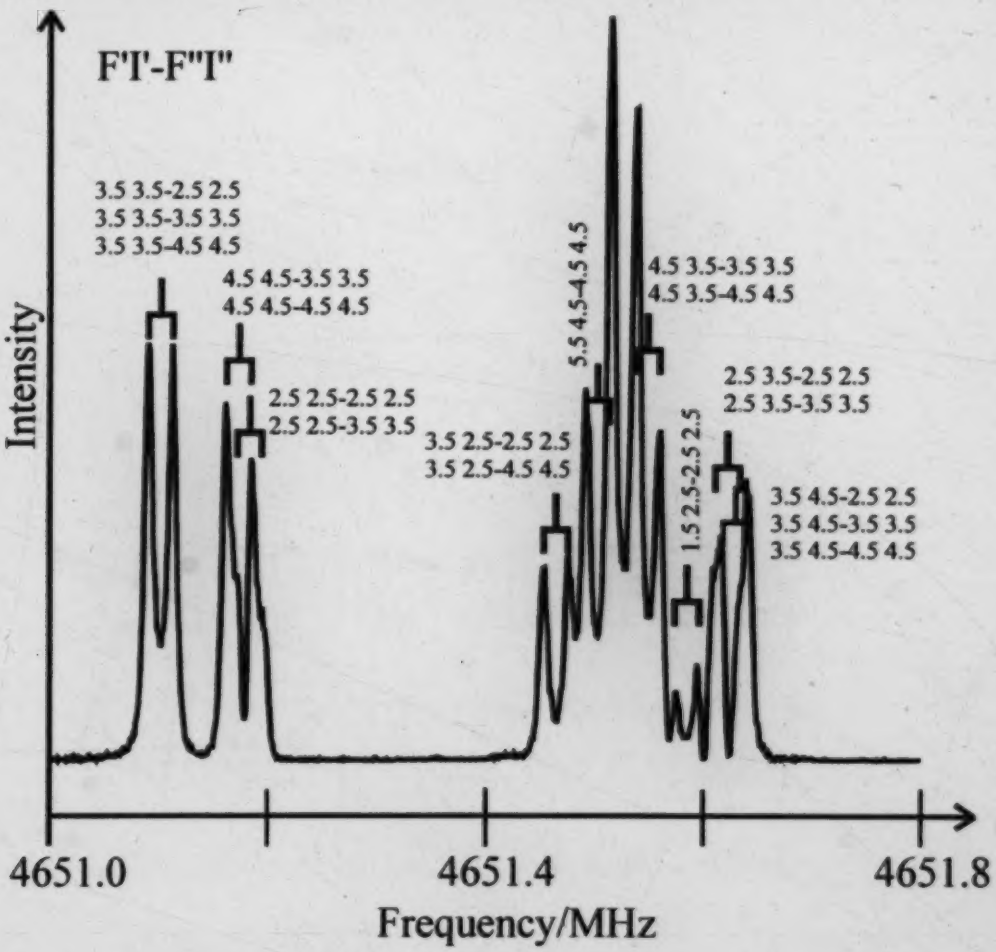

hypothetical center line frequency of the J = 1-0 transition is 4651.4192 MHz for ^{83}Kr-NH$_3$.

The transition frequencies for $\Sigma 0_a$ states of the ^{86}Kr-, ^{84}Kr-, ^{82}Kr-, and ^{80}Kr-^{15}NH$_3$ isotopomers are listed in Table A2.3. The rotational fit was done using Pickett's

program[30] and the resulting spectroscopic constants are listed in Table 3.3.

The $\Sigma 1_{1s}$ and $\Sigma 1_{1a}$ states are associated with the same nuclear spin wave function (E') and thus, only the lower energy $\Sigma 1_{1s}$ state is metastable. The $\Sigma 1_{1s}$ and $\Sigma 1_{1a}$ states are split by the inversion of the bound NH_3 moiety which is approximately 22.6 GHz in Ar-NH_3.[3] If the inversion splitting is comparable in Kr-NH_3, the higher energy $\Sigma 1_{1a}$ state will have a relative Boltzmann population of approximately 11 % at 0.5 K, the rotational temperature estimated for the molecular beam expansion. It was anticipated that the $\Sigma 1_1$ state spectrum of Kr-NH_3 would be difficult to predict since it was expected to be Coriolis perturbed as reported for the $\Sigma 1_1$ state of Ar-NH_3.[3] In Ar-NH_3, the effect of this perturbation is to push the rotational levels farther apart than predicted by a rigid diatomic energy level expression. For example, the J = 1-0 transition was reported at 5033.98 MHz, J = 2-1 at 10 130.3 MHz, and J = 3-2 at 15 326.304 MHz which shows that the spacing is greater than 2B between the successive transitions. Since the degree of perturbation in comparison with Ar-NH_3 was unknown, a broad search was conducted for the J = 1-0, J = 2-1, and J = 3-2 transitions of Kr-NH_3. A few sets of strong transitions

Table 3.3 Spectroscopic constants and derived molecular parameters for Kr-$^{15}NH_3$.

$\Sigma 0_{0a}$	^{86}Kr-$^{15}NH_3$	^{84}Kr-$^{15}NH_3$	^{82}Kr-$^{15}NH_3$	^{80}Kr-$^{15}NH_3$
Rotational constant /MHz				
B	2208.4521(2)	2217.4151(2)	2226.8093(2)	2236.6671(2)
Centrifugal distortion constant /MHz				
D_J	0.0412(1)	0.0415(1)	0.0419(1)	0.0422(1)
Standard deviation /kHz				
σ	2.3	2.1	2.1	2.1
R(Å)	3.9192	3.9194	3.9195	3.9197
ν_s (cm^{-1})	34.1	34.2	34.1	34.4
k_s (mdyn/Å)	0.0102	0.0102	0.0101	0.0102

were found that depended on Kr, as seen from the characteristic isotopic spacing, but these transitions could not be assigned to Kr-NH_3. After close consideration, it was determined that the hyperfine patterns and in some cases, the Kr isotopic spacing were just too irregular to make a convincing assignment. Furthermore, a microwave-microwave double resonance experiment was used to test whether any of the transitions were linked by a common level, and this was not the case.

b) Kr-ND_3

The rotational spectrum of the ground state of Kr-ND_3 was expected to be inversion doubled as predicted by the molecular symmetry group analysis. The $\Sigma 0_{0s}$ and $\Sigma 0_{0a}$ states are separated in energy by the inversion splitting of the bound ND_3 molecule. In free ND_3, this splitting is only 1.6 GHz which is considerably smaller than the inversion splitting in free NH_3 (23 GHz).[31] Since the two inversion states were expected to lie close in energy for Kr-ND_3, it was unclear at first whether the spectra of the two states could be resolved. This is because, as a general rule, states that lie close in energy have similar rotational constants. The resolution of the inversion states was of particular concern because of the complex hyperfine splitting expected from the four quadrupolar nuclei (^{14}N, 3D) in the molecular system. This uncertainty, however, proved to be unfounded and two sets of rotational transitions were resolved and subsequently assigned to the $\Sigma 0_{0s}$ and $\Sigma 0_{0a}$ states.

The frequencies of the transitions assigned to the two inversion states, $\Sigma 0_{0s}$ and $\Sigma 0_{0a}$, of Kr-ND_3 are given in Table A2.4 for the two most abundant isotopes of Kr. The inversion tunnelling splitting observed for the J = 1-0 rotational transition is only 84 kHz.

As a result of this small splitting, the ^{14}N nuclear quadrupole hyperfine patterns overlap for the two inversion states which complicated the spectral assignment. The higher frequency components have greater intensity and were thus assigned to the $\Sigma 0_{0s}$ state based on the nuclear spin statistical predictions. Each inversion state was fit separately using Pickett's global fitting program[30] and the spectroscopic constants are listed in Table 3.4. The deuterium nuclear quadrupole hyperfine structure could not be sufficiently resolved and was therefore neglected in the fit of the spectroscopic constants. The neglect of the deuterium hyperfine splitting did not significantly affect the rotational fit since the standard deviations obtained were on the order of 2 - 4 kHz for the isotopomers of Kr-ND_3.

The $\Sigma 1_{1s}$ and $\Sigma 1_{1a}$ states of Kr-ND_3 are associated with the same nuclear spin wave function (E'). As a result of the small energy level splitting in free ND_3 (1.6 GHz), the $\Sigma 1_{1s}$ and $\Sigma 1_{1a}$ states of Kr-ND_3 should have comparable populations and their spectra should be closely spaced. It was anticipated that the $\Sigma 1_1$ state spectra of Kr-ND_3 would be difficult to predict due to Coriolis perturbation as described above for Kr-NH_3. A broad search was conducted for the J = 1-0 transitions of Kr-ND_3. When the lower limit of the spectrometer was reached (4 GHz), a broad search for the J = 2-1 transitions became necessary. Once two closely spaced candidates were found that met the ^{14}N nuclear quadrupole hyperfine and intensity criteria, the higher J transitions were located by scanning upwards from a frequency that was approximately 2B higher than each transition.

The transition frequencies assigned to the $\Sigma 1_{1s}$ and $\Sigma 1_{1a}$ states are given in Table

Table 3.4 Spectroscopic constants and derived molecular parameters for $Kr\text{-}ND_3$, $Kr\text{-}ND_2H$, and $Kr\text{-}NDH_2$.

$\Sigma 0_{0s}/\Sigma 0_{00s}$	$^{86}Kr\text{-}ND_3$	$^{84}Kr\text{-}ND_3$	$^{86}Kr\text{-}ND_2H$	$^{84}Kr\text{-}ND_2H$	$^{86}Kr\text{-}NDH_2$	$^{84}Kr\text{-}NDH_2$
Rotational constant /MHz						
B	2036.6040(1)	2045.5943(1)	2116.4692(1)	2125.4418(1)	2206.3043(1)	2215.2573(1)
Centrifugal distortion constant /MHz						
D_J	0.0336(1)	0.0339(1)	0.0397(1)	0.0400(1)	0.0454(1)	0.0458(1)
^{14}N quadrupole hyperfine constant /MHz						
χ_{aa}	0.5219(10)	0.5193(10)	0.4310(10)	0.4381(10)	0.3594(10)	0.3529(10)
Standard deviation /kHz						
σ	3.7	3.4	3.3	3.0	4.4	5.0
R (Å)	3.9074	3.9076	3.9142	3.9144	3.9203	3.9204
v_s (cm^{-1})	33.5	33.5	32.6	32.7	32.4	32.5
k_s (mdyn/Å)	0.0107	0.0107	0.0098	0.0098	0.0092	0.0092
$\Sigma 0_{0a}/\Sigma 0_{00a}$						
B (MHz)	2036.5612(1)	2045.5515(2)	2116.5740(1)	2125.5460(1)	2206.8222(1)	2215.7765(1)
D_J (MHz)	0.0336(1)	0.0339(1)	0.0396(1)	0.0400(1)	0.0453(1)	0.0457(1)
χ_{aa} (MHz)	0.5208(13)	0.5182(13)	0.4260(10)	0.4252(10)	0.3463(10)	0.3489(10)
σ (kHz)	2.4	2.3	2.7	1.9	4.8	2.3
R (Å)	3.9074	3.9076	3.9141	3.9143	3.9203	3.9200
v_s (cm^{-1})	33.4	33.5	32.6	32.7	32.4	32.5
k_s (mdyn/Å)	0.0107	0.0107	0.0098	0.0098	0.0092	0.0093

A2.5 for the ^{86}Kr and ^{84}Kr isotopomers. The inversion tunnelling splitting observed in the J = 2-1 transition is approximately 16 MHz which is considerably larger than the analogous J = 2-1 splitting in the $\Sigma 0_0$ state (0.18 MHz). Similar intensities were observed for the two states, indicating that they lie close enough in energy that thermal relaxation effects are small. The observed intensities of the $\Sigma 1_1$ states in comparison with the $\Sigma 0_{0s}$ state are consistent with the predicted nuclear spin weights. The spectral analysis was done by first fitting the ^{14}N nuclear quadrupole hyperfine structure using a first order program. The resulting χ_{aa} values were then fixed in Pickett's program[30] while B and D_J were fit. The values of B, D_J, and χ_{aa} for the $\Sigma 1_{1s}$/ $\Sigma 1_{1a}$ states are: 1898.3210(1)/1894.0854(1) MHz, −0.3888(1)/−0.4263(1) MHz, and 1.180(19)/1.215(10) MHz for ^{86}Kr-ND_3, and 1905.7347(1)/1901.4521(1) MHz, −0.3971(1)/−0.4353(1) MHz, and 1.178(6)/1.217(11) MHz for ^{84}Kr-ND_3. The standard deviations for the rotational fits were on the order of 3 MHz. The relatively large standard deviations and the negative values for the centrifugal distortion constants D_J indicate that the $\Sigma 1_{1s}$/ $\Sigma 1_{1a}$ states are perturbed as reported previously for Ar-NH_3.[3]

c) Kr-ND_2H

The transition frequencies assigned to the $\Sigma 0_{00s}$ and $\Sigma 0_{00a}$ states of Kr-ND_2H are listed in Table A2.6 for the two most abundant isotopes of Kr. The inversion tunnelling splitting in the J = 1-0 transition is approximately 214 kHz and the ^{14}N nuclear quadrupole hyperfine structures of the two inversion states overlap for the two lowest rotational transitions. It was difficult to compare the intensities of the lowest J transitions as there was unresolved splitting and broadening of the lines due to the quadrupolar

deuterium nuclei (I = 1). The higher J transitions were not noticeably broadened, however, and a comparison of the intensities revealed that the lower frequency inversion state has approximately twice the intensity of the higher frequency state. Consequently, the lower frequency transitions were assigned to the symmetric inversion state based on the predicted spin statistical weights. This is the reverse of the assignment of the inversion components in Kr-ND_3 in which the antisymmetric inversion state transitions are at lower frequency. The analyses were performed as described above for Kr-ND_3 and the resulting spectroscopic constants are listed in Table 3.4.

d) Kr-NDH_2

The frequencies of the rotational transitions observed for the $\Sigma 0_{00s}$ and $\Sigma 0_{00a}$ states of Kr-NDH_2 are listed in Table A2.7 for the ^{86}Kr and ^{84}Kr containing isotopomers. The inversion tunnelling splitting observed for the J = 1-0 transition is on the order of 1 MHz affording complete spectral separation of the ^{14}N nuclear quadrupole hyperfine splitting patterns of the two inversion states. The spectra of the higher J transitions revealed that the lower frequency inversion components have approximately 1/3 the intensity of the higher frequency components and were thus assigned to the $\Sigma 0_{00s}$ state, as in the Kr-ND_2H isotopomer. The rotational and ^{14}N hyperfine analyses were performed as described previously for Kr-ND_3 and the resulting spectroscopic constants are listed in Table 3.4.

3.3.3 Deuterated isotopomers of Ar-NH_3

a) Ar-ND_3

The spectrum of the $\Sigma 0_{0a}$ state of Ar-ND_3 was predicted by scaling the B rotational

constant reported for Ar-NH_3 by the ratio of the reduced masses.[2] For Ar-NH_3, the $\Sigma 0_{0s}$ state has a nuclear spin weight of zero and thus, only the B constant for the $\Sigma 0_{0a}$ state was available. Since the van der Waals bond length was assumed to decrease with deuterium substitution, this scaled B constant was treated as a lower limit in the spectral search for Ar-ND_3. It was expected that the $\Sigma 0_{0s}$ state would have a similar B constant to the less intense $\Sigma 0_{0a}$ state as observed in Kr-ND_3. This assumption proved valid and the weaker $\Sigma 0_{0a}$ state transitions were found within the ^{14}N nuclear quadrupole hyperfine structure of the $\Sigma 0_{0s}$ state as seen in Figure 3.3 for the J = 1-0 transition. The inversion tunnelling splitting in the J = 1-0 transition is on the order of 60 kHz.

The rotational transitions assigned to the $\Sigma 0_{0s}$ and $\Sigma 0_{0a}$ states follow the pattern of a diatomic molecule in which the NH_3 behaves as one moiety as seen in the Kr-NH_3 dimer and its various isotopomers. The frequencies of the transitions are listed in Table A2.8. The rotational and ^{14}N hyperfine analyses were done simultaneously using Pickett's global fitting program.[30] Each inversion state was fit separately and the spectroscopic constants are listed in Table 3.5. Due to lack of resolution, the deuterium nuclear quadrupole hyperfine splitting was neglected in the fit of the spectroscopic constants. The unresolved deuterium hyperfine structure made an intensity comparison of the two states difficult since some transitions were split or broadened as shown in Figure 3.3 for the J = 1-0 transitions. In this spectrum, one hyperfine component (F'-F" = 0-1) for each inversion state is not noticeably broadened and the relative intensities are approximately 10:1 for the $\Sigma 0_{0s}$ and $\Sigma 0_{0a}$ states, respectively, as predicted by spin statistics. The neglect of the deuterium hyperfine did not have a significant effect on the rotational analysis as

Figure 3.3 Spectrum of the J = 1-0 rotational transition of Ar-ND$_3$ for the $\Sigma 0_{0s}$ and $\Sigma 0_{0a}$ inversion states. The spectral separation between the inversion states is on the order of 60 kHz and the symmetric and antisymmetric inversion components are labelled 's' and 'a', respectively. The spectrum is a composite of three different spectra recorded with 100 averaging cycles and sampling timed of 60 ns. The labelled hyperfine structure is due to the quadrupolar ^{14}N nucleus (I = 1). The additional splittings arising from the three quadrupolar deuterium nuclei (I = 1) were not assigned.

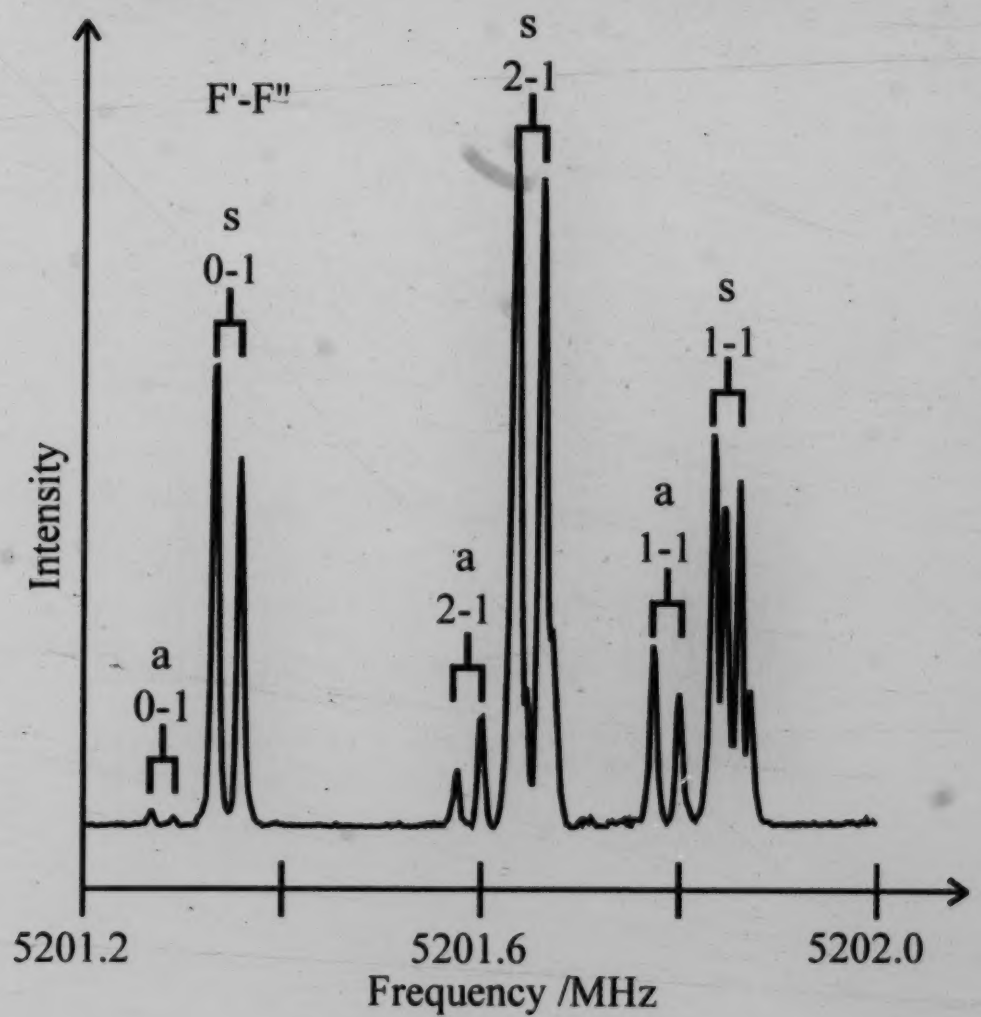

Table 3.5 Spectroscopic constants and derived molecular parameters for Ar-ND_3, Ar-ND_2H, Ar-NDH_2, and Ar-NH_3.

$\Sigma 0_{0s}/\Sigma 0_{00s}$	Ar-ND_3	Ar-ND_2H	Ar-NDH_2	Ar-NH_3[a]
Rotational constant /MHz				
B	2600.9827(1)	2680.6339(1)	2770.6781(1)	n/a
Centrifugal distortion constant /MHz				
D_J	0.06931(1)	0.08028(1)	0.08982(1)	
^{14}N quadrupole hyperfine constant /MHz				
χ_{aa}	0.6789(99)	0.5776(99)	0.4684(99)	
Standard deviation /kHz				
σ	3.8	3.1	5.0	
R (Å)	3.8151	3.8236	3.8314	
ν_s (cm^{-1})	33.6	32.7	32.5	
k_s (mdyn/Å)	0.00889	0.00811	0.00772	
$\Sigma 0_{0a}/\Sigma 0_{00a}$				
B	2600.9512(1)	2680.7697(1)	2771.2286(1)	2876.849(2)
D_J	0.06933(1)	0.08023(1)	0.08961(1)	0.0887(2)
χ_{aa}	0.6846(99)	0.5698(99)	0.4617(99)	0.350(8)
σ	3.5	3.0	3.2	
R (Å)	3.8152	3.8235	3.8310	3.8358
ν_s (cm^{-1})	33.6	32.7	32.5	34.6
k_s (mdyn/Å)	0.00888	0.00812	0.00774	0.00840

[a] Reference 2.

the standard deviations of the spectroscopic fits were on the order of 4 kHz.

It was anticipated that the $\Sigma 1_1$ state spectrum of Ar-ND_3 would be more difficult to predict since it was expected to contain Coriolis perturbation similar to that reported for the $\Sigma 1_1$ states of Ar-NH_3.[3] In Ar-NH_3, the perturbed $\Sigma 1_1$ state transitions were found at lower frequency than the ground state transitions and thus, a broad search was conducted for the J = 1-0 transition of Ar-ND_3 at lower frequencies than the ground state J = 1-0 transitions. When two closely spaced transitions were found that met the ^{14}N hyperfine and intensity criteria, the higher J transitions were located by scanning upwards from a

frequency that was approximately 2B higher than each transition.

The transition frequencies assigned to the $\Sigma 1_{1s}$ and $\Sigma 1_{1a}$ states of Ar-ND_3 are given in Table A2.8. The inversion tunnelling splitting of the J = 1-0 transition is approximately 3.3 MHz and the ^{14}N nuclear quadruple hyperfine patterns are spectrally separated for all of the observed rotational transitions. The intensities are approximately equal for the two inversion states as expected since both $\Sigma 1_1$ states are associated with the same nuclear spin function and lie close enough in energy that their populations are comparable. A rough comparison of the observed intensities is consistent with the predicted nuclear spin weights of 10 and 8 for the $\Sigma 1_1$ and $\Sigma 0_{0s}$ states, respectively. The transitions appear to be perturbed as reported for the $\Sigma 1_1$ states of Ar-NH_3 and Kr-ND_3 since the successive transitions are spaced by more than 2B. No transitions related to the perturbing states were found and the rotational and ^{14}N quadrupole coupling constants were fit simultaneously for each inversion state with standard deviations around 0.4 MHz. The values of B and D_J are: 2447.3946(1) MHz and −0.1716(1) MHz for the $\Sigma 1_{1a}$ state and 2449.04311(1) MHz and −0.1637(1) MHz for the $\Sigma 1_{1s}$ state. The ^{14}N nuclear quadrupole coupling constants, χ_{aa}, are: 1.13(1) MHz and 1.22(2) MHz for the $\Sigma 1_{1s}$ and $\Sigma 1_{1a}$ states, respectively.

b) Ar-ND_2H

Using the rotational constants of Ar-ND_3 as a guide, the analogous transitions for the $\Sigma 0_{0s}$ and $\Sigma 0_{0a}$ states of Ar-ND_2H were measured and the frequencies are listed in Table A2.9. The inversion tunnelling splitting of the J = 1-0 transition is approximately 280 kHz. As a result of the small tunnelling splitting, the ^{14}N nuclear quadrupole hyperfine

structures of the two states overlap for the two lowest rotational transitions. It was difficult to estimate the relative intensities of the two inversion tunnelling states due to unresolved deuterium nuclear quadrupole hyperfine splitting of the lowest J transitions. A comparison of the intensities of the two J = 3-2 transitions revealed that the lower frequency inversion components have approximately twice the intensity of the higher frequency components. Consequently, the higher J transitions were assigned to the symmetric inversion state, as in Kr-ND_2H. The analyses were performed as described for Ar-ND_3 and the resulting spectroscopic constants are listed in Table 3.5.

c) Ar-NDH_2

The frequencies of the transitions observed for the $\Sigma 0_{0s}$ and $\Sigma 0_{0a}$ states of Ar-NDH_2 are listed in Table A2.9. The J = 1-0 transitions of the two inversion states are separated by 1.1 MHz and the ^{14}N nuclear quadrupole hyperfine structures do not overlap for any of the measured transitions. The rotational and ^{14}N hyperfine analyses were performed as described for Ar-ND_3 and the resulting spectroscopic constants are listed in Table 3.5. The relative intensities are approximately 1 and 3 for the lower and higher frequency components, respectively. Based on nuclear spin statistical predictions, the weaker, lower frequency transitions were assigned to the symmetric inversion state as in the Kr-NDH_2.

3.3.4 Isotopomers of Ne-NH_3

a) Ne-NH_3 and Ne-$^{15}NH_3$

The first rotational transition of Ne-NH_3 was found by serendipity while scanning

for excited internal rotor state transitions of Kr-NH_3 since Ne was used as the carrier gas. A strong line was observed around 7929.6 MHz and the ^{14}N hyperfine splitting closely resembled that of a J = 1-0 transition. Assuming this to be the main isotopomer, ^{20}Ne-NH_3, the corresponding transition of ^{22}Ne-NH_3 was estimated by scaling the observed frequency by the ratio of the reduced masses. The ^{22}Ne-NH_3 transition was found within 15 MHz of this prediction. These transitions were assigned to the $\Sigma 0_{0a}$ states of the respective isotopomers and the frequencies are given in Table A2.10 along with those of the measured higher J transitions. The spectra observed are characteristic of a diatomic molecule in which the NH_3 subunit behaves as one moiety. The rotational and ^{14}N hyperfine analysis were done together in Pickett's global fitting program[30] and the resulting spectroscopic constants are reported in Table 3.6.

Rotational spectra of the $\Sigma 0_{0a}$ state of Ne-$^{15}NH_3$ were measured for the ^{20}Ne and ^{22}Ne containing isotopomers. The transition frequencies are listed in Table A2.11 and the

Table 3.6 Spectroscopic constants and derived molecular parameters for Ne-NH_3 and Ne-$^{15}NH_3$.

$\Sigma 0_{0a}$	^{22}Ne-NH_3	^{20}Ne-NH_3	^{22}Ne-$^{15}NH_3$	^{20}Ne-$^{15}NH_3$
Rotational constant /MHz				
B	3807.5520(20)	3965.8506(20)	3694.4785(4)	3853.1667(4)
Centrifugal distortion constant /MHz				
D_J	0.4708(1)	0.5164(1)	0.4410(1)	0.4851(1)
^{14}N quadrupole hyperfine constant /MHz				
χ_{aa}	0.2770(12)	0.2700(12)		
Standard deviation /kHz				
σ	13.7	15.2	11.3	13.2
R(Å)	3.7190	3.7227	3.7162	3.7199
ν_s (cm^{-1})	22.8	23.2	22.6	22.9
k_s (mdyn/Å)	0.00295	0.00291	0.00297	0.00293

spectroscopic constants determined using Pickett's program[30] are given in Table 3.6.

As for Kr-NH_3, a broad search was conducted for the $\Sigma 1_{1s}$ state of Ne-NH_3 at both higher and lower frequencies than the $\Sigma 0_{0a}$ state, but no transitions were found that could be assigned based on the expected ^{14}N nuclear quadrupole hyperfine splitting and the $^{20}Ne/^{22}Ne$ isotopic spacing.

b) Ne-ND_3

The B rotational constant of the $\Sigma 0_{0a}$ state of Ne-ND_3 was initially estimated from that of Ne-NH_3. The B constants for the $\Sigma 0_{0s}$ and $\Sigma 0_{0a}$ states of Ar-ND_3 and Kr-ND_3 differed only by 31.5 kHz and 42.8 kHz, respectively. It was anticipated that the rotational constants for the two inversion components of the ground state of Ne-ND_3 would also be very similar. This assumption proved valid and the two J = 1-0 transitions were found to be separated by approximately 59 kHz. Due to the small inversion tunnelling splitting, the ^{14}N nuclear quadrupole hyperfine structures of the two inversion states overlap. The predicted nuclear spin weights are 10 and 1 for the $\Sigma 0_{0s}$ and $\Sigma 0_{0a}$ states, respectively and consequently, the more intense, lower frequency hyperfine components were assigned to the symmetric inversion state. This is the opposite of the assignment in the Kr-ND_3 and Ar-ND_3 dimers in which the symmetric inversion components appear at higher frequency than the antisymmetric components. The transition frequencies assigned to the ^{20}Ne- and ^{22}Ne-ND_3 isotopomers are listed in Table A2.12. The ^{14}N nuclear quadrupole hyperfine structure and rotational constants were fit for each inversion state as described for Ne-NH_3 and are given in Table 3.7. The deuterium hyperfine splitting was not well enough resolved to be included in the fit. The

Table 3.7 Spectroscopic constants and derived molecular parameters for Ne-ND_3, Ne-ND_2H, and Ne-NDH_2.

$\Sigma 0_{0s}/\Sigma 0_{00s}$	^{22}Ne-ND_3	^{20}Ne-ND_3	^{22}Ne-ND_2H	^{20}Ne-ND_2H	^{22}Ne-NDH_2	^{20}Ne-NDH_2
Rotational constant /MHz						
B (MHz)	3541.3508(2)	3702.2179(2)	3619.5701(2)	3779.6415(2)	3707.0414(2)	3866.2352(2)
Centrifugal distortion constant /MHz						
D_J (MHz)	0.3879(1)	0.4283(1)	0.4230(1)	0.4660(1)	0.4535(1)	0.4985(1)
^{14}N quadrupole hyperfine constant /MHz						
χ_{aa} (MHz)	0.5258(10)	0.5224(10)	0.4399(10)	0.4401(10)	0.3574(12)	0.3501(12)
Standard deviation /kHz						
σ (kHz)	11.3	12.3	11.7	13.2	13.7	13.8
R (Å)	3.6890	3.6930	3.6990	3.7029	3.7093	3.7131
ν_s (cm^{-1})	22.6	23.0	22.3	22.7	22.4	22.7
k_s (mdyn/Å)	0.00315	0.00311	0.00300	0.00296	0.00292	0.00288
$\Sigma 0_{0a}/\Sigma 0_{00a}$						
B (MHz)	3541.3793(2)	3702.2454(2)	3619.7689(2)	3779.8453(2)	3707.5655(2)	3866.7763(2)
D_J (MHz)	0.3879(1)	0.4283(1)	0.4230(1)	0.4660(1)	0.4537(1)	0.4987(1)
χ_{aa} (MHz)	0.5139(15)	0.5230(12)	0.4379(10)	0.4294(10)	0.3533(12)	0.3510(12)
σ (kHz)	11.2	13.5	10.5	11.7	12.5	13.9
R (Å)	3.6890	3.6930	3.6989	3.7028	3.7091	3.7129
ν_s (cm^{-1})	22.6	23.0	22.3	22.7	22.4	22.7
k_s (mdyn/Å)	0.00315	0.00311	0.00300	0.00296	0.00292	0.00288

neglect of the deuterium hyperfine structure did not have a large effect on the fit as the standard deviations obtained in the analysis were only 12.3 kHz and 13.5 kHz for the $\Sigma 0_{0s}$ and $\Sigma 0_{0a}$ states of ^{20}Ne-ND_3, respectively.

As predicted for the Ne-NH_3 isotopomers, the excited internal rotor state, $\Sigma 1_{1s}$ is metastable in Ne-ND_3 since it is associated with the E' spin symmetry. For Ar-ND_3, this state was found to be less perturbed than the corresponding state in Ar-NH_3. A spectral search was conducted at both higher and lower frequencies than the ground state rotational transitions of Ne-ND_3 but no additional transitions were found that could be assigned to the $\Sigma 1_1$ tunnelling state.

c) Ne-ND_2H

The frequencies of the transitions assigned to the ground state of Ne-ND_2H are listed in Table A2.13 for both inversion components. The inversion tunnelling splitting of the J = 1-0 transition is on the order of 412 kHz and the ^{14}N nuclear quadrupole hyperfine structures of the two states do not overlap. The spectra were fit as described for Ne-NH_3 and the resulting spectroscopic constants are given in Table 3.7 for the ^{20}Ne and ^{22}Ne containing isotopomers. The more intense inversion components appear at lower frequency, as in Kr-ND_2H and Ar-ND_2H, and were thus assigned to the $\Sigma 0_{00s}$ state based on the nuclear spin statistical predictions.

d) Ne-NDH_2

The rotational spectra of the two most abundant isotopomers of Ne-NDH_2 were measured and the assigned transition frequencies for the $\Sigma 0_{0s}$ and $\Sigma 0_{0a}$ states are given in Table A2.14. The J = 1-0 rotational transitions are separated by approximately 1 MHz

allowing complete spectral separation of the ^{14}N nuclear quadrupole hyperfine components of the two inversion states. The rotational and ^{14}N hyperfine fit were done as described for Ne-NH_3 and the spectroscopic constants are given in Table 3.7. The lower frequency components were assigned to the symmetric inversion state based on the observed relative intensities. This is analogous to the assignment in the Kr-NDH_2 and Ar-NDH_2 dimers.

3.4 *Ab initio* calculations for Ne-NH_3

Three separate potential energy surfaces have been constructed for Ne-NH_3 using *ab initio* methods. Each surface represents a different geometry of the NH_3 molecule within the van der Waals complex in an attempt to model the inversion motion of NH_3. One surface corresponds to equilibrium bond angles of NH_3 (>HNH = 106.67°), another to a planar structure (>HNH = 120.00°), and the third surface was calculated for an intermediate bond angle (>HNH = 113.34°). The N-H bond length was held fixed at the experimental value of 1.01242 Å.[32] The calculations were done using the Gaussian 94 software package.[33] The interaction energies were calculated via the supermolecular approach in which the energies of the two monomers (NH_3, Ne) are subtracted from the total energy of the complex (Ne-NH_3). Dimer-centered basis sets were used in all calculations which corresponds to the counterpoise correction method of Boys and Bernardi to account for basis set superposition error.[34] The calculations were initially done using MP4 theory including single, double, triple, and quadruple excitations. Some regions of the potential energy surfaces were later re-calculated at the CCSD(T) level to

allow comparison with the calculations of the Ne_2-NH_3 and Ne_3-NH_3 complexes (see Chapters 4 and 5). The CCSD(T) level calculations were done using the MOLPRO software package.[35] The core electrons were frozen in the electron correlation treatment. The basis sets used were Dunning's[36] aug-cc-pVTZ for Ne and Sadlej's[37] VTZ for the nitrogen and hydrogen atoms which can be viewed using the Extensible Computational Chemistry Environment Basis Set Database.[38] The basis sets were supplemented with a set of bond functions (3s, 3p, 2d) placed at the midpoint of the van der Waals bond. The exponents were fixed at $\alpha_s = \alpha_p = 0.9, 0.3, 0.1$ and $\alpha_d = 0.6, 0.2$ as advocated by Tao and Klemperer for *ab initio* calculations of the Ar-NH_3 dimer.[13]

The interaction energy was determined as a function of θ, ϕ, and R (see Figure 3.1) for each of the three NH_3 geometries. Initially, rough surfaces were prepared with R ranging from 3.2 Å to 4.0 Å in increments of 0.1 Å, θ from 0° to 180° in increments of 30°, and ϕ from 0° to 60° in increments of 10°. For the planar NH_3 geometry only θ angles from 0° to 90° in increments of 30° were necessary due to symmetry and van der Waals bond lengths up to 4.2 Å were calculated. Once the potential minimum region was identified for each of the three monomer geometries, a finer grid of points, using increments of 0.05 Å for R and 10° for θ, was calculated around this minimum for each potential energy surface. The interaction energies calculated for each geometry are available in Appendix 3. Tables A3.1, A3.2, and A3.3 give the MP4 results obtained from the rough scans using each of the three NH_3 monomer geometries, >HNH of 106.67°, 113.34°, and 120.00°, respectively. The finer scan results are listed in Tables A3.4, A3.5, and A3.6 for these same geometries. The select points calculated at the CCSD(T) level of

theory are given in Tables A3.7, A3.8, and A3.9.

3.5 Discussion

3.5.1 Spectroscopic constants and derived molecular parameters for the ground state

The B rotational constants were used to calculate the van der Waals bond lengths, R, of the Kr-NH_3, Ar-NH_3, and Ne-NH_3 dimers. The van der Waals stretching frequencies, ν_s, and corresponding force constants, k_s, were calculated using the pseudodiatomic expressions: $\nu_s = (4B^3/D)^{1/2}$ and $k_s = 4\pi^2 \nu_s^2 \mu$ where μ is the pseudodiatomic reduced mass. The results are given in Tables 3.2 - 3.7 along with the spectroscopic constants of each species. Comparison of the van der Waals bond lengths of the three dimers reveals that the bond is 2.2 % longer in Kr-NH_3 than in Ar-NH_3.[2] This is slightly smaller than the bond lengthening observed upon Kr substitution in other weakly bound complexes. For example, in complexes containing Kr bound to H_2O,[25,26] CO_2,[39] N_2,[27,28] HF,[40] CO,[41,42] and HCN,[43,44] the van der Waals bond lengthens by 3 % - 4 % compared to the Ar containing counterparts. By comparison, the Ne-NH_3 bond length is 3 % shorter than that of Ar-NH_3 which is slightly longer than that extrapolated from other Rg-molecule complexes. In complexes where a Rg atom is paired with CO_2,[45] OCS,[46] or HF,[40] the van der Waals bond lengths of the Ne containing complex are approximately 5 % - 8 % shorter than those of the corresponding Ar species. Upon deuterium substitution, the van der Waals bond shortens by approximately 0.5 %, 0.3 %, and 0.1 % for the Ar-ND_3, Ar-ND_2H, and Ar-NDH_2 isotopomers, respectively. This result

is consistent with studies of deuterium substitution in other van der Waals complexes such as Ar-H_2O in which the van der Waals bond shortens by 0.3 % in Ar-D_2O and 0.2 % in Ar-HDO.[25]

The van der Waals bond is less rigid in Ne-NH_3 than in the Ar and Kr containing complexes as seen through comparison of the force constants: 0.00291 mdyn/Å , 0.0084 mdyn/Å, and 0.0102 mdyn/Å for the $\Sigma 0_{0a}$ states of ^{20}Ne-, Ar-, and ^{84}Kr-NH_3, respectively. A comparison of the force constants upon deuterium substitution reveals that the heavier ND_3 containing species have larger force constants than the NH_3 containing species. Surprisingly, the two mixed isotopomers have smaller force constants than both the NH_3 and ND_3 containing species. For example, ^{84}Kr-NH_3, -ND_3, -ND_2H, and -NDH_2 have forces constants: 0.0102 mdyn/Å, 0.0107 mdyn/Å, 0.0098 mdyn/Å, and 0.0093 mdyn/Å, respectively. This same trend occurs for the Ne and Ar dimers. This may be a result of the reduced symmetry of the ND_2H and NDH_2 monomers. For these complexes, the pseudodiatomic approximation is less valid since the ND_2H and NDH_2 moieties are expected to prefer a deuterium bonded geometry within the van der Waals complex.

The orientation of the ammonia monomer in the complex can be estimated for each dimer using the nuclear quadrupole coupling constant, χ_{aa}, obtained from the fit of the ^{14}N nuclear quadrupole hyperfine splitting. Assuming the electronic environment at the ^{14}N nucleus is not altered upon complex formation with a Rg atom, χ_{aa} is given by the relation: $\chi_{aa} = \frac{1}{2}\chi_o \langle 3\cos^2\theta - 1\rangle$, where χ_o is the quadrupole coupling constant of free NH_3 (−4.0898 MHz)[47] and θ is the angle between the C_3 axis of the ammonia monomer and the van der Waals axis (Figure 3.1). The brackets indicate averaging over the large

amplitude motions of the dimer. The χ_o value for NH_3 is assumed to be a suitable approximation for the χ_o values of the deuterated monomers since the electronic environment at the ^{14}N nucleus is essentially unaffected by deuterium substitution.[31,48] Under this assumption, the θ values calculated for the $\Sigma 0_{0a}/\Sigma 0_{00a}$ states are summarized in Table 3.8 for the various isotopomers. The supplementary angles are also solutions to the above equation and are included in Table 3.8. The second set of angles listed is closer to the values predicted for Ar-NH_3: 96.6° (empirical potential)[11] and 90°,[13] 100°,[12] 105° (*ab initio*)[14] and for Kr-NH_3: 100° (*ab initio*).[49] The solution to the above eqvation assumes only small variations in θ and in the limit of free internal rotation of the ammonia monomer, the Legendre polynomial factor in the above equation, $\langle P_2(\cos\theta)\rangle = \frac{1}{2}\langle 3\cos^2\theta - 1\rangle$, is zero. The value of this factor ranges from −0.061 (^{84}Kr-NH_3) to −0.166 (Ar-ND_3) which suggests that the χ_{aa} values obtained from the spectral fits are highly averaged over the internal motions of the ammonia subunit. For comparison, the $\langle P_2(\cos\theta)\rangle$ values of other NH_3 containing complexes are considerably larger: 0.817 (NH_3-HCN),[50] 0.776 (NH_3-CO_2),[51] 0.768 (NH_3-H_2O),[21] 0.767 (NH_3-HCCH),[52] 0.767 (NH_3-CF_3H),[53] 0.486

Table 3.8 Estimated orientation of ammonia in the Kr-NH_3, Ar-NH_3, and Ne-NH_3 dimers.

$\Sigma 0_{0a}/\Sigma 0_{00a}$		-NH_3	-NDH_2	-ND_2H	-ND_3
^{84}Kr	θ	57.2°/122.8°	58.3°/121.7°	59.1°/120.9°	60.1°/119.9°
	$\langle P_2(\cos\theta)\rangle$	-0.061	-0.085	-0.104	-0.126
Ar	θ	58.3°/121.7°	59.5°/120.5°	60.7°/119.3°	61.9°/118.1°
	$\langle P_2(\cos\theta)\rangle$	-0.086	-0.115	-0.141	-0.166
^{20}Ne	θ	57.5°/122.5°	58.3°/121.7°	59.2°/120.8°	60.1°/119.9°
	$\langle P_2(\cos\theta)\rangle$	-0.066	-0.086	-0.105	-0.128

(NH_3-HNO_3)[54]and 0.462 (NH_3-CO),[22] indicating that these complexes are comparatively more rigid. The internal motions of NH_3 are more hindered in the deuterated isotopomers of the Rg-NH_3 dimers as seen by the increasing χ_{aa} values (Tables 3.2 - 3.7) and $\langle P_2(\cos\theta)\rangle$ values (Table 3.8) upon deuterium substitution. This result is consistent with the greater tunnelling mass and lower zero point energy of the heavier isotopomers. The same was observed for the NH_3-CO complex for which the reported χ_{aa} values were: -2.028 MHz, -1.972 MHz, -1.916 MHz, and -1.890 MHz for the ND_3, ND_2H, NDH_2, and NH_3 isotopomers, respectively.[22]

A second, independent value of θ can be determined from the observed ^{83}Kr nuclear quadrupole hyperfine structure. The presence of the NH_3 molecule distorts the spherical symmetry of the electron distribution at the ^{83}Kr nucleus and leads to nuclear quadrupole hyperfine splitting. The field gradient, q_o, created by NH_3 at the Kr nucleus is given by:

$$q_o = 6\mu\left\langle\frac{\cos\theta}{R^4}\right\rangle - 12Q\left\langle\frac{P_2(\cos\theta)}{R^5}\right\rangle + \ldots$$

where $\mu = 0.57892\ ea_o$, $Q = -1.725\ ea_o^2$, etc. are the dipole, quadrupole, and higher order electric moments of NH_3,[8] R is the van der Waals bond length, and the brackets indicate averaging over the large amplitude motions. The nuclear quadrupole coupling constant depends on q_o according to the equation: $\chi_{aa}(^{83}Kr) = -Q_{Kr}(1-\gamma)eq_o/h$, where $Q_{Kr} = 0.27$ b is the nuclear quadrupole moment of ^{83}Kr,[55] and $\gamma = -75$ is the Sternheimer shielding constant[55] which accounts for the effect of the electronic cloud of the Kr atom on q_o.

Combining these equations and solving for θ yields a value of 118.6° which is similar to one set of supplementary angles calculated from the ^{14}N hyperfine structure in Table 3.8. The above expression was used to determine the extreme values for $\chi_{aa}(^{83}Kr)$ which are −10.0 MHz and 3.38 MHz for θ values of 66° (minimum) and 180° (maximum), respectively. The $\chi_{aa}(^{83}Kr)$ value fit from the spectrum of ^{83}Kr-NH_3 is −1.960 MHz, which is not close to either extreme, and most likely represents a highly averaged value. This is in accord with the observation of small $\langle P_2(\cos\theta)\rangle$ values from the ^{14}N nuclear quadrupole hyperfine analysis.

The deuterium hyperfine structure was not sufficiently resolved to include in the fit of the spectroscopic constants. For free ND_3, the χ_{aa} for deuterium[48] is estimated to be 0.200 MHz compared with −4.0898 MHz for the ^{14}N nucleus.[47] In the Ar-ND_3 complex, the ^{14}N nuclear quadrupole coupling constant is much smaller due to averaging over the large amplitude motion (~0.68 MHz) and under the same motions, one would expect the deuterium coupling constant to be only a few kHz in magnitude. The neglect of the deuterium hyperfine structure appears to have little effect on the resulting spectroscopic constants since the standard deviations of the fit were no greater than 5 kHz for the ground states of the Kr and Ar containing isotopomers.

3.5.2 The $\Sigma 1_1$ excited internal rotor state

The transitions assigned the $\Sigma 1_1$ states of Ar-ND_3 and Kr-ND_3 appear to be perturbed since the D_J constants for both inversion states are negative and the standard deviations from the fits of these states (~0.5 - 3 MHz) are considerably larger than for the

$\Sigma 0_0$ states (< 5 kHz). In Ar-NH_3, the $\Sigma 1_1$ states are subject to a Coriolis interaction with the nearby $\Pi 1_1$ states that mix the levels with the same J and the same symmetry under the D_{3h} molecular symmetry group.[3] The assignment of transitions to the perturbed $\Sigma 1_{1s}$ and $\Sigma 1_{1a}$ states of Ar-ND_3 and Kr-ND_3 was based on several observations. The observed intensities, in spite of the unresolved D splitting, approximated the predicted spin weights of 10:1:8 for the $\Sigma 0_{0s}$, $\Sigma 0_{0a}$, and $\Sigma 1_{1s}$ states, respectively. Secondly, a comparison of the ^{14}N nuclear quadrupole coupling constants revealed considerably larger χ_{aa} values in the $\Sigma 1_1$ states than in the $\Sigma 0_0$ states. This is in agreement with the χ_{aa} values reported for Ar-NH_3 which are 0.350 MHz,1.129 MHz, and 1.219 MHz for the $\Sigma 0_{0a}$, $\Sigma 1_{1s}$, and $\Sigma 1_{1a}$ states, respectively.[2,3] This observation is consistent with the different internal rotor states sampling different regions of the potential energy surface. For example, the wavefunction that is the main contributor to the $\Sigma 0_0$ internal rotor state is isotropic in both θ and ϕ, and thus the χ_{aa} value for this state experiences a different averaging effect than the $\Sigma 1_1$ state which primarily samples the region where θ is 90°.[11] The residuals of the ^{14}N hyperfine components are larger in the $\Sigma 1_1$ inversion states than in the $\Sigma 0_0$ states. This is likely due to unresolved deuterium splitting which would also be larger for this state due to the different averaging over the large amplitude motions of NH_3. Thirdly, the effect of the perturbation was similar to that observed in Ar-NH_3. For example, in Ar-NH_3, the transition frequencies for the three lowest J transitions are: 5 033.98 MHz, 10 130.3 MHz, and 15 326.304 MHz for the $\Sigma 1_{1s}$ state.[3,11] The second transition is double the first transition plus approximately 62 MHz and the third transition is triple the first transition plus approximately 224 MHz. For Ar-ND_3, the analogous center frequencies are 4

898.522 MHz, 9 803.764 MHz, and 14 721.280 MHz and the second and third transitions are roughly 7 MHz and 26 MHz higher than predicted using a rigid pseudodiatomic model. A similar comparison can be made for the $\Sigma 1_{1a}$ state as well as for Kr-ND_3 and although the magnitude of the perturbation is clearly different, the effect in which the successive J levels are pushed further apart is qualitatively similar for Ar-NH_3, Ar-ND_3, and Kr-ND_3. Schmuttenmaer *et al.*[11] calculated the bound states of Ar-ND_3 from their empirically derived Ar-NH_3 potential and predicted the two lowest J transitions to be 4914 MHz and 9836 MHz for the $\Sigma 1_{1s}$ state and 4908 MHz and 9830 for the $\Sigma 1_{1a}$ state. These predictions differ from the experimentally measured transitions in this work by approximately 15 MHz (J = 1-0) and 32 MHz (J = 2-1). A microwave-microwave double resonance technique was used to verify the relatedness of the transitions assigned to the $\Sigma 1_1$ inversion states. For each inversion state of Ar-ND_3, one ^{14}N hyperfine component of the J = 1-0 transition was pumped while the intensity of a related hyperfine component in the J = 2-1 transition was monitored. The experiment was repeated for a second ^{14}N hyperfine component in each inversion state and the intensity of the probe transition increased in both cases when the lower transition was being pumped. A similar experiment was used to verify the assignment of the $\Sigma 1_1$ states for Kr-ND_3. For this species, a component of the J = 3-2 transition was pumped while a component of the J = 4-3 transition was monitored.

The failure to locate transitions within the perturbed $\Sigma 1_1$ states of the Kr-NH_3 isotopomer can be rationalized by comparison with Ar-NH_3 and Ar-ND_3. The perturbing $\Pi 1_1$ states are closer to the $\Sigma 1_1$ states in Ar-NH_3 than in Ar-ND_3 leading to a significantly

larger perturbation in the former.[11] A similar effect is expected in Kr-NH_3. Secondly, the assignment of the perturbed $\Sigma 1_1$ states of the Ar-ND_3 and Kr-ND_3 complexes was largely aided by the fact that the inversion splitting of ND_3 is small (~1.6 GHz). The two inversion components are closely spaced in the microwave spectra and appear to experience similar degrees of perturbation from the $\Pi 1_1$ states. The larger inversion splitting of NH_3 (~23 GHz) makes the search and assignment of the perturbed states of Kr-NH_3 more difficult. The degree of perturbation may vary considerably for each inversion state and the relative population of the higher energy $\Sigma 1_{1a}$ state is significantly lower since it is not metastable. For Ar-NH_3, in fact, the microwave assignment of the $\Sigma 1_1$ states was possible only after submillimeter wave transitions between the various internal rotor states were measured.[3]

The spectroscopic constants for the $\Sigma 1_1$ states of Ar-ND_3 and Kr-ND_3 would be better determined if transitions related to the perturbing $\Pi 1_1$ states were measured. This is a difficult task since the $\Pi 1_1$ states are associated with the same nuclear spin function (E') as the $\Sigma 1_1$ states and are therefore not metastable. Schmuttenmaer *et al.*[11] predict that the $\Pi 1_{1s}$ and $\Pi 1_{1a}$ states of Ar-ND_3 are approximately 57 GHz higher than the $\Sigma 1_{1s}$ state based on their empirically derived Ar-NH_3 potential. At 0.5 K, the estimated rotational temperature of the molecular beam, the relative populations of the $\Pi 1_1$ states would be around 0.4 % based on a Boltzmann distribution. As a result of the small populations, it would be difficult to search for rotational transitions in the $\Pi 1_1$ states. A second possibility would be to measure cross-transitions between the $\Sigma 1_1$ and $\Pi 1_1$ states as Zwart *et al.*[3] reported for Ar-NH_3. They measured nineteen transitions between these states in

the microwave region such as $\Pi 1_{1a}$ (J' = 1) - $\Sigma 1_{1a}$ (J" = 2) = 15 315.276 MHz and $\Pi 1_{1s}$ (J' = 1) - $\Sigma 1_{1s}$ (J" = 2) = 36 601.36 MHz. Using the bound state calculations of Schmuttenmaer *et al.*,[11] the same two transitions for Ar-ND_3 would have frequencies of 40 599 MHz and 42 084 MHz, respectively which are beyond the upper limit of the spectrometer (26 GHz). There are no predictions available for higher J transitions of Ar-ND_3 with frequencies that may fall within the range of the spectrometer, nor are there theoretical predictions for the energy level spacings in the other Rg-NH_3 dimers.

3.5.3 Inversion tunnelling

Deuterium substitution allows the observation of inversion tunnelling splittings in the ground internal rotor states of the Rg-ND_3, Rg-ND_2H, and Rg-NDH_2 complexes. Direct measurement of the separation between the energy levels of the $\Sigma 0_{0s}$ and $\Sigma 0_{0a}$ states is not possible since these transitions are nuclear spin forbidden. As a result, the magnitude of the inversion tunnelling splittings observed in the rotational spectra must be used to extract information about the relative energy differences between the $\Sigma 0_{0s}$ and $\Sigma 0_{0a}$ states of the dimers. In general, it is expected that two states that lie close in energy have more similar rotational constants than two states that are split by a greater amount. For ^{20}Ne-ND_3, -ND_2H, and NDH_2, the differences in the B constants are 27.5 kHz, 203.8 kHz, and 541.1 kHz, respectively. This increasing difference in the rotational constants is consistent with the inversion splitting of the energy levels in free ND_3 (1.6 GHz), ND_2H (5 GHz), and NDH_2 (12 GHz).[31] The same trend is observed in the Ar/Kr analogues where the differences in B constants are: 31.5 kHz/42.8 kHz, 135.8 kHz/104.2 kHz, and

550.5 kHz/519.2 kHz, respectively. The small inversion tunnelling splittings observed for the dimers indicates that the two inversion states lie close in energy for each of these complexes. This is further supported by the measured χ_{aa} values which are the same within experimental error for the symmetric and antisymmetric inversion states of each dimer.

For the ND_2H and NDH_2 containing species, the symmetric inversion components are found at lower frequencies than the antisymmetric components when paired with Ne, Ar, and Kr. This is also the case for Ne-ND_3, but the assignment is reversed in both Ar-ND_3 and Kr-ND_3 so that the more intense symmetric components appear at higher frequencies. This reversal is a reflection of the extreme sensitivity of the rotational constants to the interaction potentials of each dimer. The ground internal rotor state, $\Sigma 0_0$, for example, mixes with higher internal rotor states, such as the $\Sigma 1_0$ state, and the degree of mixing varies for each dimer complex. Consequently, the energy level spacings in these states and the corresponding spectroscopic parameters are uniquely affected which makes direct comparisons difficult without a complete understanding of the subtleties of the interaction potentials of each Rg-NH_3 dimer. This may also explain why there is no clear trend in the observed tunnelling splittings when comparing the different Rg substituted complexes. For example, one would expect that the larger, more polarizable Kr atom would have a greater restrictive effect on the inversion motion. This means that the B constants should be more similar for the Kr containing dimers than for the Ar and Ne containing complexes yet the B constants are more different for Kr-ND_3 (42.8 kHz) than for Ar-ND_3 (31.5 kHz) and Ne-ND_3 (27.5 kHz). This apparent discrepancy

highlights the need for a more complete understanding of weak interactions with NH_3 as a function of the Rg atom size and polarizability.

3.5.4 *Ab initio* potential energy surfaces of Ne-NH_3

Three potential energy surfaces were constructed for the Ne-NH_3 dimer. The potential minimum for the NH_3 equilibrium geometry (>HNH = 106.67°) at the MP4 level is -62.7 cm^{-1} at R = 3.30 Å, θ = 90°, and ϕ = 60°. This is similar to the minimum energy of the other two surfaces: -63.2 cm^{-1} at R = 3.35 Å, θ = 90°, ϕ = 60° (>HNH = 113.34°) and -63.0 cm^{-1} at R = 3.35 Å, θ = 90°, ϕ = 60° (>HNH = 120.00°). The potential minima at the CCSD(T) level of theory correspond to the same θ and ϕ orientations of NH_3 but the minimum energies are slightly lower for the three surfaces: -63.2 cm^{-1}, -63.7 cm^{-1}, and -63.6 cm^{-1}, respectively. The minima correspond to structures in which the C_3 axis of NH_3 is perpendicular to the van der Waals bond axis with the Ne atom in the plane between two equivalent hydrogen atoms. From this orientation, the barriers to internal rotation at the MP4/CCSD(T) level about the C_3 axis of NH_3 are 17.0 cm^{-1}/17.6 cm^{-1} (>HNH = 106.67°), 17.4 cm^{-1}/17.9 cm^{-1} (>HNH = 113.34°), and 17.1 cm^{-1}/17.7 cm^{-1} (>HNH = 120.00°) at ϕ=0° for the three NH_3 geometries. Rotation in the θ coordinate has barriers at θ = 0° and θ = 180° corresponding to structures in which the C_3 axis of NH_3 is aligned with the van der Waals axis and the hydrogen atoms are pointed toward and away from the Ne atom, respectively. The barriers through θ = 0° are 34.5 cm^{-1}/33.0 cm^{-1} (>HNH = 106.67°) and 37.9 cm^{-1}/36.4 cm^{-1} (>HNH = 113.34°) for the two nonplanar NH_3 geometries at the MP4/CCSD(T) level. The barriers to rotation through θ = 180° are

smaller, 26.5 cm^{-1} and 30.9 cm^{-1} for the two surfaces, respectively. For planar NH_3, the barrier is the same, 37.3 cm^{-1}/36.3 cm^{-1} through $\theta = 0°$ and $\theta = 180°$ due to symmetry. The Ne-NH_3 potential minimum is only about half as deep as that calculated for Ar-NH_3 at the MP4 level of theory (130.1 cm^{-1}) and the barriers to internal rotation are about 65 % - 70 % of those reported for Ar-NH_3, 26.6 cm^{-1} in the ϕ coordinate, 55.2 cm^{-1} and 38.0 cm^{-1} for rotation through $\theta = 0°$ and $\theta = 180°$, respectively.[13] Comparison with Kr-NH_3 is possible at the MP2 level. The global minima are 108 cm^{-1}, 91 cm^{-1}, and 45 cm^{-1} for Kr-NH_3,[49] Ar-NH_3,[12] and Ne-NH_3, respectively. This is a crude comparison since different basis sets were used for each complex but the results appear consistent with the expectation that the smaller, less polarizable Ne atom is more weakly bound to NH_3 than either Ar or Kr.

Figure 3.4 examines the potential energy of the system as a function of the relative orientation of the NH_3 subunit. The interaction energies (MP4) along the minimum energy path for the internal rotation of NH_3 (>HNH = 106.67°) in the θ coordinate are plotted for seven different values of ϕ, ranging from $\phi = 0°$ to $\phi = 60°$. There is no ϕ dependence for the $\theta = 0°$ and $\theta = 180°$ arrangements since the C_3 axis of NH_3 is aligned with the van der Waals bond. The largest ϕ dependence occurs in the region between θ = 60° and 110°, particularly when the symmetry axis of NH_3 is perpendicular to the complex axis. The potential well is broader and the minimum shifts to larger θ values as the NH_3 molecule is rotated about its C_3 axis to smaller ϕ angles. This corresponds to the hydrogen atoms pointing away from the Ne atom for small ϕ values since around $\theta = 90°$, the small ϕ values correspond to orientations where one hydrogen atom lies between the Ne and N atoms, almost in the plane of the van der Waals axis. The system relieves the

Figure 3.4 Minimum energy (MP4) path of Ne-NH_3 from $\theta = 0°$ to $\theta = 180°$ when NH_3 is in its experimental equilibrium conformation (<HNH = 106.67°). Each curve represents a particular value of ϕ between 0° and 60°.

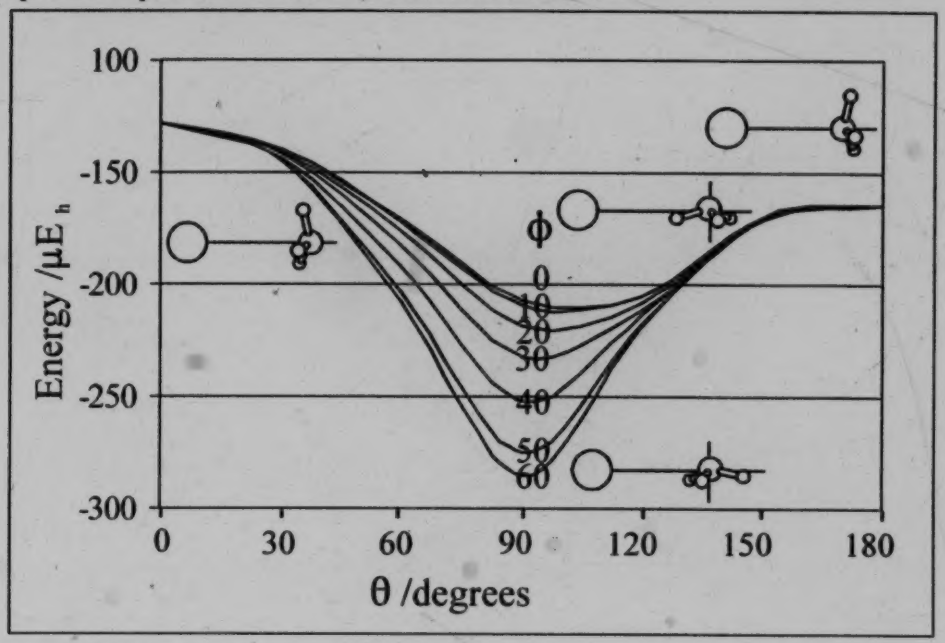

strain resulting for the repulsive interaction by slightly tilting the C_3 axis of NH_3 with respect to the van der Waals axis. From the minimum energy orientation, at $\theta = 90°$ and $\phi = 60°$, the energy varies by only 3 cm^{-1} for θ values between 80° and 100° and by 10 cm^{-1} for θ values between 70° and 110°. This relative flatness in the θ coordinate is reflected in the experimentally determined χ_{aa} value (0.2700 MHz) for ^{20}Ne-NH_3. The small magnitude of the ^{14}N nuclear quadrupole coupling constant as compared to the χ_o value of free NH_3 (−4.0898 MHz)[47] is largely a result of averaging over the internal motions of NH_3 in the θ coordinate of the complex.

The dependence of the inversion motion on the orientation of NH_3 is investigated

Figure 3.5 Comparison of the minimum energy (MP4) paths of Ne-NH_3 for the three different NH_3 monomer geometries: (—●—) >HNH = 106.67°, (·····■·····) >HNH = 113.34° and (--▲--) >HNH = 120.00°, between θ = 0° and 180° at a) ϕ = 60° and b) ϕ = 0°.

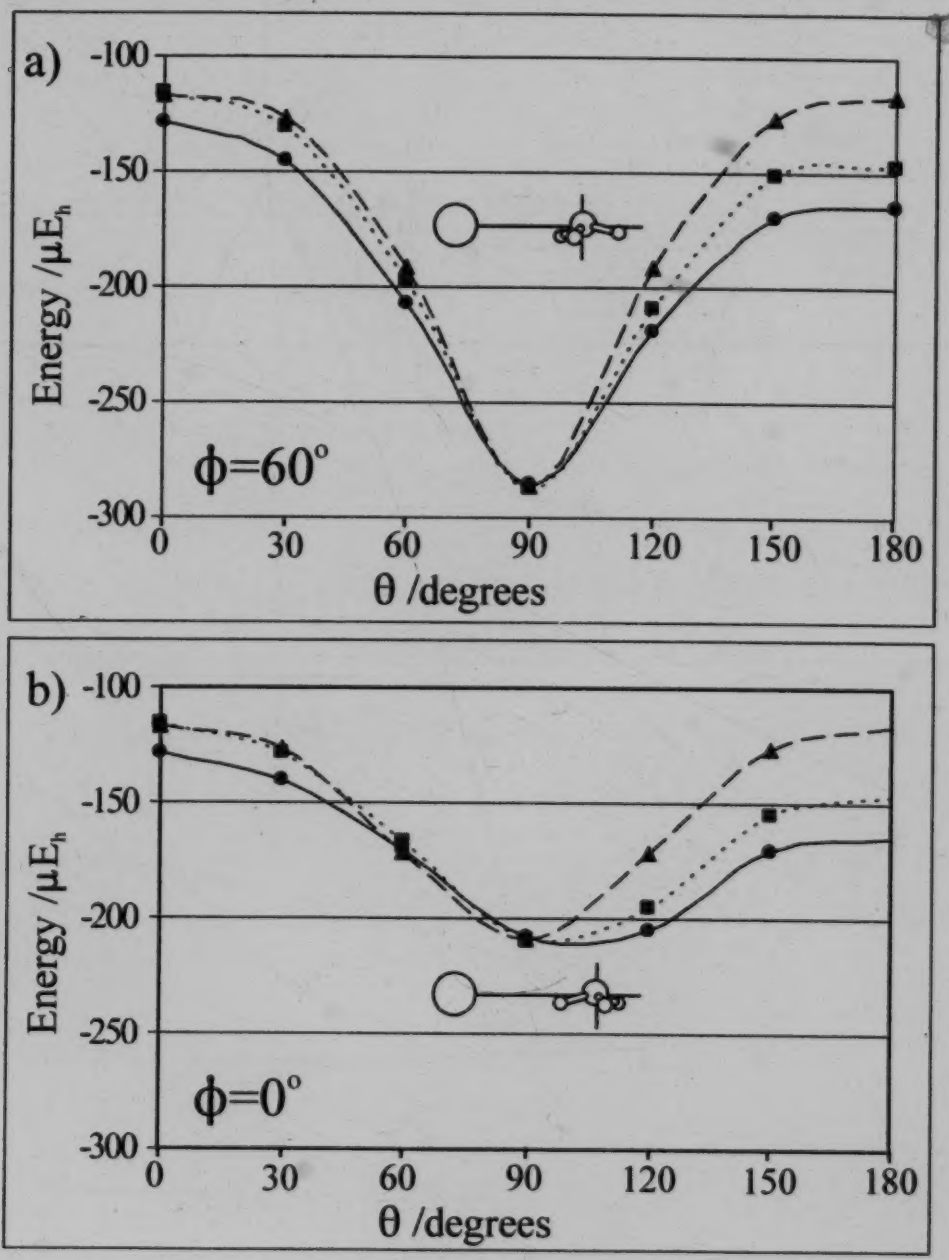

in Figures 3.5 a) and 3.5 b) which show the minimum energy (MP4) paths along the θ coordinate for each of the three NH_3 monomer geometries at $\phi = 60°$ and $\phi = 0°$. The equilibrium geometry of NH_3 has the broadest, shallowest well while the planar structure has the narrowest and deepest. The van der Waals bond lengths along the minimum energy paths are the same for all three NH_3 geometries between $\theta = 0°$ and 90°. At values of θ greater than 90°, the R coordinates along the minimum energy paths increase for the successively larger NH_3 umbrella angles. For example, at $\theta = 120°$ and $\phi = 0°$, the R coordinates along the minimum energy part are 3.50 Å, 3.60 Å, and 3.70 Å for the >HNH = 106.67°, 113.34°, and 120.00° NH_3 geometries, respectively. The largest difference between the minimum energy paths occurs at $\theta = 180°$. At this orientation, the equilibrium geometry is about 10 cm^{-1} lower in energy than the planar geometry. The three plots are the most similar between $\theta = 60°$ and 100° suggesting that the shape of the potential energy surface is not strongly influenced by the internal geometry of NH_3 when the C_3 axis of NH_3 is nearly perpendicular to the van der Waals axis. This matches the experimental observations that the inversion motion of NH_3 is barely affected in the Σ states while effectively quenched in the Π states.[3]

The dependence of the interaction energy (MP4) on the van der Waals bond length R and the NH_3 geometry is plotted in Figure 3.6 for two different orientations of NH_3, $\theta = 90°/\phi = 0°$ and $\theta = 90°/\phi = 60°$. The potential energy curves are very flat in the radial coordinate around the minimum energy orientation, $\theta = 90°/\phi = 60°$ and are insensitive to the NH_3 monomer geometry at this orientation as seen by the overlapping of the three curves corresponding to the three different umbrella angles of NH_3. This flatness

Figure 3.6 Comparison of the interaction energy (MP4) of Ne-NH_3 for the three different NH_3 geometries: (—) >HNH = 106.67°, (---) >HNH = 113.34°, and (·····) >HNH = 120.00°,as a function of the van der Waals bond length R and the orientation ϕ: (●) ϕ = 0°, (X) ϕ = 60° at θ = 90°.

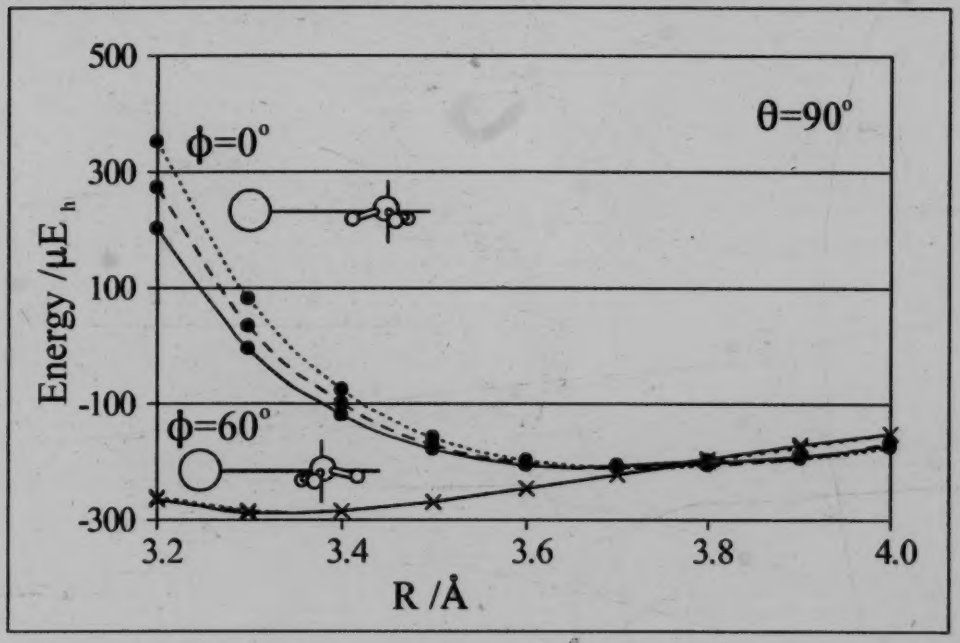

in the radial coordinate results in significant averaging over the zero point motion and is a main source of the discrepancy between the experimental (3.7 Å) and *ab initio* (3.3 Å) values for R. At small R values, the interaction energy becomes increasingly repulsive for each θ/ϕ orientation of NH_3. The interaction energy is more sensitive to ϕ at small R separations, particularly around θ = 60° - 90°. This can be seen in Figure 3.6 for θ = 90° by the large difference in the potential energy curves corresponding to ϕ = 0° and ϕ = 60°. The NH_3 monomer geometry also has a greater effect on the interaction energy at small R distances especially for orientations that are further from the minimum energy orientation. As R increases, the interaction energy becomes less dependent on the θ/ϕ orientation and

NH_3 monomer geometry as expected.

3.6 Concluding remarks

The microwave spectra of the Rg-NH_3 (Rg = Kr, Ar, Ne) dimers and their deuterated isotopomers were measured. The spectra are characteristic of diatomic molecules in which the NH_3 subunit behaves as a single moiety. The van der Waals bond lengths derived from the B rotational constants of each species deviate from those of other Rg-molecule complexes in that the bond lengths change less than expected upon Rg atom substitution. The internal rotation of NH_3 is surprisingly unhindered in all three of the Rg-NH_3 dimers as seen by the magnitudes of the ^{14}N nuclear quadrupole coupling constants. The deuterated isotopomers of the Rg-NH_3 dimers are of particular interest since an inversion tunnelling splitting is observed in the ground state spectra. The magnitude of this splitting follows the trend expected based on the energy level differences in the free ND_3, ND_2H, and NDH_2 monomers. Subtle variations in the observed ^{14}N nuclear quadrupole hyperfine structure and the inversion tunnelling splittings of the various isotopomers reveal that there are distinct differences in the internal motions of the Rg-NH_3 complexes. These cannot be extrapolated from the existing empirical potential of Ar-NH_3.[11] This is demonstrated by the inability to locate excited internal rotor state transitions of Ne-NH_3 and Kr-NH_3 and by the difference in the degree of perturbation of this state in Ar-ND_3 and Kr-ND_3. To understand the subtleties of the weak interaction on a quantitative level as a function of the Rg atom size, empirical potentials are needed for both the Ne-NH_3 and Kr-NH_3 dimers. To achieve this, a broad

range of spectroscopic data is required.

In the absence of more extensive spectroscopic studies of the Rg-NH_3 dimers, qualitative information related to the structure and dynamics of weakly bound complexes can be derived from *ab initio* methods, as demonstrated in this chapter for the Ne-NH_3 complex. For example, the depth of the potential energy surface minimum reveals that the Ne-NH_3 interaction is weaker than reported for Ar-NH_3 and Kr-NH_3 as expected for the smaller, less polarizable Ne atom.[12,49] Several topological features of the potential energy surfaces can be related to spectroscopic observations. For example, the low anisotropy in the θ coordinate around the global minimum is reflected in the size of the experimentally determined χ_{aa} values. The flatness in the R coordinate suggests that the van der Waals bond is very flexible as demonstrated by the small force constant (0.0029 mdyn/Å) of the Ne-NH_3 bond and the large differences between the experimental (3.72 Å) and *ab initio* (3.30 Å) derived bond lengths. Furthermore, the *ab initio* calculations reveal that there is little difference in energy as a function of the NH_3 monomer geometry at the potential energy surface minimum. This is in accord with the experimental observation that the inversion of NH_3 is barely affected in the Σ states.[3,11]

References

1. G. T. Fraser, D. D. Nelson Jr., A. Charo, and W. Klemperer, *J. Chem. Phys.* **82**, 2535 (1985).

2. D. D. Nelson Jr., G. T. Fraser, K. I. Peterson, K. Zhao, W. Klemperer, F. J. Lovas, and R. D. Suenram, *J. Chem. Phys.* **85**, 5512 (1986).

3. E. Zwart, H. Linnartz, W. L. Meerts, G. T. Fraser, D. D. Nelson Jr., and W. Klemperer, *J. Chem.. Phys.* **95**, 793 (1991).

4. E. Zwart and W. L. Meerts, *Chem. Phys.* **151**, 407 (1991).

5. D.-H. Gwo, M. Havenith, K. L Busarow, R. C. Cohen, C. A. Schmuttenmaer, and R. J. Saykally, *Mol. Phys.* **71**, 453 (1990).

6. C. A. Schmuttenmaer, R. C. Cohen, J. G. Loeser, and R. J. Saykally, *J. Chem. Phys.* **95**, 9 (1991).

7. A. Grushow, W. A. Burns, S. W. Reeve, M. A. Dvorak, and K. R. Leopold, *J. Chem. Phys.* **100**, 2413 (1994).

8. C. A. Schmuttenmaer, J. G. Loeser, and R. J. Saykally, *J. Chem. Phys.* **101**, 139 (1994).

9. A. Bizzarri, B. Heijmen, S. Stolte, and J. Reuss, *Z. Phys. D.* **10**, 291 (1988).

10. G. T. Fraser, A. S. Pine, and W. A. Kreiner, *J. Chem. Phys.* **94**, 7061 (1991).

11. C. A Schmuttenmaer, R. C. Cohen, and R. J. Saykally, *J. Chem. Phys.* **101**, 146 (1994).

12. G. Chałasiński, S. M. Cybulski, M. M. Szczęśniak, and S. Scheiner, *J. Chem. Phys.* **91**, 7809 (1989).

13. F. M. Tao and W. Klemperer, *J. Chem. Phys.* **101**, 1129 (1994).

14. M. Bulski, P. E. S. Wormer, and A. van der Avoird, *J. Chem. Phys.* **94**, 491 (1991).

15. J. W. I. van Bladel, A. van der Avoird, and P. E. S. Wormer, *J. Chem. Phys.* **94**, 501 (1991).

16. J. W. I. van Bladel, A. van der Avoird, and P. E. S. Wormer, *J. Phys. Chem.* **95**, 5414 (1991).

17. J. W. I. van Bladel, A. van der Avoird, and P. E. S. Wormer, *Chem. Phys.* **165**, 47 (1992).

18. D. D. Nelson Jr., G. T. Fraser, and W. Klemperer, *J. Chem. Phys.* **83**, 6201 (1985).

19. D. D. Nelson Jr., W. Klemperer, G. T. Fraser, F. J. Lovas, and R. D. Suenram, *J. Chem. Phys.* **87**, 6364 (1987).

20. E. N. Karakin, G. T. Fraser, J. G. Loeser, and R. J. Saykally, *J. Chem. Phys.* **110**, 9555 (1999).

21. P. Herbine and T. R. Dyke, *J. Chem. Phys.* **83**, 3768 (1985).

22. G. T. Fraser, D. D. Nelson Jr., K. I. Peterson, and W. Klemperer, *J. Chem. Phys.* **84**, 2472 (1986).

23. T. J. Balle and W. H. Flygare, *Rev. Sci. Instrum.* **52**, 33 (1981).

24. P. Bunker and P. Jensen, *Molecular Symmetry and Spectroscopy*, 2nd edition, NRC Research Press, Ottawa (1998).

25. G. T. Fraser, A. S. Pine, R. D. Suenram, and K. Matsumura, *J. Molec. Spectrosc.* **144**, 97 (1990).

26. J. van Wijngaarden and W. Jäger, *J. Molec. Spectrosc.* **98**, 1575 (2000).

27. W. Jäger and M. C. L. Gerry, *Chem. Phys. Lett.* **196**, 274 (1992).

28. W. Jäger, Y. Xu, N. Heineking, and M. C. L. Gerry, *J. Chem. Phys.* **99**, 7510 (1993).

29. C. H. Townes and A. L. Schawlow, *Microwave Spectroscopy*, Dover, New York (1975).

30. H. M. Pickett, *J. Molec. Spectrosc.* **148**, 371 (1991).

31. M. T. Weiss and M. W. P. Strandberg, *Phys. Rev.* **83**, 567 (1951).

32. W. S. Benedict and E. K. Plyler, *Can. J. Phys.* **35**, 1235 (1957).

33. *Gaussian 94* (Revision D.1), M. J. Frisch, G. W. Trucks, H. B. Schlegel, P. M. W. Gill, B. G. Johnson, M. A. Robb, J. R. Cheeseman, T. A. Keith, G. A. Petersson, J. A. Montgomery, K. Raghavachari, M. A. Al-Laham, V. G. Zakrzewski, J. V. Ortiz, J. B. Foresman, J. Cioslowski, B. B. Stefanov, A. Nanayakkara, M. Challacombe, C. Y Peng, P. Y. Ayala, W. Chen, M. W. Wong, J. L Andres, E. S. Replogle, R. Gomperts, R. L. Martin, D. J Fox, J. S. Binkley, D. J. Defrees, J. Baker, J. P. Stewart, M. Head-Gordon, C. Gonzalez, and J. A. Pople, Gaussian, Inc., Pittsburgh, PA, 1995.

34. S. F. Boys and F. Bernardi, *Mol. Phys.* **19**, 553 (1970).

35. *MOLPRO* (Version 2000.1), written by H. -J. Werner and P. R. Knowles, with contributions from R. D. Amos, A. Bernhardsson, A. Berning, P. Celani, D. L. Cooper, M. J. O. McNicholas, F. R. Manby, W. Meyer, M. E. Mura, A. Nicklass, P. Palmieri, R. Pitzer, G. Rauhut, M. Schütz, H. Stoll, A. J. Stone, R. Tarroni, and T. Thorsteinsson, University of Birmingham, UK, 1999.

36. T. H. Dunning, Jr. *J. Chem. Phys.* **90**, 1007 (1989).

37. A. J. Sadlej, *Collec. Czech. Chem. Commun.* **53**, 1995 (1988).

38. Basis sets were obtained from the Extensible Computational Chemistry Environment Basis Set Database, as developed and distributed by the Molecular Science Computing Facility, Environmental and Molecular Sciences Laboratory which is part of the Pacific Northwest Laboratory, P.O. Box 999, Richland, Washington 99352, USA, and funded by the U.S. Department of Energy. The Pacific Northwest Laboratory is a multi-program laboratory operated by Battelle Memorial Institute for the U.S. Department of Energy under contract DE-AC06-76RLO 1830.

39. G. T. Fraser, A. S. Pine, and R. D. Suenram, *J. Chem. Phys.* **88**, 6157 (1988).

40. G. T. Fraser and A. S. Pine, *J. Chem. Phys.* **85**, 2502 (1986).

41. K. A. Walker, T. Ogata, W. Jäger, M. C. L. Gerry, and I. Ozier, *J. Chem. Phys.* **106**, 7519 (1997).

42. T. Ogata, W. Jäger, I. Ozier, and M. C. L. Gerry, *J. Chem. Phys.* **98**, 9399 (1993).

43. E. J. Campbell, L. W. Buxton, and A. C. Legon, *J. Chem. Phys.* **78**, 3483 (1983).

44. K. R. Leopold, G. T. Fraser, F. J. Lin, D. D. Nelson Jr., and W. Klemperer, *J. Chem. Phys.* **81**, 4922 (1984).

45. M. Iida, Y. Ohshima, and Y. Endo, *J. Phys. Chem.* **97**, 357 (1993).

46. F. J. Lovas and R. D. Suenram, *J. Chem. Phys.* **87**, 2010 (1987).

47. M. D. Marshall and J. S. Muenter, *J. Molec. Spectrosc.* **85**, 322 (1986).

48. G. Herrmann, *J. Chem. Phys.* **29**, 875 (1958).

49. G. Chałasiński, M. M. Szczęśniak, and S. Scheiner, *J. Chem. Phys.* **97**, 8181 (1992).

50. G. T. Fraser, K. R. Leopold, D. D. Nelson Jr., A. Tung, and W. Klemperer, *J. Chem. Phys.* **80**, 3073 (1984).

51. G. T. Fraser, K. R. Leopold, and W. Klemperer, *J. Chem. Phys.* **81**, 2577 (1984).

52. G. T. Fraser, K. R. Leopold, and W. Klemperer, *J. Chem. Phys.* **80**, 1423 (1984).

53. G. T. Fraser, F. J. Lovas, R. D. Suenram, D. D. Nelson Jr., and W. Klemperer, *J. Chem. Phys.* **84**, 5983 (1986).

54. M. E. Ott and K. R. Leopold, *J. Phys. Chem. A.* **103**, 1322 (1999).

55. E. J. Campbell, L. W. Buxton, M. R. Keenan, and W. H. Flygare, *Phys. Rev. A.* **24**, 812 (1981).

CHAPTER 4

Investigation of the Rg_2-NH_3 van der Waals trimers: Rotational spectra and *ab initio* calculations

4.1 Introduction

Three body nonadditive terms are known to be important contributors to the interaction energy of van der Waals trimers. High resolution spectra of such systems provide experimental evidence of these nonadditive contributions and thus supply meaningful information for deriving and testing the theoretical descriptions of nonadditive terms. Significant work has been done on several van der Waals trimers such as Ar_2-HCl,[1,2,3,4] Ar_2-HF,[5,6,7] and Ar_2-H_2O.[8,9] These complexes are prototypes for the study of nonadditive effects since the binary potentials involved (Ar-Ar,[10,11,12] Ar-HCl,[13] Ar-HF,[14] Ar-H_2O)[15,16] are well characterized. This allows the three body contributions to the interaction energies to be isolated.

The rotational spectra of the Rg-NH_3 dimers (Rg = Kr, Ar, Ne) described in Chapter 3 have provided information about the structures and dynamics of the binary complexes as a function of the Rg atom size and polarizability. Despite the widespread interest in Ar-NH_3 (References 1 - 17 of Chapter 3), there have been no previous spectroscopic or theoretical studies of the Rg_2-NH_3 trimers. A microwave investigation of the Rg_2-NH_3 complexes affords the opportunity to study the dependence of the NH_3 internal dynamics on the Rg cluster size and promises to further the understanding of three body nonadditive contributions to the interaction energies of van der Waals trimers.

This is particularly true for Ar_2-NH_3 since the binary potentials of Ar-NH_3[17] and Ar-Ar[10, 11,12] are well known. The rotational spectra of the trimers may be complemented by the construction of *ab initio* potential energy surfaces that characterize the weak interaction, as shown for the Rg-NH_3 dimers in Chapter 3. This is most feasible for the Ne_2-NH_3 trimer since the basis sets required for Ne are smaller than for larger Rg atoms and as a result, the calculations are less limited by the availability of computational resources.

This chapter describes the first spectroscopic study of the ground internal rotor state of five different isotopomers of Ar_2-NH_3 and eight different isotopomers of Ne_2-NH_3. The ^{14}N nuclear quadrupole hyperfine splitting as well as the inversion tunnelling splitting of the deuterated isotopomers are analyzed in terms of the dynamics of NH_3 within the two trimer complexes. Comparisons are drawn with the rotational spectra of the Rg-NH_3 dimers in Chapter 3. In addition, three potential energy surfaces for the Ne_2-NH_3 complex were constructed at the CCSD(T) level of theory. The main topological features of the potential energy surfaces are discussed in terms of experimentally determined spectroscopic parameters and comparisons are made with the *ab initio* results of the Ne-NH_3 dimer.

4.2 Experimental Method

The rotational spectra of the Ar_2-NH_3 and Ne_2-NH_3 trimers were recorded between 3.9 GHz and 19 GHz using the Fourier transform microwave spectrometer described in Chapter 2 and Section 3.2. The trimer complexes were produced via molecular beam expansion of a gas mixture through a pulsed nozzle that is 0.8 mm (General Valve Corp.,

Series 9) in diameter. The Ar_2-NH_3 complexes were generated using a gas sample consisting of 0.5 % NH_3 and 5 % Ar. Neon was used as a backing gas to obtain a total pressure of 10 - 12 atm. Argon was not added to the sample mixture for the measurement of the Ne_2-NH_3 trimer spectra. The ^{22}Ne containing isotopomers were measured in their natural abundances (8.82 % ^{22}Ne) while isotopically enriched samples were used to record the spectra of the ^{15}N (Cambridge Isotopes Laboratories: 98 % $^{15}NH_3$) and deuterium (Cambridge Isotopes Laboratories: 99 % ND_3) containing isotopomers. The spectra of the Rg_2-ND_2H and Rg_2-NDH_2 complexes were recorded using the ND_3 containing gas mixture. The intensities of the transitions increased dramatically for the partially deuterated species after the gas mixture was left in the sample containment system for several hours.

4.3 Spectral search and assignment

As described in Chapter 3, the NH_3 molecule undergoes large amplitude motions within the Rg-NH_3 (Rg = Kr, Ar, Ne) van der Waals dimer complexes. This leads to the observation of excited internal rotor states as well as an inversion tunnelling splitting in the microwave spectra of the dimers. Similar results are expected for the Ar_2-NH_3 and Ne_2-NH_3 trimers. Both van der Waals trimers are predicted to be asymmetric tops and the rotational energy levels are labelled with the quantum numbers $J_{K_aK_c}$. The allowed transitions of Ar_2-NH_3 and Ne_2-NH_3 can be determined via molecular symmetry group analyses as described below.[18]

4.3.1 Isotopomers of Ar_2-NH_3

The rotational spectrum of the Ar_2-NH_3 trimer was predicted to be that of an oblate asymmetric top as reported for Ar_2-H_2O.[8,9] In the Ar_2-H_2O trimer, the H_2O subunit undergoes nearly free internal rotation and was subsequently treated as a spherical moiety in the rotational analysis. The structure of Ar_2-NH_3 was estimated using a similar pseudotriatomic model. Figure 4.1 shows the geometry of the Ar_2-NH_3 complex in its principal inertial axis system. Due to large amplitude motions of NH_3, there is only a nonzero dipole moment contribution along the *b*-axis of the trimer. The expected rotational transitions are *b*-type and obey the selection rules: $\Delta J = 0$ or ± 1, $\Delta K_a = \pm 1$ {± 3,

Figure 4.1 Geometry of the Ar_2-NH_3 trimer in the principal inertial axis system.

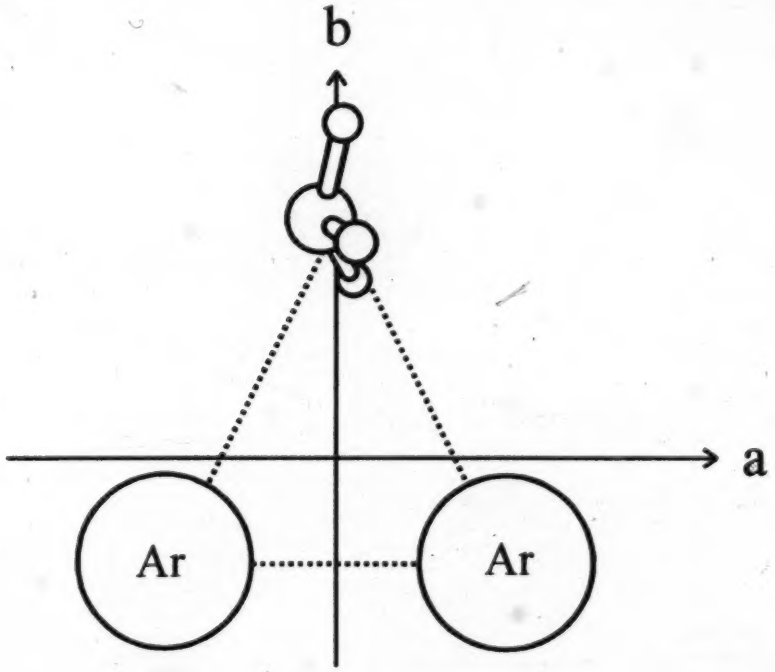

±5, ...} and $\Delta K_c = \pm1$ {±3, ±5, ...}. The nuclear spin statistics associated with each isotopomer depend on the presence of identical Ar, hydrogen, and deuterium nuclei. The nuclear spin weights of the various rotational levels were verified using molecular symmetry group theoretical analyses.[18] The results are summarized for each isotopomer in Table 4.1.

a) Ar_2-NH_3 and Ar_2-$^{15}NH_3$

The Ar_2-NH_3 and Ar_2-$^{15}NH_3$ complexes belong to the G_{24} molecular symmetry group (Appendix 1, Table A1.3). The total wavefunction must be antisymmetric for the operation that interchanges two protons and symmetric for the interchange of the two Ar nuclei. The A_3 and A_4 irreducible representations meet these criteria. The nuclear spin function of the three protons spans the representation: $4A_1 \oplus 2E_1$. The vibrational symmetry of the symmetric/antisymmetric inversion component is A_1/A_4. The symmetry of the asymmetric rotor wavefunction depends on whether K_a and K_c are even(e) or odd(o). The rotational levels (K_aK_c) have the following symmetries under G_{24}: A_1(ee), B_2(eo), B_1(oe), and A_2(oo). For the ground internal rotor state, the symmetric inversion component has a nuclear spin statistical weight of zero and no rotational transitions are observable. For the antisymmetric component, the 'ee' and 'oo' rotational levels can combine with the A_1 nuclear spin function but the 'eo' and 'oe' levels have nuclear spin statistical weights of zero. Thus, only *b*-type transitions between the 'ee' and 'oo' levels are allowed for the antisymmetric inversion component of the ground internal rotor state of Ar_2-NH_3 and Ar_2-$^{15}NH_3$. The predicted energy level diagram is shown in Figure 4.2.

The rotational constants of Ar_2-NH_3 were estimated using the structure

Table 4.1 Summary of the molecular symmetry group theory analysis for the metastable states of the Ar_2-NH_3 isotopomers.

	Ar_2-NH_3	Ar_2-ND_3	Ar_2-ND_2H	Ar_2-NDH_2
Molecular symmetry group	G_{24}	G_{24}	G_8	G_8
Total symmetry required[a]	A_3/A_4	A_1/A_2	A_1/A_2	A_3/A_4
Nuclear spin symmetry[b]	$4A_1 \oplus 2E_1$	$10A_1 \oplus A_3 \oplus 8E_1$	$6A_1 \oplus 3A_3$	$3A_1 \oplus A_3$
Rotational symmetry[c]	K_aK_c = ee/eo/oe/oo $A_1/B_2/B_1/A_2$			
NH_3 inversion symmetry	symmetric/antisymmetric A_1/A_4			
NH_3 internal rotation symmetry	ground state/first excited state A_1/E_1		n/a	
Rovibrational symmetry[d]	K_aK_c = ee/eo/oe/oo			
$\Sigma 0_{0s}$	$A_1/B_2/B_1/A_2$		$A_1/B_2/B_1/A_2$	
$\Sigma 0_{0a}$	$A_4/B_3/B_4/A_3$		$A_4/B_3/B_4/A_3$	
$\Sigma 1_{1s}$	$E_1/E_4/E_3/E_2$		n/a	
Predicted nuclear spin statistical weights	$\Sigma 0_{0s}$:$\Sigma 0_{0a}$:$\Sigma 1_{1s}$		$\Sigma 0_{0s}$:$\Sigma 0_{0a}$	
	0:4:2	10:1:8	6:3	1:3

[a] refers to the symmetry of the total wavefunction upon exchange of identical fermions or bosons.

[b] refers to the symmetry of the nuclear spin function of the identical hydrogen or deuterium nuclei only.

[c] depends on whether K_a and K_c are even (e) or odd (o).

[d] includes the NH_3 inversion and NH_3 internal rotation symmetries.

constructed from the bond lengths of the Ar-Ar (3.821 Å)[10, 11] and Ar-NH_3 (3.8359 Å)[19] dimers. The $J_{K_aK_c} = 1_{11}$-0_{00} transition was found within 10 MHz of this prediction. In total, 18 rotational transitions of Ar_2-NH_3 were measured and the ^{14}N nuclear quadrupole hyperfine structures were resolved and assigned. The transition frequencies are listed in Appendix 4 (Table A4.1). The ^{14}N hyperfine and rotational analyses were done

Figure 4.2 Predicted energy level diagram for the Ar_2-NH_3 asymmetric top. The transitions are *b*-type transitions and dotted lines denote energy levels with nuclear spin statistical weights of zero.

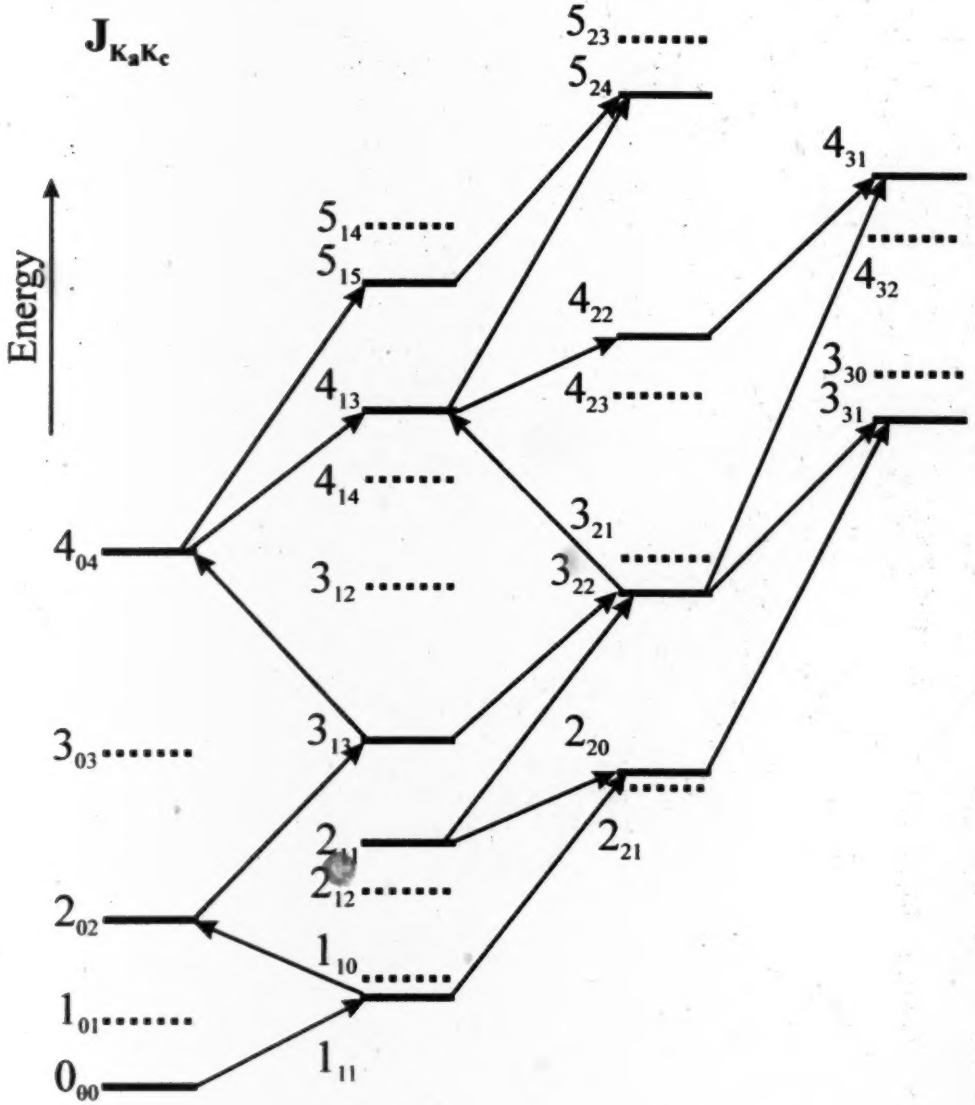

simultaneously using Pickett's global fitting routine.[20] The spectroscopic constants obtained using Watson's *IIr* S-reduction Hamiltonian[21] are given in Table 4.2.

The analogous rotational transition frequencies for the Ar_2-$^{15}NH_3$ isotopomer are listed in Table A4.2. The rotational analysis was done using Pickett's program[20] and the resulting spectroscopic constants are listed in Table 4.2.

It can be shown from the molecular symmetry group analysis of the NH_3 and $^{15}NH_3$ containing isotopomers that there is a second metastable internal rotor state of the trimer complex. This state is associated with the E_1 nuclear spin function. As described in Chapter 3 for the Rg-NH_3 complexes, this excited internal rotor state is believed to be Coriolis perturbed by nearby internal rotor states. A broad search was conducted for rotational transitions associated with this excited state of Ar_2-NH_3 at both higher and lower frequencies than the ground state transitions. No transitions were found that met the

Table 4.2 Spectroscopic constants for Ar_2-NH_3 and Ar_2-$^{15}NH_3$.

$\Sigma 0_{0a}$	Ar_2-NH_3	Ar_2-$^{15}NH_3$
Rotational constants /MHz		
A	3252.7345(2)	3109.6578(3)
B	1735.3628(2)	1735.3608(3)
C	1122.7410(1)	1105.0596(2)
Centrifugal distortion constants /MHz		
D_J	0.0146(1)	0.0142(1)
D_{JK}	0.0431(1)	0.0426(1)
D_K	0.0501(1)	0.0420(1)
d_1	-6.5(1)	-6.6(1)
d_2	-1.9(2)	-2.0(1)
^{14}N quadrupole hyperfine constants /MHz		
χ_{aa}	0.0643(10)	
χ_{bb}	0.6221(15)	
Standard deviation /kHz		
σ	3.0	2.8

criteria based on the expected ^{14}N nuclear quadrupole hyperfine splitting.

b) Ar_2-ND_3

Like Ar_2-NH_3, the Ar_2-ND_3 isotopomer belongs to the G_{24} molecular symmetry group (Table A1.3). The interchange of any two identical deuterium nuclei (as well as the Ar nuclei) is governed by Bose-Einstein statistics. The 'eo' and 'oe' levels have nuclear spin statistical weights of zero for both inversion states of the ground internal rotor state. Thus for Ar_2-ND_3, two *b*-type spectra consisting of transitions between the 'ee' and 'oo' rotational levels are expected. The symmetric and antisymmetric inversion states are predicted to have relative intensities of 10 and 1, respectively. In the Rg-ND_3 dimers (Rg=Ne, Ar, Kr), the B rotational constants for the two inversion states differ by only tens of kHz resulting in overlap of the ^{14}N nuclear quadrupole hyperfine splitting patterns. A smaller inversion tunnelling splitting was expected for Ar_2-ND_3 and it was initially unclear whether the inversion motion would be quenched by the presence of two Rg atom binding partners.

The transition frequencies assigned to the ground internal rotor state of Ar_2-ND_3 are listed in Table A4.3. Eleven rotational transitions were measured and the inversion tunnelling splitting was resolved in all but two of these. The more intense inversion tunnelling components appear at higher frequency for most of the transitions and were subsequently assigned to the symmetric inversion state based on the nuclear spin statistical predictions. The inversion tunnelling splitting is 165 kHz for the $J_{K_aK_c} = 1_{11}$-0_{00} transition. The ^{14}N hyperfine and rotational analyses were done for each state as described for Ar_2-NH_3. The spectroscopic constants are listed in Table 4.3. The three quadrupolar

deuterium nuclei in Ar_2-ND_3 do not produce a large enough splitting for analysis. The neglect of the deuterium hyperfine did not have a significant effect on the spectral analysis as the standard deviations of the fits were on the order of 3 kHz for each of the two inversion states.

As described above for Ar_2-NH_3, there is an additional metastable internal rotor state of the Ar_2-ND_3 which is associated with the E_1 nuclear spin function. The Coriolis

Table 4.3 Spectroscopic constants for Ar_2-ND_3, Ar_2-ND_2H, and Ar_2-NDH_2.

$\Sigma 0_{0s}/\Sigma 0_{00s}$	Ar_2-ND_3	Ar_2-ND_2H	Ar_2-NDH_2
Rotational constants /MHz			
A	2853.4841(5)	2971.2187(5)	3100.9124(5)
B	1734.5786(3)	1735.1551(3)	1735.3875(3)
C	1071.7340(2)	1087.5263(2)	1104.1585(2)
Centrifugal distortion constants /MHz			
D_J	0.0132(1)	0.0137(1)	0.0145(1)
D_{JK}	0.0511(1)	0.0499(1)	0.0438(1)
D_K	0.0133(1)	0.0327(1)	0.0539(1)
d_1	-6.9(1)	-6.7(1)	-6.2(1)
d_2	-2.5(1)	-2.2(1)	-1.5(1)
^{14}N quadrupole hyperfine constants /MHz			
χ_{aa}	0.1871(12)	0.1356(10)	0.0947(11)
χ_{bb}	1.2460(15)	1.0314(16)	0.8175(18)
Standard deviation /kHz			
σ	2.9	3.9	4.5
$\Sigma 0_{0a}/\Sigma 0_{00a}$			
A	2853.3238(4)	2971.2198(6)	3101.5091(5)
B	1734.5796(2)	1735.1710(4)	1735.4259(3)
C	1071.7289(2)	1087.5635(2)	1104.2785(2)
D_J	0.0131(1)	0.0138(1)	0.0142(1)
D_{JK}	0.0514(1)	0.0489(1)	0.0477(1)
D_K	0.0133(1)	0.0336(1)	0.0502(1)
d_1	-6.9[a]	-6.7(1)	-6.6(1)
d_2	-2.5[a]	-2.1(1)	-2.0(1)
χ_{aa}	0.1837(16)	0.1417(13)	0.0940(10)
χ_{bb}	1.2490(22)	1.0223(16)	0.8191(17)
σ	3.3	3.1	2.3

[a] Fixed at value from symmetric inversion state.

perturbation observed in the Ar-ND_3 dimer was smaller than that in Ar-NH_3 and thus it was hoped that the excited internal rotor state of Ar_2-ND_3 would be more readily assigned than that of Ar_2-NH_3. A broad search for transitions associated with this state was conducted at both higher and lower frequencies than the ground state but no reasonable candidates were located.

c) Ar_2-ND_2H

The Ar_2-ND_2H isotopomer belongs to the G_8 molecular symmetry group (Table A1.4) and the total wavefunction must be symmetric with respect to the interchange of the two deuterium nuclei and the interchange of the two Ar nuclei. The rotational spectrum of Ar_2-ND_2H is expected to be composed of two sets of *b*-type transitions between 'ee' and 'oo' rotational levels. The relative intensities expected are 6 and 3 for the symmetric and antisymmetric components, respectively. There is no feasible internal rotation motion of ND_2H that interchanges the deuterium nuclei and thus there are no metastable excited internal rotor states.

In total, 11 rotational transitions of Ar_2-ND_2H were measured and assigned to the two inversion components of the ground internal rotor state. The transition frequencies are listed in Table A4.4. The inversion tunnelling splitting is approximately 36 kHz in the $J_{K_aK_c} = 1_{11}$-0_{00} transition. As a result of the small tunnelling splitting, the ^{14}N nuclear quadrupole hyperfine patterns overlap for many of the transitions of the two inversion states. The symmetric state inversion components appear at lower frequency than the antisymmetric components for most of the rotational transitions measured. The assignment of this isotopomer was tedious since the inversion tunnelling splitting was

very small and for certain transitions, the small differences in the rotational constants cause the symmetric components to be at higher frequency. As a result, careful intensity measurements were necessary to assign the individual ^{14}N hyperfine components to the correct inversion state. The ^{14}N hyperfine and rotational analyses were done as described for Ar_2-NH_3 and the spectroscopic constants are listed in Table 4.3.

d) Ar_2-NDH_2

The Ar_2-NDH_2 complex also belongs to the G_8 molecular symmetry group (Table A1.4) but the total wavefunction must be antisymmetric with respect to the interchange of the two hydrogen nuclei. The expected transitions are *b*-type between the 'ee' and 'oo' rotational levels. The symmetric and antisymmetric inversion states have relative nuclear spin statistical weights of 1 and 3, respectively. As described for Ar_2-ND_2H, only the ground internal rotor state is metastable and sufficiently populated at the temperatures in the molecular beam expansion for spectroscopic study.

The frequencies of the 11 rotational transition assigned to each of the two inversion components of the ground internal rotor state of Ar_2-NDH_2 are given in Table A4.5. The $J_{K_aK_c} = 1_{11}$-0_{00} transitions are split by approximately 290 kHz due to inversion tunnelling of NDH_2. The ^{14}N nuclear quadrupole hyperfine patterns are spectrally separated for all but one of the rotational transitions measured. The lower frequency transitions were assigned to the symmetric inversion state for most of the transitions based on the nuclear spin statistical predictions. The spectra were fit as described for Ar_2-NH_3 and the resulting spectroscopic constants are given in Table 4.3.

4.3.2 Isotopomers of Ne_2-NH_3

The structure of Ne_2-NH_3 was estimated by treating NH_3 as a sphere and using the dimer bond lengths reported for Ne-Ne (3.29 Å)[22] and Ne-NH_3 (3.72 Å). Figure 4.3 a) shows the geometries of the $^{20}Ne_2$ and $^{22}Ne_2$ isotopomers in their respective principal inertial axis systems. In contrast to Ar_2-NH_3, the *a*-axis is the symmetry axis of the Ne_2-NH_3 trimer. The dipole moment of the NH_3 monomer is expected to average out over the large amplitude internal motions of NH_3 and only *a*-type transitions are anticipated. The selection rules for *a*-type transitions are: $\Delta J = 0$ or ± 1, $\Delta K_a = 0$ (± 2, ± 4, ...) and $\Delta K_c = \pm 1$ (± 3, ± 5, ...). For the $^{20}Ne^{22}Ne$ containing species, the symmetry about the *a*-axis is broken as seen in Figure 4.3 b) and as a result, both *a*- and *b*-type transitions are predicted. The nuclear spin statistics associated with each isotopomer depend on the presence of identical Ne, hydrogen, and deuterium nuclei. The spin weights of the various rotational levels were verified using molecular symmetry group theoretical analyses[18] and the results are summarized in Table 4.4 for each isotopomer.

a) $^{20}Ne^{22}Ne$-NH_3 and $^{20}Ne^{22}Ne$-$^{15}NH_3$

The $^{20}Ne^{22}Ne$ containing isotopomers belong to the D_{3h} molecular symmetry group (Table A1.1). The total wavefunction must be antisymmetric with respect to the interchange of any two protons. The symmetric state has a nuclear spin statistical weight of zero and cannot be observed. For the antisymmetric component, however, all rotational levels are present and *a*- and *b*-type transitions between these energy levels are expected. From the structure in Figure 4.3 b), the dipole moment component along the *b*-axis is predicted to be much smaller than that along the *a*-axis. Consequently, the *b*-type

Figure 4.3 Geometries of the Ne_2-NH_3 trimers in the principal inertial axis system. The NH_3 subunit is treated as a sphere due to large amplitude internal motions. a) The $^{20}Ne_2$ (or $^{22}Ne_2$) containing isotopomers have twofold symmetry about the *a*-axis. b) For the $^{20}Ne^{22}Ne$ isotopomers, the *a*- and *b*-axes are slightly rotated as a result of the asymmetric mass distribution.

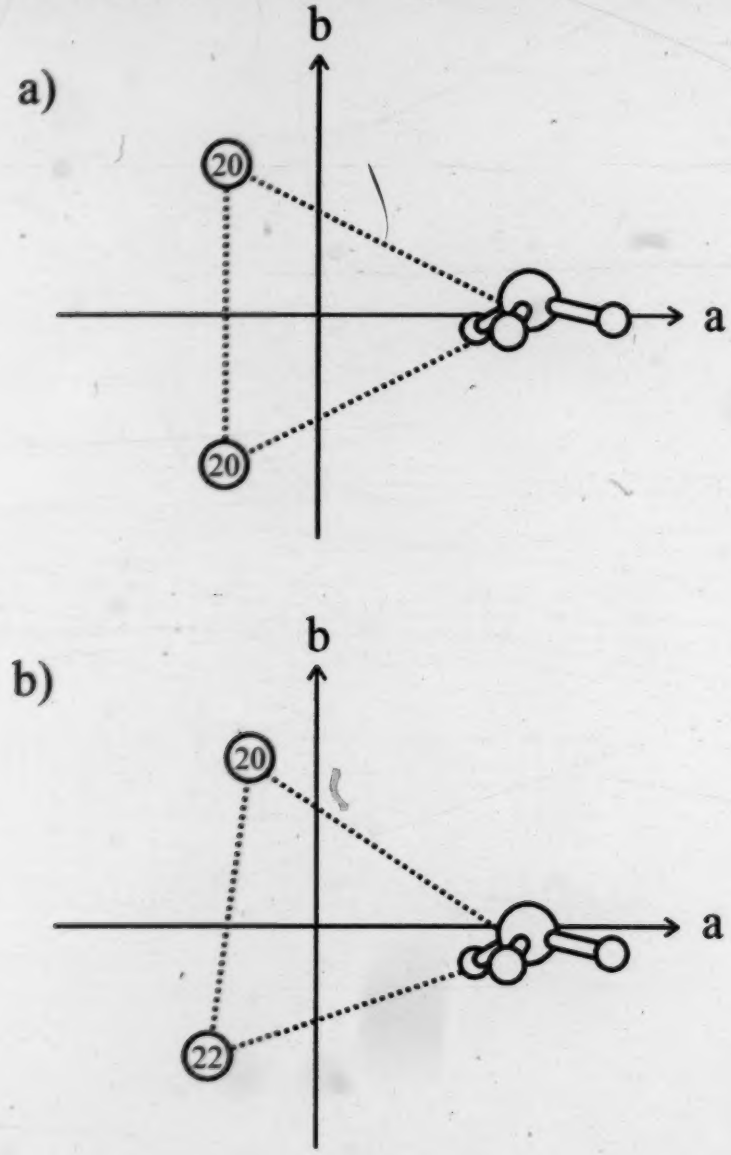

Table 4.4 Summary of molecular symmetry group theory analysis for the metastable states of the Ne_2-NH_3 isotopomers.

	$^{20}Ne^{22}Ne$-NH_3	$^{20}Ne_2$-NH_3	$^{20}Ne_2$-ND_3	$^{20}Ne_2$-ND_2H	$^{20}Ne_2$-NDH_2
Molecular symmetry group	D_{3h}	G_{24}	G_{24}	G_8	G_8
Total symmetry required[a]	A_2'/A_2''	A_3/A_4	A_1/A_2	A_1/A_2	A_3/A_4
Nuclear spin symmetry[b]	$4A_1'\oplus 2E'$	$4A_1\oplus 2E_1$	$10A_1\oplus A_3\oplus 8E_1$	$6A_1\oplus 3A_3$	$3A_1\oplus A_3$
Rotational symmetry[c]			K_aK_c= ee/eo/oe/oo		
	$A_1'/A_1''/A_1'/A_1''$			$A_1/A_2/B_1/B_2$	
NH_3 inversion symmetry			symmetric/antisymmetric		
	A_1'/A_2''			A_1/A_4	
NH_3 internal rotation symmetry			ground state/first excited state		
	A_1'/E'		A_1/E_1		n/a
Rovibrational symmetry[d]			K_aK_c= ee/eo/oe/oo		
$\Sigma 0_{0s}$	$A_1'/A_1''/A_1'/A_1''$		$A_1/A_2/B_1/B_2$		$A_1/A_2/B_1/B_2$
$\Sigma 0_{0a}$	$A_2''/A_2'/A_2''/A_2'$		$A_4/A_3/B_4/B_3$		$A_4/A_3/B_4/B_3$
$\Sigma 1_{1s}$	$E'/E''/E'/E''$		$E_1/E_2/E_3/E_4$		n/a
Predicted nuclear spin statistical weights		$\Sigma 0_{0s}$:$\Sigma 0_{0a}$:$\Sigma 1_{1s}$			$\Sigma 0_{0s}$:$\Sigma 0_{0a}$
	0:4:2	0:4:2	10:1:8	6:3	1:3

[a] refers to the symmetry of the total wavefunction upon exchange of identical fermions or bosons.
[b] refers to the symmetry of the nuclear spin function of the identical hydrogen or deuterium nuclei only.
[c] depends on whether K_a and K_c are even (e) or odd (o).
[d] includes the NH_3 inversion and NH_3 internal rotation symmetries.

transitions are expected to be much weaker than the *a*-type transitions and require longer microwave excitation pulses for observation. The reduced symmetry of the $^{20}Ne^{22}Ne$-NH_3 complex made this species a particularly good candidate for beginning the spectroscopic study. Using the structure estimated from the dimer bond lengths, the $J_{K_aK_c}=1_{01}$-0_{00} transition, whose frequency is approximately given by B+C, was found within 25 MHz of the initial prediction. The A rotational constant was not as well predicted from the estimated structure and it was necessary to scan wider frequency regions to find the higher J, *a*-type transitions that depend on the A constant. After more transitions were found and assigned with the help of the ^{14}N nuclear quadrupole hyperfine structure, the three rotational constants were better determined and the weaker *b*-type transitions could then be predicted within a few MHz.

The frequencies of the transitions assigned to the antisymmetric inversion component of the ground internal rotor state of $^{20}Ne^{22}Ne$-NH_3 are listed in Appendix 4 (Table A4.6). The assignment was confirmed by the presence of several closed loops due to the observation of both *a*- and *b*-type transitions. In total, nine *a*-type and six *b*-type transitions were measured. As expected, the *b*-type transitions are considerably weaker than the *a*-type transitions. An intensity comparison is shown for the $J_{K_aK_c} = 1_{01}$-0_{00} (*a*-type) and 1_{11}-0_{00} (*b*-type) transitions in Figure 4.4. The ^{14}N nuclear quadrupole hyperfine splitting was fit using a first order program and the residuals from this fit are given in Table A4.6 beside the transition frequencies. The hypothetical center line frequencies were subject to rotational analysis using Watson's *III*' A-reduction Hamiltonian.[21] During the initial rotational fit, the Δ_K and Δ_{JK} centrifugal distortion constants were highly

Figure 4.4 Spectra comparing the relative intensities of: a) *a*-type and b) *b*-type transitions observed for the $^{20}Ne^{22}Ne$-NH_3 isotopomer. The ^{14}N nuclear quadrupole hyperfine splitting was fit to obtain χ_{aa} = 0.333(3) MHz and χ_{bb} = −0.055(4) MHz for this isotopomer.

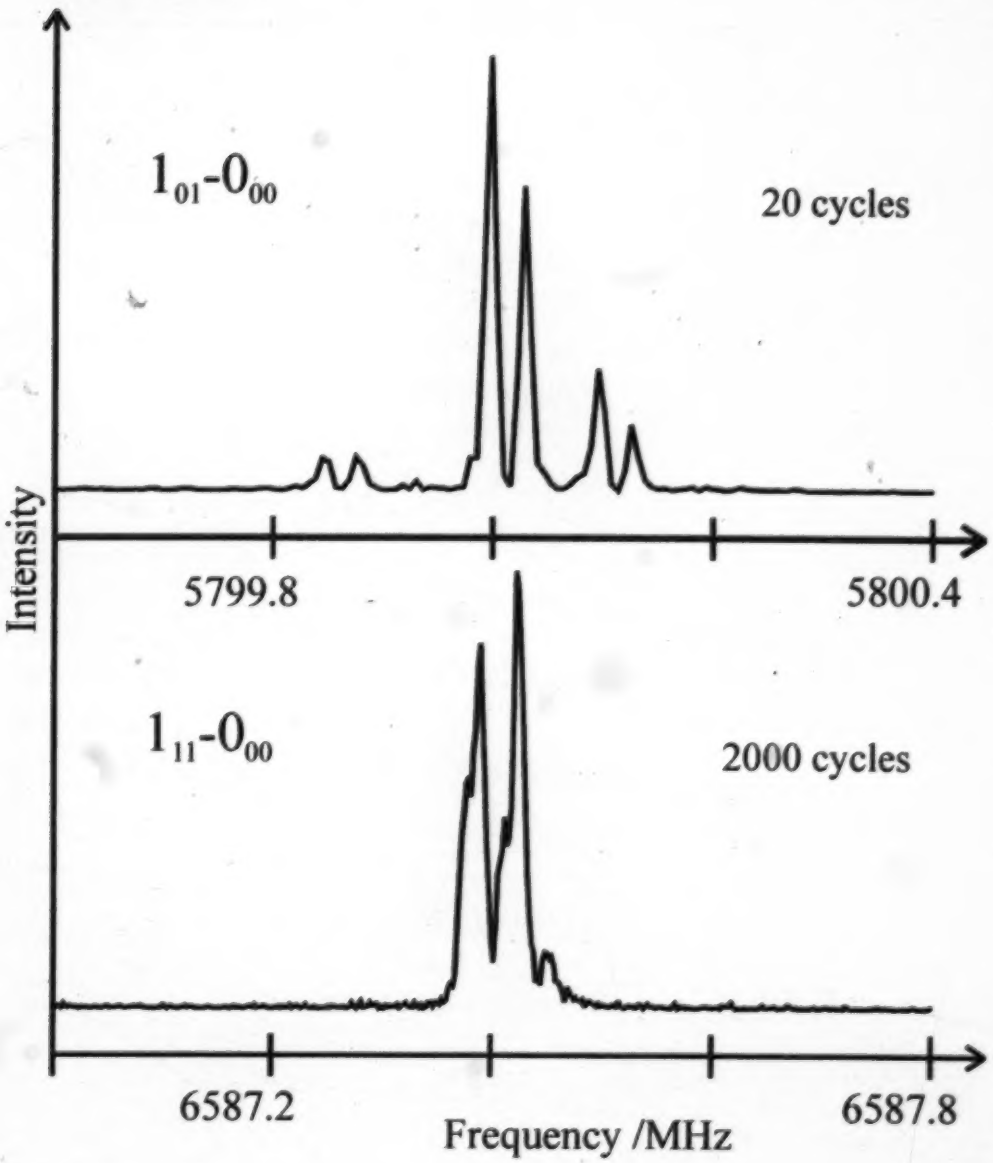

correlated. To estimate Δ_K, a harmonic force field calculation was done using the ASYM20 program.[23] The NH_3 subunit was treated as a sphere and the Ne-Ne and Ne-NH_3 bond lengths were fixed at the dimer values of 3.29 Å and 3.72 Å, respectively. There are three vibrational modes for this pseudotriatomic molecule. For the $^{20}Ne^{22}Ne$-NH_3 isotopomer, having C_s symmetry, each of these vibrational modes has A symmetry. The harmonic force field calculation was carried out in an iterative manner in tandem with the rotational analysis.[22] Initial estimates of the five centrifugal distortion constants from the preliminary rotational fit were used in the first iteration of the force field calculation. The Δ_K value determined from the force field program was then held fixed in the next rotational fit to obtain new values of Δ_J, Δ_{JK}, δ_J, and δ_K. These values, along with the refined Δ_K value were then included in the second iteration of the harmonic force field calculation. This procedure was repeated until it converged for the Δ_J, Δ_{JK}, and Δ_K constants. The δ_J and δ_K constants were not well-predicted by the force field calculation. The value of Δ_K determined in the final iteration of ASYM20 was then held fixed in the rotational analysis to determine the three rotational constants and the other four centrifugal distortion constants listed in Table 4.5. The frequencies of the hypothetically unsplit rotational transitions are included in Table A4.6 along with the (observed – calculated) values from the rotational analysis.

The measured transition frequencies of the $^{20}Ne^{22}Ne$-$^{15}NH_3$ isotopomer are listed in Table A4.7. The force constants determined for the $^{20}Ne^{22}Ne$-NH_3 isotopomer were used to predict the Δ_K constant for $^{20}Ne^{22}Ne$-$^{15}NH_3$ and this value was held fixed in rotational analysis. The resulting spectroscopic constants are listed in Table 4.5.

Table 4.5 Spectroscopic constants for $^{22}Ne^{20}Ne$-NH_3 and $^{22}Ne^{20}Ne$-$^{15}NH_3$.

$\Sigma 0_{0a}$	$^{22}Ne^{20}Ne$-NH_3	$^{22}Ne^{20}Ne$-$^{15}NH_3$
Rotational constants /MHz		
A	4568.56(8)	4565.97(11)
B	3780.16(13)	3638.89(18)
C	2020.33(2)	1978.40(3)
Centrifugal distortion constants /MHz		
Δ_J	0.643(3)	0.644(4)
Δ_{JK}	-1.052(3)	-1.071(5)
Δ_K[a]	0.4675	0.4839
δ_J	0.088(8)	0.102(10)
δ_K	0.088(37)	0.099(46)
^{14}N quadrupole hyperfine constants /MHz		
χ_{aa}	0.333(3)	
χ_{bb}	-0.055(4)	
Standard deviation /kHz		
σ	85	132

[a] D_K fixed at value from harmonic force field calculation.

b) $^{20}Ne_2$-NH_3, $^{20}Ne_2$-$^{15}NH_3$, and $^{22}Ne_2$-NH_3

The isotopomers that contain NH_3 and $^{15}NH_3$ paired with two identical Ne atoms belong to the G_{24} molecular symmetry group (Table A1.3). The total wavefunction must be symmetric upon exchange of the two Ne nuclei and antisymmetric upon exchange of any two protons. The molecular symmetry group analysis is similar to that in Section 4.3.1 a) for Ar_2-NH_3 however the symmetry of the rotational part of the wavefunction changes for the Ne containing trimer. This is a result of the different symmetry axes of the two Rg_2-NH_3 trimers as seen in Figures 4.1 and 4.3. For the ground internal rotor states of $^{20}Ne_2$-NH_3, $^{20}Ne_2$-$^{15}NH_3$, and ^{22}Ne-NH_3, the symmetric inversion component has a nuclear spin statistical weight of zero and no rotational transitions are observable. For the antisymmetric component, only the K_a = even rotational levels have nonzero spin

statistical weights. The rotational spectra are therefore expected to consist of *a*-type transitions between K_a = even levels for the antisymmetric inversion component only. The predicted energy level diagram for the $^{20}Ne_2$-NH_3, $^{22}Ne_2$-NH_3, and $^{20}Ne_2$-$^{15}NH_3$ isotopomers is shown in Figure 4.5.

The rotational constants of $^{20}Ne_2$-NH_3 were estimated using the structure constructed from the bond lengths of the Ne-Ne and Ne-NH_3 dimers. The $J_{K_aK_c} = 1_{01}$-0_{00} transition was found within 20 MHz of this prediction. As expected for the more

Figure 4.5 Predicted energy level diagram for the $^{20}Ne_2$ and $^{22}Ne_2$ containing isotopomers of the Ne_2-NH_3 asymmetric top. The transtions are *a*-type transitions and dotted lines denote energy levels with nuclear spin statistical weights of zero. The dashed arrows denote transitions that were not observed.

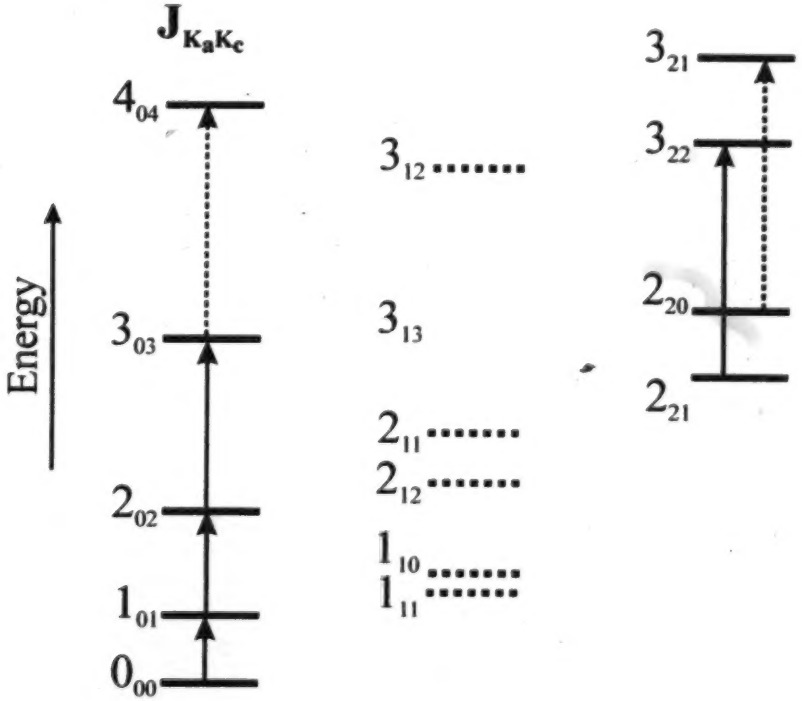

abundant isotopomer, the observed transition was more intense than the 1_{01}-0_{00} transition of $^{20}Ne^{22}Ne$-NH_3. The assignment to the $^{20}Ne_2$-NH_3 isotopomer was verified by the observed ^{14}N nuclear quadrupole hyperfine splitting which was similar to that measured for $^{20}Ne^{22}Ne$-NH_3. Three higher J, *a*-type transitions involving $K_a = 0$ and $K_a = 2$ energy levels were located by scanning a larger frequency range. The four transitions were assigned to the antisymmetric inversion component of the ground internal rotor state of $^{20}Ne_2$-NH_3 and the frequencies are listed in Table A4.8. The ^{14}N nuclear quadrupole hyperfine splitting was fit using a first order program and the hypothetical center line frequencies were then rotationally analyzed. There are not enough rotational transitions in the range of the spectrometer to provide the information necessary to fit for all three asymmetric top rotational constants and the required centrifugal distortion constants. The centrifugal distortion constants were estimated in ASYM20 using the force constants determined from the harmonic force field calculation of $^{20}Ne^{22}Ne$-NH_3. The δ_J and δ_K constants were estimated by comparing the values calculated in the harmonic force field program for $^{20}Ne^{22}Ne$-NH_3 and $^{20}Ne^{22}Ne$-$^{15}NH_3$ with the δ_J and δ_K values determined from the rotational analysis of these two isotopomers. The differences between the calculated and fit values were then used to scale the δ_J and δ_K values calculated in the force field program for $^{20}Ne_2$-NH_3. All five of the estimated centrifugal distortion constants were held fixed in the rotational analysis to determine the three rotational constants. The results are summarized in Table 4.6.

The corresponding rotational transitions were measured for the $^{22}Ne_2$-NH_3 and $^{20}Ne_2$-$^{15}NH_3$ species. The transitions observed for the $^{22}Ne_2$-NH_3 isotopomer are much

Table 4.6 Spectroscopic constants for Ne_2-NH_3 and Ne_2-$^{15}NH_3$.

$\Sigma 0_{0a}$	$^{20}Ne_2$-NH_3	$^{20}Ne_2$-$^{15}NH_3$	$^{22}Ne_2$-NH_3
Rotational constants /MHz			
A	4755(4)	4753(6)	4689(3)
B	3845.1(6)	3702.0(8)	3819.9(5)
C	2076.6(5)	2033.6(8)	1887.5(5)
Centrifugal distortion constants /MHz			
Δ_J[a]	0.706	0.697	0.598
Δ_{JK}[a]	-1.153	-1.165	-0.935
Δ_K[a]	0.526	0.544	0.411
δ_J[a]	0.100	0.102	0.075
δ_K[a]	0.097	0.099	0.079
^{14}N quadrupole hyperfine constants /MHz			
χ_{aa}	0.335(5)		0.347(5)
χ_{bb}	-0.056(8)		-0.11(3)
Standard deviation /kHz			
σ	615	761	624

[a] Centrifugal distortion constants fixed at values from harmonic force field calculation.

weaker than those assigned to the ^{20}Ne containing species and the ^{14}N nuclear quadrupole hyperfine splitting was only well-resolved for the lowest J transition. The transition frequencies are listed in Tables A4.8 and A4.9 for the $^{22}Ne_2$-NH_3 and $^{20}Ne_2$-$^{15}NH_3$ isotopomers, respectively. The rotational transitions, as well as the ^{14}N nuclear quadrupole hyperfine structure for $^{22}Ne_2$-NH_3 species, were fit as described above for $^{20}Ne_2$-NH_3. The resulting spectroscopic constants are given in Table 4.6.

There is a second metastable internal rotor state for each of the NH_3 and $^{15}NH_3$ containing isotopomers which is associated with the E'/E_1 nuclear spin function for the isotopomers under the D_{3h}/G_{24} molecular symmetry groups, respectively. A broad search was conducted for rotational transitions associated with this excited internal rotor state of Ne_2-NH_3 at both higher and lower frequencies than the ground state transitions. No

transitions were found that met the criteria for the ^{14}N nuclear quadrupole hyperfine splitting and the isotopic spacing expected for the $^{20}Ne_2$, $^{22}Ne^{20}Ne$, and $^{22}Ne_2$ containing isotopomers.

c) $^{20}Ne_2$-ND_3

The $^{20}Ne_2$-ND_3 isotopomer also belongs to the G_{24} molecular symmetry group (Table A1.3) and the interchange of any two identical deuterium nuclei and the two Ne nuclei is governed by Bose-Einstein statistics. For both inversion components of the ground internal rotor state, the K_a = odd rotational levels have nuclear spin statistical weights of zero. Thus, for the $^{20}Ne_2$-ND_3 isotopomer, two *a*-type spectra consisting of transitions between K_a = even levels are expected with relative intensities of 10 and 1 for the symmetric and antisymmetric inversion states, respectively. The inversion tunnelling splitting was anticipated to be small, on the order of that observed for the Ar_2-ND_3 trimer.

The transition frequencies of the two inversion components of the ground internal rotor state of $^{20}Ne_2$-ND_3 are listed in Table A4.10. The more intense transitions appear at lower frequency and were assigned to the symmetric state as predicted by the molecular symmetry group analysis. The inversion tunnelling splitting is very small; about 20 kHz for the $J_{K_aK_c} = 1_{01}$-0_{00} transition. As a result, the ^{14}N nuclear quadrupole hyperfine splitting patterns overlap for the two states and the assignment had to be done carefully. For the symmetric inversion state, four *a-type* rotational transitions were assigned. Only three rotational transitions could be distinguished for the antisymmetric state due to the large degree of overlap with the more intense transitions of the symmetric state. The ^{14}N hyperfine and rotational analyses were done for each state as described for $^{20}Ne_2$-NH_3.

The spectroscopic constants are listed in Table 4.7. The presence of three quadrupolar deuterium nuclei did not produce noticeable line broadening or additional splitting of any of the rotational transitions.

As for the NH_3 and $^{15}NH_3$ containing species, there is an excited internal rotor state of the ND_3 containing isotopomer that is metastable since it is associated with the E_1 nuclear spin function. The Coriolis perturbation observed in the Ar-ND_3 dimer was

Table 4.7 Spectroscopic constants for $^{20}Ne_2$-ND_3, $^{20}Ne_2$-ND_2H, and $^{20}Ne_2$-NDH_2.

$\Sigma 0_{0s}/\Sigma 0_{00s}$	$^{20}Ne_2$-ND_3	$^{20}Ne_2$-ND_2H	$^{20}Ne_2$-NDH_2
Rotational constants /MHz			
A	4756(11)	4757(7)	4755[b]
B	3484(1)	3592.1(9)	3709.9(4)
C	1968(1)	2001.1(9)	2037.0(1)
Centrifugal distortion constants /kHz			
Δ_J[a]	682	689	697
Δ_{JK}[a]	-1193	-1180	-1166
Δ_K[a]	578	562	545
δ_J[a]	106	105	103
δ_K[a]	103	101	99
^{14}N quadrupole hyperfine constants /MHz			
χ_{aa}	0.630(6)	0.529(5)	0.415(12)
χ_{bb}	-0.06(1)	-0.03(1)	-0.05(2)
Standard deviation /kHz			
σ	914	689	382
$\Sigma 0_{0a}/\Sigma 0_{00a}$			
A	4756[b]	4757[b]	4755(6)
B	3483.7(5)	3591.8(3)	3711.0(8)
C	1968.3(1)	2001.3(8)	2037.2(8)
Δ_J[a]	0.682	0.689	0.697
Δ_{JK}[a]	-1.193	-1.180	-1.166
Δ_K[a]	0.578	0.562	0.545
δ_J[a]	0.106	0.105	0.103
δ_K[a]	0.103	0.101	0.099
χ_{aa}	0.636(8)	0.528(6)	0.439(8)
χ_{bb}	-0.06[c]	-0.03(1)	-0.06(2)
σ	481	328	753

[a] Centrifugal distortion constants fixed at values from harmonic force field calculation.
[b] Rotational constant fixed at value from other inversion tunnelling component.
[c] Fixed at value from symmetric inversion state.

smaller than that in Ar-NH_3 and it was therefore hoped that the excited internal rotor state of $^{20}Ne_2$-ND_3 would be more readily assigned. A broad search for transitions associated with this state was conducted at both higher and lower frequencies than the ground state but no reasonable candidates were located.

d) $^{20}Ne_2$-ND_2H

The $^{20}Ne_2$-ND_2H isotopomer belongs to the G_8 symmetry group (Table A1.4). The total wavefunction must be symmetric with respect to the interchange of the two Ne nuclei and the two deuterium nuclei. As in $^{20}Ne_2$-ND_3, the K_a = odd rotational levels have nuclear spin statistical weights of zero. Thus, the rotational spectrum of $^{20}Ne_2$-ND_2H is expected to contain two sets of *a-type* transitions between K_a = even levels. The relative intensities are predicted to be 6 and 3 for the symmetric and antisymmetric components, respectively. Due to the reduced symmetry of ND_2H, there is no feasible internal motion that interchanges the identical deuterium nuclei. Consequently there are no metastable excited internal rotor states of the $^{20}Ne_2$-ND_2H isotopomer.

The rotational spectrum of the ground internal rotor state of $^{20}Ne_2$-ND_2H was measured and the frequencies of the transitions within the two inversion states are listed in Table A4.11. The observed inversion tunnelling splitting is approximately 300 kHz for the $J_{K_aK_c} = 1_{01}$-0_{00} transition. The ^{14}N nuclear quadrupole hyperfine splitting patterns overlap for the two states and the lower frequency, more intense transitions were assigned to the symmetric state as predicted by nuclear spin statistics. As in the $^{20}Ne_2$-ND_3 isotopomer, four *a*-type transitions were assigned for the symmetric inversion state and three for the antisymmetric state. The ^{14}N hyperfine and rotational analyses were done

using the method outlined for the $^{20}Ne_2$-NH_3 isotopomer. The spectroscopic constants are listed in Table 4.7.

e) $^{20}Ne_2$-NDH_2

The $^{20}Ne_2$-NDH_2 complex also belongs to the G_8 molecular symmetry group (Table A1.4). The total wavefunction must be symmetric with respect to the operation which interchanges the two Ne nuclei and antisymmetric upon exchange of the two protons. For both inversion states, the K_a = odd rotational levels have nuclear spin statistical weights of zero. The expected transitions are *a*-type between the K_a = even rotational levels for each of the two inversion states of $^{20}Ne_2$-NDH_2. The symmetric and antisymmetric inversion components have relative spin weights of 1 and 3, respectively. As described for $^{20}Ne_2$-ND_2H, only the ground internal rotor state is metastable for $^{20}Ne_2$-NDH_2.

The frequencies of the rotational transitions assigned to the two inversion components of the ground internal rotor state of $^{20}Ne_2$-NDH_2 are given in Table A4.12. The $J_{K_aK_c} = 1_{01}$-0_{00} transitions are split by approximately 906 kHz allowing complete spectral separation of the ^{14}N nuclear quadrupole hyperfine patterns. The lower frequency transitions were assigned to the symmetric inversion state based on the molecular symmetry group analysis since they have approximately 1/3 the intensity of the higher frequency transitions. Four *a*-type transitions were measured for the antisymmetric inversion state and three transitions were measured for the symmetric state. The spectra were fit as described for $^{20}Ne_2$-NH_3 and the resulting spectroscopic constants are given in Table 4.7.

4.4 *Ab initio* calculations for Ne_2-NH_3

Ab initio calculations were done at the CCSD(T) level of theory using the MOLPRO software package.[24] The coupled cluster method was chosen since it provides a higher level electron correlation treatment than MP4. This is necessary to recover the dispersion nonadditivity component of the interaction energy for trimers and larger clusters containing nonpolar species.[25] As described for Ne-NH_3 in Section 3.4, three separate potential energy surfaces were constructed for the Ne_2-NH_3 trimer. These correspond to three NH_3 umbrella angles: >HNH = 106.67°, >HNH = 113.34°, and >HNH = 120.00°. The N-H bond length was held fixed at the experimental value of 1.01242 Å.[26] The interaction energy of the trimer was calculated using the supermolecular approach[27] and the basis sets are the same as those outlined in Section 3.4 for the Ne-NH_3 dimer.[28,29] A set of (3s, 3p, 2d) bond functions was placed at the midpoint of all three van der Waals bonds.

The interaction energy was determined as a function of θ, β, ϕ, and R (see Figure 4.6) for each of the three NH_3 geometries. To reduce the dimension of the calculation, the Ne-Ne van der Waals bond length was fixed at 3.29 Å as estimated for the Ne_2 dimer.[22] This was assumed to be a reasonable value since the Ne-Ne bond length in other van der Waals trimers such as Ne_2Ar (3.264 Å)[30] and Ne_2-N_2O (3.307 Å)[31] are in the same range. Two different values of β were considered: 0° and 90°, where β is the angle between the C_3 axis of NH_3 and the *ab*-plane of the complex. For each β value, the distance R was varied from 2.75 Å to 3.70 Å in steps of 0.05 Å and the angle θ was varied between 0° and 180° in increments of 30°. These calculations were initially done for two ϕ values: 0°

Figure 4.6 Coordinate system of Ne_2-NH_3 used for the *ab initio* calculations. R is the distance between the center of mass of the Ne_2 subunit and the nitrogen atom. The angle θ is the angle between the C_3 axis of NH_3 and R. When $\theta = 0°$, the C_3 axis of NH_3 is aligned with R and the hydrogen atoms point toward Ne_2. β is the angle between the *ab*-plane and the C_3 axis of NH_3 and is 0° when the C_3 axis of NH_3 lies in the *ab*-plane. The angle ϕ describes the orientation of NH_3 upon rotation about its C_3 axis. For the orientation where $\theta = 90°$ and $\beta = 90°$, ϕ is 0° when one hydrogen atom is pointed toward the midpoint of the Ne-Ne bond and ϕ is 60° when a hydrogen atom is pointed toward each Ne atom.

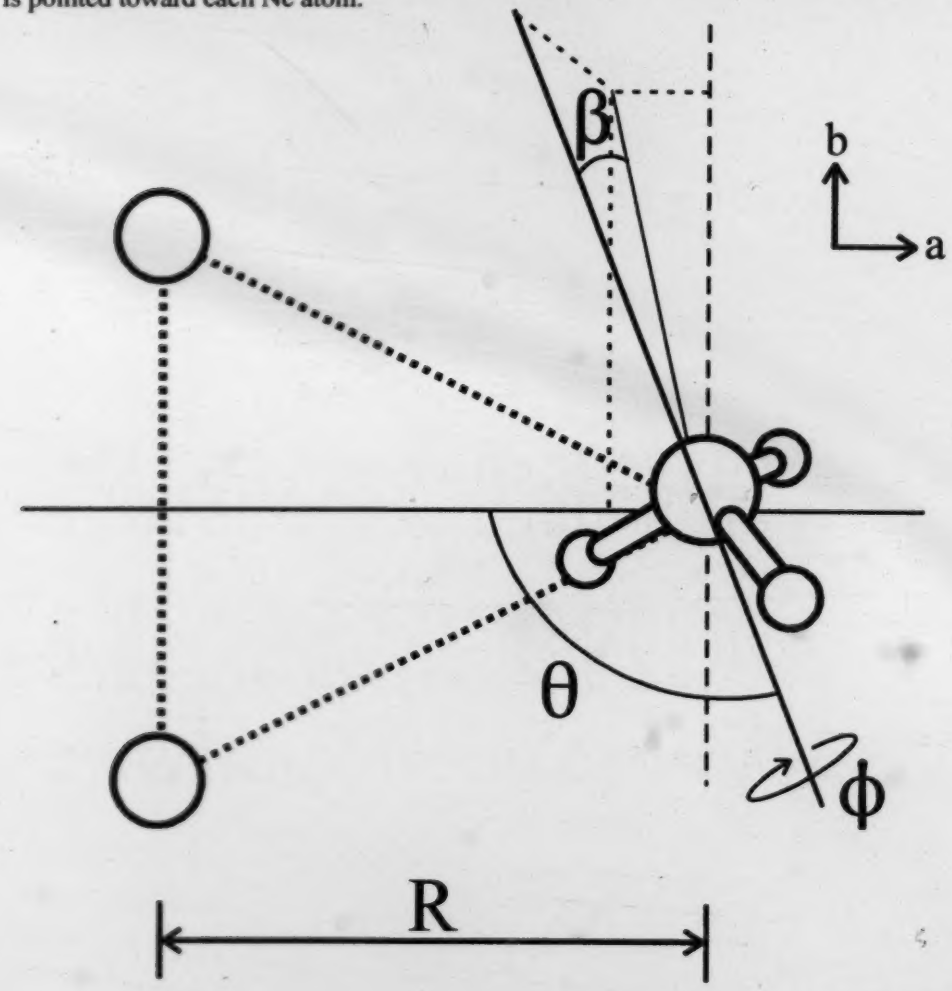

and 60°. Once the potential energy surface minimum was located as a function of these coordinates, the angle, ϕ was varied between 0° and 60° in steps of 10° at the θ and β values corresponding to the minimum energy structure. Tabulations of the *ab initio* data for the Ne_2-NH_3 trimer are given in Appendix 5, Tables A5.1 - A5.6.

4.5 Discussion

4.5.1 Spectroscopic constants and derived molecular parameters

The microwave transitions observed for the Ar_2-NH_3 and Ne_2-NH_3 trimers are consistent with the isosceles triangular structures shown in Figures 4.1 and 4.3 a). Comparison of the rotational constants of the various isotopomers shows that there is only a small variation in the rotational constant corresponding to the symmetry axis upon isotopic substitution within the NH_3 subunit. For example, in the $^{20}Ne_2$-NH_3 trimer, ΔA is only 2 MHz upon ^{15}N substitution while B and C change by 143 MHz and 43 MHz, respectively. The effect in Ar_2-NH_3 is even smaller as ΔB changes by only 2 kHz upon ^{15}N substitution. This can be understood by considering the structure shown in Figure 4.1. The center of mass of the NH_3 molecule lies on the *b*-axis and thus NH_3 makes only a small contribution to the moment of inertia about this axis. In fact, the B constant of Ar_2-NH_3 (1735.3628 MHz) is close to those of Ar_2-H_2O (1731.7811 MHz)[8,9] and Ar_2 (1733.1 MHz).[10,11] This suggests that the NH_3 subunit does not significantly contribute to the B rotational constant which is plausible if NH_3 undergoes nearly free internal rotation.

The ^{14}N nuclear quadrupole hyperfine splitting observed in the spectra of several isotopomers proved to be an invaluable tool in the assignment of the rotational

transitions. The nuclear quadrupole coupling constants obtained from fitting the spectra depend on the orientation of NH_3 within the complex and are also averaged over the large amplitude motions of NH_3. As described in Chapter 3, an effective orientation of NH_3 within a van der Waals complex can be estimated using the expression: $\chi_{aa} = \frac{1}{2}\chi_o\langle 3\cos^2\theta - 1\rangle$, where χ_o is the quadrupole coupling constant of the free NH_3. For Ar_2-NH_3, the χ_{bb} value is needed to determine the angle between the C_3 axis of NH_3 and the *b*-axis of the trimer and for Ne_2-NH_3, the χ_{aa} value is used. The angles calculated from this expression are given in Table 4.8 for the various isotopomers along with the Legendre factors, $\langle P_2(\cos\theta)\rangle = \frac{1}{2}\langle 3\cos^2\theta - 1\rangle$. The Legendre factors are small compared to those of other NH_3 containing van der Waals complexes such as NH_3-HCN (0.817),[32] NH_3-CO_2 (0.776),[33] and NH_3-H_2O (0.768)[34] which suggests that the NH_3 moiety continues to undergo large amplitude motions despite being bound to two Rg atoms. The Legendre factor increases with deuterium substitution in the trimer complexes. For example, the values for the $^{20}Ne_2$ containing trimer are: −0.082(NH_3), −0.107 (NDH_2), −0.129 (ND_2H), and −0.156 (ND_3). The same trend was reported for the Rg-NH_3 dimers and was attributed to the larger tunnelling mass and lower zero point energies of the heavier isotopomers. Comparison of the χ_{aa} values obtained for the Ne_2-NH_3 trimers shows an

Table 4.8 Estimated orientation of ammonia in the Ar_2-NH_3 and Ne_2-NH_3 trimers.

$\Sigma 0_{0a}$		-NH_3	-NDH_2	-ND_2H	-ND_3
Ar_2	θ	63.0°/117.0°	64.0°/116.0°	64.9°/115.1°	66.1°/113.9°
	$\langle P_2(\cos\theta)\rangle$	-0.190	-0.211	-0.230	-0.253
$^{20}Ne_2$	θ	58.1°/121.9°	59.2°/120.8°	60.2°/119.8°	61.4°/118.6°
	$\langle P_2(\cos\theta)\rangle$	-0.082	-0.107	-0.129	-0.156

increase of 20 % - 25 % for each isotopomer relative to the χ_{aa} value of the corresponding Ne-NH_3 isotopomer. For Ar_2-NH_3, the change is even more dramatic as the χ_{bb} values increase by 50 % - 125 % in comparison to the χ_{aa} value of the Ar-NH_3 dimer. The consistency of this trend across the various isotopomers suggests that there are discernible differences in the internal motions of NH_3 in the trimer and dimer complexes. The larger χ values in the former suggests that internal rotation of NH_3 in the θ coordinate is comparatively more hindered in the trimer. This may be physically explained by the creation of a more anisotropic environment for the NH_3 molecule when bound to two Rg atoms compared to one.

The centrifugal distortion constants determined for the $^{20}Ne^{22}Ne$-NH_3 and $^{20}Ne^{22}Ne$-$^{15}NH_3$ species are relatively large, on the order of hundreds of kHz, suggesting that the trimers are quite flexible. In fact, the relatively large (observed – calculated) values from the rotational fits are indicative of the inadequacy of the semi-rigid rotor Hamiltonian for these systems. This is further supported by the size of the inertial defects, $\Delta_o = I_C - I_B - I_A$, which should be zero for the ground state of a planar rigid molecule.[35] For $^{20}Ne^{22}Ne$-NH_3, Δ_o is 5.831 amu Å^2. The $^{20}Ne^{22}Ne$-NH_3 trimer is not strictly speaking a planar molecule, since the three hydrogen atoms lying outside the *ab*-plane also contribute to the inertial defect. If the masses of the three hydrogen atoms are considered to be delocalized over the surface of a sphere with a radius of the N-H bond length, the contribution of NH_3 to the planar moment, P_c, is 1.025 amu Å^2. The contribution to the inertial defect is -2.05 amu Å^2 since $P_c = -\frac{1}{2}\Delta_o$. Thus, the hydrogen atoms outside the *ab*-plane lower the experimentally determined inertial defect and the corrected Δ_o may

actually be on the order of 8 amu Å^2. This is larger than the inertial defects determined for the $^{20}Ne_2Ar$ and $^{20}Ne_2{}^{84}Kr$ trimers, 6.127 amu Å^2 and 6.168 amu Å^2, respectively.[36,22] Assuming planarity for Ar_2-NH_3, the inertial defect is smaller, 3.535 amu Å^2, which is similar to that reported for Ar_2-H_2O, 3.542 amu Å^2.[8,9] With the inclusion of the out-of-plane hydrogen contribution, the inertial defects increase to 5.585 amu Å^2 and 4.760 amu Å^2 for Ar_2-NH_3 and Ar_2-H_2O, respectively. By comparison, chemically bound molecules have considerably smaller inertial defects. For example, the inertial defect of water is 0.0486 amu Å^2.[35] Due to the non-rigidity of the van der Waals trimers, the rotational constants should be regarded as highly averaged over large amplitude zero point vibrational motions and it is therefore difficult to extract accurate structural information from the microwave spectra alone. If the NH_3 is treated as a sphere, moment of inertia equations can provide an estimate of the effective van der Waals bond lengths.[8,9] This approach neglects the contribution of the hydrogen atoms since the NH_3 subunit is treated as a point mass. For Ar_2-NH_3, the moment of inertia equations are: $I_a = \mu_c R^2$, $I_b = I(Ar_2) = \frac{1}{2}mr^2$, $I_c = \frac{1}{2}mr^2+\mu_c R^2$; where μ_c is the pseudodiatomic (Ar_2,NH_3) reduced mass of the trimer, m is the mass of Ar, r is the Ar-Ar distance, and R is the center of mass distance between Ar_2 and NH_3. The expressions for I_a and I_b are interchanged for the Ne_2-NH_3 trimer. The Rg-NH_3 bond length can be calculated trigonometrically from the values of r and R. The Rg-Rg and Rg-NH_3 bond lengths calculated for the trimers are compared with the dimer values in Table 4.9. The Rg-Rg and Rg-NH_3 bonds decrease by 0.001 Å - 0.03 Å in the trimers relative to the corresponding dimers. This suggests that while pairwise additive contributions dominate the total interaction energy, three body nonadditive

Table 4.9 Comparison of bond lengths (Å) for various van der Waals dimers and trimers.

	trimers		dimers	
	R(RG-X)	r(RG-RG)	R(RG-X)	r(RG-RG)
Ar_2-NH_3	3.835	3.818	3.836[a]	3.821[b]
Ar_2-H_2O[c]	3.687	3.822	3.6907[d]	
Ar_2-Ne[e]	3.595	3.818	3.607[f]	
Ne_2-NH_3	3.695	3.260	3.723	3.29[g]
Ne_2-Ar[e]	3.590	3.264	3.607[f]	

[a] Reference 19.
[b] Reference 10, 11.
[c] Reference 8, 9.
[d] G. T. Fraser, A. S. Pine, R. D. Suenram, and K. Matsumura, *J. Molec. Spectrosc.* **144**, 97 (1990).
[e] Reference 36.
[f] J. -U. Grabow, A. S. Pine, G. T. Fraser, F. J. Lovas, T. Emilsson, E. Arunan, and H. S. Gutowsky, *J. Chem. Phys.* **102**, 1181 (1995).

effects are also involved. A similar reduction in the van der Waals bond lengths were reported for the Ar_2-H_2O,[8,9] Ar_2-Ne, and Ne_2-Ar trimers[36] as shown in Table 4.9. Conversely, the Rg-Rg bonds are lengthened in van der Waals trimers that involve linear molecules as reported for Ar_2-HCl,[1] Ar_2-OCS,[37] Ar_2-CO_2,[38] Ar_2-N_2O, and Ne_2-N_2O.[31] This disparity demonstrates the need for further spectroscopic and theoretical studies to fully understand the nature of individual nonadditive contributions as a function of the properties of the molecular substituents.

4.5.2 Inversion tunnelling

Inversion tunnelling splittings were observed in the ground state rotational spectra of the deuterated Ar_2-NH_3 and Ne_2-NH_3 trimers, as reported in Chapter 3 for the deuterated Rg-NH_3 dimers. Since the rotational constants of the $^{20}Ne_2$ containing

isotopomers were not well determined, the most instructive comparison of the inversion tunnelling splittings for these isotopomers is to consider the spacing between the two 1_{01}-0_{00} (*a*-type) transitions, whose frequencies are approximately equal to (B+C), instead of comparing the differences in rotational constants. These transitions are split by 19.9 kHz, 298.1 kHz, and 906.2 kHz in $^{20}Ne_2$-ND_3, -ND_2H, and -NDH_2 respectively. The magnitude of the splitting increases with successive hydrogen substitution which is in agreement with the inversion tunnelling splittings reported for the Rg-ND_3, -ND_2H, and -NDH_2 dimers in Chapter 3. The same trend is observed upon comparison of the energy difference between the two inversion states of the free monomers: 1.6 GHz (ND_3), 5 GHz (ND_2H), and 12 GHz (NDH_2).[39] The small inversion tunnelling splittings in the $^{20}Ne_2$ containing trimers suggest that the two inversion states lie close in energy in each of the deuterated isotopomers. This is further supported by the observed ^{14}N nuclear quadrupole hyperfine splitting since the χ_{aa} and χ_{bb} values are the same within experimental error for both inversion states of the deuterated isotopomers of Ne_2-NH_3. For the Ar_2-NH_3 trimer, the 1_{11}-0_{00} (*b*-type) transition, with a transition frequency of approximately (A+C), is split by 165.1 kHz, 36.1 kHz, and 712.0 kHz, for the isotopomers containing ND_3, ND_2H, and NDH_2, respectively. The increase in the inversion tunnelling splittings between the ND_2H and NDH_2 species follows the expected trend, but the magnitude of the splitting observed in the Ar_2-ND_3 isotopomer is anomalously large by comparison. If the relative positions of the two inversion split 1_{11}-0_{00} transitions are considered, however, the magnitudes and signs of the inversion tunnelling splittings (antisymmetric – symmetric state) are consistent with the expected trend since the symmetric state transitions are found at

higher frequency in Ar_2-ND_3. Thus, the inversion tunnelling splittings in Ar_2-ND_3, -ND_2H, and -NDH_2 should actually be reported as: -165.1 kHz, 36.1 kHz, and 712.0 kHz, respectively.

A comparison of the inversion tunnelling splittings observed for the deuterated Rg_2-NH_3 and Rg-NH_3 complexes is easily drawn. The dimers were fit to a diatomic model yielding the rotational constant B or ½(B+C). It is therefore simple to compare the difference in (B+C) for the deuterated Ne-NH_3 dimers and deuterated Ne_2-NH_3 trimers and this comparison is valid since the B and C axes are perpendicular to the symmetry axes in both complexes. For the Ne-ND_3, -ND_2H, and -NDH_2 dimers, the inversion splittings in (B+C) are larger: 55.0 kHz, 407.6 kHz, and 1082.2 kHz, than in the corresponding Ne containing trimers: 19.9 kHz, 298.1 kHz, and 906.2 kHz, respectively. For the Ar_2-NH_3 trimer, the comparison of tunnelling splittings is made between (B+C) of the deuterated Ar-NH_3 dimers and (A+C) of the deuterated Ar_2-NH_3 trimers since the *a*- and *c*-axes are perpendicular to the symmetry axis of Ar_2-NH_3. The inversion splittings are then -63.0 kHz, 271.6 kHz, and 1101.0 kHz in the Ar-ND_3, Ar-ND_2H, and Ar-NDH_2 dimers and -165.1 kHz, 38.3 kHz, and 716.7 kHz in the corresponding Ar_2 containing trimers, respectively. It is tempting to suggest that the smaller inversion splittings observed for the trimers relative to the dimers is an indication that the inversion motion is more hindered in the trimer. This statement must be made with caution for several reasons. First, the magnitude of the rotational constants of the various dimer and trimer complexes have not been considered. These are very different because of the different masses and structures involved and any comparison would need to take this into account.

Secondly, the observed tunnelling splittings are not a direct measure of the energy differences between the two inversion states and should instead be regarded as general indicators of the relative energy splittings of the inversion states. The fact that inversion tunnelling splittings were observed for the trimers is an important result in itself. This provides physical evidence of the minimum energy structures of the complexes. The inversion motion is expected to be quenched if the potential along the inversion coordinate is not symmetric.[17] Thus, the observation of two inversion components in the spectra of the deuterated Ar_2-NH_3 and Ne_2-NH_3 species points to structures in which the C_3 axis of NH_3 is, on average, perpendicular to the symmetry axis of the respective trimer.

4.5.3 *Ab initio* potential energy surfaces of Ne_2-NH_3

The potential energy surface minimum for the Ne_2-NH_3 trimer is -131.1 cm^{-1} for the experimental equilibrium geometry of NH_3 (<HNH = 106.67°) at the CCSD(T) level of theory. The structural coordinates at this minimum energy are R = 3.10 Å, $\theta = 90°$, $\beta = 90°$, and $\phi = 60°$ (Figure 4.6) which corresponds to a trimer structure in which the C_3 axis of NH_3 is perpendicular to the *ab*-plane with two hydrogen atoms pointed toward the two Ne atoms. The same relative orientation of NH_3 was found for the other two surfaces with minima of -130.9 cm^{-1} (<HNH = 113.34°) and -130.6 cm^{-1} (<HNH = 120.00°) at R values of 3.10 Å and 3.15 Å, respectively. From this minimum energy orientation, the barrier to internal rotation of NH_3 about its C_3 axis is 4.5 cm^{-1} through the $\phi = 0°$ position for the equilibrium NH_3 geometry. The minimum energy path between $\phi = 0°$ and $\phi = 60°$ requires no change in the radial coordinate, R. For rotation in the θ coordinate, the

highest barriers exist at $\theta = 0°$ and $\theta = 180°$ for the two nonplanar geometries of NH_3. The barriers are 39.7 cm^{-1}/29.8 cm^{-1}(0°/180°) and 45.5 cm^{-1}/35.9 cm^{-1} for the <HNH = 106.67° and <HNH = 113.34° NH_3 geometries, respectively. For the planar geometry of NH_3, the barrier is 42.3 cm^{-1} through $\theta = 0°$ and $\theta = 180°$ due to symmetry.

The main topological features of the Ne_2-NH_3 potential energy surfaces can be compared with those of Ne-NH_3 reported in Section 3.5.4 at the CCSD(T) level of theory. For Ne-NH_3, the minimum energy (−63.20 cm^{-1}) geometry is that in which the C_3 axis of NH_3 is aligned perpendicular to the van der Waals bond with two hydrogen atoms pointed toward the Ne atom. The barrier for internal rotation of NH_3 in the ϕ coordinate of the dimer is 17.6 cm^{-1} at the CCSD(T) level of theory which is almost a factor of four greater than the equivalent motion in the trimer (4.5 cm^{-1}). This internal rotation is a tunnelling motion in which the NH_3 rotates about its C_3 axis and corresponds to the $\Sigma 1_1$ excited internal rotor state. The smaller barrier for the internal rotation tunnelling motion in the trimer complex suggests that the two metastable internal rotor states ($\Sigma 0_0$ and $\Sigma 1_1$) are separated by a greater energy in Ne_2-NH_3 than in Ne-NH_3. The corresponding tunnelling splitting is thus expected to be larger in the trimer spectrum. This increases the uncertainty in predicting the frequencies of the excited internal rotor state transitions and may explain why the $\Sigma 1_1$ state transitions were not observed for the trimers. In contrast, the barriers for internal rotation of NH_3 in the θ coordinate (through $\theta = 0°/180°$) are several wavenumbers smaller in the Ne-NH_3 (33.0 cm^{-1}/26.0 cm^{-1} and 36.4 cm^{-1}/29.9 cm^{-1} for the <HNH = 106.67° and <HNH = 113.3° surfaces, respectively) than in Ne_2-NH_3. The minimum energy paths from $\theta = 0°$ to $\theta = 180°$ are compared for the Ne-NH_3 and Ne_2-

NH_3 complexes (<HNH = 106.67°) in Figure 4.7 at the CCSD(T) level of theory. The minimum energy path requires 0.4 Å of radial variation for the trimer and 0.5 Å for the dimer. The potential well is more anisotropic for Ne_2-NH_3 suggesting that there are distinct differences in the angular dependencies of the dimer and trimer complexes. The dimer potential well is shallower and narrower than the trimer potential well. The narrower well leads to higher zero point energies for the dimer and consequently, a higher

Figure 4.7 Comparison of the minimum energy [CCSD(T)] paths of the Ne-NH_3 dimer (- - ▲- -) and the Ne_2-NH_3 (—●—) trimer calculated at the CCSD(T) level of theory as a function of the θ coordinate for $\phi = 60°$, $\beta = 90°$, <HNH = 106.67°. The global minimum of each curve was set to 0.0 μE_h and the other energies along the minimum energy paths were adjusted accordingly.

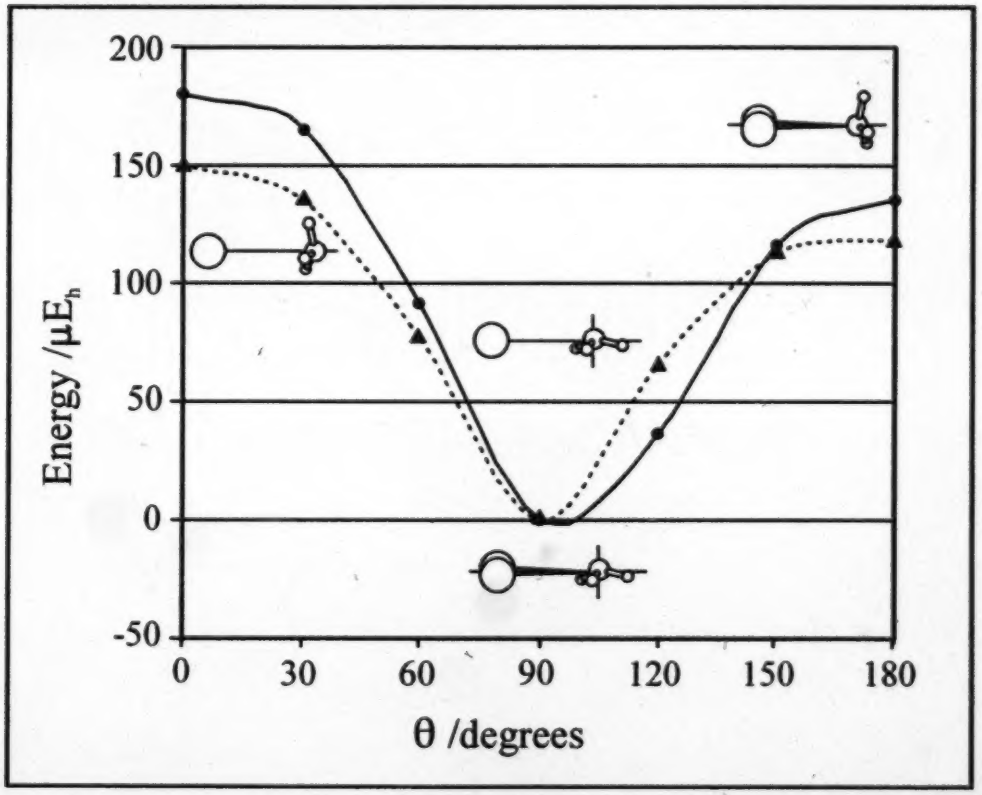

tunnelling probability. This effect combined with the smaller barriers through $\theta = 0°$ and $\theta = 180°$ for the Ne-NH_3 dimer suggest that internal rotation in the θ coordinate is comparatively less hindered in the dimer than in the trimer. This is experimentally manifested in the smaller χ_{aa} values of the dimer complex relative to the trimer.

The minimum energy paths calculated for the trimer from $\theta = 0°$ to $\theta = 180°$ are compared for the three different NH_3 internal geometries in Figure 4.8 for the $\beta = 90°/\phi =$

Figure 4.8 Comparison of the minimum energy [CCSD(T)] paths of Ne_2-NH_3 as a function of the θ coordinate for $\phi = 60°$, $\beta = 90°$. Each curve represents a different umbrella angle of NH_3: <HNH = 106.67° (—●—), <HNH = 113.34° (– –■– –), and <HNH = 120.00° (- - ▲- -).

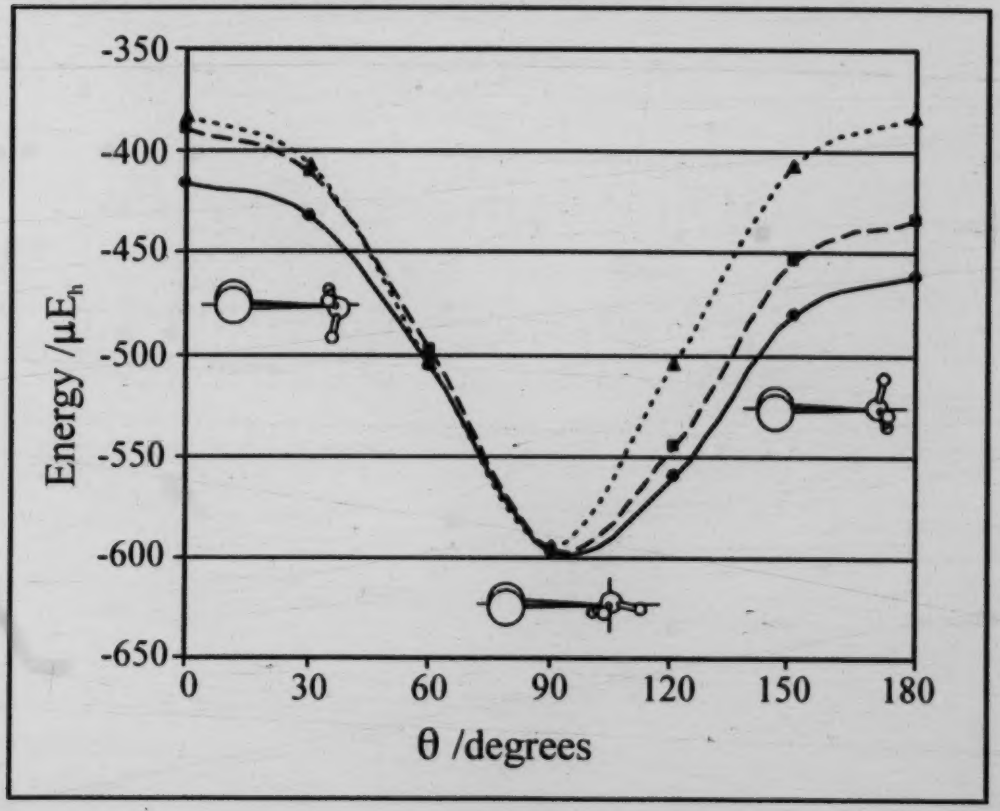

60° orientation. The equilibrium geometry of NH_3 has the shallowest, broadest potential well and the planar geometry, the deepest, narrowest well. The interaction energies are the most similar between $\theta = 60°$ to $\theta = 90°$ suggesting that the internal geometry of NH_3 has little influence at these orientations. In contrast, the largest differences in the minimum energy paths occur at $\theta = 0°$ and $\theta = 180°$ when the C_3 axis of NH_3 is aligned with the symmetry axis of the trimer. This is in close agreement with the *ab initio* potential of Ne-NH_3 and with the experimental observation that the NH_3 inversion is quenched in the Π internal rotor states of Ar-NH_3 and barely affected in the Σ states.[17,40] The ground internal rotor state reported here for Ne_2-NH_3 corresponds to a Σ state and the minimum energy paths plotted in Figure 4.8 support the notion that the presence of two Ne atoms does not quench the NH_3 inversion as long as the inversion motion samples a symmetric environment. The spectral evidence for this lies in the observation of inversion tunnelling splitting in the spectra of the deuterated isotopomers of Ne_2-NH_3.

The dependence of the interaction energy on R, the distance between the center of mass of Ne_2 and nitrogen, is shown in Figure 4.9 for two different θ orientations of NH_3: $\theta = 90°$ and $\theta = 180°$, at $\beta = 90°/\phi = 60°$ for the three NH_3 monomer geometries. In Figure 4.9 a), the potential energy curves are very flat in the radial coordinate around the minimum energy orientation: R = 3.10 Å, $\theta = 90°$, $\beta = 90°$, and $\phi = 60°$. The distance R = 3.10 Å corresponds to a Ne-NH_3 van der Waals bond length of 3.51 Å which is longer than the theoretical value extracted from the potential energy surface of the Ne-NH_3 dimer (3.35 Å) in Chapter 3. This contradicts the experimentally derived bond lengths which were consistent with a shortening of the Ne-NH_3 bond in the trimer relative to the

Figure 4.9 Comparison of the interaction energy [CCSD(T)] of Ne_2-NH_3 as a function of the R coordinate for three different umbrella angles of NH_3: <HNH = 106.67° (—●—), <HNH = 113.34° (– –■– –), and <HNH = 120.00° (- - ▲- -). The NH_3 orientations correspond to: a) $\theta = 90°$, $\phi = 60°$, $\beta = 90°$ and b) $\theta = 180°$, $\phi = 60°$, $\beta = 90°$.

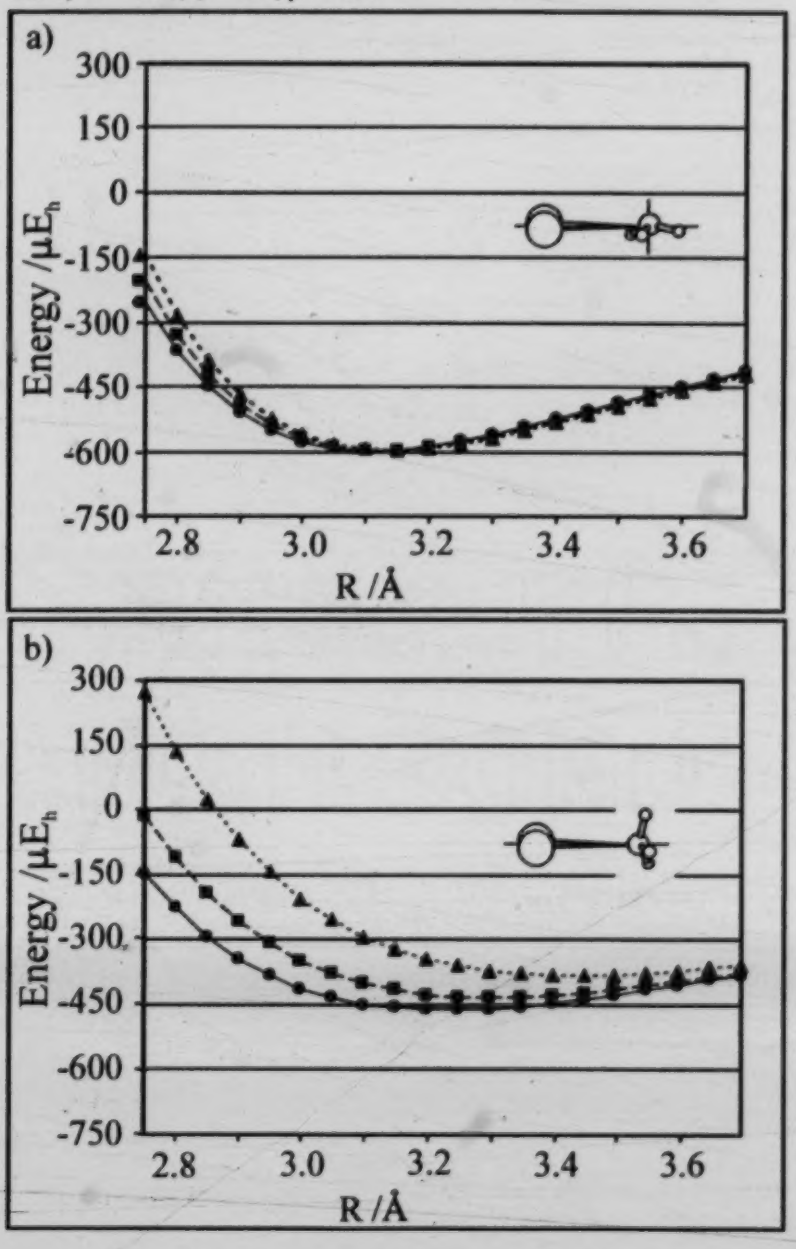

dimer. Furthermore, the theoretically determined Ne-NH_3 bond length (3.51 Å) in Ne_2-NH_3 is shorter than that estimated from the rotational constants (3.695 Å). This discrepancy is mainly due to the fact that the experimental value is highly averaged over the zero point vibrational motions of the complex as seen by the large inertial defects of the trimers. The flexibility of the complex is intrinsically linked to the flatness in the radial coordinate predicted by the *ab initio* calculations. The potential energy curves in Figure 4.9 a) are relatively insensitive to the NH_3 monomer geometry with the greatest discrepancy appearing at small R values. By comparison, the internal geometry of NH_3 has a much greater effect on the interaction energy for orientations that are further from the minimum energy structure, such as $\theta = 180°$ (Figure 4.9 b). As R increases, the interaction energy becomes less dependent on the NH_3 geometry and the θ orientation as expected.

The ϕ dependence ($\phi = 0°/\phi = 60°$) of the interaction energy is shown in Figure 4.10 as a function of R for two different orientations of NH_3: $\beta = 0°$ and $\beta = 90°$, at $\theta = 90°$. The similarity of the plots in Figure 4.10 a) corresponding to $\phi = 0°$ and $\phi = 60°$ demonstrates that the interaction energy is relatively insensitive to the angle ϕ near the minimum energy β/θ orientation of NH_3. This is in strong contrast to the analogous potential energy curves of the Ne-NH_3 dimer which reveal a strong ϕ dependence near the minimum energy orientation of NH_3. Figure 4.10 b) shows a much greater ϕ dependence for the trimers at the $\beta = 0°$ orientation of NH_3 when $\theta = 90°$. An increased sensitivity to ϕ is actually observed for each θ value between 30° and 150° when the potential energy curves are compared for $\beta = 0°$ and $\beta = 90°$. This occurs because at the $\beta = 0°$ orientation,

Figure 4.10 Comparison of the interaction energy [CCSD(T)] of Ne_2-NH_3 as a function of the R coordinate for two different ϕ orientations: $\phi = 0°$ (- - ●- -) and $\phi = 60°$ (—●—). The NH_3 orientations correspond to: a) $\theta = 90°$, $\beta = 90°$ and b) $\theta = 90°$, $\beta = 0°$.

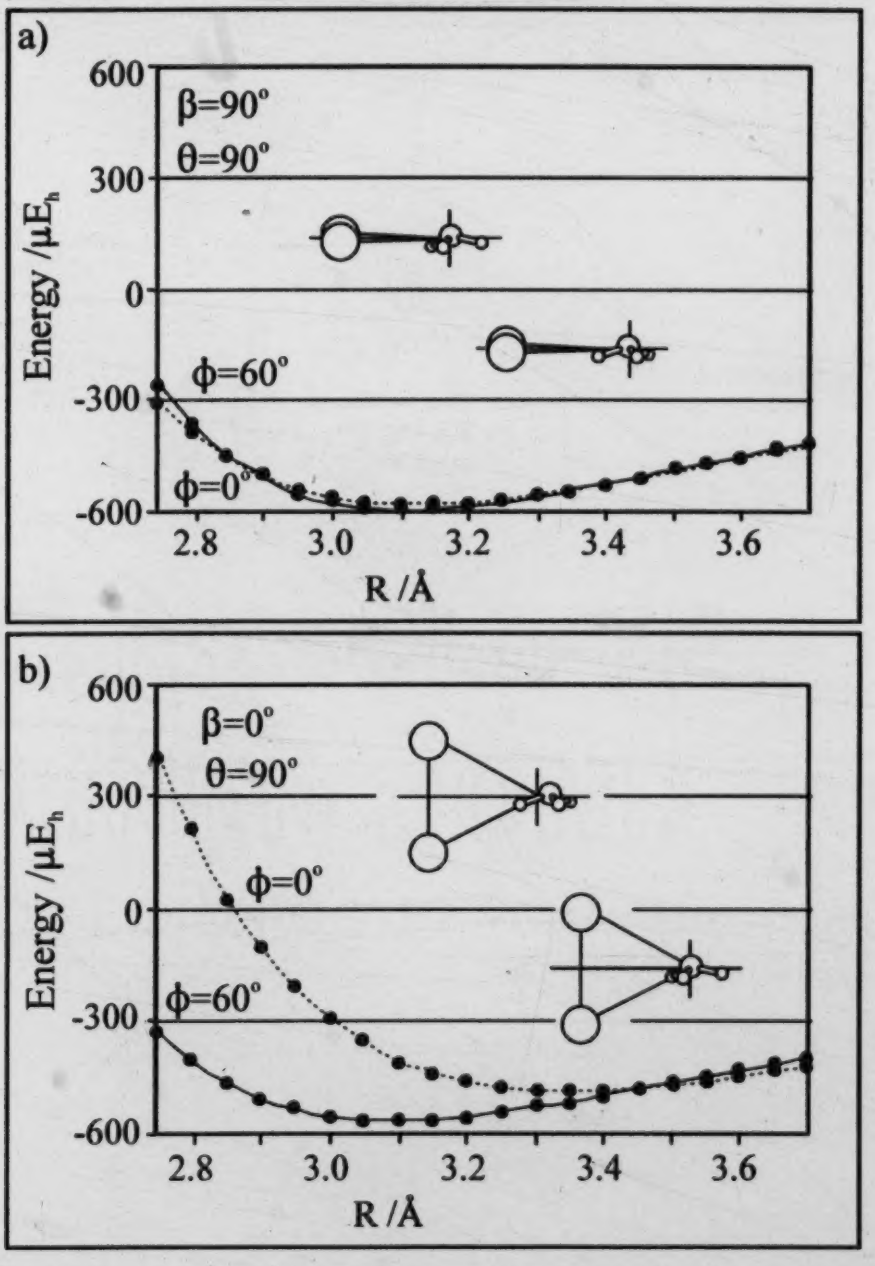

there is always one hydrogen atom lying in the *ab*-plane with the Ne_2 subunit for $\phi = 0°$ and $\phi = 60°$. The $\phi = 0°$ potential energy curve is more repulsive at small θ values since this hydrogen atom points towards Ne_2 at this orientation. As expected, the ϕ and β dependences decrease for larger R separations.

4.6 Concluding remarks

The first high resolution spectra of the Ar_2-NH_3 and Ne_2-NH_3 complexes were reported. The asymmetric top rotational spectra described correspond to the ground internal rotor states of the two trimers. The van der Waals bond lengths derived from the rotational constants reveal the presence of three body nonadditive contributions to the weak interaction. The three body effects are highly dependent on the nature of the molecular substituent and therefore, the measurement of high resolution spectra for a broad range of van der Waals trimers is necessary to elucidate the functional form of various three body terms. Furthermore, the microwave spectra reveal that the NH_3 molecule continues to undergo large amplitude internal motions when bound to two Rg atoms. This is supported by the small ^{14}N nuclear quadrupole coupling constants determined for the various isotopomers of the two trimers. Inversion tunnelling splittings were observed for each of the deuterated isotopomers which provides physical insight into the structures of the complexes. The observation of inversion doubling indicates that the NH_3 is oriented such that its C_3 axis is, on average, perpendicular to the trimer symmetry axis. This is in accord with the minimum energy structure predicted by the *ab initio* calculations of Ne_2-NH_3 and is further reinforced by the determination that the

potential minimum is insensitive to the NH_3 monomer geometry. Furthermore, the potential energy surfaces are very flat in the radial coordinate in the region around the potential minimum. This reinforces the experimental determination of large inertial defects for the Ne_2-NH_3 complex. Comparison of the potential energy surfaces of Ne_2-NH_3 with those of Ne-NH_3 provide insight into differences in the internal dynamics of NH_3 in the two complexes. For example, the barrier to internal rotation of NH_3 about its C_3 axis is significantly smaller in the trimer than in the Ne-NH_3 dimer. In contrast, the barriers are larger for rotation in the θ coordinate of the trimer than in the dimer. This is linked to the experimental observation of larger ^{14}N nuclear quadrupole coupling constants in the trimer complexes. Thus, the *ab initio* studies have been extremely useful in identifying differences in the anisotropies of the weak interactions of the $Rg_{1,2}$-NH_3 complexes. These variations are reflected in the rotational spectra of the Rg-NH_3 and Rg_2-NH_3 complexes since the spectra are highly averaged over different large amplitude motions of the NH_3 moiety.

References

1. T. D. Klots, C. Chuang, R. S. Ruoff, T. Emilsson, and H. S. Gutowsky, *J. Chem. Phys.* **86**, 5315 (1987).

2. M. J. Elrod, R. J. Saykally, A. R. Cooper, and J. M. Hutson, *Mol. Phys.* **81**, 579 (1994).

3. A. Ernesti and J. M. Hutson, *J. Chem. Phys.* **106**, 6288 (1997).

4. D. T. Anderson, S. Davis, and D. J. Nesbitt, *J. Chem. Phys.* **107**, 1115 (1997).

5. H. S. Gutowsky, T. D. Klots, C. Chuang, C. A. Schmuttenmaer, and T. Emilsson, *J. Chem. Phys.* **83**, 4817 (1985); **86**, 569 (1987).

6. J. T. Farrel Jr. and D. J. Nesbitt, *J. Chem. Phys.* **105**, 9421 (1996).

7. R. Moszynski, P. E. S. Wormer, T. G. A. Heijmen, and A. van der Avoird, *J. Chem. Phys.* **108**, 579 (1988).

8. E. Arunan, T. Emilsson, and H. S. Gutowsky, *J. Am. Chem. Soc.* **116**, 8418 (1994).

9. E. Arunan, C. E. Dykstra, T. Emilsson, and H. S. Gutowsky, *J. Chem. Phys.* **105**, 8495 (1996).

10. E. A. Colbourn and A. E. Douglas, *J. Chem. Phys.* **65**, 1741 (1976).

11. P. R. Herman, P. E. LaRocque, and B. P. Stoicheff, *J. Chem. Phys.* **89**, 4535 (1988).

12. R. Aziz, *J. Chem. Phys.* **99**, 4518 (1993).

13. J. M. Hutson, *J. Chem. Phys.* **96**, 4237 (1992).

14. J. M. Hutson, *J. Chem. Phys.* **96**, 6752 (1992).

15. R. C. Cohen and R. J. Saykally, *J. Chem. Phys.* **94**, 7991 (1990); **98**, 6007 (1993).

16. J. M. Hutson, *J. Chem. Phys.* **92**, 157 (1990).

17. C. A. Schmuttenmaer, R. C. Cohen, and R. J. Saykally, *J. Chem. Phys.* **101**, 146 (1994).

18. P. Bunker and P. Jensen, *Molecular Symmetry and Spectroscopy*, 2nd edition, NRC Research Press, Ottawa (1998).

19. D. D. Nelson Jr., G. T. Fraser, K. I. Peterson, K. Zhao, W. Klemperer, F. J. Lovas, and R. D. Suenram, *J. Chem. Phys.* **85**, 5512 (1986).

20. H. M. Pickett, *J. Molec. Spectrosc.* **148**, 371 (1991).

21. J. K. G. Watson, *Vibrational Spectra and Structure*, Vol. 6, Elsevier, New York (1977).

22. Y. Xu, W. Jäger, and M. C. L. Gerry, *J. Chem. Phys.* **100**, 4171 (1994).

23. ASYM20 (Version 2.1), written by L. Hedberg, and I. M. Mills, Oregon State University, USA, and University of Reading, U., December 1992.

24. *MOLPRO* (Version 2000.1), written by H. -J. Werner and P. R. Knowles, with contributions from R. D. Amos, A. Bernhardsson, A. Berning, P. Celani, D. L. Cooper, M. J. O. McNicholas, F. R. Manby, W. Meyer, M. E. Mura, A. Nicklass, P. Palmieri, R. Pitzer, G. Rauhut, M. Schütz, H. Stoll, A. J. Stone, R. Tarroni, and T. Thorsteinsson, University of Birmingham, UK, 1999.

25. G. Chałasiński and M. M. Szczęśniak, *Chem. Rev.* **100**, 4227 (2000); **94**, 1723 (1994).

26. W. S. Benedict and E. K. Plyler, *Can. J. Phys.* **35**, 1235 (1957).

27. S. F. Boys and F. Bernardi, *Mol. Phys.* **19**, 553 (1970).

28. T. H. Dunning Jr., *J. Chem. Phys.* **90**, 1007 (1989).

29. A. J. Sadlej, Collec. *Czech. Chem. Commun.* **53**, 1995 (1988).

30. Y. Xu and W. Jäger, *J. Chem. Phys.* **107**, 4788 (1997).

31. M. S. Ngarī and W. Jäger, *J. Chem. Phys.* **111**, 3919 (1999).

32. G. T. Fraser, K. R. Leopold, D. D. Nelson Jr., A. Tung, and W. Klemperer, *J. Chem. Phys.* **80**, 3073 (1984).

33. G. T. Fraser, K. R. Leopold, and W. Klemperer, *J. Chem. Phys.* **81**, 2577 (1984).

34. P. Herbine and T. R. Dyke, *J. Chem. Phys.* **83**, 3768 (1985).

35. W. Gordy and R. L Cook, *Microwave molecular spectra*, 3rd edition, Wiley, New York (1984).

36. Y. Xu and W. Jäger, *J. Chem. Phys.* **107**, 4788 (1997).

37. Y. Xu, M. C. L. Gerry, J. P Connelly, and B. J. Howard, *J. Chem. Phys.* **98**, 2735 (1993).

38. Y. Xu, W. Jäger, and M. C. L. Gerry, *J. Molec. Spectrosc.* **157**, 132 (1993).

39. M. T. Weiss and M. W. P. Strandberg, *Phys. Rev.* **83**, 567 (1951).

40. E. Zwart, H. Linnartz, W. L. Meerts, G. T. Fraser, D. D. Nelson Jr., and W. Klemperer, *J. Chem. Phys.* **95**, 793 (1991).

CHAPTER 5

Investigation of the Rg_3-NH_3 van der Waals tetramers: Rotational spectra and *ab initio* calculations

5.1 Introduction

The ability to produce larger van der Waals clusters in a molecular beam expansion affords the opportunity to extend the study of three body nonadditive effects to higher orders. For example, several tetramer complexes of the Rg_3-molecule type have been investigated in the microwave region. The first of these to be studied involved the linear molecules HF,[1,2] HCl,[3] and HCN[4] partnered with Ar_3. The symmetric top spectra observed correspond to structures in which the three Rg atoms form an equilateral triangle and the linear molecule is weakly bound to one face with the hydrogen end pointed towards the Rg atoms. Recently, spectra of Ar_3-H_2X type complexes (X = O, S)[5] were reported. Despite the C_{2v} symmetry of the H_2O and H_2S subunits, the observed spectra were also those of symmetric top complexes. This was attributed to large amplitude internal motions of the molecular substituent within the cluster, leading to a symmetric averaging about the C_3 axis of the tetramer.

Chapters 3 and 4 described the structures and dynamics of the Rg-NH_3 and Rg_2-NH_3 complexes. A microwave investigation of the Rg_3-NH_3 tetramers is the next step in the study of the solvation of NH_3 with Rg atoms. The spectra contain valuable information about three and four body nonadditive effects and provide further insight into the effect of the Rg atom cluster size on the internal motions of NH_3. An *ab initio* study

of Ne_3-NH_3 promises to provide a useful comparison with the experimental results of the tetramer complex and with the previously described potential energy surfaces of Ne-NH_3 and Ne_2-NH_3.

The current chapter describes the first high resolution microwave spectra of five isotopomers of Ar_3-NH_3 and eleven isotopomers of Ne_3-NH_3. The spectra are assigned to the ground internal rotor states of the two quaternary complexes. The ^{14}N nuclear quadrupole hyperfine structure and inversion tunnelling splitting are analyzed and discussed in terms of the structures and dynamics of the tetramers relative to the Rg-NH_3 dimers and Rg_2-NH_3 trimers. Three *ab initio* potential energy surfaces were constructed for Ne_3-NH_3 at the CCSD(T) level of theory. The theoretical results are described and compared with the observed tetramer spectra. Furthermore, comparisons are made with the potential energy surfaces of Ne-NH_3 and Ne_2-NH_3 in Chapter 3 and 4, respectively.

5.2 Experimental Method

The rotational spectra of the Ar_3-NH_3 and Ne_3-NH_3 tetramer complexes were recorded between 4 GHz and 17 GHz using the microwave spectrometer described in Chapter 2 and Section 3.2. The complexes were produced in a molecular beam expansion of a gas mixture through a pulsed nozzle with an orifice diameter of 0.8 mm (General Valve Corp., Series 9). The gas sample was prepared at room temperature and consisted of approximately 0.5 % NH_3 and 5 % Ar using Ne as a backing gas to obtain a total pressure of 12 atm for Ar_3-NH_3. To record the spectra of Ne_3-NH_3, no argon gas was added to the sample system. The ^{22}Ne containing species were measured in natural

abundance (8.82 % ^{22}Ne). Isotopically enriched samples were used to record the spectra of the ^{15}N (Cambridge Isotopes: 98 % $^{15}NH_3$) and deuterium (Cambridge Isotopes: 99 % ND_3) containing isotopomers. The intensity of the ND_2H and NDH_2 containing species increased dramatically after the ND_3 containing gas mixture was left in the sample system for several hours.

5.3 Spectral search and assignment

The combined microwave spectroscopic and *ab initio* studies of the Rg_2-NH_3 complexes in Chapter 4 demonstrated that the internal rotation and inversion of the NH_3 molecule is not significantly hindered when bound to two Rg atoms. If the NH_3 moiety continues to undergo large amplitude motions in the Rg_3-NH_3 tetramer complexes, the rotational spectra observed will be those of symmetric tops provided all three Rg atoms are the same. If composed of at least two different Rg atoms, the tetramer complexes are asymmetric tops. The allowed transitions of each species can be determined via molecular symmetry group theory.[6]

5.3.1 Isotopomers of Ar_3-NH_3

The rotational spectrum of Ar_3-NH_3 was predicted to be that of an oblate symmetric top similar to that reported earlier for Ar_3-H_2O.[5] Figure 5.1 shows the geometry of the Ar_3-NH_3 tetramer in the principal inertial axis system. The energy levels of a symmetric top are labelled with the quantum numbers J_K and the selection rules for rotational transitions are: $\Delta J = \pm 1$, $\Delta K = 0$. The van der Waals bond lengths were

Figure 5.1 Geometry of the Ar_3-NH_3 oblate symmetric top in the principal inertial axis system.

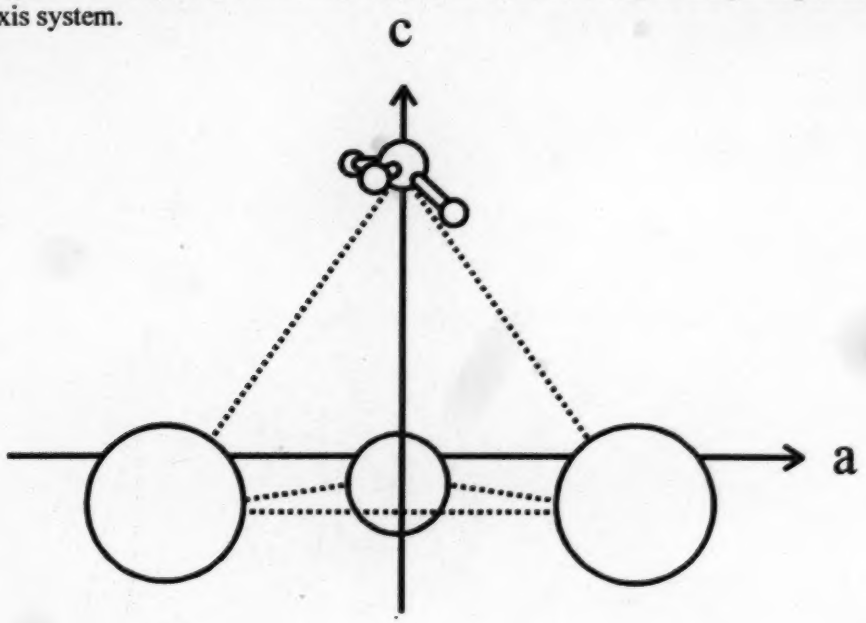

estimated through comparison of the structures determined for other Ar_3-molecule van der Waals complexes. For example, the Ar-Ar bond length is relatively constant in the Ar_3 containing tetramers with HCl (3.851 Å),[1,2] HCN (3.85 Å),[4] and H_2O (3.848 Å)[5] and was assumed to be similar in Ar_3-NH_3. The Ar-NH_3 bond length was approximated to be equal to the dimer value (3.836 Å)[7] since in complexes such as Ar_3-Ne,[8] the Ar-Ne bond lengthens by only 0.003 Å in the tetramer relative to the dimer.[9] From the estimated structure, the B constant was predicted within 4 MHz of that determined in this work for Ar_3-NH_3. For the previously studied Ar_3-molecule complexes, only transitions corresponding to levels with K = 3n (n = 0, 1, 2, ...) were observed. A similar spectrum was expected for Ar_3-NH_3 and the presence and absence of energy levels was verified by

a molecular symmetry group theoretical analysis[6] which is summarized in Table 5.1.

a) Ar_3-NH_3 and Ar_3-$^{15}NH_3$

The complete nuclear permutation inversion group for Ar_3-NH_3 is G_{72}, the direct product of the $C_{3v}(Ar_3)$ and $D_{3h}(NH_3)$ molecular symmetry groups. After labelling the

Table 5.1 Summary of molecular symmetry group theory analysis for the metastable states of the Rg_3-NH_3 isotopomers.

	Rg_3-NH_3	Rg_3-ND_3	Rg_3-ND_2H	Rg_3-NDH_2
Molecular symmetry group	G_{36}	G_{36}	G_{12}	G_{12}
Total symmetry required[a]	A_2/A_4	A_1/A_3	A_1'/A_2'	A_1''/A_2''
Nuclear spin symmetry[b]	$4A_1\oplus 2E_1$	$10A_1\oplus A_3\oplus 8E_1$	$6A_1'\oplus 3A_1''$	$3A_1'\oplus A_1''$
Rotational symmetry				
K=0 (even J/odd J)		A_1/A_3		A_1'/A_2'
K=3n		$A_1\oplus A_3$		$A_1'\oplus A_2'$
K≠3n		E_3		E'
NH_3 inversion symmetry		symmetric/antisymmetric		
		A_1/A_4		A_1'/A_2''
NH_3 internal rotation symmetry		ground state/first excited state		
		A_1/E_1		n/a
Rovibrational symmetry[c]	$\Sigma 0_{0s}$	$\Sigma 0_{0a}$ $\Sigma 1_{1s}$	$\Sigma 0_{0s}$	$\Sigma 0_{0a}$
K=0 (even J/odd J)	A_1/A_3	A_4/A_2 E_1/E_2	A_1'/A_2'	A_2''/A_1''
K=3n	$A_1\oplus A_3$	$A_4\oplus A_2$ $E_1\oplus E_1$	$A_1'\oplus A_2'$	$A_2''\oplus A_1''$
K≠3n	E_3	E_4 G	E'	E''
Predicted nuclear spin statistical weights	$\Sigma 0_{0s}$:$\Sigma 0_{0a}$:$\Sigma 1_{1s}$		$\Sigma 0_{0s}$:$\Sigma 0_{0a}$	
	0:4:2	10:1:8	6:3	1:3

[a] refers to the symmetry of the total wavefunction upon exchange of identical fermions or bosons.

[b] refers to the symmetry of the nuclear spin function of the identical hydrogen or deuterium nuclei only.

[c] includes the NH_3 inversion and NH_3 internal rotation symmetries.

three Ar atoms (1, 2, 3) and the three hydrogen atoms (A, B, C), 72 permutation operations can be carried out which produce 72 differently labelled combinations of Ar and hydrogen nuclei within the tetramer. These 72 distinct versions can be generated using various combinations of feasible motions of the Ar_3-NH_3 complex. These feasible motions include rotations of the entire complex as well as tunnelling motions of the substituents within the complex such as the NH_3 inversion motion. To simplify the analysis, the elements requiring a change in the handedness of the Ar_3 ring were removed since no evidence of this tunnelling motion was found in the spectra or in previous studies of other Ar_3 containing tetramers. This reduction permits the use of the G_{36} character table (Table A1.5). The total wavefunction is of A_2 or A_4 symmetry since it must be symmetric with respect to the interchange of any two Ar nuclei and antisymmetric with respect to the interchange of any two hydrogen nuclei. The eight nuclear spin states of the three hydrogen atoms span the representation: $4A_1 \oplus 2E_1$. The vibrational symmetries of the symmetric and antisymmetric inversion states are A_1 and A_4, respectively. The symmetries of the symmetric rotor wavefunctions for the ground internal rotor state alternate as A_1/A_3 for even/odd J values when K = 0. Only the antisymmetric state has the correct rovibrational symmetry to combine with the nuclear spin function symmetry to achieve the required total symmetry, A_2 or A_4. The symmetric inversion state has a nuclear spin statistical weight of zero. When K = 3 (or a multiple of 3), the rotational wavefunction has $A_1 \oplus A_3$ symmetry for each J and, as in the case of K = 0, only the antisymmetric inversion component is expected to be observed. For the $K \neq 3n$ (where n = 0, 1, 2, ...) levels, the rovibrational symmetries are E_3 (symmetric) and E_4

(antisymmetric) and both inversion states have nuclear spin statistical weights of zero. Thus, the spectra of these isotopomers are expected to contain rotational transitions between levels with K = 3n (n = 0, 1, 2, ...) corresponding to the antisymmetric inversion component of the ground internal rotor state. The predicted energy level diagram for an oblate symmetric top is shown in Figure 5.2.

In total, 11 transitions of the Ar_3-NH_3 isotopomer were measured and the frequencies are listed in Appendix 6 (Table A6.1). The lowest J transition, $J_K = 1_0$-0_0, is beyond the lower limit of the microwave spectrometer (4 GHz). The measured transitions were assigned to the antisymmetric inversion component of the ground internal rotor state of Ar_3-NH_3. As predicted by the molecular symmetry group analysis, only states with K = 3n (n = 0, 1, 2) were observed. The assignment of transitions to the K = 0, K = 3, and K = 6 progressions was confirmed by the observation that the second progression began for transitions originating in levels where J = 3 and the third appeared only for the transition originating in J = 6. The K = 0 transitions appear at lower frequency than the K = 3 and K = 6 transitions, corresponding to a negative D_{JK} constant, confirming that Ar_3-NH_3 is an oblate symmetric top. Nuclear quadrupole hyperfine structure arising from the ^{14}N nucleus was resolved for the two lowest J transitions observed. The ^{14}N hyperfine and rotational analyses were done simultaneously using a standard symmetric top energy level expression in Pickett's global fitting program.[10] The resulting spectroscopic constants are given in Table 5.2.

The analogous 11 rotational transitions were measured for the Ar_3-$^{15}NH_3$ isotopomer and the corresponding transition frequencies are listed in Table A6.2. The

Figure 5.2 Predicted energy level diagram for the Ar_3-NH_3 oblate symmetric top. The dotted line denotes the energy levels with nuclear spin statistical weights of zero.

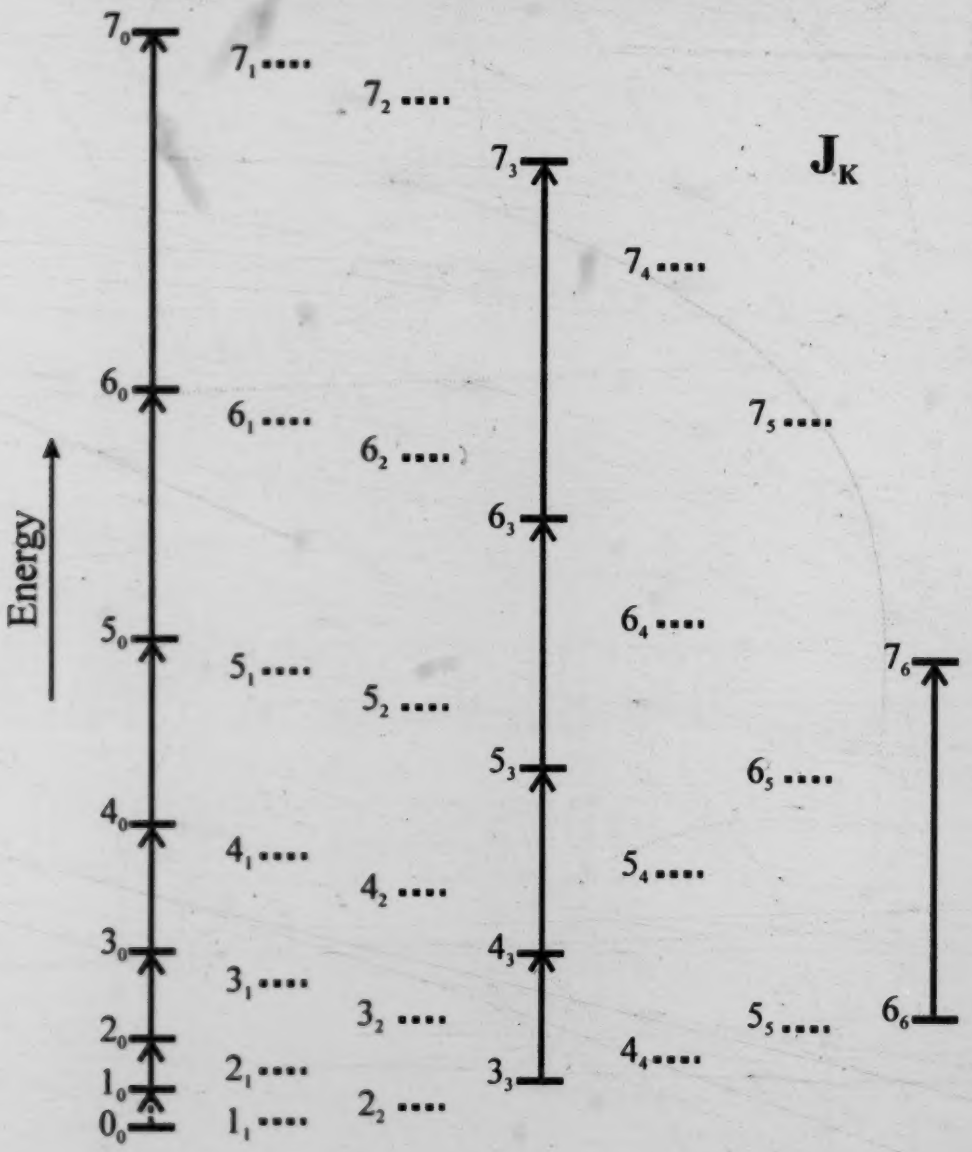

Table 5.2 Spectroscopic constants for Ar_3-NH_3 and Ar_3-$^{15}NH_3$.

$\Sigma 0_{0a}$	Ar_3-NH_3	Ar_3-$^{15}NH_3$
Rotational constant /MHz		
B	1145.8853(1)	1127.3190(1)
Centrifugal distortion constants /kHz		
D_J	6.4(1)	6.1(1)
D_{JK}	-3.6(1)	-2.9(1)
^{14}N quadrupole hyperfine constant /MHz		
χ_{aa}	0.1458(15)	
Standard deviation /kHz		
σ	6.5	1.2

spectroscopic constants were fit as described above and the results are given in Table 5.2. Comparison of the intensities revealed that the $J_K = 4_3$-3_3 transition is more intense than the 4_0-3_0 transition. This is in accord with the oblate symmetric top energy level diagram shown in Figure 5.2. The K = 3 energy levels are lower in energy than the K = 0 energy levels and thermal relaxation can occur between them. The same intensity phenomenon was noted for the other isotopomers but accurate intensity comparisons were hindered by the presence of the ^{14}N nuclear quadrupole hyperfine splitting.

There is a second metastable internal rotor state for Ar_3-NH_3 and Ar_3-$^{15}NH_3$ that is associated with the E_1 nuclear spin function. The allowed transitions within this state are predicted to have half the intensity of the ground state transitions due to nuclear spin statistics. The positions of these transitions cannot be predicted from the ground state spectrum and thus a spectral search was carried out at both higher and lower frequencies than the ground state transition frequencies. The search proved to be very difficult since the tetramer signals were weak. In the end, no transitions were found that could be assigned to the excited internal rotor state based on the expected intensity and ^{14}N nuclear

quadrupole hyperfine splitting.

b) Ar_3-ND_3

Using the G_{36} character table as for Ar_3-NH_3, the symmetries of the rovibrational wavefunctions of Ar_3-ND_3 are the same as for Ar_3-NH_3 in the ground internal rotor state. The interchange of any two Ar nuclei or deuterium nuclei is governed by Bose-Einstein statistics. It can be shown for the ground internal rotor state that the $K = 3n$ ($n = 0, 1, 2, ...$) energy levels have nonzero nuclear spin statistical weights for both inversion components. The relative intensities of the symmetric and antisymmetric state transitions are predicted to be 10 and 1, respectively. The $K \neq 3n$ levels are missing due to nuclear spin statistics. The inversion components were expected to be closely spaced in the microwave spectrum as seen previously in the RG-ND_3 and RG_2-ND_3 species. For the Ar_3-ND_3 tetramer, it was unclear whether the presence of three Ar atoms would appreciably hinder the ND_3 inversion and thus whether two sets of rotational transitions could be resolved. With careful measurement however, both inversion components were observed and assigned for the ground state of Ar_3-ND_3.

The transition frequencies recorded for Ar_3-ND_3 are listed in Table A6.3. These were assigned to the $K = 0$, $K = 3$, and $K = 6$ progressions of the two inversion components of the ground internal rotor state. The inversion tunnelling splitting of the $J_K = 2_0$-1_0 transition is 74.3 kHz and the ^{14}N nuclear quadrupole hyperfine structures of the two inversion states overlap for the lowest J transitions. The inversion components at higher frequency are more intense and were consequently assigned to the symmetric inversion state based on the predicted spin weights. In total, 11 rotational transitions were

assigned for the symmetric inversion state and eight were assigned for the weaker antisymmetric state. The ^{14}N nuclear quadrupole hyperfine splitting was resolved and assigned for the more intense symmetric inversion state but additional splitting due to the presence of the three deuterium nuclei was not observed. For Ar-ND_3, the deuterium hyperfine structure was visible for the J = 1-0 transition but collapsed for the higher transitions. For the Ar_3-ND_3 tetramer, the lowest J transition is beyond the range of the spectrometer and no evidence of deuterium splitting or broadening was apparent for the higher J transitions. The ^{14}N hyperfine and rotational analyses were performed as described for Ar_3-NH_3 and the results are listed in Table 5.3. The ^{14}N nuclear quadrupole coupling constant, χ_{cc}, from the symmetric inversion state was fixed in the fit of the antisymmetric state since the transitions were too weak to measure the hyperfine splitting

Table 5.3 Spectroscopic constants for Ar_3-ND_3, Ar_3-ND_2H, and Ar_3-NDH_2.

$\Sigma 0_{0s}/\Sigma 0_{00s}$	Ar_3-ND_3	Ar_3-ND_2H	Ar_3-NDH_2
Rotational constant /MHz			
B	1088.5846(1)	1106.5279(1)	1125.1954(1)
Centrifugal distortion constants /kHz			
D_J	5.4(1)	5.9(1)	6.3(1)
D_{JK}	-0.84(1)	-2.0(1)	-3.1(1)
^{14}N quadrupole hyperfine constant /MHz			
χ_{cc}	0.3221(18)	0.2914(21)	0.2180(18)
Standard deviation /kHz			
σ	4.3	2.7	5.4
$\Sigma 0_{0a}/\Sigma 0_{00a}$			
B	1088.5666(1)	1106.5386(1)	1125.2947(1)
D_J	5.4(1)	5.9(1)	6.3(1)
D_{JK}	-0.84(1)	-2.0(1)	-3.1(1)
χ_{cc}	0.3221[a]	0.2866(21)	0.2155(18)
σ	2.8	1.8	5.2

[a] Fixed at value from symmetric inversion state.

in the latter. The ^{14}N nuclear quadrupole hyperfine structures of the two inversion states should be similar since they lie close in energy. This approximation appears to be valid since the standard deviations of the spectroscopic fits are small, 4.3 kHz and 2.8 kHz for the symmetric and antisymmetric inversion states, respectively.

c) Ar_3-ND_2H

The three Ar atoms and two deuterium atoms in Ar_3-ND_2H can be labelled and permuted to create 24 distinct versions of the complex and thus, the complete nuclear permutation inversion group is G_{24}. Neglecting the tunnelling motion that requires flipping the Ar_3 ring, the G_{12} character table (Table A1.6) contains the essential permutation elements for the molecular symmetry group analysis. The total wavefunction must be symmetric upon exchange of the two deuterium nuclei or any two Ar nuclei. For the ground internal rotor state, two inversion tunnelling components are expected for the transitions between K = 3n (n = 0, 1, 2, ...) levels with relative nuclear spin statistical weights of 6 and 3 for the symmetric and antisymmetric states, respectively. The $K \neq 3n$ levels have nuclear spin statistical weights of zero. Unlike in the Ar_3-NH_3 and the Ar_3-ND_3 isotopomers, there is no feasible internal rotation of ND_2H that interchanges the two like deuterium atoms and only the ground internal rotor state is metastable.

The microwave spectrum of Ar_3-ND_2H was recorded, and the transition frequencies assigned to each inversion component of the ground internal rotor state are listed in Table A6.4 for the K = 0, K = 3, and K = 6 progressions. The two inversion components are closely spaced, which made it difficult to sort out the ^{14}N nuclear quadrupole hyperfine and inversion tunnelling components of the $J_K = 2_0$-1_0 transition.

Examination of higher J transitions helped to confirm the assignment and it was determined that the lower frequency components were those of the symmetric inversion state since the observed intensity was approximately twice that of the higher frequency components. The inversion components are separated by approximately 42.1 kHz for the 2_0-1_0 transition. Eleven rotational transitions were measured for each of the two inversion states. The ^{14}N hyperfine and rotational analyses were done simultaneously and the resulting spectroscopic constants are listed in Table 5.3. A sample spectrum of the J_K = 4_3-3_3 and 4_0-3_0 transitions for the two inversion states is shown in Figure 5.3. The K = 3 transitions are split from the K = 0 transitions by approximately 120 kHz and the inversion tunnelling splitting is on the order of 80 kHz. The confirmation of the assignment of this spectrum relied on the measurement of several higher rotational transitions to ensure consistent trends in the observed splittings of the K = 0/K = 3 transitions and the inversion tunnelling components.

d) Ar_3-NDH_2

The G_{12} molecular symmetry group can also be used to predict the spectrum for the Ar_3-NDH_2 tetramer. For this complex, the exchange of the two like hydrogen nuclei is governed by Fermi-Dirac statistics. The rovibrational symmetries are the same as for Ar_3-ND_2H and it can be shown that the K = 3n (n = 0, 1, 2, ...) levels have nuclear spin statistical weights of 1 and 3 for the symmetric and antisymmetric inversion components of the ground internal rotor state, respectively. As derived for Ar_3-ND_2H, the $K \neq 3n$ levels have nuclear spin statistical weights of zero and there are no metastable excited internal rotor states.

Figure 5.3 Spectrum of the $J_K = 4_0$-3_0 and $J_K = 4_3$-3_3 transitions of Ar_3-ND_2H. The inversion tunnelling components are labelled 's' and 'a' for the symmetric and antisymmetric states, respectively. There is no observable ^{14}N nuclear quadrupole hyperfine splitting in this spectrum since the most intense ^{14}N hyperfine components overlap for these rotational transitions.

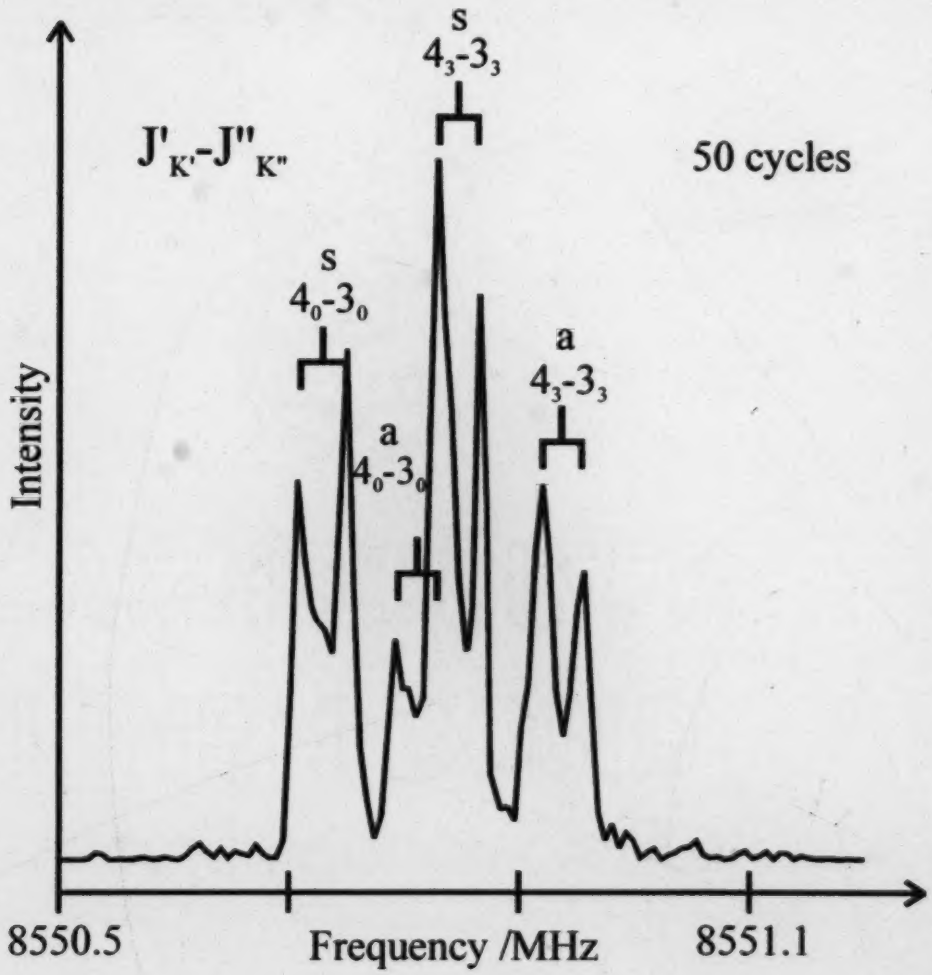

The transition frequencies recorded for Ar_3-NDH_2 are given in Table A6.5. These are assigned to 11 rotational transitions involving the K = 0, K = 3, and K = 6 progressions of the symmetric and antisymmetric inversion components of the ground internal rotor state. The inversion tunnelling components were split by 398 kHz for the $J_K = 2_0$-1_0 transition and as a result, the ^{14}N nuclear quadrupole hyperfine structures do not overlap for the two states. As in the Ar_3-ND_2H species, the lower frequency components were assigned to the symmetric inversion state on the basis of the observed intensities. The ^{14}N hyperfine and rotational analyses were performed as described above and the spectroscopic constants are listed in Table 5.3.

5.3.2 Isotopomers of Ne_3-NH_3

In contrast to the spectroscopic studies of Ar_3-molecule tetramers, only one Ne_3 containing van der Waals complex, Ne_3Ar, has been previously investigated.[8] The Ne_3Ar tetramer is a prolate symmetric top and the Ne-Ne and Ne-Ar bond lengths were reported to be 0.01 Å and 0.006 Å shorter than the respective dimer values. The Ne_3-NH_3 complex was similarly predicted to be a prolate symmetric top. Assuming dimer values for the Ne-Ne (3.29 Å)[8] and Ne-NH_3 (3.723 Å) bond lengths, the B rotational constant was predicted within 2 MHz for $^{20}Ne_3$-NH_3. The presence of ^{22}Ne in 8.82 % natural abundance allows the production of four different isotopomers of Ne_3-NH_3 before ^{15}N or deuterium substitution is considered. These isotopomers have very distinct spectra. The $^{20}Ne_3$ and $^{22}Ne_3$ containing species are prolate symmetric tops as shown in Figure 5.4 a) in the principal inertial axis system. The $^{20}Ne_2{}^{22}Ne$ and $^{20}Ne^{22}Ne_2$ containing isotopomers are

Figure 5.4 Geometries of the Ne_3-NH_3 isotopomers in the principal inertial axis system. a) The $^{20}Ne_3$ and $^{22}Ne_3$ containing isotopomers are prolate symmetric tops. b) The $^{20}Ne_2{}^{22}Ne$ and c) $^{20}Ne^{22}Ne_2$ containing isotopomers are asymmetric tops.

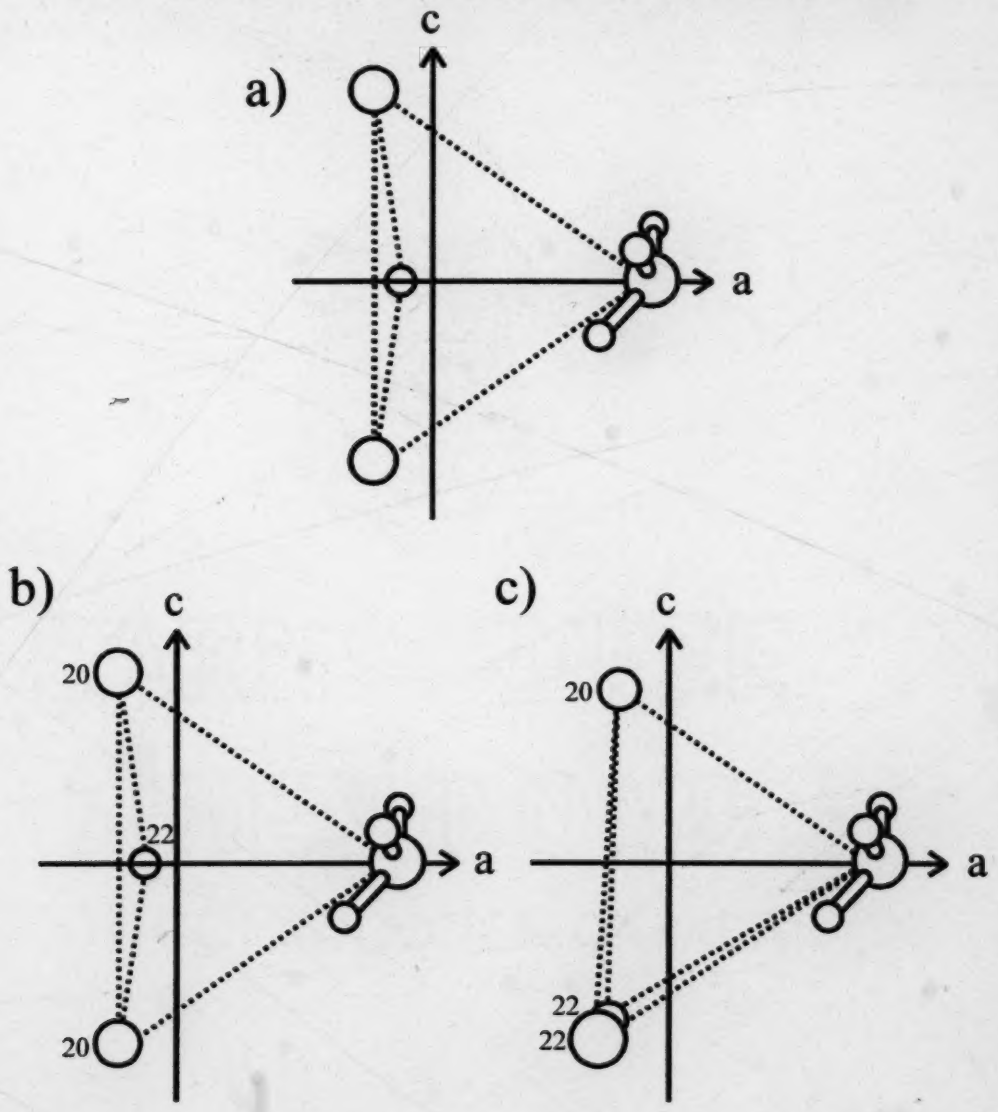

asymmetric tops as depicted in Figures 5.4 b) and 5.4 c), respectively. The $^{20}Ne_2{}^{22}Ne$ containing species has nonzero dipole moment contributions along the *a*- and *b*-axes and both *a*- and *b*-type rotational spectra are anticipated. The *a*- and *b*-type transitions follow the selection rules: $\Delta J = (0, \pm1)$, $\Delta K_a = 0$ ($\pm2, \pm4, ...$), $\Delta K_c = \pm1$ ($\pm3, \pm5, ...$) and $\Delta J = (0, \pm1)$, $\Delta K_a = \pm1$ ($\pm3, \pm5, ...$), $\Delta K_c = \pm1$ ($\pm3, \pm5, ...$), respectively. The $^{20}Ne^{22}Ne_2$-NH_3 complex has nonzero dipole moment contributions along the *a*- and *c*-axes and the expected transitions are *a*- and *c*-type where the selection rules for the latter are: $\Delta J = (0, \pm1)$, $\Delta K_a = \pm1$ ($\pm3, \pm5,...$), $\Delta K_c = 0$ ($\pm2, \pm4,...$). The nuclear spin statistical weights of the various symmetric rotor and asymmetric rotor energy levels can be determined by a molecular symmetry group theoretical analyses of each isotopomer.[6]

a) $^{20}Ne_3$-NH_3, $^{22}Ne_3$-NH_3, $^{20}Ne_3$-$^{15}NH_3$, and $^{22}Ne_3$-$^{15}NH_3$

The molecular symmetry group analysis of the prolate symmetric tops containing NH_3 or $^{15}NH_3$ is analogous to that described in Section 5.3.1 a) for Ar_3-NH_3. The change in the symmetry axes of the tetramer complexes, that is the *c*-axis for Ar_3-NH_3 and the *a*-axis for Ne_3-NH_3, does not influence the symmetry of the rotational part of the wavefunction for symmetric tops as it does for the Ar_2-NH_3 and Ne_2-NH_3 asymmetric tops in Chapter 4. Thus, the rotational spectra of the symmetric top Ne_3-NH_3 species will be comparable to those of Ar_3-NH_3 and involve transitions between the $K = 3n$ ($n = 0, 1, 2, ...$) levels of the anstisymmetric inversion state. Energy levels with $K \neq 3n$ have nuclear spin statistical weights of zero. The predicted energy level diagram for the Ne_3-NH_3 prolate symmetric top is shown in Figure 5.5. In comparison to an oblate symmetric top, the $K = 3$ levels are shifted to higher energy than the $K = 0$ levels in a prolate symmetric

Figure 5.5 Predicted energy level diagram for the $^{20}Ne_3$-NH_3 and $^{22}Ne_3$-NH_3 prolate symmetric tops. The dotted lines denote energy levels with nuclear spin statistical weights of zero and the dashed arrow represents transitions that were not observed.

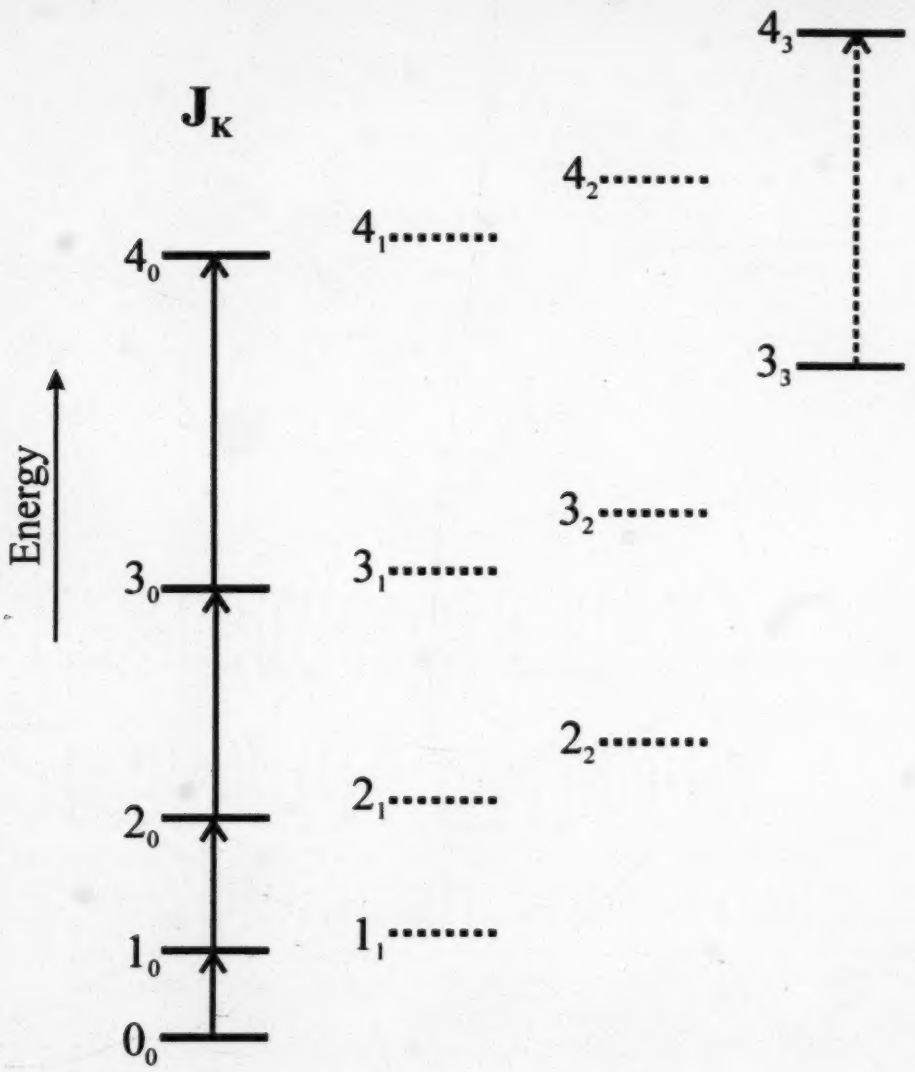

top.[11]

In total, four rotational transitions of the $^{20}Ne_3$-NH_3 and $^{22}Ne_3$-NH_3 isotopomers were measured and assigned to the antisymmetric inversion component of the ground internal rotor state. The transition frequencies are listed in Table A6.6. For a prolate symmetric top, the D_{JK} constant should be positive and thus the transitions in the K = 3 progression should appear at lower frequency than those in the K = 0 progression. The highest J transition measured corresponds to J = 4-3, but only the K = 0 component was observed despite a careful search over tens of MHz for the weaker K = 3 component. The ^{14}N hyperfine and rotational analyses were done simultaneously using Pickett's global fitting program as described for Ar_3-NH_3.[10] The resulting spectroscopic constants are given in Table 5.4.

The corresponding four transitions were measured for the $^{20}Ne_3$-$^{15}NH_3$ and $^{22}Ne_3$-$^{15}NH_3$ isotopomers and the transition frequencies are listed in Table A6.7. The spectroscopic constants are given in Table 5.4.

As in Ar_3-NH_3 there is a second metastable state of $^{20}Ne_3$-NH_3 associated with the

Table 5.4 Spectroscopic constants obtained for Ne_3-NH_3 and Ne_3-$^{15}NH_3$.

0_{0a}	$^{22}Ne_3$-NH_3	$^{20}Ne_3$-NH_3	$^{22}Ne_3$-$^{15}NH_3$	$^{20}Ne_3$-$^{15}NH_3$
Rotational constant /MHz				
B	1971.5299(2)	2074.4130(1)	1925.4918(2)	2025.5516(2)
Centrifugal distortion constant /kHz				
D_J	64.1(1)	71.3(1)	59.8(1)	66.7(1)
^{14}N quadrupole hyperfine constant /MHz				
χ_{aa}	0.4007(18)	0.3939(12)		
Standard deviation /kHz				
σ(kHz)	2.7	3.2	0.9	1.0

E_1 nuclear spin function. A spectral search was carried out at both higher and lower frequencies than the ground state transition frequencies but no transitions were found that could be assigned to the excited internal rotor state based on the expected intensity and ^{14}N hyperfine splitting.

b) $^{20}Ne_3$-ND_3

The molecular symmetry group analysis of $^{20}Ne_3$-ND_3 follows that of Ar_3-ND_3 in Section 5.3.1 b). The ground state rotational spectrum should be similar to that observed for $^{20}Ne_3$-NH_3 symmetric rotor, with the addition of an inversion tunnelling splitting. The symmetric and antisymmetric inversion components have nuclear spin statistical weights of 10 and 1, respectively.

In total, four rotational transitions were measured and assigned to the two inversion components of the ground internal rotor state of $^{20}Ne_3$-ND_3. The corresponding frequencies are listed in Table A6.8. The higher frequency inversion tunnelling transitions are more intense and were consequently assigned to the symmetric inversion state as predicted by the molecular symmetry group analysis. The inversion tunnelling splitting was not resolved for the lowest energy transition, $J_K = 1_0$-0_0. For the 2_0-1_0 transition, the symmetric and antisymmetric state transitions are separated by approximately 10 kHz. For the weaker antisymmetric state, the ^{14}N nuclear quadrupole hyperfine splitting was not resolved since it overlaps closely with that of the more intense symmetric tunnelling state. Consequently, it was necessary to fix the χ_{aa} constant at the symmetric state value during the fit of the antisymmetric state transitions. The ^{14}N hyperfine and rotational fit were done using Pickett's program[10] and the spectroscopic constants are given in Table

5.5.

A spectral search was carried out for the excited internal rotor state associated with the E_1 nuclear spin function at both higher and lower frequencies than the ground state transitions. As in the other tetramer species, no transitions were found that matched the intensity and ^{14}N hyperfine patterns expected for the excited state.

c) $^{20}Ne_3$-ND_2H

The $^{20}Ne_3$-ND_2H tetramer follows the molecular symmetry group analysis outlined in Section 5.3.1 c) for Ar_3-ND_2H. The symmetric top spectrum of the ground internal state of $^{20}Ne_3$-ND_2H is therefore expected to be split into two inversion tunnelling components with relative intensities of 6 and 3 for the symmetric and antisymmetric states, respectively.

The transition frequencies assigned to the two inversion tunnelling components of

Table 5.5 Spectroscopic constants for Ne_3-ND_3, Ne_3-ND_2H, and Ne_3-NDH_2.

$\Sigma 0_{0s}/\Sigma 0_{00s}$	$^{20}Ne_3$-ND_3	$^{20}Ne_3$-ND_2H	$^{20}Ne_3$-NDH_2
Rotational constant /MHz			
B	1943.7354(1)	1984.0396(2)	2027.0382(2)
Centrifugal distortion constant /kHz			
D_J	57.1(1)	63.1(1)	68.40(1)
^{14}N quadrupole hyperfine constant /MHz			
χ_{aa}	0.694(1)	0.639(2)	0.510(1)
Standard deviation /kHz			
σ	3.3	7.5	6.6
$\Sigma 0_{0a}/\Sigma 0_{00a}$			
B	1943.7307(1)	1984.1007(2)	2027.2749(2)
D_J	57.1[a]	63.0(1)	68.4(1)
χ_{aa}	0.694[a]	0.643(3)	0.501((1)
σ	4.7	8.5	3.3

[a] Fixed at value from symmetric inversion state.

the ground internal rotor state of $^{20}Ne_3$-ND_2H are listed in Table A6.9. Four transitions were measured for each state and the inversion tunnelling splitting is approximately 140 kHz for the $J_K = 1_0$-0_0 transition. The ^{14}N nuclear quadrupole hyperfine patterns overlap for the lowest J transition only. The more intense components appear at lower frequency and were therefore assigned to the symmetric inversion state. This is the opposite of the assignment in the ND_3 containing isotopomer. The rotational and ^{14}N hyperfine fit were done as described for $^{20}Ne_3$-NH_3 and the spectroscopic constants are listed in Table 5.5.

d) $^{20}Ne_3$-NDH_2

The molecular symmetry group analysis of $^{20}Ne_3$-NDH_2 tetramer is analogous to that described for Ar_3-NDH_2 in Section 5.3.1 d). The ground internal rotor state spectrum should be split into two due to the inversion of the NDH_2 moiety. The nuclear spin statistical weights are 1 and 3 for the symmetric and antisymmetric inversion states, respectively.

Four rotational transitions were measured and assigned for the $^{20}Ne_3$-NDH_2 isotopomer. The transition frequencies for the two inversion tunnelling components of the ground internal rotor state are given in Table A6.10. The inversion tunnelling components are split by 475 kHz for the lowest transition, $J_K = 1_0$-0_0, allowing complete spectral separation of the ^{14}N nuclear quadrupole hyperfine patterns of the two inversion states. As in the $^{20}Ne_3$-ND_2H isotopomer, the lower frequency components were assigned to the symmetric inversion state based on the predicted intensities. The transitions were fit as described for $^{20}Ne_3$-NH_3 and the spectroscopic constants are listed in Table 5.5.

e) $^{20}Ne_2{}^{22}Ne$-NH_3 and $^{20}Ne_2{}^{22}Ne$-$^{15}NH_3$

The three hydrogen nuclei and two ^{20}Ne nuclei in $^{20}Ne_2{}^{22}Ne$-NH_3 can be labelled (A, B, C) and (1, 2), respectively and permuted to create 24 distinct versions of the complex. The complete nuclear permutation inversion group is then G_{24} and can be reduced to G_{12} if the tunnelling motion that reverses the handedness of the Ne_3 ring is neglected. The set of permutation elements required to characterize the feasible motions in $^{20}Ne_2{}^{22}Ne$-NH_3 is isomorphic to the set in Table A1.6 for Ar_3-ND_2H with the mapping scheme: (123)→(ABC), (23)*→(AB), (AB)→(12)*. The molecular symmetry analysis is described briefly below and summarized in Table 5.6. The total wavefunction symmetry must be A_2' or A_2'' and the hydrogen nuclear spin function is of $4A_1'\oplus 2E_1'$ symmetry. For the ground internal rotor state, the rovibrational symmetry alternates A_1'/A_1'' for even/odd values of K_c for the symmetric inversion component and A_2'/A_2'' for the antisymmetric inversion component. Thus, all rotational levels in the antisymmetric inversion state have nonzero spin statistical weights and *a*- and *b*-type transitions are expected between these energy levels as shown in the predicted energy level diagram in Figure 5.6. The rotational energy levels of the symmetric inversion state of $^{20}Ne_2{}^{22}Ne$-NH_3 have nuclear spin statistical weight of zero.

In total, 17 rotational transitions were measured for the antisymmetric inversion component of the ground internal rotor state of $^{20}Ne_2{}^{22}Ne$-NH_3 and the transition frequencies are given in Table A6.11. These include 14 *a*-type transitions and three *b*-type transitions. The *b*-type transitions were observed to be much weaker than the *a*-type transitions due to the smaller dipole moment component along the *b*-axis of the tetramer

Table 5.6 Summary of molecular symmetry group theory analysis for the metastable states of the $^{20}Ne_2{}^{22}Ne$-NH_3 and $^{20}Ne^{22}Ne_2$-NH_3 isotopomers.

	$^{20}Ne_2{}^{22}Ne$-NH_3	$^{20}Ne^{22}Ne_2$-NH_3
Molecular symmetry group	G_{12}	G_{12}
Total symmetry required[a]	A_2'/A_2''	A_1/A_3
Nuclear spin symmetry[b]	$4A_1'\oplus 2E'$	$10A_1\oplus A_3\oplus 8E_1$
Rotational symmetry[c]	K_aK_c=ee/eo/oe/oo	
	$A_1'/A_1''/A_1'/A_1''$	$A_1'/A_1''/A_1''/A_1'$
NH_3 inversion symmetry	symmetric/antisymmetric	
	A_1'/A_2'	
NH_3 internal rotation symmetry	ground state/first excited state	
	A_1'/E'	
Rovibrational symmetry[d]	K_aK_c=ee/eo/oe/oo	
$\Sigma 0_{0s}$	$A_1'/A_1''/A_1'/A_1''$	$A_1'/A_1''/A_1''/A_1'$
$\Sigma 0_{0a}$	$A_2'/A_2''/A_2'/A_2''$	$A_1'/A_2''/A_2''/A_1'$
$\Sigma 1_{1s}$	$E'/E''/E'/E''$	$E'/E''/E''/E'$
Predicted nuclear spin statistical weights	$\Sigma 0_{0s}:\Sigma 0_{0a}:\Sigma 1_{1s}$	
	0:4:2	0:4:2

[a] refers to the symmetry of the total wavefunction upon exchange of identical fermions or bosons.
[b] refers to the symmetry of the nuclear spin function of the identical hydrogen or deuterium nuclei only.
[c] depends on whether K_a and K_c are even (e) or odd (o).
[d] includes the NH_3 inversion and NH_3 internal rotation symmetries.

as shown from the geometry in Figure 5.4 b). A comparison of the observed intensities of the lowest energy *a*-type ($J_{K_aK_c} = 1_{01}$-0_{00}) and *b*-type (1_{11}-0_{00}) transitions is shown in Figure 5.7. The ^{14}N nuclear quadrupole hyperfine structure was first fit using a first order program and the resulting χ_{aa} and χ_{bb} constants were held fixed during the rotational fit. The rotational fit was done in Pickett's program using Watson's *I'* S-reduction

Figure 5.6 Predicted energy level diagram for the $^{20}Ne_2{}^{22}Ne$-NH_3 and $^{20}Ne^{22}Ne_2$-NH_3 asymmetric tops. All rotational levels have nonzero spin statistical weights. The solid arrows denote the *a*-type transitions that have been observed for both isotopomers. The dotted arrows correspond to the *b*-type transitions measured for $^{20}Ne_2{}^{22}Ne$-NH_3 and the dashed arrows denote the *c*-type transitions measured for $^{20}Ne^{22}Ne_2$-NH_3.

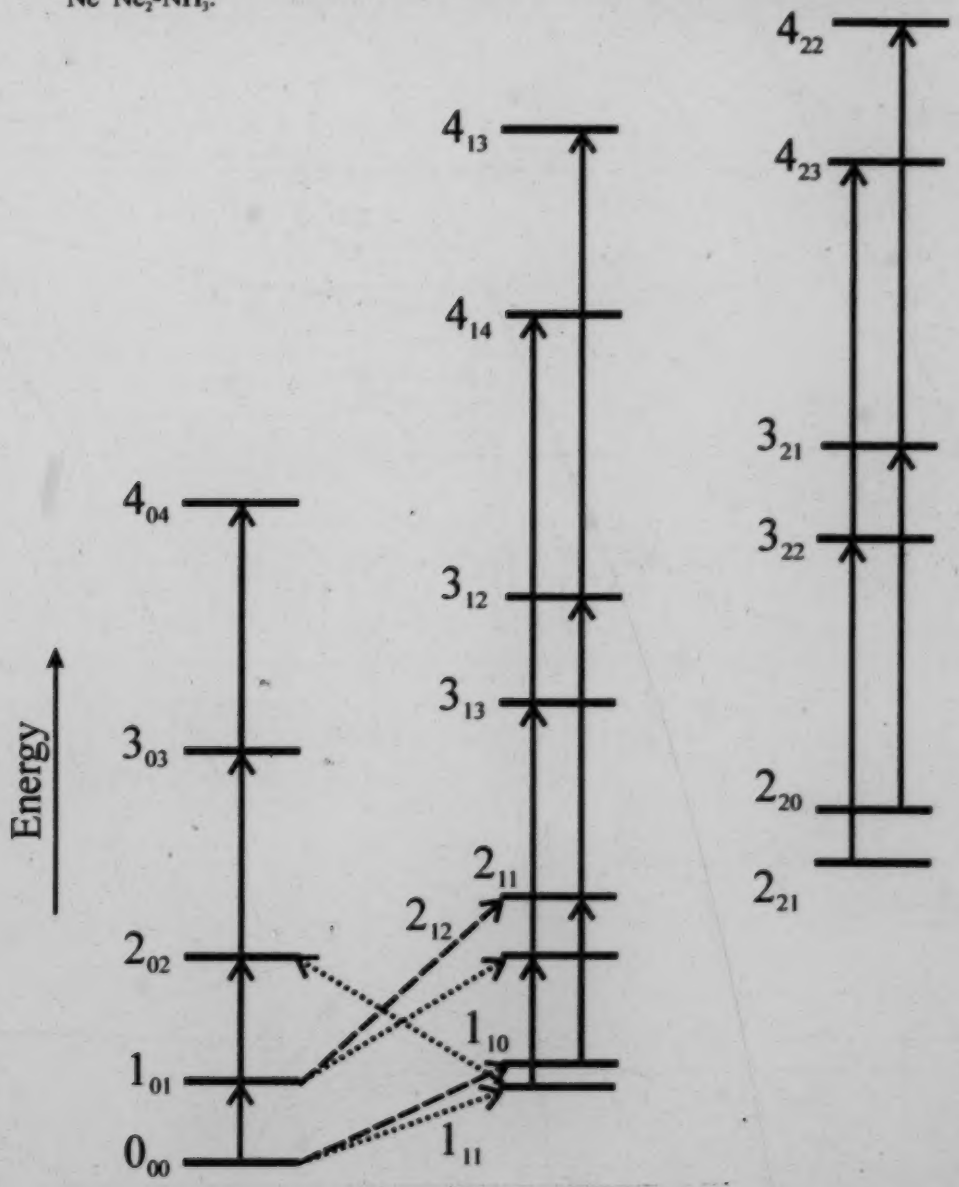

Figure 5.7 Spectra comparing the relative intensities of a) *a*-type and b) *b*-type transitions observed for $^{20}Ne_2{}^{22}Ne$-NH_3. The ^{14}N hyperfine splitting was fit to obtain χ_{aa} = 0.393(7) MHz and χ_{bb} = -0.141(11) MHz.

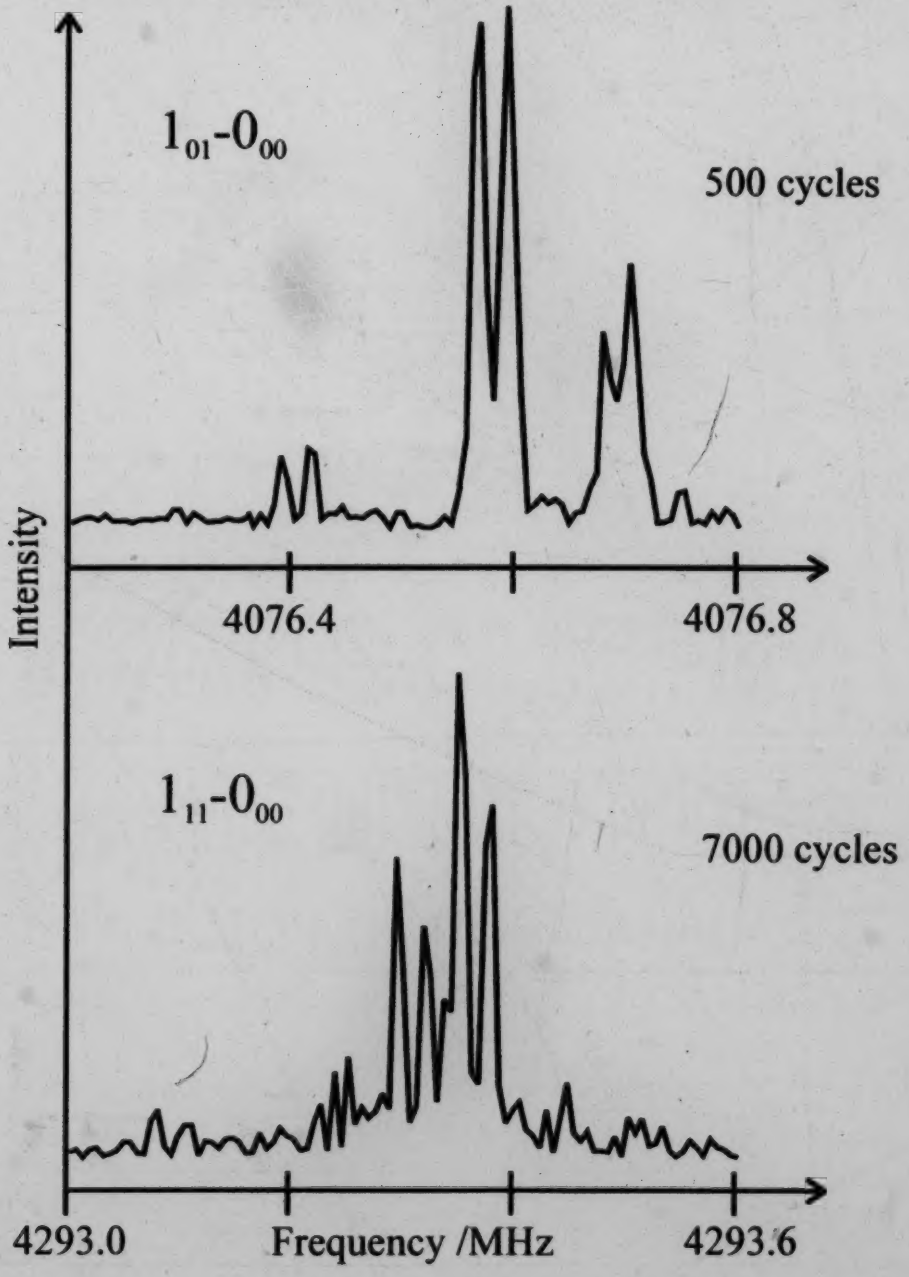

Hamiltonian.[10] The A rotational constant and D_K centrifugal distortion constant were highly correlated in the preliminary fit and as a result, D_K was neglected in the final analysis. The spectroscopic constants determined for $^{20}Ne_2{}^{22}Ne$-NH_3 are listed in Table 5.7.

The corresponding 17 rotational transitions were measured and assigned for the $^{20}Ne_2{}^{22}Ne$-$^{15}NH_3$ isotopomer and the frequencies are listed in Table A6.12. The rotational fit was analogous to that described above for the NH_3 containing species and the resulting spectroscopic constants are given in Table 5.7.

f) $^{20}Ne^{22}Ne_2$-NH_3 and $^{20}Ne^{22}Ne_2$-$^{15}NH_3$

The G_{12} character table (Table A1.6) is also used in the molecular symmetry group analysis of the $^{20}Ne^{22}Ne_2$-NH_3 isotopomer using the same mapping scheme described for $^{20}Ne_2{}^{22}Ne$-NH_3. The results are summarized in Table 5.6. Due to the different orientation

Table 5.7 Spectroscopic constants for $^{20}Ne_2{}^{22}Ne$-NH_3 and $^{20}Ne^{22}Ne_2$-NH_3.

0_{0a}	$^{20}Ne_2{}^{22}Ne$-NH_3	$^{20}Ne_2{}^{22}Ne$-$^{15}NH_3$	$^{20}Ne^{22}Ne_2$-NH_3	$^{20}Ne^{22}Ne_2$-$^{15}NH_3$
Rotational constants /MHz				
A	2281.1446(6)	2280.9266(8)	2213.8723(8)	2213.8077(7)
B	2064.2307(3)	2015.4579(4)	2032.7092(3)	1984.4307(2)
C	2012.6450(3)	1965.9071(3)	1976.2194(3)	1930.7222(2)
Centrifugal distortion constants /kHz				
D_J	69.6(1)	64.8(1)	66.9(1)	62.3(1)
D_{JK}	80.9(1)	84.9(1)	76.0(1)	79.6(1)
d_1	-2.22(1)	-1.96(1)	-1.76(1)	-1.50(1)
d_2	-1.22(1)	-1.02(1)	1.32(1)	1.02(1)
^{14}N quadrupole hyperfine constants /MHz				
χ_{aa}	0.393(7)		0.389(5)	
χ_{bb}	-0.141(11)		-0.113(8)	
Standard deviation /kHz				
σ /kHz	17.4	5.1	10.0	7.8

in the principal inertial axis system in comparison to the $^{20}Ne_2{}^{22}Ne$-NH_3 isotopomer, (Figure 5.4), the rotational symmetries alternate A_1'/A_1'' for even/odd values of K_b. The asymmetric rotor energy levels (K_aK_c) therefore have the following rovibrational symmetries: A_1' (ee, oo)/A_1'' (eo, oe) for the symmetric inversion component and A_2' (ee, oo)/A_2'' (eo, oe) for the antisymmetric inversion component of the ground internal rotor state. All rotational levels in the antisymmetric inversion state have nonzero spin statistical weights and *a*- and *c*-type transitions are expected since there is a nonzero dipole moment contribution along the *a*- and *c*-axes as demonstrated in Figure 5.4 c). The predicted energy level scheme is shown in Figure 5.6. For the symmetric inversion state of $^{20}Ne^{22}Ne_2$-NH_3, no rotational transitions are observable as the energy levels have nuclear spin statistical weights of zero.

Sixteen rotational transitions were assigned to the antisymmetric inversion component of the ground internal rotor state of the $^{20}Ne^{22}Ne_2$-NH_3 complex, including 14 *a*-type and two *c*-type transitions. The transition frequencies are summarized in Table A6.13. The *c*-type transitions are extremely weak and could only be observed after several thousand averaging cycles. This is a combination of the small dipole moment contribution along the *c*-axis of the complex and the low abundance of the $^{20}Ne^{22}Ne_2$-NH_3 species in the molecular beam expansion. The spectroscopic constants were determined following the procedure described for the $^{20}Ne_2{}^{22}Ne$-NH_3 isotopomer and are listed in Table 5.7.

The corresponding rotational transitions for the $^{20}Ne_2{}^{22}Ne$-$^{15}NH_3$ isotopomer are given in Table A6.14. The rotational fit was analogous to that described above for the

$^{20}Ne^{22}Ne_2$-NH_3 containing species and the spectroscopic constants are listed in Table 5.7.

5.4 *Ab initio* calculations for Ne_3-NH_3

Ab initio calculations were done at the CCSD(T) level of theory using the MOLPRO software package.[12] Three separate potential energy surfaces were constructed for the Ne_3-NH_3 tetramer which correspond to three NH_3 umbrella angles: >HNH = 106.67°, >HNH = 113.34°, and >HNH = 120.00°. The N-H bond length was held fixed at the experimental value of 1.01242 Å.[13] The interaction energy of the tetramer was calculated via the supermolecular approach.[14] Preliminary calculations were attempted using the basis sets described in Section 3.4 for the Ne-NH_3 dimer[15,16] augmented with six sets of (3s, 3p, 2d) bond functions. These did not run to completion due to the 16 GB scratch file size limitation of the MOLPRO software package. As a result, the *ab initio* calculations for the Ne_3-NH_3 tetramer had to be done using a smaller Ne basis set, Dunning's aug-cc-pVDZ.[15] To allow comparison with the potential energy surfaces of the dimer and trimer complexes, select regions of the Ne-NH_3 dimer and Ne_2-NH_3 trimer potential energy surfaces were re-calculated using the smaller Ne basis set.

The interaction energy was determined as a function of θ, ϕ, and R (Figure 5.8) for each of the three NH_3 monomer geometries. To reduce the dimension of the calculations, the C_3 axis of NH_3 was constrained to lie in the *ac*-plane. This particular position of the C_3 axis was chosen since the NH_3 substituent is then symmetrically oriented about the *ac*-plane for all θ values when $\phi = 0°$ or $\phi = 60°$. This allows the investigation of the NH_3 inversion motion in a symmetric environment when the C_3 axis

Figure 5.8 Coordinate system of Ne_3-NH_3 used for the *ab initio* calculations. R is the distance between the center of mass of the Ne_3 ring and the nitrogen atom. All of the calculations were done by restricting the C_3 axis of NH_3 to orientations lying in the *ac*-plane. The angle θ denotes the angle between the C_3 axis of NH_3 and R. When $\theta = 0°$, the C_3 axis of NH_3 is aligned with R and the hydrogen atoms point toward the Ne_3 ring. The angle ϕ describes the orientation of NH_3 upon rotation about its C_3 axis. When $\theta = 90°$, $\phi = 0°$ corresponds to the orientation in which the C_3 axis of NH_3 is perpendicular to R and one hydrogen atom is pointed toward the Ne_3 ring. When $\theta = 90°$ and $\phi = 60°$, two hydrogen atoms point towards the Ne_3 ring.

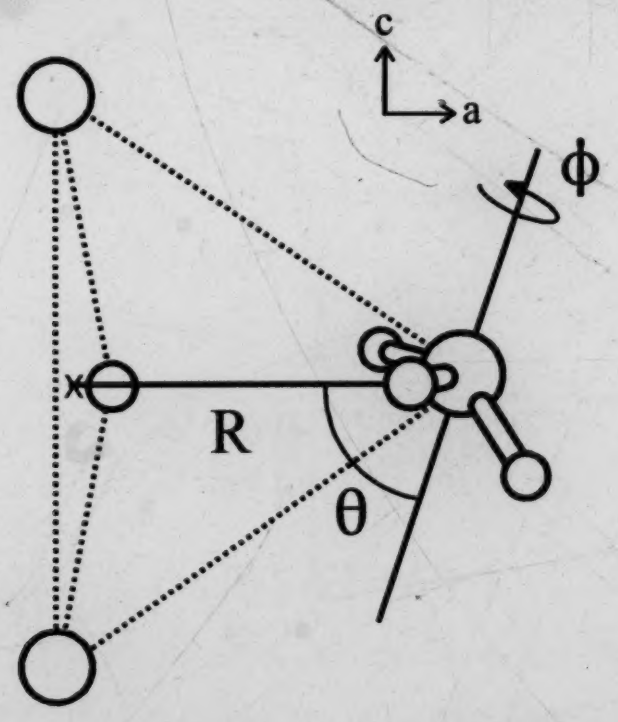

of NH_3 is perpendicular to R. As described in Section 4.4, the Ne-Ne van der Waals bond length[8] was fixed at 3.29 Å to further reduce the degrees of freedom to a computationally manageable level. The angle θ was varied between 0° and 180° in increments of 30° for two different values of ϕ, 0° and 60°. For each value of θ, the distance R was varied in

steps of 0.1 Å until the minimum energy was located. Steps of 0.05 Å were then taken to each side of this minimum to reduce the uncertainty in the radial coordinate. An additional angle, $\theta = 105°$, was included to further narrow the position of the potential energy surface minimum. The *ab initio* results for the Ne_3-NH_3 complex are summarized in Appendix 7 (Tables A7.1, A7.2, and A7.3) for the three NH_3 monomer geometries. The new points calculated for Ne-NH_3 and Ne_2-NH_3 using the smaller Ne basis set are included in Appendices 3 (Tables A3.10, A3.11, A3.12) and 5 (Tables A5.7, A5.8, A5.9), with the previously discussed *ab initio* results of the dimer and trimer, respectively.

5.5 Discussion

5.5.1 Spectroscopic constants and derived molecular parameters

The observed microwave spectra of the Ar_3-NH_3, $^{20}Ne_3$-NH_3, and $^{22}Ne_3$-NH_3 tetramers are those of symmetric tops. For Ar_3-NH_3, only the $K = 3n$ ($n = 0, 1, 2$) energy levels are present and the negative sign determined for D_{JK} is consistent with an oblate symmetric top structure. The absence of other K transitions points to a structure in which the three Ar atoms are symmetrically arranged in a triangle about the C_3 axis of the tetramer as reported for the Ar_3-HX and Ar_3-H_2X species. For the symmetric top Ne_3-NH_3 isotopomers, only the $K = 0$ transitions were found. Since the complex is expected to be a prolate symmetric top, the $K = 3$ progression is higher in energy than the $K = 0$ progression and the energy levels were most likely too sparsely populated due to thermal relaxation for transitions to be measured.

The presence of ^{14}N nuclear quadrupole hyperfine structure helped with the

assignment of rotational transitions, particularly for the two asymmetric tops, $^{20}Ne_2{}^{22}Ne$-NH_3 and $^{20}Ne^{22}Ne_2$-NH_3. Since the spectra of the various isotopomers of Ar_3-NH_3 and Ne_3-NH_3 support a model in which the NH_3 undergoes large amplitude internal motions, the ^{14}N nuclear quadrupole coupling constants should be viewed as highly averaged over these motions. Following the analysis of the Rg-NH_3 dimers and Rg_2-NH_3 trimers, the following equation defines the relationship between ^{14}N nuclear quadrupole coupling constant and the orientation and dynamics of the NH_3 subunit in Ar_3-NH_3: $\chi_{cc} = \frac{1}{2}\chi_o(NH_3)\langle 3\cos^2\theta - 1\rangle$ where χ_o is the quadrupole coupling constant of free NH_3 (-4.0898 MHz), θ is the angle between the C_3 axis of NH_3 and the C_3 axis of the tetramer, and the brackets indicate averaging over the large amplitude motions of the tetramer. For Ne_3-NH_3, the χ_{aa} value is used in the above equation. The Legendre factor, $P_2\langle\cos\theta\rangle = \frac{1}{2}\langle 3\cos^2\theta - 1\rangle$, is zero in the limit of free internal rotation of NH_3. The results for θ and $P_2\langle\cos\theta\rangle$ are given in Table 5.8 for the symmetric top isotopomers containing Ar_3 and $^{20}Ne_3$. As seen in the dimers and trimers, the Legendre factor increases for the heavier, deuterated isotopomers due to the larger tunnelling masses and lower zero point energies. The Legendre factors of the Rg-NH_3 and Rg_2-NH_3 complexes are included in Table 5.8 for comparison. Surprisingly, the values for the Ar_3 containing isotopomers are smaller than those for the Ne_3 containing isotopomers. This is the reverse of the trend observed in the dimers and trimers for which the Ne analogues have smaller $P_2\langle\cos\theta\rangle$ values as expected for the more weakly bound complexes. In the Ne containing clusters, the Legendre factors increase in moving from the dimer to the trimer and then again to the tetramer suggesting that the internal rotation of NH_3 in the θ coordinate becomes

Table 5.8 Estimated orientation of ammonia in the Ar_3-NH_3 and Ne_3-NH_3 complexes.

$\Sigma 0_{0a}/\Sigma 0_{00a}$		-NH_3	-NDH_2	-ND_2H	-ND_3
tetramers					
Ar_3	θ	56.2°/123.8°	56.9°/123.1°	57.6°/122.4°	58.0°/122.0°
	$\langle P_2(\cos\theta)\rangle$	-0.036	-0.053	-0.070	-0.079
$^{20}Ne_3$	θ	58.8°/121.2°	60.2°/120.0°	61.4°/118.6°	62.0°/118.0°
	$\langle P_2(\cos\theta)\rangle$	-0.096	-0.125	-0.156	-0.170
trimers					
Ar_2	$\langle P_2(\cos\theta)\rangle$	-0.190	-0.211	-0.230	-0.253
$^{20}Ne_2$	$\langle P_2(\cos\theta)\rangle$	-0.082	-0.107	-0.129	-0.156
dimers					
Kr	$\langle P_2(\cos\theta)\rangle$	-0.061	-0.085	-0.104	-0.126
Ar	$\langle P_2(\cos\theta)\rangle$	-0.086	-0.115	-0.141	-0.166
Ne	$\langle P_2(\cos\theta)\rangle$	-0.066	-0.086	-0.105	-0.128

successively more hindered when solvated by additional Ne atoms. The same effect occurs between the Ar-NH_3 dimer and Ar_2-NH_3 trimer but the Ar_3-NH_3 tetramer has a surprisingly small $P_2\langle\cos\theta\rangle$ value by comparison. This suggests that the barrier to internal rotation of NH_3 in the θ coordinate is comparatively lower in the Ar_3-NH_3 complex. In a physical sense, the NH_3 molecule experiences a more isotropic environment when bound to three Ar atoms instead of one or two. This is supported by the infrared study by Abouaf-Marguin *et al.*[17] in which the authors found that NH_3 undergoes nearly free internal rotation when enclosed in solid Ar matrices. The contradictory observations for the Ar and Ne containing tetramers indicate that the internal motions of NH_3 are still influenced by the size and polarizability of the individual Rg atoms in the tetramer clusters. This will be reflected in the potential energy surfaces of the two quaternary complexes.

With large amplitude motions and only one rotational constant available from the analysis of symmetric top transitions, quantitative structural information cannot be extracted from the rotational spectra alone. Assuming a spherical geometry of NH_3, a rough estimate of the Rg-Rg and Rg-NH_3 bond lengths can be made using the following expression for a symmetric top molecule:[11]

$$I_B = m_{Rg}\, d^2(1 - \cos\alpha) + m_{Rg}\, m_{NH_3}\, d^2\, (1+2\cos\alpha) / (3m_{Rg}+m_{NH_3}),$$

where d is the distance from the Rg atom to the center of mass of NH_3 and α is the Rg-(NH_3)-Rg angle. Using the B rotational constants for the Rg_3-NH_3 and Rg_3-$^{15}NH_3$ isotopomers (where Rg = Ar, ^{20}Ne), a set of two equations is formed for each tetramer which can be solved for d and α. The Rg-Rg bond length can be determined trigonometrically and the results are given in Table 5.9 for Ar_3-NH_3 and Ne_3-NH_3 along with the corresponding van der Waals bond lengths of the Rg-NH_3 dimers and Rg_2-NH_3 trimers. For both the Ar and Ne containing complexes, the Rg-NH_3 bond decreases in length as the size of the cluster increases. The decrease is on the order of 0.022 Å in the Ar containing species between the tetramer and dimer complexes and 0.014 Å for the corresponding Ne species. Another trend is the lengthening of the Rg-Rg bond in the Rg_3-NH_3 tetramers relative to the Rg_2-NH_3 trimers. The Ar-Ar bond lengthens by 0.048 Å and the Ne-Ne bond lengthens by 0.128 Å. Similar trends are observed in the van der Waals bond lengths of the $Ar_{1,2,3}$-H_2O, $Ar_{1,2,3}$-Ne, and $Ne_{1,2,3}$-Ar complexes which are provided in Table 5.9 for comparison. These small variations in the van der Waals bond lengths as a function of the Rg cluster size indicate that the nonadditive contributions to the interaction energies of these systems are not negligible.

Table 5.9 Comparison the of bond lengths (Å) for various van der Waals dimers, trimers, and tetramers.

	R(Ar-X)	r(Ar-Ar)		R(Ne-X)	r(Ne-Ne)
Ar_3-NH_3	3.814	3.866	Ne_3-NH_3	3.681	3.388
Ar_2-NH_3	3.835	3.818	Ne_2-NH_3	3.695	3.260
Ar-NH_3	3.8359	n/a	Ne-NH_3	3.723	n/a
Ar_3-H_2O[a]	3.675	3.848			
Ar_2-H_2O[b]	3.867	3.822			
Ar-H_2O[c]	3.691	n/a			
Ar_3-Ne[d]	3.610	3.826	Ne_3-Ar[d]	3.601	3.280
Ar_2-Ne[d]	3.595	3.818	Ne_2-Ar[d]	3.605	3.282
Ar-Ne[e]	3.607	n/a	Ne-Ar[e]	3.607	n/a

[a] Reference 5.
[b] E. Arunan, C. E. Dykstra, T. Emilsson, and H. S. Gutowsky, *J. Chem. Phys.* **105**, 495 (1996).
[c] G. T. Fraser, A. S. Pine, R. D. Suenram, and K. Matsumura, *J. Molec. Spectrosc.* **144**, 97 (1990).
[d] Reference 8.
[e] J. -U. Grabow, A. S. Pine, G. T. Fraser, F. J. Lovas, T. Emilsson, E. Arunan, and H. S. Gutowsky, *J. Chem. Phys.* **102**, 1181 (1995).

5.5.2 Inversion tunnelling

For each of the deuterium containing isotopomers, a tunnelling splitting due to the inversion of the ammonia subunit within the complex was observed. The differences in the B rotational constants, $B_{antisymmetric} - B_{symmetric}$, of the two inversion states of the Ar_3-ND_3, Ar_3-ND_2H, and Ar_3-NDH_2 isotopomers are: -18.0 kHz, 10.7 kHz, and 100.2 kHz, respectively. For the $^{20}Ne_3$ analogues, the differences in B are: -4.7 kHz, 61.1 kHz, and 236.7 kHz, respectively. As in the deuterated isotopomers of the Rg-NH_3 and Rg_2-NH_3 complexes, the small differences in rotational constants indicate that the two inversion states lie close in energy. This is further substantiated by the similarity in the observed ^{14}N nuclear quadrupole coupling constants. These differ by only a few kHz for the two

inversion components of the Rg_3-ND_2H and Rg_3-NDH_2 complexes.

The inversion tunnelling splittings in the Ar and Ne containing tetramers increase with successive hydrogen substitution as reported previously for the dimer and trimer cofnplexes. This is consistent with the trend observed for the energy level separations in the monomers: 1.6 GHz, 5 GHz, and 12 GHz for free ND_3, ND_2H, and NDH_2, respectively.[18] In Ar_3-ND_3 and Ne_3-ND_3, the symmetric inversion component is found at higher frequency than the antisymmetric component. The same phenomenon was observed in Ar-ND_3, Kr-ND_3, and Ar_2-ND_3 and is the reverse of the assignment in all of the other isotopomers studied. These subtle deviations are a reflection of the sensitive relationship between the intermolecular potential energy surface of each cluster and the complicated internal dynamics of the NH_3 subunit. For each isotopomer of each Rg_n-NH_3 complex, the bound state energy levels vary. This leads to marked differences in the dynamics of each system by way of: i) the degree of the mixing of internal rotor states, ii) the tunnelling probabilities and iii) the barriers to internal motions. These variations are apparent in the rotational spectrum of each species. Although a complete understanding of the inversion dynamics of NH_3 cannot be extracted from the rotational spectra alone, microwave spectroscopy provides information that is essential for the construction of accurate empirical potentials that include this motion. This is because the high resolution of the FTMW technique allows the measurement of the extremely small inversion tunnelling splittings that are characteristic of the deuterated Rg_n-NH_3 complexes.

The inversion tunnelling splittings observed in the deuterated Rg_3-NH_3 tetramers are compared with those of the Rg-NH_3 dimers and Rg_2-NH_3 trimers in Table 5.10. With

the exception of Ar_3-ND_3, the inversion tunnelling splitting decreases as additional Rg atoms are added to the cluster. This appears to indicate that the NH_3 inversion motion becomes more hindered in the larger clusters. As discussed in Section 4.5.2, this observation can be misleading since the masses of the clusters have not been considered when comparing the differences in the rotational constants. Furthermore, it must be stressed that the observed inversion tunnelling splittings are only secondary indications of the energy differences between the symmetric and antisymmetric states and not direct measures of the inversion splittings. The observation of both inversion components is telling in itself since it confirms that the NH_3 inversion motion is not quenched when bound to three Rg atoms. This suggests that the C_3 axis of NH_3 lies, on average, perpendicular to the C_3 axis of the Rg_3 ring since the inversion motion would be quenched if the environment along the inversion coordinate was asymmetric. In fact, from an infrared study of NH_3 and its deuterated isotopomers embedded in Rg matrices, the

Table 5.10 Comparison of the inversion tunnelling splittings (kHz) for the RG-NH_3, RG_2-NH_3, and RG_3-NH_3 complexes.

	-ND_3	-ND_2H	-NDH_2
Ar_3[a]	-36.0	21.4	200.4
Ar_2[b]	-165.1	36.1	712.0
Ar[a]	-63.0	271.6	1101.0
$^{20}Ne_3$[a]	-9.4	122.2	473.4
$^{20}Ne_2$[d]	19.9	298.1	906.2
Ne[a]	55.0	407.6	1082.2
Kr[a]	-85.6	208.4	1038.4

[a] $2(B_{antisymmetric} - B_{symmetric})$
[b] $(A+C)_{antisymmetric} - (A+C)_{symmetric}$
[c] $(B+C)_{antisymmetric} - (B+C$

inversion barrier was predicted to increase by only 10 % in comparison to the free monomer.[17]

5.5.3 *Ab initio* potential energy surfaces of Ne_3-NH_3

The potential energy surface minimum calculated for the Ne_3-NH_3 tetramer is -225.4 cm^{-1} for the experimental equilibrium geometry of NH_3 (<HNH = 106.67°) at the CCSD(T) level of theory. The structural coordinates at this minimum energy are: R = 2.95 Å, θ = 105°, and ϕ = 0° which corresponds to a tetramer structure in which the C_3 axis of NH_3 is nearly parallel to the plane containing the three Ne atoms (Figure 5.8). The R separation (2.95 Å) corresponds to a Ne-NH_3 bond length of 3.51 Å in the tetramer complex. This is the same bond length calculated for the Ne_2-NH_3 trimer and is slightly shorter than that estimated from the B rotational constant of the Ne_3-NH_3 tetramer (3.68 Å). The ϕ orientation of NH_3 at the potential energy surface minimum is such that one hydrogen atom is pointed towards the Ne_3 ring. The same relative orientation of NH_3 was found for the two surfaces corresponding to the other umbrella angles of NH_3 with minima of -220.4 cm^{-1} (<HNH = 113.34°) and -213.8 cm^{-1} (<HNH = 120.00°) at R = 3.05 Å. For internal rotation in the θ coordinate, there are barriers at θ = 0° and θ = 180° for the two nonplanar geometries of NH_3. The barriers are 46.6 cm^{-1}/22.3 cm^{-1}(0°/180°) and 48.6 cm^{-1}/27.9 cm^{-1} for the <HNH = 106.67° and <HNH = 113.34° NH_3 geometries, respectively. For the planar geometry of NH_3, the barrier is 39.8 cm^{-1} through θ = 0° and θ = 180° due to symmetry.

The topologies of the Ne_3-NH_3 potential energy surfaces can be compared with

those of the Ne-NH_3 dimer and Ne_2-NH_3 trimer calculated at the CCSD(T) level of theory using the aug-cc-pVDZ basis set for Ne. The minimum energies for the dimer and trimer complexes using the aug-cc-pVDZ basis set are 60.1 cm^{-1} and 127.9 cm^{-1}, respectively for the equilibrium NH_3 monomer geometry. The minimum energy paths from $\theta = 0°$ to $\theta = 180°$ are compared for the Ne-NH_3, Ne_2-NH_3, and Ne_3-NH_3 complexes in Figure 5.9 and the structures near the potential minima are shown for each cluster. The C_3 axis of NH_3 is nearly perpendicular to the axis joining the nitrogen atom and the center of mass of the

Figure 5.9 Comparison of the minimum energy [CCSD(T)] paths of the Ne-NH_3 dimer (- - ▲- -), the Ne_2-NH_3 (—●—) trimer, and the Ne_3-NH_3 (– –■– –) tetramer as a function of the θ coordinate for <HNH = 106.67°. The dimer and trimer minimum energy paths correspond to the $\phi = 60°$ orientation while the tetramer path corresponds to $\phi = 0°$. The global minimum of each curve was set to 0.0 μE_h and the other energies along the minimum energy paths were adjusted accordingly.

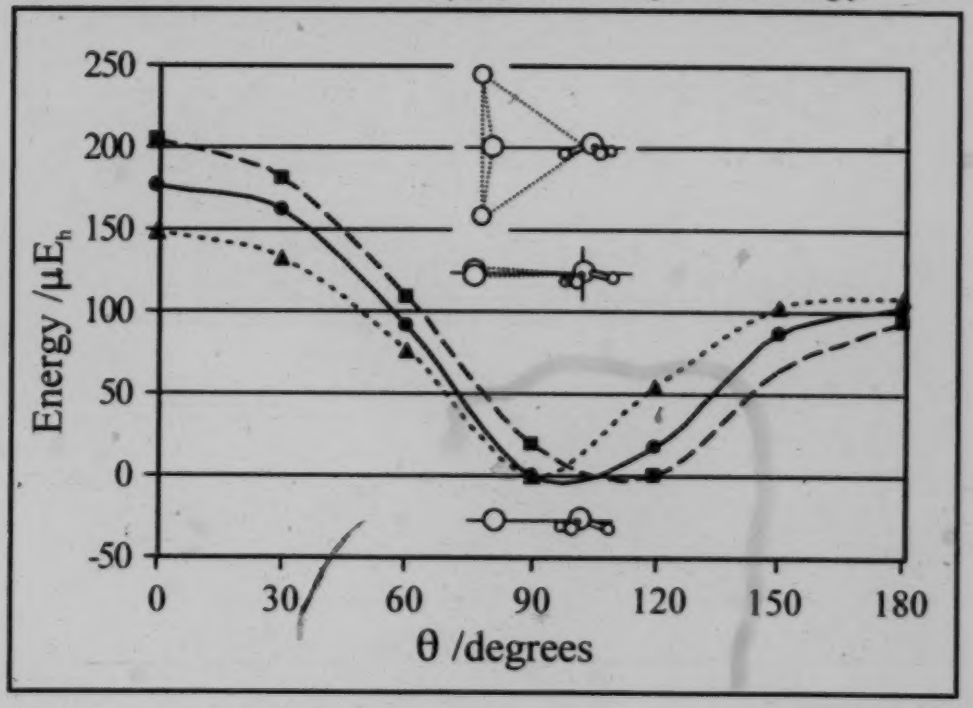

Ne_n (n = 1, 2, 3) moiety. For the Ne_3-NH_3 tetramer, the NH_3 subunit is rotated by 60° about its C_3 axis (ϕ = 0°) relative to the dimer and trimer to minimize the repulsion between the hydrogen atoms and the Ne_3 ring. For rotation through the ϕ = 60° orientation of the tetramer, the barrier is 14 cm^{-1} for the potential energy surface corresponding to <HNH = 106.67°. The barrier for internal rotation of NH_3 through θ = 0° increases as more Ne atoms are added to the complex. For example, the barriers in the dimer, trimer, and tetramer are: 32.5 cm^{-1}, 38.6 cm^{-1}, and 45.0 cm^{-1}, respectively for the equilibrium NH_3 monomer geometry. For rotation through θ = 180°, the barriers are similar in each cluster: 23.8 cm^{-1}, 22.5 cm^{-1}, and 20.7 cm^{-1} for Ne-NH_3, Ne_2-NH_3, and Ne_3-NH_3, respectively. The minimum energy path requires 0.4 Å of radial variation in the tetramer, 0.3 Å in the trimer, and 0.5 Å in the dimer. A comparison of the anisotropies of the potential energy curves as a function of the θ coordinate (Figure 5.9) demonstrates that the angular dependency of the NH_3 orientation is unique in each of the complexes. The potential well becomes broader and deeper with the addition of Ne atoms and the minimum shifts to larger θ values. This corresponds to structures in which the C_3 axis of NH_3 is tilted so that the hydrogen atoms are farther away from the Ne atoms. As discussed in Section 4.5.3, the broadening of the potential well as successive Ne atoms are added leads to lower zero point energies for the larger clusters. As a result, the tunnelling probability decreases as the size of the van der Waals cluster increases. This effect, combined with the larger barriers to internal rotation through θ = 0° for the trimer and tetramer complexes, suggests that motion in the θ coordinate becomes comparatively more hindered with successive Ne atom solvation. This is experimentally supported by

the determination of increasing χ_{aa} values in moving from Ne-NH_3 to Ne_2-NH_3 to Ne_3-NH_3.

The minimum energy paths calculated for the Ne_3-NH_3 tetramer from $\theta = 0°$ to $\theta = 180°$ are compared for the three different NH_3 internal geometries in Figure 5.10 at $\phi = 0°$. As reported previously for the dimer and trimer complexes, the interaction energies are the most similar between $\theta = 60°$ and $\theta = 90°$. This indicates that the internal geometry of NH_3 has little influence at these orientations and is in accord with the experimental

Figure 5.10 Comparison of the minimum energy [CCSD(T)] paths of Ne_3-NH_3 as a function of the θ coordinate for $\phi = 0°$ with the C_3 axis of NH_3 lying in the *ac*-plane of the tetramer. Each curve represents a different umbrella angle of NH_3: <HNH = 106.67° (—●—), <HNH = 113.34° (– –■– –), and <HNH = 120.00° (- - ▲- -).

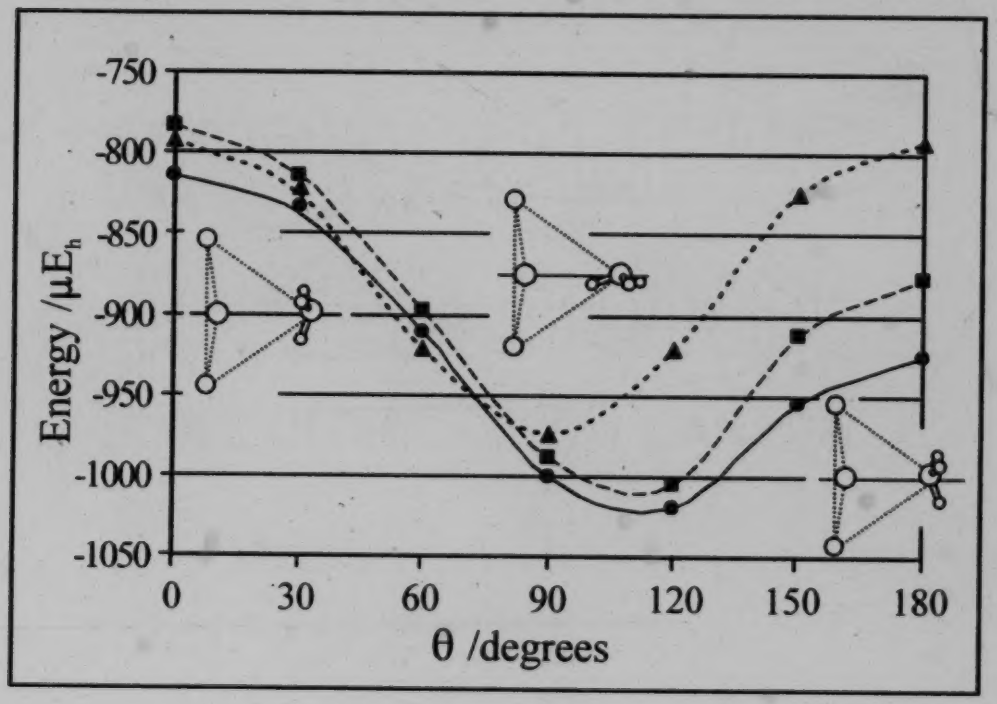

observation that the NH_3 inversion is barely affected if the motion occurs along a symmetric coordinate.[19] Thus, the experimental observation of two inversion tunnelling components in the microwave spectra of the deuterated isotopomers of Ne_3-NH_3 is consistent with the assignment to a Σ state, such as the ground internal rotor state of the tetramer complexes. The largest discrepancies between the minimum energy paths are at θ values approaching 180° when the C_3 axis of NH_3 is nearly aligned with the symmetry axis of the tetramer and the hydrogen atoms are pointed away from the Ne_3 ring. This orientation of NH_3 corresponds to a Π internal rotor state of the complex and the inversion tunnelling motion is expected to be quenched for such a geometry.[20]

A comparison of the *ab initio* results for the Ne-NH_3 dimer (Tables A3.7 - A3.12) at the CCSD(T) level reveals that the use of the larger basis set (aug-cc-pVTZ) for Ne lowers the dimer interaction energies by 1 cm^{-1} to 3 cm^{-1} relative to the same geometries calculated using the aug-cc-pVDZ basis set. This affects the topologies of the calculated potential energy surfaces. For example, the use of the larger Ne basis set increases the barriers for the internal rotation of NH_3. The barriers are 0.4 cm^{-1} and 2.2 cm^{-1} higher for rotation through $\theta = 0°$ and $\theta = 180°$, respectively for the potential energy surface corresponding to the equilibrium geometry of NH_3. The discrepancies are larger for the Ne_2-NH_3 trimer (Tables A5.1 - A5.3, A5.7 - A5.9). The interaction energies are 2 cm^{-1} to 7 cm^{-1} lower using the larger Ne basis set and the barriers through $\theta = 0°$ and $\theta = 180°$ are increased by 1.0 cm^{-1} and 7.3 cm^{-1}, respectively. Since the *ab initio* potential energy surfaces of the Ne_3-NH_3 tetramer could not be calculated using the larger Ne basis set, the interaction energies should be regarded with caution. While the predicted trends seem to

be qualitatively consistent with the experimental observations and with the *ab initio* results of the dimer and trimer complexes, the topologies of the tetramer potential energy surfaces cannot be accurately determined if the basis set used did not sufficiently describe the polarizability of the Ne atom. This is a particular problem for primarily dispersion bound complexes, such as Ne_3-NH_3 because the dispersion contributions to the interaction energies are not well-recovered using basis sets with limited diffuse and polarization functions. The aug-cc-pVDZ basis set, for example, does not include any orbitals of *f* symmetry on the Ne atom. For the Ar-Ar and Ar-HCl dimers, MP4 level *ab initio* calculations that neglected *f* orbitals recovered only 50 % - 60 % of the interaction energy. With the addition of *f* functions, 80 % of the interaction energy was recovered.[21] The situation may not be as extreme in Ne_3-NH_3 since the Ne atom is smaller and less polarizable than Ar and the neglect of higher order polarization functions such as *f* orbitals is partially counteracted by the addition of bond functions which improve the saturation of the dispersion term.[22]

5.6 Concluding remarks

Microwave rotational spectra corresponding to the ground internal rotor state of two Rg_3-NH_3 van der Waals tetramers were reported for the first time. The spectra observed for the Ar_3-NH_3, $^{20}Ne_3$-NH_3, and $^{22}Ne_3$-NH_3 complexes are consistent with symmetric top structures. The two mixed Ne isotopomers, $^{20}Ne_2{}^{22}Ne$-NH_3 and $^{20}Ne^{22}Ne_2$-NH_3, are asymmetric tops. The rotational constants of the various isotopomers were used to estimate the van der Waals bond lengths in the tetramers. Comparison of these with the

bond lengths derived from the rotational spectra of the dimer and trimer complexes provides evidence of the importance of nonadditive effects in the Rg_2-NH_3 and Rg_3-NH_3 clusters. The small values of the ^{14}N nuclear quadrupole coupling constants, in comparison to other NH_3 containing van der Waals complexes, reveal that the NH_3 moiety continues to undergo large amplitude motions in the θ coordinate (Figure 5.8) when bound to three Rg atoms. Through comparison of the χ_{aa} values determined for the Ne_n-NH_3 (n = 1, 2, 3) complexes, the internal rotation appears to become more hindered as the number of Ne atoms increases. This is consistent with the topologies of the *ab initio* potential energy surfaces of the Ne containing complexes. With successive Ne atom addition, the potential well becomes broader and deeper. In contrast, for Ar_3-NH_3, the ^{14}N nuclear quadrupole coupling constants are surprisingly small compared to those of the dimer and trimer complexes which suggests that motion in the θ coordinate is less hindered in the tetramer complex. This indicates that the identities of the Rg atom substituents have a critical effect on the anisotropies of the potential energy surfaces of quaternary van der Waals complexes. The observation of two inversion tunnelling states for the deuterated isotopomers of Ar_3-NH_3 and Ne_3-NH_3 supports minimum energy structures in which the C_3 axis of NH_3 is parallel to the plane of the Rg_3 ring. Furthermore, for the inversion to occur in a symmetric environment, the C_3 axis of NH_3 must lie in the *ac*-plane of the tetramers. This is supported by the *ab initio* potential energy surfaces of Ne_3-NH_3 which show little dependence on the NH_3 monomer geometry at this orientation. Comparison of the inversion tunnelling splittings in the deuterated Rg_n-NH_3 (n = 1, 2, 3) species provides evidence of subtle differences in the inversion

dynamics of NH_3 as a function of the Rg cluster environment. Since the observed spectra are sensitive reflections of the topologies of the potential energy surfaces, the precise measurement of the small inversion tunnelling splittings is crucial to the development of accurate intermolecular interaction potentials that include intramolecular modes such as NH_3 inversion.

References

1. H. S. Gutowsky, T. D. Klots, C. Chuang, J. D. Keen, C. A. Schmuttenmaer, and T. Emilsson, *J. Am. Chem. Soc.* **107**, 7174 (1985).

2. T. D. Klots and H. S. Gutowsky, *J. Am. Chem. Soc.* **109**, 5633 (1987).

3. T. D. Klots, R. S. Ruoff, C. Chuang, T. Emilsson, and H. S. Gutowsky, *J. Chem. Phys.* **87**, 4383 (1987).

4. H. S. Gutowsky, E. Arunan, T. Emilsson, S. L. Tschopp, and C. E. Dykstra, *J. Chem. Phys.* **103**, 3917 (1995).

5. E. Arunan, T. Emilsson, H. S. Gutowsky, and C. E. Dykstra, *J. Chem. Phys.* **114**, 1242 (2001).

6. P. R. Bunker and P. Jensen, *Molecular Symmetry and Spectroscopy*, 2nd edition, NRC Press, Ottawa (1998).

7. D. D. Nelson Jr., G. T. Fraser, K. I. Peterson, K. Zhao, W. Klemperer, F. J. Lovas, and R. D. Suenram, *J. Chem. Phys.* **85**, 5512 (1986).

8. Y. Xu and W. Jäger, *J. Chem. Phys.* **107**, 4788 (1997).

9. J. -U. Grabow, A. S. Pine, G. T. Fraser, F. J. Lovas, R. D. Suenram, T. Emilsson, E. Arunan, and H. S. Gutowsky, *J. Chem. Phys.* **102**, 1181 (1995).

10. H. M. Pickett, *J. Molec. Spectrosc.* **148**, 371 (1991).

11. C. H. Townes and A. L. Schawlow, *Microwave Spectroscopy*, Dover, New York (1975).

12. *MOLPRO* (Version 2000.1), written by H. -J. Werner and P. R. Knowles, with contributions from R. D. Amos, A. Bernhardsson, A. Berning, P. Celani, D. L. Cooper, M. J. O. McNicholas, F. R. Manby, W. Meyer, M. E. Mura, A. Nicklass, P. Palmieri, R. Pitzer, G. Rauhut, M. Schütz, H. Stoll, A. J. Stone, R. Tarroni, and T. Thorsteinsson, University of Birmingham, UK, 1999.

13. W. S. Benedict and E. K. Plyler, *Can. J. Phys.* **35**, 1235 (1957).

14. S. F. Boys and F. Bernardi, *Mol. Phys.* **19**, 553 (1970).

15. T. H. Dunning Jr., *J. Chem. Phys.* **90**, 1007 (1989).

16. A. J. Sadlej, *Collec. Czech. Chem. Commun.* **53**, 1995 (1988).

17. L. Abouaf-Marguin, M. E. Jacox, and D. E. Milligan, *J. Molec. Spectrosc.* **67**, 24 (1977).

18. M. T. Weiss and M. W. P. Strandberg, *Phys. Rev.* **83**, 322 (1981).

19. E. Zwart, H. Linnartz, W. L. Meerts, G. T. Fraser, D. D. Nelson Jr., and W. Klemperer, *J. Chem. Phys.* **95**, 793 (1991).

20. C. A. Schmuttenmaer, R. C. Cohen, and R. J. Saykally, *J. Chem. Phys.* **101**, 146 (1994).

21. G. Chałasiński and M. M. Szczęśniak, *Chem. Rev.* **94**, 1723 (1994).

22. G. Chałasiński and M. M. Szczęśniak, *Chem. Rev.* **100**, 4227 (2000).

CHAPTER 6

General Conclusions

High resolution microwave spectra of the Rg_n-NH_3 (n = 1, 2, 3) series provide information about the internal dynamics of NH_3 as it is increasingly solvated by Rg atoms. Since NH_3 has been studied in solid Rg matrices,[1] the Rg_n-NH_3 van der Waals complexes, in a sense, bridge the gap between isolated systems and condensed phases. An important part of understanding weak interactions on the microscopic level involves the accurate characterization of the nonadditive contributions to the intermolecular interaction energies as a function of the properties of the molecular substituents. Before now, spectroscopic studies of nonadditive effects have focused on the simplest van der Waals systems such as Rg clusters, and the Rg_n-HX type complexes. Recent spectroscopic studies of the Ar_2-H_2X (X = O)[2,3] and Ar_3-H_2X (X = O, S)[4] complexes demonstrate the desire to understand the nature of nonadditive contributions in more complicated systems. The extension to the Rg_n-NH_3 complexes described in this work provides a further challenge due to the soft NH_3 inversion coordinate.

In this work, rotational spectra of the van der Waals complexes consisting of one ammonia molecule bound to one, two, or three Rg atoms were measured via FTMW spectroscopy. These include the first spectroscopic studies of the Ne-NH_3 and Kr-NH_3 van der Waals dimers, the Rg_2-NH_3 trimers, and the Rg_3-NH_3 tetramers. The Ar-NH_3 dimer was the subject of a number of previous investigations, however, the current work describes the first high resolution spectroscopic study of the deuterated isotopomers.

Since one inversion component is missing for the ground state of the Rg-NH_3 complexes, the spectra of Ar-ND_3, Ar-ND_2H, and Ar-NDH_2 represent the first measurements of inversion tunnelling splittings in the ground internal rotor state of this prototypical complex.

The spectra of the Rg_n-NH_3 (n = 1, 2, 3) complexes were used to extract information about the structures and dynamics of each system as a function of the Rg atom size and the Rg cluster size. For example, the rotational constants were used to estimate the van der Waals bond lengths for each complex. It was determined that the Rg-NH_3 bond decreases in length as Rg atoms are added to the complex (Table 5.9). In contrast, the Rg-Rg bonds lengthen in the tetramers relative to the trimers. These changes can be regarded as experimental evidence of nonadditive contributions to the interaction energies of the Rg_n-NH_3 (n = 2, 3) systems. Information about the internal dynamics of NH_3 can be extracted from the analysis of the ^{14}N nuclear quadrupole hyperfine structure and from the resolution of the ammonia inversion tunnelling splittings for the deuterated isotopomers. In the Ne containing complexes, the χ_{aa} values get larger as the size of the Ne cluster increases suggesting that the internal rotation of NH_3 in the θ coordinate becomes successively more hindered as it is solvated with additional Ne atoms. This motion in the θ coordinate varies the angle of the C_3 axis of NH_3 with respect to the symmetry axis of the cluster. The same trend is seen between the Ar-NH_3 dimer and Ar_2-NH_3 trimer but the χ_{cc} value of the Ar_3-NH_3 tetramer is surprisingly small by comparison. This apparent discrepancy between the Ne and Ar containing clusters highlights the need to understand the dynamics of these complexes on a deeper level. The inversion

tunnelling splittings (Table 5.10) resolved in the spectra of the ND_3, ND_2H, and NDH_2 containing isotopomers are sensitive to the relative energy difference between the two inversion states of the various complexes. For example, the tunnelling splittings observed for the deuterated Rg_n-NH_3 (n = 1, 2, 3) complexes decrease with successive deuterium substitution. This follows the trend of the decreasing energy differences between the two inversion states in the free monomers: 12 GHz (NDH_2), 5 GHz (ND_2H), and 1.6 GHz (ND_3).[5] Furthermore, the inversion tunnelling splittings decrease as the number of Rg atoms in the complex increases which may be an indication of a more restricted inversion motion. The one exception to this trend is the Ar_n-ND_3 (n = 1, 2, 3) series.

The rotational spectra reported in this work were complemented by the construction of a series of *ab initio* potential energy surfaces for the Ne-NH_3, Ne_2-NH_3, and Ne_3-NH_3 complexes. The *ab initio* calculations appear to capture the main topological features of the potential energy surfaces and are consistent with several experimental observations. For example, the appearance of two inversion tunnelling components in the ground state spectra is indicative of cluster structures in which the C_3 axis of NH_3 is perpendicular to the axis of highest symmetry of the cluster. The geometries corresponding to the potential energy surface minima of Ne-NH_3, Ne_2-NH_3, and Ne_3-NH_3 are consistent with these inversion tunnelling observations. Furthermore, the increasing depth and broadness of the potential well with the addition of Ne atoms is in agreement with the experimentally observed trend that the ^{14}N nuclear quadrupole coupling constants increase in the larger Ne containing clusters.

The current research provides a foundation for further spectroscopic and

theoretical investigations of the Rg_n-NH_3 (n = 1, 2, 3) complexes. In order to construct accurate empirical or semi-empirical potentials, it is first necessary to obtain spectroscopic information that is sensitive to a larger region of the potential energy surface. This requires the measurement of excited van der Waals vibrational modes in the submillimeter and far infrared regions and investigations of excited NH_3 monomer vibrations in the infrared region. Following the development of better interaction potentials, it will be possible to measure the rotational spectra of excited internal rotor states of the Rg_n-NH_3 (n = 1, 2, 3) complexes with as much accuracy and precision as reported in the current work for the ground internal rotor states. Once more spectroscopic information is available, mathematical models for the interactions in the various Rg_n-NH_3 (n = 1, 2, 3) complexes can be derived and tested. The success of these models lies in the accuracy of their characterization of nonadditive contributions and the incorporation of intramolecular degrees of freedom of NH_3.

As demonstrated in this work for the Ne_n-NH_3 (n = 1, 2, 3) complexes, *ab initio* calculations can successfully reproduce the main features of the intermolecular potential energy surfaces of these weakly bound complexes. With rapid advances in computational algorithms and computer hardware, such calculations are becoming feasible for larger molecular systems at higher levels of theory. In order to successfully employ *ab initio* theories to achieve accurate and detailed descriptions of weak interactions, it is necessary to determine how the calculated interaction energies can be partitioned into the individual contributions. Such partitioning is natural to the perturbation approach and individual energy components can be identified using formalisms from symmetry adapted

perturbation theory (SAPT).[6] The partitioning of interaction energies in this manner is crucial because the individual energy contributions have different origins, properties and behaviours and as a result, each term will dominate at different regions of the potential energy surface.[7] The separation of the individual energy contributions will allow the establishment of the connections between the interaction energies of van der Waals complexes and the intrinsic monomer properties, that is the multipole moments and polarizabilities, of the cluster substituents. This affords a more physical interpretation of *ab initio* derived interaction potentials. The accuracies of *ab initio* potential energy surfaces are evaluated by their ability to reproduce spectroscopic observables. In this respect, parallel advances in high resolution spectroscopy and *ab initio* methods can be combined to develop accurate models of intermolecular interactions on the microscopic level.

References

1. L. Abouaf-Marguin, M. E. Jacox, and D. E. Milligan, *J. Molec. Spectrosc.* **67**, 24 (1977).

2. E. Arunan, T. Emilsson, and H. S. Gutowsky, *J. Am. Chem. Soc.* **116**, 8418 (1994).

3. E. Arunan, T. Emilsson, and H. S. Gutowsky, *J. Chem. Phys.* **105**, 8495 (1996).

4. E. Arunan, T. Emilsson, H. S. Gutowsky, and C. E. Dykstra, *J. Chem. Phys.* **114**, 1242 (2001).

5. M. T. Weiss and M. W. P. Strandberg, *Phys. Rev.* **83**, 567 (1951).

6. B. Jeziorski, R. Moszynski, and K. Szalewicz, *Chem. Rev.* **94**, 1887 (1994).

7. G. Chałasiński and M. M. Szczęśniak, *Chem. Rev.* **100**, 4227 (2000).

APPENDIX 1

Molecular symmetry group tables

Table A1.1 The D_{3h} molecular symmetry group.

	E	(123)	(23)	E*	(123)*	(23)*
A_1'	1	1	1	1	1	1
A_1''	1	1	1	-1	-1	-1
A_2'	1	1	-1	1	1	-1
A_2''	1	1	-1	-1	-1	1
E'	2	-1	0	2	-1	0
E''	2	-1	0	-2	1	0

Table A1.2 The C_{2v} molecular symmetry group.

	E	(12)	E*	(12)*
A_1	1	1	1	1
A_2	1	1	-1	-1
B_1	1	-1	-1	1
B_2	1	-1	1	-1

Table A1.3 The G_{24} molecular symmetry group.

	E	(AB)	(123)	(23)	(AB)(123)	(AB)(23)	E*	(AB)*	(123)*	(23)*	(AB)(123)*	(AB)(23)*
A_1	1	1	1	1	1	1	1	1	1	1	1	1
A_2	1	1	1	1	1	1	-1	-1	-1	-1	-1	-1
A_3	1	1	1	-1	1	-1	1	1	1	-1	1	-1
A_4	1	1	1	-1	1	-1	-1	-1	-1	1	-1	1
B_1	1	-1	1	1	1	-1	1	-1	1	1	-1	-1
B_2	1	-1	1	1	1	-1	-1	1	-1	-1	1	1
B_3	1	-1	1	-1	1	1	1	-1	1	-1	-1	1
B_4	1	-1	1	-1	1	1	-1	1	-1	1	1	-1
E_1	2	2	-1	0	1	0	2	2	-1	0	-1	0
E_2	2	2	-1	0	1	0	-2	-2	1	0	1	0
E_3	2	-2	-1	0	1	0	2	-2	-1	0	1	0
E_4	2	-2	-1	0	-1	0	-2	2	1	0	-1	0

Table A1.4 The G_8 molecular symmetry group.

	E	(AB)	(23)	(AB)(23)	E*	(AB)*	(23)*	(AB)(23)*
A_1	1	1	1	1	1	1	1	1
A_2	1	1	1	1	-1	-1	-1	-1
A_3	1	1	-1	-1	1	1	-1	-1
A_4	1	1	-1	-1	-1	-1	1	1
B_1	1	-1	1	-1	1	-1	1	1
B_2	1	-1	1	-1	-1	1	-1	1
B_3	1	-1	-1	1	1	-1	-1	1
B_4	1	-1	-1	1	-1	1	1	-1

Table A1.5 The G_{36} molecular symmetry group.

	E	(ABC)	(AB)*	(123)	(ABC)(123)	(AB)(123)*	(23)	(ABC)(23)	(AB)(23)*
A_1	1	1	1	1	1	1	1	1	1
A_2	1	1	1	1	1	1	-1	-1	-1
A_3	1	1	-1	1	1	-1	1	1	-1
A_4	1	1	-1	1	1	-1	-1	-1	1
E_1	2	2	2	-1	-1	-1	0	0	0
E_2	2	2	-2	-1	-1	1	0	0	0
E_3	2	-1	0	2	-1	0	2	-1	0
E_4	2	-1	0	2	-1	0	-2	1	0
G	4	-2	0	-2	1	0	0	0	0

Table A1.6 The G_{12} molecular symmetry group.

	E	(123)	(23)*	(AB)	(123)(AB)	(23)(AB)*
A_1'	1	1	1	1	1	1
A_1''	1	1	1	-1	-1	-1
A_2'	1	1	-1	1	1	-1
A_2''	1	1	-1	-1	-1	1
E'	2	-1	0	2	-1	0
E''	2	-1	0	-2	1	0

APPENDIX 2

Tables of microwave transition frequencies measured for the Rg-NH_3 dimers

Table A2.1 Measured transition frequencies (MHz) for the $\Sigma 0_{0a}$ state of Kr-NH_3.

		^{86}Kr-NH_3		^{84}Kr-NH_3		^{82}Kr-NH_3		^{80}Kr-NH_3	
J'-J"	F'-F"	$\nu_{obs.}$	$\Delta\nu$[a]	$\nu_{obs.}$	$\Delta\nu$	$\nu_{obs.}$	$\Delta\nu$	$\nu_{obs.}$	$\Delta\nu$
1-0	0-1	4624.1572	-0.5	4642.0480	-0.3	4660.8012	-0.3	4680.4807	0.3
	2-1	4624.2670	-1.4	4642.1590	-1.1	4660.9110	-2.2	4680.5911	0.5
	1-1	4624.3401	-2.1	4642.2340	-0.7	4660.9860	-1.7	4680.6650	0.9
2-1	1-1	9247.3562	-1.7	9283.1306	-1.4	9320.6284	-0.6	9359.9743	-2.2
	3-2	9247.4718	-3.8	9283.2477	-3.2	9320.7421	-5.8	9360.0952	1.5
	2-1	9247.4832	2.4	9283.2580	1.8	9320.7553	2.1		
	1-0	9247.5420	-3.2	9283.3197	1.4	9320.8143	-1.0		
	2-2	9247.5525	-2.1	9283.3270	-3.8			9360.1688	-3.6
3-2	4-3	13868.5215	4.4	13922.1627	3.5	13978.3855	3.9	14037.3836	5.1
	3-2	13868.5215	1.5	13922.1627	0.5	13978.3855	0.9	14037.3836	2.2
4-3	5-4	18486.3219	6.1	18557.8054	5.7	18632.7266	6.6	18711.3414	-0.1
	4-3	18486.3219	4.3	18557.8054	3.9	18632.7266	4.8	18711.3414	-2.0
5-4	6-5	23099.7897	-2.3	23189.0823	-1.9	23282.6631	-2.4		
	5-4	23099.7897	-3.6	23189.0823	-3.2	23282.6631	-3.8		

[a] $\Delta\nu = \nu_{obs} - \nu_{calc}$ in kHz.

Table A2.2 Measured transition frequencies (MHz) for the $\Sigma 0_{0a}$ states of $^{83}Kr\text{-}NH_3$ and $^{83}Kr\text{-}^{15}NH_3$.

	$^{83}Kr\text{-}NH_3$					$^{83}Kr\text{-}^{15}NH_3$	
J'-J"	F'I'-F"I"	ν_{obs}	$\Delta\nu$[a]	J'-J"	F'-F"	ν_{obs}	$\Delta\nu$
1-0	3.5 4.5-2.5 2.5	4651.6292	-1.7	1-0	2.5-3.5	4444.1072	0.1
	3.5 4.5-3.5 3.5	4651.6292	-1.7		4.5-3.5	4444.0256	0.1
	3.5 4.5-4.5 4.5	4651.6292	-1.7		3.5-3.5	4443.6662	-0.2
	2.5 3.5-2.5 2.5	4651.6220	4.1				
	2.5 3.5-3.5 3.5	4651.6220	4.1				
	1.5 2.5-2.5 2.5	4651.5864	-0.4	2-1	2.5-3.5	8887.1304	2.5
	4.5 3.5-3.5 3.5	4651.5508	-0.5		4.5-3.5	8886.9541	1.1
	4.5 3.5-4.5 4.5	4651.5508	-0.5		3.5-3.5	8886.9541	1.1
	5.5 4.5-4.5 4.5	4651.5056	0.5		1.5-2.5	8886.9239	-8.1
	3.5 2.5-2.5 2.5	4651.4660	-1.6		5.5-4.5	8886.8984	1.4
	3.5 2.5-4.5 4.5	4651.4660	-1.6		2.5-2.5	8886.6887	1.5
	2.5 2.5-2.5 2.5	4651.1846	-2.5		4.5-4.5	8886.5943	0.4
	2.5 2.5-3.5 3.5	4651.1846	-2.5		3.5-4.5	8886.5943	0.4
	4.5 2.5-3.5 3.5	4651.1749	2.8		3.5-2.5	8886.5120	-0.3
	4.5 4.5-4.5 4.5	4651.1749	2.8				
	3.5 3.5-2.5 2.5	4651.1032	0.0				
	3.5 3.5-3.5 3.5	4651.1032	0.0				
	3.5 3.5-4.5 4.5	4651.1032	0.0				

[a] $\Delta\nu = \nu_{obs} - \nu_{calc}$ in kHz.

Table A2.3 Measured transition frequencies (MHz) for the $\Sigma 0_{0a}$ state of $Kr\text{-}^{15}NH_3$.

	$^{86}Kr\text{-}^{15}NH_3$		$^{84}Kr\text{-}^{15}NH_3$		$^{82}Kr\text{-}^{15}NH_3$		$^{80}Kr\text{-}^{15}NH_3$	
J'-J"	ν_{obs}	$\Delta\nu$[a]	ν_{obs}	$\Delta\nu$	ν_{obs}	$\Delta\nu$	ν_{obs}	$\Delta\nu$
1-0	4416.7367	-2.7	4434.6623	-1.8	4453.4495	-1.5	4473.1644	-0.8
2-1	8832.4885	-1.6	8868.3296	-1.8	8905.8950	-1.5	8945.3159	-0.6
3-2	13246.2637	0.1	13300.0047	-2.7	13356.3305	-0.8	13415.4411	1.3
4-3	17657.0751	3.7	17728.6917	3.6	17803.7536	3.8	17882.5207	-0.5
5-4	22063.9230	-1.8	22153.3822	-1.7	22247.1450	-1.7		

[a] $\Delta\nu = \nu_{obs} - \nu_{calc}$ in kHz.

Table A2.4 Measured transition frequencies (MHz) for the $\Sigma 0_0$ states of Kr-ND_3.

		^{86}Kr-ND_3				^{84}Kr-ND_3			
		$\Sigma 0_{0s}$		$\Sigma 0_{0a}$		$\Sigma 0_{0s}$		$\Sigma 0_{0a}$	
J'-J"	F'-F"	ν_{obs}	$\Delta\nu$[a]	ν_{obs}	$\Delta\nu$	ν_{obs}	$\Delta\nu$	ν_{obs}	$\Delta\nu$
1-0	0-1	4072.8136	1.0	4072.7241	-3.3	4090.7938	0.5	4090.7081	-0.2
	2-1	4073.0448	-2.7	4072.9591	-2.7	4091.0238	-3.2	4090.9398	-1.6
	1-1	4073.2000	-4.0	4073.1147	-3.3	4091.1803	-2.4	4091.0970	0.1
2-1	1-1	8145.0748	-4.2	8144.9083	0.1	8181.0284	-3.6	8180.8614	0.1
	3-2	8145.3266	-2.1	8145.1564	-1.1	8181.2784	-2.1	8181.1073	-2.0
	2-1	8145.3475	7.6	8145.1706	2.0	8181.2989	7.2	8181.1210	0.6
	1-0	8145.4727	3.3			8181.4241	2.6		
	2-2	8145.4943	-2.2			8181.4450	-2.4		
3-2	2-2	12215.7582	1.1	12215.5035	2.3	12269.6696	1.2	12269.4124	0.7
	4-3	12215.9851	-0.6	12215.7301	0.8	12262.8957	-0.2	12269.6379	-0.8
	3-2	12215.9851	-6.9	12215.7301	-5.4	12269.8957	-6.4	12269.6379	-7.0
	3-3	12216.1577	-2.0			12270.0668	-2.2		
4-3	5-4	16284.2212	2.7	16283.8813	3.8	16356.0692	3.1	16355.7258	3.3
	4-3	16284.2212	-1.3	16283.8813	-0.1	16356.0692	-0.9	16355.7258	-0.6
	3-2	16284.2401	6.5	16283.8958	3.2	16356.0873	6.1	16355.7430	5.5
5-4	6-5	20349.2201	-1.4	20348.7955	-1.2	20438.9772	-1.5	20438.5468	-1.3
	5-4	20349.2201	-4.2	20348.7955	-4.0	20438.9772	-4.2	20438.5468	-4.1

[a] $\Delta\nu=\nu_{obs} - \nu_{calc}$ in kHz.

Table A2.5 Measured transition frequencies (MHz) for the $\Sigma 1_1$ states of Kr-ND_3.

		^{86}Kr-ND_3				^{86}Kr-ND_3			
		$\Sigma 1_{1s}$		$\Sigma 1_{1a}$		$\Sigma 1_{1s}$		$\Sigma 1_{1a}$	
J'-J"	F'-F"	ν_{obs}	$\Delta\nu$[a]	ν_{obs}	$\Delta\nu$	ν_{obs}	$\Delta\nu$	ν_{obs}	$\Delta\nu$
2-1	1-1	7601.9119	-12.3	7585.6307	-9.0	7631.7367	0.6	7615.2658	-10.0
	3-2	7602.5143	25.5	7586.2293	8.2	7632.2972	-2.6	7615.8669	8.9
	1-0	7602.7958	-13.2	7586.5516	0.8	7632.6214	2.0	7616.1894	1.1
3-2	2-2	11432.1386	3.9	11410.8988	3.9	11477.5463	1.5	11456.0974	4.8
	4-3	11432.6495	-2.1	11411.4316	4.5	11478.0588	-2.0	11456.6299	4.3
	3-3	11433.0430	-1.8	11411.8236	-8.4	11478.4539	0.5	11457.0220	-9.2
4-3	5-4	15290.2119	-0.6	15266.5804	1.6	15351.7723	-5.6	15327.9530	-2.0
	3-2	15290.2440	0.6	15266.6090	-1.6	15351.8143	5.6	15327.9889	2.0
5-4	6-5	19175.5418	-2.0	19151.6212	-2.7	19253.7617	-2.9	9229.6997	-2.9
	5-4	19175.5666	2.0	19151.6479	2.7	19253.7883	2.9	19229.7270	2.9

[a] $\Delta\nu=\nu_{obs} - \nu_{calc}$ in kHz.

Table A2.6 Measured transition frequencies (MHz) for the $\Sigma 0_{00}$ states of Kr-ND_2H.

		^{86}Kr-ND_2H				^{84}Kr-ND_2H			
		$\Sigma 0_{00s}$		$\Sigma 0_{00a}$		$\Sigma 0_{00s}$		$\Sigma 0_{00a}$	
J'-J"	F-F"	ν_{obs}	$\Delta\nu$[a]	ν_{obs}	$\Delta\nu$	ν_{obs}	$\Delta\nu$	ν_{obs}	$\Delta\nu$
1-0	0-1	4232.5614	-2.8	4232.7809	4.5	4250.5027	-1.7	4250.7234	4.1
	2-1	4232.7545	-3.6	4232.9683	0.2	4250.6960	-5.6	4250.9099	-0.8
	1-1	4232.8854	-2.0	4233.0956	-0.3	4250.8290	-4.0	4251.0384	0.1
2-1	1-1	8464.3897	-2.0	8464.8118	-2.6	8500.2672	0.1	8500.6902	-1.3
	3-2	8464.5975	-0.4	8465.0165	-1.7	8500.4751	-1.7	8500.8926	-2.4
	2-1	8464.6141	6.9	8465.0300	2.6	8500.4929	6.7	8500.9059	1.8
	1-0	8464.7142	-0.7	8465.1341	0.2			8501.0100	-0.4
	2-2	8464.7310	-5.5	8465.1601	4.9			8501.0304	-1.3
3-2	2-2	12694.3385	2.3	12694.9716	0.0	12748.1312	0.9	12748.7634	-2.0
	4-3	12694.5276	2.5	12695.1577	0.5	12748.3232	1.0	12748.9542	2.6
	3-2	12694.5276	-2.6	12695.1577	-4.6	12748.3232	-4.3	12748.9542	-2.5
	2-1	12694.5485	-3.2	12695.1775	-6.1	12748.3486	-0.8	12748.9764	1.6
	3-3	12694.6712	2.5	12695.2996	0.4	12748.4689	0.6	12749.0961	2.7
4-3	5-4	16921.5955	2.2	16922.4403	0.8	16993.2844	1.2	16994.1280	1.3
	4-3	16921.5955	-1.1	16922.4403	-2.4	16993.2844	-2.1	16994.1280	-1.9
	3-2	16921.6108	5.0	16922.4547	2.9	16993.2991	3.2	16994.1423	3.3
5-4	6-5	21144.8499	-1.9	21145.9161	1.3	21234.4001	-0.3	21235.4617	-0.1
	5-4	21144.8499	-4.1	21145.9161	-1.0	21234.4001	-2.6	21235.4617	-2.3

[a] $\Delta\nu = \nu_{obs} - \nu_{calc}$ in kHz.

Table A2.7 Measured transition frequencies (MHz) for the $\Sigma 0_{00}$ states of Kr-NDH_2.

		^{86}Kr-NDH_2				^{84}Kr-NDH_2			
		$\Sigma 0_{00a}$		$\Sigma 0_{00s}$		$\Sigma 0_{00a}$		$\Sigma 0_{00s}$	
J'-J"	F'-F"	ν_{obs}	$\Delta\nu$[a]	ν_{obs}	$\Delta\nu$	ν_{obs}	$\Delta\nu$	ν_{obs}	$\Delta\nu$
1-0	0-1	4412.2498	2.5	4413.2921	1.9	4430.1559	0.8	4431.1961	0.2
	2-1	4412.4016	-7.5	4413.4413	-4.7	4430.3097	-4.2	4431.3489	-4.0
	1-1	4412.5109	-6.0	4413.5428	-7.1	4430.4166	-3.1	4431.4484	-9.2
2-1	1-1	8823.5830	-2.1	8825.6654	-1.3	8859.3863	-1.8	8861.4701	0.1
	3-2	8823.7544	-2.8	8825.8291	-3.3	8859.5541	-2.9	8861.6333	-3.7
	2-1	8823.7651	0.3	8825.8410	1.2	8859.5621	-2.5	8861.6454	0.9
	1-0	8823.8649	10.2	8825.9396	13.2	8859.6675	14.7	8861.7422	10.5
	2-2							8861.7620	12.9
3-2	2-2	13232.7650	2.6	13235.8883	1.6	13286.4464	4.5	13289.5724	3.4
	4-3	13232.9193	-0.6	13236.0371	-1.3	13286.5974	0.9	13289.7217	-0.2
	3-2	13232.9193	-4.9	13236.0371	-5.4	13286.5974	-3.3	13289.7217	-4.3
	2-1					13286.6145	-3.8	13289.7378	-5.7
	3-3	13233.0392	-0.5	13236.1513	-2.5	13286.7096	-4.5	13289.8304	7.8
4-3	5-4	17638.8161	3.1	17642.9842	2.3	17710.3421	3.4	17714.5183	2.2
	4-3	17638.8161	0.4	17642.9842	-0.4	17710.3421	0.7	17714.5183	-0.4
5-4	6-5	22040.3484	-0.1	22045.5780	0.8	22129.6869	0.5	22134.9264	1.9
	5-4	22040.3484	-2.0	22045.5780	-1.0	22129.6869	-1.3	22134.9264	0.1

[a] $\Delta\nu = \nu_{obs} - \nu_{calc}$ in kHz.

Table A2.8 Measured transition frequencies (MHz) for the $\Sigma 0_0/\Sigma 1_1$ states of Ar-ND_3.

		$\Sigma 0_{0a}$		$\Sigma 0_{0s}$		$\Sigma 1_{1a}$		$\Sigma 1_{1s}$	
J'-J"	F'-F"	ν_{obs}	$\Delta\nu$[a]	ν_{obs}	$\Delta\nu$	ν_{obs}	$\Delta\nu$	ν_{obs}	$\Delta\nu$
1-0	0-1	5201.3470	-1.7	5201.2816	-1.1	4897.9244	4.3	4894.6282	-2.8
	2-1	5201.6515	-2.7	5201.5901	-0.7	4898.4434	-18.3	4895.1515	15.0
	1-1	5201.8562	-1.7	5201.7898	-6.4	4898.8367	4.3	4895.5414	17.8
2-1	1-1	10401.3701	-3.3	10401.2441	0.3	9803.1521	-9.6	9796.9480	-1.5
	3-2	10401.6944	-3.9	10401.5674	-4.1	9803.7485	10.8	9797.5436	24.6
	2-1	10401.7068	-6.1	10401.5829	-3.2	9803.7835	20.0		
	1-0	10401.8848	2.2			9804.0725	8.1	9797.8348	-7.3
	2-2	10401.9132	-3.4			9804.0953	-29.3	9797.8858	-15.8
3-2	2-2	15598.1106	5.5	15597.9151	3.7				
	4-3	15598.4041	1.6	15598.2107	-0.7	14721.2646	-0.6	14712.8090	-1.6
	3-2	15598.4167	6.1	15598.2206	1.0	14721.2833	3.8	14712.8348	10.0
	2-1	15598.4512	6.7	15598.2554	1.7	14721.3365	-3.2	18712.8758	-8.5
	3-3	15598.6300	1.2	15598.4477	8.1				
4-3	5-4	20790.1098	0.0	20789.8522	-3.9	19654.5612	-5.2	19644.6656	-5.1
	4-3	20790.1173	-0.6	20789.8611	-0.2	19654.5766	1.1	19644.6801	0.4
	3-2	20790.1289	-3.5	20789.8752	-0.8	1965.6054	4.1	19644.7098	4.6

[a] $\Delta\nu = \nu_{obs} - \nu_{calc}$ in kHz.

Table A2.9 Measured transition frequencies (MHz) for the $\Sigma 0_{00}$ states of Ar-ND_2H and Ar-NDH_2.

		Ar-ND_2H				Ar-NDH_2			
		$\Sigma 0_{00s}$		$\Sigma 0_{00a}$		$\Sigma 0_{00s}$		$\Sigma 0_{00a}$	
J'-J"	F'-F"	ν_{obs}	$\Delta\nu$[a]	ν_{obs}	$\Delta\nu$	ν_{obs}	$\Delta\nu$	ν_{obs}	$\Delta\nu$
1-0	0-1	5360.6570	-0.8	5360.9338	0.3	5540.7587	-4.0	5541.8666	-1.4
	2-1	5360.9141	-3.6	5361.1922	2.3	5540.9675	-0.6	5542.0701	-5.6
	1-1	5361.0906	-0.4	5361.3582	-2.7	5541.1093	-4.8	5542.2127	-1.5
2-1	1-1	10719.6734	-4.2	10720.2253	-0.9	11079.5995	-4.6	11081.8136	-1.9
	3-2	10719.9530	-1.1	10720.4963	-2.6	11079.8238	-4.5	11082.0351	-0.6
	2-1	10719.9702	3.8	10720.5132	2.1			11082.0463	0.0
	1-0	10720.1105	-0.3	10720.6551	1.5	11079.9547	-0.8	11082.1607	-1.6
	2-2	10720.1371	-2.6	10720.6748	-7.3	11079.9740	-4.9	11082.1821	-3.3
3-2	2-2	16074.8759	3.0	16075.6951	-1.0	16614.1651	7.3	16617.4888	3.1
	4-3	16075.1261	0.2	16075.9451	-0.6	16614.3675	4.5	16617.6887	0.7
	3-2	16075.1410	8.2	16075.9562	3.7	16614.3754	6.8	16617.6989	5.4
	2-1	16075.1597	-2.0	16075.9821	1.1	16614.3973	5.3	16617.7225	6.0
	3-3	16075.3174	-1.0	16076.1410	5.3	16614.5230	3.8	16617.8439	2.0
4-3	5-4	21424.5114	-3.1	21425.6100	-2.6	22142.4231	-5.5	22146.8803	-4.1
	3-2	21424.5314	0.2	21425.6290	-0.1	22142.4382	-4.0	22146.8959	-1.9

[a] $\Delta\nu=\nu_{obs}-\nu_{calc}$ in kHz.

Table A2.10 Measured transition frequencies (MHz) for the $\Sigma 0_{0a}$ state of Ne-NH_3.

		^{22}Ne NH_3		^{20}Ne NH_3	
J'-J"	F'-F"	ν_{obs}	$\Delta\nu$[a]	ν_{obs}	$\Delta\nu$
1-0	0-1	7613.0655	-16.9	7929.4828	-18.0
	2-1	7613.1890	-18.1	7929.6014	-20.9
	1-1	7613.2683	-21.9	7929.6792	-24.1
2-1	1-1	15215.0187	13.7	15846.7586	14.7
	3-2	15215.1469	9.4	15846.8836	10.5
	2-1	15215.1547	11.2	15846.8910	12.1
	1-0	15215.2181	5.4	15846.9553	8.9
	2-2	15215.2324	5.8	15846.9640	4.1
3-2	4-3	22794.4563	-9.7	23739.3223	-11.0
	3-2	22794.4563	-13.0	23739.3223	-14.2

[a] $\Delta\nu=\nu_{obs}-\nu_{calc}$ in kHz.

Table A2.11 Measured transition frequencies (MHz) for the $\Sigma 0_{0a}$ state of Ne-$^{15}NH_3$.

	^{22}Ne-$^{15}NH_3$		^{20}Ne-$^{15}NH_3$	
J'-J"	ν_{obs}	$\Delta\nu^a$	ν_{obs}	$\Delta\nu$
1-0	7387.1778	-15.1	7704.3755	-17.6
2-1	14763.8133	12.1	15397.1586	14.1
3-2	22119.2370	-3.0	23066.6091	-3.5

[a] $\Delta\nu=\nu_{obs} - \nu_{calc}$ in kHz.

Table A2.12 Measured transition frequencies (MHz) for the $\Sigma 0_0$ states of Ne-ND_3.

		^{22}Ne-ND_3				^{20}Ne-ND_3			
		$\Sigma 0_{0s}$		$\Sigma 0_{0a}$		$\Sigma 0_{0s}$		$\Sigma 0_{0a}$	
J'-J"	F'-F"	ν_{obs}	$\Delta\nu^a$	ν_{obs}	$\Delta\nu$	ν_{obs}	$\Delta\nu$	ν_{obs}	$\Delta\nu$
1-0	0-1	7080.8757	-11.1	7080.9187	-16.8	7402.4474	-13.9	7402.5004	-15.8
	2-1	7081.1057	-17.8	7081.1630	-18.3	7402.6739	-22.4	7402.7330	-18.5
	1-1	7081.2629	-18.3			7402.8319	-21.2	7402.8871	-21.3
2-1	1-1	14152.7360	10.0	14152.8496	2.8	14794.9125	8.6	14795.0303	15.1
	3-2	14152.9871	9.5	14153.1010	8.2	14795.1635	9.5	14795.2782	12.7
	2-1					14795.1764	11.2		
	1-0	14153.1329	12.5	14153.2388	6.5	14795.3084	12.6	14795.4139	6.5
	2-2	14153.1524	5.7	14153.2685	10.5	14795.3259	4.0	14795.4437	10.1
3-2	2-2	21205.9665	-3.8			22166.8119	-1.3		
	4-3	21206.2009	0.2	21206.3701	-4.0	22167.0400	-2.1	22167.2108	-1.5
	3-2	21206.2009	-6.0	21206.3701	-10.7	22167.0400	-8.3	22167.2108	-7.7
	2-1	21206.2419	8.7			22167.0806	6.2	22167.2381	-6.5
	3-3	21206.3645	-11.4			22167.2051	-11.1		

[a] $\Delta\nu=\nu_{obs} - \nu_{calc}$ in kHz.

Table A2.13 Measured transition frequencies (MHz) for the $\Sigma 0_{00}$ states of Ne-ND_2H.

		^{22}Ne-ND_2H				^{20}Ne-ND_2H			
		$\Sigma 0_{00s}$		$\Sigma 0_{00a}$		$\Sigma 0_{00s}$		$\Sigma 0_{00a}$	
J'-J"	F'-F"	ν_{obs}	$\Delta\nu$[a]	ν_{obs}	$\Delta\nu$	ν_{obs}	$\Delta\nu$	ν_{obs}	$\Delta\nu$
1-0	0-1	7237.2164	-11.8	7237.6136	-13.2	7557.1854	-13.5	7557.5995	-12.5
	2-1	7237.4069	-19.3	7237.8088	-15.1	7557.3761	-20.8	7557.7883	-16.9
	1-1	7237.5386	-19.6	7237.9378	-17.5	7557.5063	-22.7	7557.9158	-18.2
2-1	1-1	14464.5341	9.8	14465.3313	11.3	15103.4436	10.3	15104.2644	9.2
	3-2	14464.7413	6.5	14465.5351	5.5	15103.6512	7.2	15104.4688	8.1
	2-1	14464.7573	13.0	14465.5488	9.8	15103.6698	16.4	15104.4820	12.1
	1-0	14464.8622	8.0	14465.6545	6.0	15103.7703	6.8	15104.5861	8.8
	2-2	14464.8796	3.4	14465.6743	4.0	15103.7903	4.8		
3-2	4-3	21671.7241	-6.9	21672.9149	-6.9	22627.5060	-7.9	22628.7347	-6.6
	3-2	21671.7241	-12.1	21672.9149	-12.1	22627.5060	-13.1	22628.7347	-11.7
	2-1	21671.7576	-0.6	21672.9492	0.3	22627.5402	-0.9	22628.7675	-0.4

[a] $\Delta\nu = \nu_{obs} - \nu_{calc}$ in kHz.

Table A2.14 Measured transition frequencies (MHz) for the $\Sigma 0_{00}$ states of Ne-NDH_2.

		^{22}Ne-NDH_2				^{20}Ne-NDH_2			
		$\Sigma 0_{00s}$		$\Sigma 0_{00a}$		$\Sigma 0_{00s}$		$\Sigma 0_{00a}$	
J'-J"	F'-F"	ν_{obs}	$\Delta\nu$[a]	ν_{obs}	$\Delta\nu$	ν_{obs}	$\Delta\nu$	ν_{obs}	$\Delta\nu$
1-0	0-1	7412.0753	-14.6	7413.1280	-11.4	7730.2868	-14.5	7731.3672	-15.2
	2-1	7412.2326	-18.2	7413.2788	-19.5	7730.4374	-21.5	7731.5209	-19.4
	1-1	7412.3361	-21.9	7413.3853	-19.0	7730.5442	-19.7	7731.6237	-21.9
2-1	1-1	14813.4907	16.8	14815.5796	14.0	15448.8309	17.4	15450.9890	16.9
	3-2	14813.6518	6.8	14815.7416	6.9	15448.9885	7.4	15451.1480	8.0
	1-0	14813.7495	7.5	14815.8402	9.6	15449.0853	9.2	15451.2452	9.9
	2-2	14813.7724	12.6	14815.8576	9.4	15449.1042	10.6	15451.2633	10.4
3-2	4-3	22193.2536	-9.5	22196.3769	-7.8	23143.5608	-7.6	23146.7896	-7.1
	3-2	22193.2536	-13.8	22196.3769	-12.0	23143.5608	-11.8	23146.7896	-11.3
	2-1	22193.2860	0.7	22196.4065	-0.1	23143.5886	-1.5	23146.8163	-2.1

[a] $\Delta\nu = \nu_{obs} - \nu_{calc}$ in kHz.

APPENDIX 3

Tables of *ab initio* data for the Ne-NH_3 dimer

Table A3.1 Interaction energies (μE_h) of Ne-NH_3 calculated at the MP4 level for the equilibrium geometry of NH_3 (>HNH=106.67°).

				ϕ=0°			
R / θ	0°	30°	60°	90°	120°	150°	180°
3.20	309.8	431.4	644.8	200.3	-74.2	7.3	61.9
3.30	129.6	194.1	292.4	-5.5	-153.0	-84.6	-47.8
3.40	14.3	44.0	75.9	-121.4	-191.4	-136.2	-112.3
3.50	-56.6	-47.5	-52.2	-180.2	-204.7	-161.6	-146.8
3.60	-97.7	-100.1	-123.1	-204.4	-202.9	-170.3	-162.0
3.70	-119.2	-127.6	-158.0	-207.7	-192.7	-168.6	-164.7
3.80	-127.6	-138.8	-170.6	-199.4	-178.1	-160.8	-160.0
3.90	-128.2	-139.8	-169.9	-194.9	-161.8	-149.8	-150.8
4.00	-123.7	-134.9	-161.7	-167.8	-145.1	-137.2	-139.3
				ϕ=10°			
3.20	309.8	420.2	591.0	160.0	-81.4	6.8	61.9
3.30	129.6	186.9	258.7	-30.3	-157.2	-84.9	-47.8
3.40	14.3	39.5	55.2	-136.0	-193.6	-136.4	-112.3
3.50	-56.6	-50.3	-64.2	-188.6	-205.7	-161.7	-146.8
3.60	-97.7	-101.8	-129.9	-208.6	-203.1	-170.3	-162.0
3.70	-119.2	-128.4	-161.4	-209.5	-192.6	-168.5	-164.7
3.80	-127.6	-139.2	-172.0	-199.6	-177.7	-160.8	-160.0
3.90	-128.2	-140.0	-170.1	-184.2	-161.2	-149.8	-150.8
4.00	-123.7	-134.9	-161.1	-166.7	-144.5	-137.2	-139.3
				ϕ=20°			
3.20	309.8	390.0	450.3	58.5	-100.5	5.2	61.9
3.30	129.6	167.4	170.1	-92.1	-168.0	-85.7	-47.8
3.40	14.3	27.2	0.8	-172.3	-199.4	-136.7	-112.3
3.50	-56.6	-57.8	-96.6	-208.7	-208.3	-161.7	-146.8
3.60	-97.7	-106.3	-148.1	-218.6	-203.9	-170.1	-162.0
3.70	-119.2	-131.0	-170.8	-213.3	-192.1	-168.5	-164.7
3.80	-127.6	-140.4	-175.8	-199.8	-176.7	-160.8	-160.0
3.90	-128.2	-140.5	-170.7	-182.3	-159.9	-149.6	-150.8
4.00	-123.7	-134.8	-160.0	-163.6	-143.1	-137.1	-139.3
				ϕ=30°			
3.20	309.8	349.5	274.3	-64.1	-124.8	3.3	61.9
3.30	129.6	141.2	59.4	-166.2	-181.9	-86.8	-47.8
3.40	14.3	10.7	-67.1	-215.3	-206.6	-137.2	-112.3
3.50	-56.6	-67.9	-136.8	-232.0	-211.3	-161.9	-146.8
3.60	-97.7	-112.2	-170.5	-229.6	-204.6	-171.2	-162.0
3.70	-119.2	-134.3	-182.1	-216.8	-191.4	-168.4	-164.7
3.80	-127.6	-141.9	-180.4	-198.9	-175.3	-160.6	-160.0
3.90	-128.2	-141.0	-171.1	-179.1	-158.2	-149.6	-150.8
4.00	-123.7	-134.8	-158.0	-159.3	-141.3	-136.9	-139.3

Table A3.1 continued.

				ϕ=40°			
3.20	309.8	310.0	116.5	-170.8	-147.5	1.3	61.9
3.30	129.6	115.8	-39.8	-230.4	-194.6	-87.8	-47.8
3.40	14.3	-5.4	-127.9	-252.0	-213.1	-137.7	-112.3
3.50	-56.6	-77.9	-172.5	-251.2	-214.0	-162.0	-146.8
3.60	-97.7	-118.1	-190.3	-238.2	-205.0	-170.1	-162.0
3.70	-119.2	-137.5	-191.6	-218.9	-190.5	-168.1	-164.7
3.80	-127.6	-143.6	-183.6	-197.3	-173.6	-160.4	-160.0
3.90	-128.2	-141.5	-170.8	-175.5	-156.2	-149.3	-150.8
4.00	-123.7	-134.7	-155.6	-154.7	-139.3	-136.7	-139.3
				ϕ=50°			
3.20	309.8	281.7	11.4	-239.9	-162.5	0.0	61.9
3.30	129.6	97.6	-105.5	-271.4	-203.4	-88.6	-47.8
3.40	14.3	-16.9	-168.0	-275.2	-217.4	-137.9	-112.3
3.50	-56.6	-85.0	-195.9	-264.0	-215.8	-162.2	-146.8
3.60	-97.7	-122.3	-202.9	-243.0	-205.0	-170.1	-162.0
3.70	-119.2	-139.7	-197.5	-219.7	-189.7	-168.1	-164.7
3.80	-127.6	-144.7	-185.4	-195.6	-172.5	-160.2	-160.0
3.90	-128.2	-141.9	-170.0	-172.6	-154.8	-149.2	-150.8
4.00	-123.7	-134.5	-153.6	-151.3	-137.8	-136.6	-139.3
				ϕ=60°			
3.20	309.8	271.4	-24.9	-263.3	-168.8	-0.6	61.9
3.30	129.6	91.0	-128.4	-285.5	-206.5	-88.8	-47.8
3.40	14.3	-21.1	-181.8	-283.0	-218.9	-138.1	-112.3
3.50	-56.6	-87.5	-203.9	-267.2	-216.3	-162.1	-146.8
3.60	-97.7	-123.8	-207.2	-244.7	-205.1	-170.0	-162.0
3.70	-119.2	-140.1	-199.5	-219.8	-189.3	-168.1	-164.7
3.80	-127.6	-145.1	-186.0	-195.0	-172.0	-160.1	-160.0
3.90	-128.2	-142.0	-169.8	-171.5	-154.4	-149.2	-150.8
4.00	-123.7	-134.5	-152.7	-149.9	-137.3	-136.6	-139.3

Table A3.2 Interaction energies (μE_h) of Ne-NH_3 calculated at the MP4 level for the intermediate geometry of NH_3 (>HNH=113.34°).

				ϕ=0°			
R / θ	0°	30°	60°	90°	120°	150°	180°
3.20	332.2	384.3	555.0	271.6	-4.7	83.1	149.1
3.30	154.6	174.6	241.1	35.0	-109.8	-29.7	17.1
3.40	39.2	40.8	48.6	-99.9	-165.4	-96.7	-64.4
3.50	-33.5	-41.6	-64.5	-170.5	-189.7	-133.3	-111.9
3.60	-77.1	-89.7	-126.8	-201.4	-195.1	-150.2	-136.7
3.70	-101.3	-115.3	-156.6	-208.6	-189.4	-154.6	-146.7
3.80	-112.7	-126.3	-166.7	-202.3	-177.4	-151.2	-147.3
3.90	-115.6	-128.2	-164.9	-188.7	-162.8	-143.2	-141.9
4.00	-113.4	-124.3	-156.3	-171.8	-146.9	-132.9	-133.3
				ϕ=10°			
3.20	332.2	376.0	507.5	223.8	-15.6	82.1	149.1
3.30	154.6	169.3	211.3	5.8	-116.1	-30.2	17.1
3.40	39.2	37.6	30.5	-117.0	-168.9	-96.9	-64.4
3.50	-33.5	-43.6	-75.2	-180.0	-191.5	-133.5	-111.9
3.60	-77.1	-91.0	-132.5	-206.1	-195.8	-150.3	-136.7
3.70	-101.3	-115.9	-159.4	-210.4	-189.4	-154.5	-146.7
3.80	-112.7	-126.6	-167.7	-202.3	-177.1	-151.1	-147.3
3.90	-115.6	-128.2	-164.8	-187.8	-162.2	-143.1	-141.9
4.00	-113.4	-124.3	-155.6	-170.4	-146.3	-132.8	-133.3
				ϕ=20°			
3.20	332.2	353.9	383.5	104.5	-43.9	79.5	149.1
3.30	154.6	155.1	133.6	-66.5	-132.6	-31.6	17.1
3.40	39.2	28.6	-16.9	-159.2	-177.8	-97.6	-64.4
3.50	-33.5	-49.1	-103.0	-2031.	-195.7	-133.8	-111.9
3.60	-77.1	-94.1	-148.0	-217.4	-197.1	-150.3	-136.7
3.70	-101.3	-117.7	-167.0	-214.6	-189.2	-154.4	-146.7
3.80	-112.7	-127.5	-170.4	-202.1	-176.0	-150.9	-147.3
3.90	-115.6	-128.4	-164.6	-185.3	-160.6	-143.0	-141.9
4.00	-113.4	-124.1	-154.1	-166.7	-144.6	-132.6	-133.3
				ϕ=30°			
3.20	332.2	324.3	229.3	-38.0	-80.2	76.1	149.1
3.30	154.6	135.8	37.0	-152.4	-153.6	-33.7	17.1
3.40	39.2	16.5	-75.8	-208.7	-189.0	-98.7	-64.4
3.50	-33.5	-56.5	-137.5	-229.7	-200.9	-134.2	-111.9
3.60	-77.1	-98.5	-166.8	-229.7	-198.8	-150.5	-136.7
3.70	-101.3	-120.0	-176.2	-218.3	-188.6	-154.3	-146.7
3.80	-112.7	-128.5	-173.5	-201.0	-174.4	-150.8	-147.3
3.90	-115.6	-128.6	-164.2	-181.5	-158.4	-142.8	-141.9
4.00	-113.4	-144.0	-151.6	-161.5	-142.1	-132.4	-133.3

Table A3.2 continued.

			ϕ=40°				
3.20	332.2	295.2	91.3	-160.3	-113.5	72.4	149.1
3.30	154.6	117.3	-49.2	-225.5	-172.6	-35.6	17.1
3.40	39.2	4.7	-128.3	-250.2	-199.1	-99.7	-64.4
3.50	-33.5	-63.7	-167.9	-251.3	-205.3	-134.6	-111.9
3.60	-77.1	-102.7	-183.1	-239.1	-199.8	-150.5	-136.7
3.70	-101.3	-122.3	-183.6	-220.4	-187.8	-154.2	-146.7
3.80	-112.7	-129.5	-175.8	-198.7	-172.5	-150.5	-147.3
3.90	-115.6	-128.9	-163.2	-176.9	-156.0	-142.4	-141.9
4.00	-113.4	-123.7	-148.9	-156.0	-139.6	-132.2	-133.3
			ϕ=50°				
3.20	332.2	-274.4	-0.2	-238.2	-136.0	70.0	149.1
3.30	154.6	103.8	-106.4	-271.5	-185.4	-37.0	17.1
3.40	39.2	-3.7	-162.7	-276.1	-205.7	-100.4	-64.4
3.50	-33.5	-68.8	-187.8	-264.3	-208.2	-134.8	-111.9
3.60	-77.1	-105.7	-193.7	-244.3	-200.3	-150.6	-136.7
3.70	-101.3	-123.9	-188.2	-220.7	-186.9	-154.2	-146.7
3.80	-112.7	-130.2	-176.7	-196.7	-171.0	-150.4	-147.3
3.90	-115.6	-129.1	-162.2	-173.3	-154.2	-142.4	-141.9
4.00	-113.4	-123.6	-146.7	-151.9	-137.8	-132.0	-133.3
			ϕ=60°				
3.20	332.2	266.9	-31.9	-264.4	-143.9	69.2	149.1
3.30	154.6	99.1	-126.0	-287.1	-189.9	-37.5	17.1
3.40	39.2	-6.8	-174.5	-284.6	-207.9	-100.7	-64.4
3.50	-33.5	-70.8	-194.5	-268.5	-209.2	-134.9	-111.9
3.60	-77.1	-106.7	-197.3	-245.9	-200.6	-150.6	-136.7
3.70	-101.3	-124.5	-189.8	-220.8	-186.7	-154.2	-146.7
3.80	-112.7	-130.5	-177.0	-195.7	-170.5	-153.4	-147.3
3.90	-115.6	-129.2	-161.8	-172.0	-153.6	-142.3	-141.9
4.00	-113.4	-123.6	-145.8	-150.4	-137.1	-131.8	-133.3

Table A3.3 Interaction energies (μE_h) of Ne-NH_3 calculated at the MP4 level for the planar geometry of NH_3 (>HNH=120.00°).

			ϕ=0°				ϕ=10°	
R / θ	0°	30°	60°	90°	0°	30°	60°	90°
3.20	309.2	257.3	252.4	349.7	309.2	254.0	225.9	295.3
3.30	140.7	96.8	53.9	79.3	140.7	94.7	37.6	46.6
3.40	30.7	-4.9	-63.6	-76.4	30.7	-6.2	-73.1	-95.3
3.50	-38.8	-66.9	-128.4	-159.6	-38.8	-67.7	-133.7	-169.8
3.60	-80.5	-102.5	-160.0	-197.8	-80.5	-102.8	-162.7	-202.8
3.70	-103.7	-120.2	-171.1	-209.0	-103.7	-120.3	-172.0	-210.9
3.80	-114.6	-126.6	-169.6	-204.8	-114.6	-126.7	-169.6	-204.9
3.90	-117.1	-125.8	-161.3	-192.3	-117.1	-125.8	-160.7	-191.2
4.00	-114.5	-120.6	-149.2	-175.7	-114.5	-120.6	-148.5	-74.2
4.10	-108.9	-112.9	-135.6	-157.9	-108.9	-112.9	-134.7	-156.2
4.20	-101.4	-104.1	-121.8	-140.4	-101.4	-104.0	-120.9	-138.4
			ϕ=20°				ϕ=30°	
3.20	309.2	245.2	157.1	158.0	309.2	233.4	71.3	6.3
3.30	140.7	89.2	-4.4	-35.9	140.7	81.9	-56.8	-134.4
3.40	30.7	-9.5	-97.8	-142.8	30.7	-14.0	-128.4	-199.5
3.50	-38.8	-69.7	-147.3	-195.5	-38.8	-72.3	-164.1	-225.6
3.60	-80.5	-103.9	-169.4	-214.9	-80.5	-105.1	-177.3	-228.7
3.70	-103.7	-120.7	-174.5	-215.0	-103.7	-121.4	-177.2	-218.9
3.80	-114.6	-126.7	-169.6	-204.1	-114.6	-126.8	-169.2	-202.5
3.90	-117.1	-125.7	-159.3	-188.1	-117.1	-125.4	-157.0	-183.2
4.00	-114.5	-120.4	-146.2	-169.7	-114.5	-120.0	-143.2	-163.5
4.10	-108.9	-122.6	-132.3	-151.2	-108.9	-112.2	-128.9	-144.6
4.20	-101.4	-103.7	-118.5	-1335.5	-101.4	-103.2	-115.2	-126.8
			ϕ=40°				ϕ=50°	
3.20	309.2	221.7	-6.1	-145.1	309.2	213.3	-57.7	-232.4
3.30	140.7	74.4	-103.8	-217.2	140.7	69.2	-134.8	-268.8
3.40	30.7	-18.5	-155.6	-246.3	30.7	-21.7	-173.6	-275.0
3.50	-38.8	-74.8	-178.7	-249.9	-38.8	-76.6	-188.3	-264.4
3.60	-80.5	-106.4	-184.1	-239.2	-80.5	-107.4	-188.4	-244.7
3.70	-103.7	-121.9	-179.2	-221.1	-103.7	-122.3	-180.2	-221.5
3.80	-114.6	-126.9	-168.4	-199.8	-114.6	-126.9	-167.5	-197.4
3.90	-117.1	-125.3	-154.7	-178.1	-117.1	-125.0	-152.9	-174.2
4.00	-114.5	-119.6	-140.1	-157.3	-114.5	-119.4	-137.8	-152.5
4.10	-108.9	-111.7	-125.7	-137.9	-108.9	-111.4	-123.1	-133.2
4.20	-101.4	-101.8	-111.8	-120.5	-101.4	-102.4	-109.4	-116.0

Table A3.3 continued.

		ϕ=60°		
3.20	309.2	210.2	-75.6	-261.7
3.30	140.7	67.3	-145.6	-285.9
3.40	30.7	-22.9	-179.8	-284.5
3.50	-38.8	-77.4	-191.6	-269.0
3.60	-80.5	-107.8	-189.8	-246.5
3.70	-103.7	-122.4	-180.5	-221.5
3.80	-114.6	-126.9	-166.6	-196.3
3.90	-117.1	-121.5	-152.2	-172.7
4.00	-114.5	-119.3	-137.0	-150.9
4.10	-108.9	-111.3	122.6	-131.5
4.20	-101.4	-102.4	108.6	-114.5

Table A3.4 Finer scan interaction energies (μE_h) of Ne-NH_3 calculated at the MP4 level for the equilibrium geometry of NH_3 (>HNH=106.67°).

			ϕ=60°				
R / θ	60°	70°	80°	90°	100°	110°	120°
3.20	-24.9	-138.6	-222.3	-263.3	-260.9	-224.8	-168.8
3.25	-84.4	-178.9	-247.0	-278.4	-273.2	-240.3	-191.6
3.30	-128.4	-206.7	-261.8	-285.5	-278.5	-248.7	-206.5
3.35	-159.9	-224.8	-268.9	-285.4	-278.3	-251.6	-215.2
3.40	-181.8	-235.1	-270.4	-283.0	-274.2	-250.3	-218.9
3.45	-195.9	-239.5	-267.5	-276.3	-267.2	-245.9	-219.1
			ϕ=50°				
3.20	11.4	-102.2	-191.2	-239.9	-245.2	-214.9	-162.5
3.25	-55.5	-150.3	-222.6	-260.	-261.1	-232.8	-187.4
3.30	-105.5	-184.3	-242.9	-271.4	-269.3	-243.1	-203.4
3.35	-142.2	-207.3	-254.6	-276.0	-271.6	-247.5	-2129
3.40	-168.0	-221.7	-259.5	-275.2	-269.3	-247.5	-217.4
3.45	-185.2	-229.4	-259.4	270.5	-263.7	-244.0	-218.0
			ϕ=40°				
3.20	116.5	4.3	-99.3	-170.8	-199.0	-186.9	-147.5
3.25	27.9	-66.3	-150.7	-206.6	-225.6	-211.5	-175.7
3.30	-39.8	-118.5	-187.1	-230.4	-242.3	-227.2	-194.6
3.35	-90.6	-156.2	-211.7	-244.8	-251.4	-235.8	-206.6
3.40	-127.9	-182.5	-227.0	-252.0	-254.6	-239.0	-213.1
3.45	-154.4	-199.7	-235.3	-253.6	-253.3	-238.2	-282.4

Table A3.4 continued.

				ϕ=30°			
3.20	274.3	167.6	43.0	-64.1	-128.5	-145.2	-124.8
3.25	153.3	62.9	-39.0	-123.5	-171.3	-179.6	-158.5
3.30	59.4	-17.2	-100.1	-166.2	-200.9	-203.1	-181.9
3.35	-12.7	-77.4	-144.5	-196.0	-220.3	-218.0	-197.3
3.40	-67.1	-121.6	-175.9	-215.3	-231.7	-226.2	-206.6
3.45	-107.6	-153.2	-196.8	-226.7	-236.9	-229.4	-210.8

Table A3.5 Finer scan interaction energies (μE_h) of Ne-NH_3 calculated at the MP4 level for the intermediate geometry of NH_3 (>HNH=113.34°).

				ϕ=60°			
R / θ	60°	70°	80°	90°	100°	110°	120°
3.20	-31.9	-142.7	-224.9	-264.4	-257.9	-213.0	-143.9
3.25	-86.0	-179.9	-248.5	-279.7	-271.8	-231.4	-171.3
3.30	-126.0	-205.4	-262.4	-287.1	-278.1	-242.2	-189.9
3.35	-154.7	-221.8	-268.8	-288.1	-278.8	-246.8	-201.6
3.40	-174.5	-230.9	-269.7	-284.6	-275.2	-247.0	-207.9
3.45	-187.3	-234.6	-266.5	-277.8	-268.6	-243.7	-210.2
				ϕ=50°			
3.20	-0.2	-108.3	-192.9	-238.2	-238.7	-200.1	-136.0
3.25	-61.0	-223.5	-223.5	-259.5	-257.0	-221.6	-165.3
3.30	-106.4	-184.5	-243.1	-271.5	-267.0	-234.7	-185.4
3.35	-139.4	-205.6	-254.2	-276.5	-270.5	-241.4	-198.4
3.40	-162.7	-218.6	-258.9	-276.1	-269.3	-243.1	-205.7
3.45	-178.2	-225.4	-258.4	-271.6	-264.3	-241.0	-208.6
				ϕ=40°			
3.20	91.3	-7.6	-98.1	-160.3	-181.8	-162.7	-113.5
3.25	11.6	-73.8	-149.5	-199.2	-213.4	-193.1	-148.1
3.30	-49.2	-122.7	-185.9	-225.5	-233.9	-213.3	-172.6
3.35	-94.8	-157.8	-210.5	-241.6	-245.9	-225.5	-189.0
3.40	-128.3	-182.1	-225.8	-250.2	-251.3	-231.7	-199.1
3.45	-151.9	-198.0	-234.0	-253.1	-251.7	-233.2	-204.1
				ϕ=30°			
3.20	229.3	148.0	50.7	-38.0	-93.7	-105.9	-80.2
3.25	120.9	48.8	-33.2	-104.3	-145.5	-149.6	-122.8
3.30	37.0	-26.7	-95.5	-152.4	-182.1	-180.4	-153.6
3.35	-27.3	-83.3	-141.1	-186.	-207.0	-201.2	-174.9
3.40	-75.8	-125.0	-173.2	-208.7	-222.6	-213.9	-189.0
3.45	-111.8	-154.6	-194.7	-222.6	-231.1	-220.7	-197.2

Table A3.6 Finer scan interaction energies (μE_h) of Ne-NH_3 calculated at the MP4 level for the planar geometry of NH_3 (>HNH=120.00°).

			ϕ=60°				ϕ=50°	
R / θ	60°	70°	80°	90°	60°	70°	80°	90°
3.20	-75.6	-171.8	-238.4	-261.7	-57.7	-147.1	-209.9	-232.4
3.25	-116.2	-199.4	-257.2	-278.2	-102.2	-180.5	-235.5	-255.4
3.30	-145.6	-217.4	-267.6	-285.9	-134.8	-203.2	-251.3	-268.8
3.35	-166.2	-228.0	-271.3	-287.1	-157.9	-217.4	-259.4	-274.7
3.40	-179.8	-232.7	-270.2	-284.5	-173.6	-224.7	-261.8	-275.0
3.45	-187.9	-233.0	-265.3	-277.1	-183.2	-227.9	-259.7	-271.1
3.50	-191.6	-230.2	-257.9	-269.0	-188.3	-226.7	-254.3	-264.4
			ϕ=40°				ϕ=30°	
3.20	-6.1	-78.0	-127.3	-145.1	71.3	29.0	2.5	6.3
3.25	-62.0	-126.8	-171.8	-187.9	8.6	-43.5	-70.9	-80.2
3.30	-103.8	-161.8	-202.5	-217.2	-56.8	-97.7	-124.9	-134.4
3.35	-134.1	-186.1	-222.7	-235.3	-98.2	-137.2	-163.7	-173.1
3.40	-155.6	-201.8	-234.5	-246.3	-128.4	-165.0	-190.4	-199.5
3.45	-170.0	-210.9	-239.9	-250.4	-149.8	-183.8	-207.6	-216.1
3.50	-178.7	-214.7	-240.5	-249.9	-164.1	-195.4	-217.6	-225.6

Table A3.7 Interaction energies (μE_h) of Ne-NH_3 calculated at the CCSD(T) level for the equilibrium geometry of NH_3 (>HNH=106.67°).

				ϕ=0°			
R / θ	0°	30°	60°	90°	120°	150°	180°
3.40					-195.1		
3.45					-203.7		
3.50				-180.5	-207.5	-167.0	-152.9
3.55				-195.7	-207.8	-172.4	-161.8
3.60				-204.3	-205.2	-174.7	-167.1
3.65	-123.7			-207.9	-200.6	-174.5	-169.2
3.70	-131.2		-160.7	-207.5		-172.3	-169.0
3.75	-135.6	-143.1	-168.8	-198.9		-168.7	-167.0
3.80	-137.5	-146.3	-172.6	-192.1			-163.5
3.85	-137.6	-147.4	-173.3				-159.0
3.90	-136.1	-145.9	-171.4				-153.8
3.95	-133.6	-143.4	-167.8				
4.00	-130.2	-139.8					
				ϕ=60°			
3.20				-266.3			
3.25				-280.5			
3.30			-136.5	-287.3	-210.7		
3.35			-167.04	-287.9	-218.9		
3.40			-187.96	-284.1	-222.3		
3.45			-201.26	-277.0	-222.1		
3.50			-208.66		-219.0	-167.5	-152.9
3.55		-121.1	-211.42		-213.8	-172.5	-161.8
3.60		-135.0	-210.71		-207.2	-174.5	-167.1
3.65	-123.7	-144.2	-207.44		-199.5	-174.1	-169.2
3.70	-131.2	-149.7	-202.22			-171.8	-169.0
3.75	-135.6	-152.1				-168.1	-167.0
3.80	-137.5	-152.4				-163.3	-163.5
3.85	-137.6	-150.8				-157.8	-159.0
3.90	-136.14	-147.8					-153.8
3.95	-133.59	-143.9					
4.00	-130.19	-139.3					

Table A3.8 Interaction energies (μE_a) of Ne-NH_3 calculated at the CCSD(T) level for the equilibrium geometry of NH_3 (>HNH=113.34°).

				ϕ=0°			
R / θ	0°	30°	60°	90°	120°	150°	180°
3.50					-193.8		-120.7
3.55					-197.8	-150.8	-134.6
3.60				-201.6	-198.3	-156.6	-144.1
3.65				-207.3	-196.1	-159.5	-150.0
3.70			-160.1	-208.5	-191.9	-159.9	-152.9
3.75	-119.6	-131.2	-166.6	-206.4	-186.2	-158.5	-153.6
3.80	-122.9	-134.5	-169.3	-201.9		-155.6	-152.5
3.85	-124.3	-135.4	-169.2	-195.6		-151.7	-150.0
3.90	-124.1	-134.8	-166.9				-146.4
3.95	-122.7	-132.8	-162.9				
4.00	-120.3	-129.7					
				ϕ=60°			
3.20				-268.1			
3.25				-282.7			
3.30				-289.4	-195.6		
3.35			-162.5	-290.0	-206.8		
3.40			-181.3	-286.2	-212.6		
3.45			-193.5	-279.0	-214.4		
3.50			-200.0		-212.9	-142.6	-120.7
3.55			-202.3		-209.1	-151.5	-134.6
3.60		-118.5	-201.5		-203.6	-156.9	-144.1
3.65		-128.1	-198.1		-196.8	-159.3	-150.0
3.70		-134.2	-193.1			-159.4	-152.9
3.75	-119.6	-137.4				-157.8	-153.6
3.80	-122.9	-138.5				-154.8	-152.5
3.85	-124.3	-137.7				-150.8	-150.0
3.90	-124.1	-135.7					-146.4
3.95	-122.7	-132.7					
4.00	-120.3	-128.9					

Table A3.9 Interaction energies (μE_h) of Ne-NH_3 calculated at the CCSD(T) level for the planar geometry of NH_3 (>HNH=120.00°).

		ϕ=0°		
R / θ	0°	30°	60°	90°
3.60			-164.7	-198.4
3.65			-171.7	-206.3
3.70		-129.0	-174.8	-209.2
3.75	-120.1	-132.5	-174.8	-208.3
3.80	-123.4	-133.9	-172.8	-204.6
3.85	-124.8	-133.6	-168.8	-199.0
3.90	-124.6	-131.9		-191.8
3.95	-123.2	-129.2		
4.00	-120.9			
		ϕ=60°		
3.20				-265.8
3.25				-281.4
3.30				-288.8
3.35				-289.9
3.40			-186.3	-286.4
3.45			-193.7	-279.5
3.50			-196.9	
3.55			-196.7	
3.60			-194.2	
3.65			-189.7	
3.70		-131.1		
3.75	-120.1	-133.6		
3.80	-123.4	-134.2		
3.85	-124.8	-133.2		
3.90	-124.6	-131.1		
3.95	-123.2	-128.1		
4.00	-120.9			

Table A3.10 Interaction energies (μE_h) of Ne-NH_3 calculated at the CCSD(T) level for the equilibrium geometry of NH_3 (>HNH)=106.67°) using the aug-cc-pVDZ basis set for Ne.

				ϕ=0°			
R / θ	0°	30°	60°	90°	120°	150°	180°
3.40					-186.1		
3.45					-194.9		
3.50					-199.0	-165.7	-153.6
3.55					-199.3	-169.9	-160.9
3.60				-188.5	-197.0	-171.0	-164.6
3.65				-194.7	-192.5	-169.5	-165.4
3.70			-146.9	-196.7		-166.4	-164.0
3.75	-122.6	-130.1	-157.1	-195.3		-161.9	-160.8
3.80	-125.1	-134.2	-162.8	-191.6			-156.5
3.85	-125.7	-136.0	-164.9				-151.2
3.90	-124.7	-135.9	-164.3				-145.3
3.95	-122.7	-134.1	-161.7				
4.00	-119.8	-131.1					
				ϕ=60°			
3.20				-246.5			
3.25				-262.7			
3.30			-110.5	-271.7	-208.4		
3.35			-144.1	-273.8	-216.2		
3.40			-167.7	-271.2	-219.1		
3.45			-183.3	-265.3	-218.2		
3.50			-192.7		-214.4	-166.8	-153.6
3.55		-104.4	-197.1		-208.7	-170.6	-160.9
3.60		-119.9	-197.9		-201.6	-171.3	-164.6
3.65		-130.3	-195.8		-193.4	-169.7	-165.4
3.70		-136.7	-191.8		-184.6	-166.5	-164.0
3.75	-122.6	-140.1	-186.1			-161.8	-160.8
3.80	-125.1	-141.0	-179.3			-156.3	-156.5
3.85	-125.7	-140.1				-150.1	-151.2
3.90	-124.7	-137.8					-145.3
3.95	-122.7	-134.4					
4.00	-119.8	-130.3					

Table A3.11 Interaction energies (μE_h) of Ne-NH_3 calculated at the CCSD(T) level for the intermediate geometry of NH_3 (>HNH)=113.34°) using the aug-cc-pVDZ basis set for Ne.

				ϕ=0°			
R / θ	0°	30°	60°	90°	120°	150°	180°
3.50					-182.2		-119.0
3.55					-186.8	-146.4	-131.7
3.60				-185.9	-188.0	-151.2	-139.9
3.65				-193.9	-182.7	-153.3	-144.6
3.70			-147.1	-197.5	-171.2	152.9	-146.6
3.75	-107.4	-119.2	-155.6	-197.3		-150.9	-146.4
3.80	-111.4	-123.2	-159.9	-194.5		-147.5	-144.5
3.85	-113.0	-124.9	-161.1	-189.5		-143.1	-141.3
3.90	-112.7	-124.7	-160.0	-183.1			-137.2
3.95	-111.7	-123.2	-156.9				
4.00	-109.7	-120.7					
				ϕ=60°			
3.20				-246.9			
3.25				-263.9			
3.30			-112.59	-272.6	-190.5		
3.35			-144.73	-275.0	-201.7		
3.40			-163.81	-272.7	-207.4		
3.45			-177.61	-266.9	-208.8		
3.50			-185.72		-206.9	-139.6	-119.0
3.55			-189.27		-202.8	-147.5	-131.7
3.60		-105.3	-189.56		-197.0	-151.8	-139.9
3.65		-115.6	-187.42		-190.0	-153.4	-144.6
3.70		-122.2	-183.26		-182.1	-150.4	-146.6
3.75	-107.4	-125.9	-171.05			-146.8	-146.4
3.80	-111.4	-127.4				-142.3	-144.5
3.85	-113.0	-127.1				-137.2	-141.3
3.90	-112.7	-125.4				-131.6	-137.2
3.95	-111.7	-122.9					
4.00	-109.7	-119.4					

Table A3.12 Interaction energies (μE_h) of Ne-NH_3 calculated at the CCSD(T) level for the planar geometry of NH_3 (>HNH)=120.00°) using the aug-cc-pVDZ basis set for Ne.

		ϕ=0°		
R / θ	0°	30°	60°	90°
3.50				
3.55				
3.60			-149.6	-181.7
3.65			-158.5	-192.7
3.70		-119.0	-163.2	-197.8
3.75		-122.5	-164.5	-199.0
3.80	-113.0	-124.0	-163.4	-197.1
3.85	-114.2	-123.7	-160.4	-192.8
3.90	-113.9	-122.1		-179.7
3.95	-112.5	-119.5		-171.8
4.00	-110.2			
		ϕ=60°		
3.20				-241.9
3.25				-260.3
3.30				-271.1
3.35				-273.4
3.40			-174.6	-272.4
3.45			-182.7	-267.1
3.50			-186.5	
3.55			-186.8	
3.60			-184.7	
3.65			-180.6	
3.70		-121.3		
3.75		-123.6		
3.80	-113.0	-124.1		
3.85	-114.2	-123.1		
3.90	-113.9	-121.0		
3.95	-112.5	-118.2		
4.00	-110.2			

APPENDIX 4

Tables of microwave transition frequencies measured for the Rg_2-NH_3 trimers

Table A4.1 Measured transition frequencies (MHz) for the $\Sigma 0_{0a}$ state of Ar_2-NH_3.

$J'_{Ka'Kc'}$ - $J''_{Ka''Kc''}$	F'-F''	ν_{obs}	$\Delta\nu$[a]	$J'_{Ka'Kc'}$ - $J''_{Ka''Kc''}$	F'-F''	ν_{obs}	$\Delta\nu$[a]
1_{11}-0_{00}	0-1	4375.1668	-0.5	3_{31}-$3'_{22}$	3-4	9197.5376	0.9
	1-1	4375.2926	0.0		3-3	9197.5376	0.9
	2-1	4375.3762	0.0		4-4	9197.5728	0.3
					4-3	9197.5728	0.3
2_{02}-1_{11}	1-1	4047.1989	0.4				
	2-1	4047.2799	0.2	4_{04}-3_{13}	5-4	9667.8162	-2.1
	3-2	4047.3114	0.3		4-3	9667.8162	-1.1
	2-2	4047.3647	1.5		3-2	9667.8330	2.5
	1-0	4047.4062	-1.2				
				4_{13}-3_{22}	4-3	8528.6958	-1.6
2_{20}-1_{11}	2-1	11642.3932	-0.2		5-4	8528.7494	0.6
	1-1	11642.4743	-0.2				
	2-2	11642.4743	-2.6	4_{31}-3_{22}	4-3	21029.0213	-4.0
	3-2	11642.5291	0.0		5-4	21029.0654	-3.4
	1-0	11642.6842	0.8				
				4_{13}-4_{04}	4-4	6251.8998	0.3
2_{20}-2_{11}	3-3	4701.9412	-2.0		5-5	6252.0826	4.1
	2-2	4701.9776	-3.2		3-3	6252.1212	-3.4
3_{13}-2_{02}	2-2	8624.7707	0.0	4_{22}-4_{13}	4-4	4635.0351	6.7
	2-1	8624.8546	2.7		5-5	4635.0701	4.9
	4-3	8624.8673	-0.6				
	3-2	8624.9440	-0.3	4_{31}-4_{22}	5-5	7865.2443	-7.8
	3-3	8624.9953	-1.2		4-4	7865.2922	-4.9
3_{22}-2_{11}	2-1	13122.6889	-0.9	5_{15}-4_{04}	6-5	12584.8178	2.0
	3-3	13122.7415	2.0		4-3	12584.8178	1.6
	4-3	13122.7415	2.0		5-4	12584.8477	0.7
	3-2	13122.8284	-0.6				
	2-2	13122.8284	-0.7	5_{24}-4_{13}	4-3	16728.3573	-0.9
					6-5	16728.3817	3.4
3_{31}-2_{20}	2-1	17618.3503	-3.6		5-4	16728.4659	2.4
	4-3	17618.3705	0.1				
	3-2	17618.3890	2.2	5_{24}-5_{15}	5-5	10395.5170	-0.2
					6-6	10395.6459	3.6
3_{22}-3_{13}	3-3	7391.0187	-0.8				
	4-3	7391.0187	-0.8				
	2-3	7391.0187	-0.8				
	4-4	7391.1497	1.7				
	3-4	7391.1497	1.7				
	3-2	7391.1920	-1.0				
	2-2	7391.1920	-1.0				

[a] $\Delta\nu = \nu_{obs} - \nu_{calc}$ in kHz.

Table A4.2 Measured transition frequencies (MHz) for the $\Sigma 0_{0a}$ state of Ar_2-$^{15}NH_3$.

$J'_{Ka'Kc'}$ - $J''_{Ka''Kc''}$	ν_{obs}	$\Delta\nu^a$	$J'_{Ka'Kc'}$ - $J''_{Ka''Kc''}$	ν_{obs}	$\Delta\nu$
1_{11}-0_{00}	4214.5573	-2.4	4_{04}-3_{13}	9605.3961	-2.8
2_{02}-1_{11}	4134.2463	3.3	4_{13}-3_{22}	8868.7991	-2.0
2_{20}-1_{11}	11234.1827	0.2	4_{31}-3_{22}	20368.0106	-3.7
2_{20}-2_{11}	4293.6267	-3.0	4_{13}-4_{04}	6315.8591	-0.5
3_{13}-2_{02}	8394.5280	1.1	4_{22}-4_{13}	4396.0413	5.3
3_{22}-2_{11}	12640.6735	-1.0	4_{31}-4_{22}	7103.1726	-4.5
3_{31}-2_{20}	16884.8444	4.4	5_{15}-4_{04}	12335.0504	1.1
3_{22}-3_{13}	7052.4555	-1.8	5_{24}-4_{13}	16167.2449	2.1
3_{31}-3_{22}	8537.7982	3.0	4_{24}-5_{15}	10148.0540	0.9

[a] $\Delta\nu = \nu_{obs} - \nu_{calc}$ in kHz.

Table A4.3 Measured transition frequencies (MHz) for the $\Sigma 0_0$ states of Ar_2-ND_3.

		$\Sigma 0_{0s}$		$\Sigma 0_{0a}$	
$J'_{K_aK_c'}$ $J''_{K_aK_c''}$	F'-F"	ν_{obs}	$\Delta\nu^a$	ν_{obs}	$\Delta\nu^a$
1_{11}-0_{00}	0-1	3924.8156	3.2	3924.6454	0.0
	1-1	3925.0499	-0.8	3924.8848	-0.3
	2-1	3925.2079	-1.6		
2_{02}-1_{11}	1-1	4274.2520	0.2		
	3-2	4274.4876	-1.4	4274.6154	-7.2
	1-0	4274.6514	2.5	4274.7839	-0.5
2_{20}-1_{11}	2-1	10511.8436	-2.4	10511.3960	5.8
	3-2	10512.1512	5.4	10511.6917	1.5
	1-0	10512.4574	-5.0		
3_{13}-2_{02}	2-2	7978.1250	-3.2		
	4-3	7978.3692	3.2		
	3-2	7978.4994	-2.0		
	3-3	7978.6466	4.2		
3_{22}-2_{11}	2-1	11772.2932	1.3	11771.7956	-2.8
	4-3	11772.3849	-1.5	11771.8928	-0.7
	3-2	11772.5560	-0.6	11772.0617	-3.1
3_{31}-2_{20}	2-1	15565.2613	-1.0		
	4-3	15565.3061	0.4	15564.4840	5.5
	3-2	15565.3462	-0.6	15564.5231	3.0
3_{22}-3_{13}	3-3	6456.7303	-1.5	6456.2727	-2.8
	4-4	6457.0084	0.2	6456.5506	-1.1
	2-2	6457.1064	1.4		
3_{31}-3_{22}	3-3	7367.4910	2.6	7366.6867	-4.3
	4-4	7367.5923	4.0	7366.7882	-1.4
	2-2	7367.6181	-5.2	7366.8218	-2.3
4_{04}-3_{13}	5-4	9445.9757	3.6		
	4-3	9445.9922	-1.7		
4_{13}-3_{22}	4-3	9420.3263	-5.4	9420.7547	-3.3
	5-4	9420.3857	-3.2	9420.8156	-0.8
	3-2	9420.4104	6.7	9420.8347	3.3
4_{13}-4_{04}	4-4	6431.0706	1.1		
	5-5	6431.4254	0.4		
	3-3	6431.5168	0.4		

[a] $\Delta\nu = \nu_{obs} - \nu_{calc}$ in kHz.

Table A4.4 Measured transition frequencies (MHz) for the $\Sigma 0_{00}$ states of Ar_2-ND_2H.

		$\Sigma 0_{00s}$		$\Sigma 0_{00a}$	
$J'_{Ka'Kc'}$ $J''_{Ka''Kc''}$	F'-F''	ν_{obs}	$\Delta\nu^a$	ν_{obs}	$\Delta\nu^a$
1_{11}-0_{00}	0-1	4058.3565	-3.7	4058.4065	3.1
	1-1	4058.5618	0.0	4058.5979	-3.7
	2-1	4058.6973	1.2		
2_{02}-1_{11}	1-1	4213.2817	2.9		
	3-2	4213.4810	9.0		
	1-0	4213.6054	-9.4	4213.7363	-2.1
2_{20}-1_{11}	2-1	10841.9966	-2.8	10842.0274	3.8
	3-2	10842.2444	4.9	10842.2633	0.5
	1-0	10842.4974	-2.5	10842.5213	0.9
3_{13}-2_{02}	2-2	8170.9195	-2.1	8171.1173	-4.7
	4-3	8171.1061	0.7	8171.3062	-0.8
	3-2	8171.2239	1.4	8171.4222	-0.5
3_{22}-2_{11}	2-1	12172.5560	-4.3		
	4-3	12172.6408	0.6	12172.7638	-0.1
	3-2	12172.7900	5.8	12172.9094	4.0
3_{31}-2_{20}	3-3	16172.3459	-4.1		
	4-3	16172.4244	0.9	16172.4866	2.3
	3-2	16172.4566	0.9	16172.5145	-0.9
	2-2	16172.5549	-0.2		
3_{22}-3_{13}	3-3			6727.4650	-3.8
	4-4	6727.8287	-1.6	6727.6867	-4.8
	3-4	6727.8287	-1.6	6727.6867	-4.8
	3-2	6727.9071	-1.2	6727.7730	3.6
	2-2	6727.9071	-1.2	6727.7730	3.6
3_{31}-3_{22}	3-3	7902.1891	7.2	7902.0786	5.7
	4-4	7902.2578	2.3	7902.1497	0.8
	2-2	7902.2737	-7.5	7902.1668	-8.6
4_{04}-3_{13}	5-4	9528.4508	-3.4	9528.7198	-0.2
	4-3	9528.4731	6.5	9528.7328	0.1
4_{13}-3_{22}	4-3	9178.7429	-1.0	9178.9411	-1.0
	5-4	9178.8028	-2.2	9179.0020	1.2
4_{13}-4_{04}	4-4	6377.8864	1.7	6377.6782	0.0
	5-5	6378.1817	0.6	6377.9712	-1.0
	3-3	6378.2581	0.8	6378.0487	0.9

[a] $\Delta\nu = \nu_{obs} - \nu_{calc}$ in kHz.

Table A4.5 Measured transition frequencies (MHz) for the $\Sigma 0_{00}$ states of Ar_2-NDH_2.

		$\Sigma 0_{00s}$		$\Sigma 0_{00a}$	
$J'_{Ka'Kc'}$-$J''_{Ka''Kc''}$	F'-F''	ν_{obs}	$\Delta\nu$[a]	ν_{obs}	$\Delta\nu$[a]
1_{11}-0_{00}	0-1	4204.7140	-1.6	4205.4309	0.8
	1-1	4204.8812	3.0	4205.5932	0.0
	2-1	4204.9916	5.0	4205.7014	-0.6
2_{02}-1_{11}	1-1			4139.6740	-2.2
	2-1			4139.7971	3.1
	3-2			4139.8255	-1.5
	2-2	4140.0308	-5.1	4139.9037	1.0
	1-0	4140.0773	-3.3	4139.9469	-1.2
2_{20}-1_{11}	2-1	11208.9382	-2.6	11210.6354	0.2
	3-2	11209.1272	2.2	11210.8209	0.1
	1-0	11209.3335	3.7	11211.0241	-0.1
3_{13}-2_{02}	2-2	8381.3033	-3.2	8382.3928	1.1
	4-3	8381.4037	0.5	8382.5248	-3.0
	3-2	8381.1710	0.7	8382.6260	1.2
3_{22}-2_{11}	2-1	12611.3780	-0.4	12613.5227	-1.3
	4-3	12611.3780	-0.4	12613.5227	-1.3
	3-2	12611.4998	5.2	12613.6418	1.3
	2-2	12611.4998	5.2	12613.6418	1.3
3_{31}-2_{20}	4-3	16839.1205	-7.7	16842.1934	-2.7
	3-2	16839.1582	6.2	16842.2234	3.4
3_{22}-3_{13}	3-3	7030.6489	2.3	7031.8365	0.9
	4-3	7030.6489	2.3	7031.8365	0.9
	2-3	7030.6489	2.3	7031.8365	0.9
	4-4	7030.8242	5.1	7032.0097	1.4
	3-4	7030.8242	5.1	7032.0097	1.4
	3-2	7030.8687	-10.8	7032.0620	-6.7
	2-2	7030.8687	-10.8	7032.0620	-6.7
3_{31}-3_{22}	3-4	8496.1192	3.7	8496.5991	-1.7
	3-3	8496.1192	3.7	8496.5991	-1.7
	3-2	8496.1192	3.7	8496.5991	-1.7
	4-4	8496.1667	-0.9	8496.6536	1.0
	4-3	8496.1667	-0.9	8496.6536	1.0
4_{04}-3_{13}	5-4	9602.1202	0.0	9602.9037	3.7
4_{13}-3_{22}	4-3	8889.8454	3.1	8888.9066	-3.7
	5-4	8889.8976	-3.1	8888.9691	0.0
4_{13}-4_{04}	4-4			6317.8430	1.8
	5-5	6318.5997	0.0	6318.0768	-0.6
	3-3			6318.1424	4.3

[a] $\Delta\nu = \nu_{obs} - \nu_{calc}$ in kHz.

Table A4.6 Measured transition frequencies (MHz) for the $\Sigma 0_{0a}$ state of $^{22}Ne^{20}Ne$-NH_3.

$J'_{Ka'Kc'}$ $J''_{Ka''Kc''}$	F'-F''	ν_{obs}	$\Delta\nu$	$J'_{Ka'Kc'}$ $J''_{Ka''Kc''}$	F'-F''	ν_{obs}	$\Delta\nu$
1_{01}-0_{00}		5800.0240[a]	54.5[b]	2_{12}-1_{01}		10624.6256	-59.5
	0-1	5799.8569	-0.6[c]		3-2	10624.6223	0.0
	2-1	5800.0079	0.6				
	1-1	5800.1073	0.1	2_{11}-2_{02}		5481.7697	39.0
					2-2	5481.6980	-2.4
1_{11}-0_{00}		6587.4070	14.6		3-3	5481.7919	2.4
	1-1	6587.3965	3.0				
	2-1	6587.4071	-2.6	3_{03}-2_{02}		14320.9901	57.8
	0-1	6587.4335	-0.4		4-3	14320.9854	2.4
					3-2	14320.9982	-1.4
2_{02}-1_{01}		10414.0420	-32.2		2-1	14320.9982	-1.0
	1-1	10413.8754	0.1				
	3-2	10414.0337	-1.1	3_{13}-2_{12}		14147.0372	57.4
	2-1	10414.0438	1.6		4-3	14147.0267	0.0
	1-0	10414.1292	4.2		2-1	14147.0372	3.2
	2-2	10414.1373	-4.8		3-2	14147.0554	-3.2
2_{11}-1_{10}		13349.9078	-154.4	3_{22}-2_{21}		17372.8525	7.4
	1-0	13349.7582	3.0		2-1	17372.7693	0.1
	3-2	13349.8837	-6.2		4-3	17372.8276	-1.0
	2-1	13349.9944	-3.2		3-2	17372.9368	0.9
2_{12}-1_{11}		9837.2409	-17.9	3_{03}-2_{12}		14110.4047	86.9
	1-0	9837.1405	-3.6		4-3	14110.3930	-0.7
	3-2	9837.2213	3.1		3-2	14110.4284	0.7
	2-1	9837.3247	0.5				
				3_{13}-2_{02}		14357.6197	-31.2
2_{11}-2_{12}		5271.1890	63.4		4-3	14357.6113	-1.8
	2-2	5271.1322	-1.0		3-2	14357.6298	2.2
	3-3	5271.2060	1.0		2-1	14357.6298	-0.3
2_{02}-1_{11}		9626.6566	10.1	4_{04}-3_{03}		18276.9418	-70.9
	3-2	9626.6333	3.3		3-2	18276.9330	-3.8
	2-1	9626.7502	-3.3		5-4	18276.9330	3.8

[a] Hypothetical center line frequency.

[b] $\Delta\nu=\nu_{obs}-\nu_{calc}$ in kHz from rotational analysis of center line frequency.

[c] $\Delta\nu=\nu_{obs}-\nu_{calc}$ in kHz from ^{14}N hyperfine analysis.

Table A4.7 Measured transition frequencies (MHz) for the $\Sigma 0_{0s}$ state of $^{22}Ne^{20}Ne$-$^{15}NH_3$.

$J'_{K_aK_cv'}$ $J''_{K_aK_cv'}$	ν_{obs}	$\Delta\nu^a$	$J'_{K_aK_cv'}$ $J''_{K_aK_cv'}$	ν_{obs}	$\Delta\nu$
1_{01}-0_{00}	5616.8779	100.7	3_{03}-2_{02}	14054.0023	102.8
1_{11}-0_{00}	6542.7160	114.9	3_{13}-2_{12}	13822.7090	45.3
2_{02}-1_{01}	10203.8117	8.1	3_{12}-2_{11}	18290.0150	-46.9
2_{11}-1_{10}	12884.9065	-225.3	3_{12}-3_{13}	9440.9386	6.1
2_{12}-1_{11}	9570.4923	-103.4	3_{22}-2_{21}	16824.2387	71.9
2_{11}-2_{12}	4973.6236	107.4	3_{03}-2_{12}	13761.4836	199.9
2_{02}-1_{11}	9277.9735	-6.1	3_{13}-2_{02}	14115.2277	-51.8
2_{12}-1_{01}	10496.3304	-89.1	4_{04}-3_{03}	17908.9571	-86.9
2_{11}-2_{02}	5266.1513	1.2			

[a] $\Delta\nu=\nu_{obs}-\nu_{calc}$ in kHz from rotational analysis.

Table A4.8 Measured transition frequencies (MHz) for the $\Sigma 0_{0a}$ states of $^{20}Ne_2$-NH_3 and $^{22}Ne_2$-NH_3.

		$^{20}Ne_2$-NH_3		$^{22}Ne_2$-NH_3	
$J'_{K_aK_c}$ $J''_{K_aK_c}$	F-F''	ν_{obs}	$\Delta\nu$	ν_{obs}	$\Delta\nu$
1_{01}-0_{00}		5920.6477[a]	583.2[b]	5707.4968	-592.0
	0-1	5920.4789	-0.9[c]	5707.3248	1.8
	2-1	5920.6315	0.6	5707.4797	0.3
	1-1	5920.7319	0.3	5707.5816	-2.1
2_{02}-1_{01}		10708.9874	0.0	10113.4810	0.0
	1-1			10113.3147	-2.2
	3-2	10708.9786	-1.6	10113.4768	0.4
	2-1	10708.9891	1.6		
	1-0			10113.5794	1.8
3_{03}-2_{02}		14737.6924	0.0	13741.6931	0.0
	2-2	14737.5357	1.9		
	4-3	14737.6877	2.4		
	3-2	14737.6985	-3.4	13741.6877	0.0
	2-1	14737.6985	-3.1		
	3-3	14737.8121	2.3		
3_{22}-2_{21}		17733.6937	-194.4	17039.6903	197.3
	2-1	17733.6126	2.9		
	4-3	17733.6654	-4.2	17093.6654	0.0
	3-2	17733.7791	1.3		

[a] Hypothetical center line frequency.
[b] $\Delta\nu=\nu_{obs}-\nu_{calc}$ in kHz from rotational analysis of center line frequency.
[c] $\Delta\nu=\nu_{obs}-\nu_{calc}$ in kHz from ^{14}N hyperfine analysis.

Table A4.9 Measured transition frequencies (MHz) for the $\Sigma 0_{0a}$ state of $^{20}Ne_2$-$^{15}NH_3$.

$J'_{K_aK_c}$-$J''_{K_aK_c}$	ν_{obs}	$\Delta\nu$[a]
1_{01}-0_{00}	5734.5064	721.4
2_{02}-1_{01}	10487.0390	0.0
3_{03}-2_{02}	14464.5173	0.0
3_{22}-2_{21}	17126.8864	-240.5

[a] $\Delta\nu=\nu_{obs}-\nu_{calc}$ in kHz from rotational analysis.

Table A4.10 Measured transition frequencies (in MHz) for the $\Sigma 0_0$ states of $^{20}Ne_2$-ND_3.

		$\Sigma 0_{0a}$		$\Sigma 0_{0s}$	
$J'_{K'a'c'}$ $J''_{K''a''c''}$	F'-F''	ν_{obs}	$\Delta\nu$	ν_{obs}	$\Delta\nu$
1_{01}-0_{00}		5451.4491[a]	867.4[b]	5451.4627	259.2
	0-1	5451.1389	5.4[c]		
	2-1	5451.4131	-4.4	5451.4330	-0.9
	1-1	5451.6059	-1.0	5451.6180	0.9
2_{02}-1_{01}		10125.8194	0.0	10125.8629	-371.9
	1-1	10125.4913	-3.9	10125.5290	0.8
	3-2	10125.8083	4.9	10125.8446	-0.8
	2-1	10125.8248	-3.2		
	1-0	10125.9695	0.8		
	2-2	10126.0188	1.4		
3_{03}-2_{02}		14043.5794	0.0	14043.6290	158.9
	4-3	14043.5609	-3.2	14043.6087	-0.3
	2-1	14053.5982	3.2	14043.6454	0.3
3_{22}-2_{21}		16330.3238	-289.1		
	4-3	16330.2782	-0.3		
	3-2	16330.4823	0.3		

[a] Hypothetical center line frequency.
[b] $\Delta\nu = \nu_{obs} - \nu_{calc}$ in kHz from rotational analysis of center line frequency.
[c] $\Delta\nu = \nu_{obs} - \nu_{calc}$ in kHz from ^{14}N hyperfine analysis.

Table A4.11 Measured transition frequencies (MHz) for the $\Sigma 0_{00}$ states of $^{20}Ne_2$-ND_2H.

		$\Sigma 0_{00s}$		$\Sigma 0_{00a}$	
$J'_{Ka'Kc'}$ $J''_{Ka''Kc''}$	F'-F''	ν_{obs}	$\Delta\nu$	ν_{obs}	$\Delta\nu$
1_{01}-0_{00}		5592.2092[a]	653.8[b]	5592.5058	163.3
	0-1	5591.9446	0.1[c]	5592.2373	-3.9
	2-1	5592.1815	-1.3	5592.4796	0.3
	1-1	5592.3428	1.2	5592.6417	3.6
2_{02}-1_{01}		10310.7659	0.0	10311.1788	-260.5
	1-1	10310.4890	-2.1	10310.9080	4.8
	3-2	10310.7509	-0.8	10311.1608	-3.5
	2-1	10310.7816	5.6	10311.1911	1.2
	1-0	10310.8899	1.7	10311.2963	-3.7
	2-2	10310.9304	-4.4	10311.3499	1.2
3_{03}-2_{02}		14257.3515	0.0	14258.0429	114.1
	4-3	14257.5165	-1.6	14258.0281	-1.1
	3-2	14257.5485	-2.9	14258.0598	-3.4
	2-1	14257.5485	4.4	14258.0598	4.6
3_{22}-2_{21}		16750.9266	-217.9		
	4-3	16750.8903	1.7		
	3-2	16751.0576	-1.7		

[a] Hypothetical center line frequency.
[b] $\Delta\nu=\nu_{obs}-\nu_{calc}$ in kHz from rotational analysis of center line frequency.
[c] $\Delta\nu=\nu_{obs}-\nu_{calc}$ in kHz from ^{14}N hyperfine analysis.

Table A4.12 Measured transition frequencies (MHz) for the $\Sigma 0_{00}$ states of $^{20}Ne_2$-NDH_2.

		$\Sigma 0_{00a}$		$\Sigma 0_{00a}$	
$J'_{Ka'Kc'}$ $J''_{Ka''Kc''}$	F'-F''	ν_{obs}	$\Delta\nu$	ν_{obs}	$\Delta\nu$
1_{01}-0_{00}		5746.3497[a]	169.3[b]	5747.0225	714.7
	0-1	5746.1358	-6.2[c]	5747.0225	-5.5
	2-1	5746.3298	0.9	5747.2360	10.2
	1-1	5746.4589	5.3	5747.3529	-4.7
2_{02}-1_{01}		10503.5077	-311.4	10504.4372	0.0
	1-1	10503.2957	-1.1	10504.4372	0.1
	3-2	10503.5036	5.7	10504.6462	-2.4
	2-1	10503.5234	12.5	10504.6661	6.1
	1-0	10503.6060	2.4	10504.7686	1.9
	2-2	10503.6209	-14.7	10504.7861	-5.7
3_{03}-2_{02}		14485.5809	143.5	14486.9874	0.0
	4-3	14485.5681	-3.3	14486.9874	-3.7
	3-2	14485.5946	0.4	14487.0151	1.1
	2-1	14485.5946	2.9	14487.0151	2.6
3_{22}-2_{21}				17214.4841	-238.2
	4-3			17214.4841	0.0

[a] Hypothetical center line frequency.
[b] $\Delta\nu=\nu_{obs}-\nu_{calc}$ in kHz from rotational analysis of center line frequency.
[c] $\Delta\nu=\nu_{obs}-\nu_{calc}$ in kHz from ^{14}N hyperfine analysis.

APPENDIX 5

Tables of *ab initio* data for the Ne_2-NH_3 trimer

Table A5.1 Interaction energies (μE_h) of Ne_2-NH_3 calculated at the CCSD(T) level for the equilibrium geometry of NH_3 (>HNH=106.67°) at β=90°.

				ϕ=0°			
R / θ	0°	30°	60°	90°	120°	150°	180°
2.75	488.5	206.9	116.9	-301.1	-446.3	-259.0	-144.6
2.80	294.2	59.6	-30.0	-386.6	-491.4	-323.2	-226.6
2.85	134.9	-60.9	-149.2	-452.2	-523.8	-373.2	-292.0
2.90	5.3	-158.3	-244.8	-501.0	-545.8	-411.3	-343.4
2.95	-99.4	-236.3	-320.4	-535.8	-558.5	-439.4	-383.0
3.00	-183.3	-297.9	-379.0	-559.1	-564.8	-459.1	-412.8
3.05	-249.3	-345.6	-423.3	-573.1	-564.7	-471.9	-434.1
3.10	-300.9	-381.8	-455.6	-579.2	-560.3	-479.0	-448.6
3.15	-340.1	-408.4	-478.2	-579.6	-552.4	-481.4	-457.3
3.20	-369.2	-426.8	-492.7	-574.1	-541.7	-480.1	-461.3
3.25	-390.1	-438.8	-500.4	-565.5	-529.1	-475.6	-461.4
3.30	-404.1	-445.3	-502.8	-553.7	-514.8	-468.8	-458.5
3.35	-412.4	-447.5	-500.9	-540.5	-499.4	-460.1	-453.1
3.40	-416.4	-446.1	-495.5	-524.4	-483.3	-449.9	-445.8
3.45	-416.5	-441.8	-487.5	-507.9	-466.8	-438.8	-436.9
3.50	-413.7	-435.4	-477.5	-490.7	-450.3	-426.9	-426.9
3.55	-408.7	-427.3	-465.7	-473.2	-433.8	-414.5	-416.0
3.60	-401.9	-417.8	-452.9	-455.6	-417.6	-401.8	-404.6
3.65	-393.8	-407.3	-439.4	-438.2	-401.7	-388.9	-392.9
3.70	-384.7	-396.5	-425.5	-421.1	-386.3	-376.3	-380.9
				ϕ=60°			
2.75	488.5	845.0	451.9	-254.5	-385.0	-216.4	-144.6
2.80	294.2	567.5	215.7	-366.6	-448.2	-291.1	-226.6
2.85	134.9	343.6	28.0	-450.2	-494.0	-349.5	-292.0
2.90	5.3	162.1	-119.6	-510.2	-525.6	-394.2	-343.4
2.95	-99.4	16.3	-234.2	-551.7	-545.7	-427.3	-383.0
3.00	-183.3	-100.2	-321.6	-577.8	-556.7	-451.0	-412.8
3.05	-249.3	-192.2	-387.1	-592.3	-560.1	-466.7	-434.1
3.10	-300.9	-263.8	-434.6	-597.2	-558.0	-476.0	-448.6
3.15	-340.1	-318.6	-467.6	-595.1	-551.6	-480.0	-457.3
3.20	-369.2	-359.6	-489.0	-587.4	-541.6	-479.1	-461.3
3.25	-390.1	-389.3	-501.2	-575.7	-529.1	-476.3	-461.4
3.30	-404.1	-409.8	-506.3	-560.8	-514.7	-470.2	-458.5
3.35	-412.4	-422.9	-505.4	-543.9	-499.2	-462.0	-453.1
3.40	-416.4	-429.8	-500.0	-525.7	-482.8	-452.1	-445.8
3.45	-416.5	-432.2	-492.1	-506.6	-466.1	-441.1	-436.9
3.50	-413.7	-430.5	-480.5	-487.1	-449.2	-430.4	-426.9
3.55	-408.7	-426.2	-467.5	-467.7	-432.5	-416.9	-416.0

Table A5.1 continued.

3.60	-401.9	-419.4	-453.6	-448.5	-416.0	-404.2	-404.6
3.65	-393.8	-410.9	-438.9	-429.7	-399.9	-391.5	-392.9
3.70	-384.7	-401.1	-423.8	-411.6	-384.3	-379.2	-380.9

Table A5.2 Interaction energies (μE_h) of Ne_2-NH_3 calculated at the CCSD(T) level for the intermediate geometry of NH_3 (>HNH=113.34°) at β=90°.

				ϕ=0°			
R / θ	0°	30°	60°	90°	120°	150°	180°
2.75	438.7	179.7	62.5	-257.2	-383.8	-131.3	-13.2
2.80	265.2	46.7	-71.6	-352.0	-440.2	-237.9	-111.6
2.85	123.2	-62.4	-180.3	-425.5	-482.3	-298.8	-191.7
2.90	6.4	-151.0	-267.1	-480.9	-512.2	-346.7	-256.2
2.95	-88.6	-222.2	-335.3	-521.2	-532.2	-383.4	-307.3
3.00	-165.3	-278.9	-388.1	-549.1	-544.2	-410.9	-347.1
3.05	-226.2	-322.8	-427.5	-566.9	-549.1	-430.5	-377.5
3.10	-274.3	-356.6	-455.9	-575.9	-549.0	-443.6	-399.8
3.15	-311.3	-381.5	-475.4	-578.3	-544.5	-451.2	-415.5
3.20	-339.3	-399.2	-487.5	-575.3	-536.6	-454.4	-425.6
3.25	-359.8	-410.9	-493.5	-568.2	-526.0	-454.0	-431.1
3.30	-374.0	-417.7	-494.5	-557.5	-513.5	-450.7	-432.9
3.35	-383.0	-420.4	-491.6	-544.4	-499.7	-445.1	-431.6
3.40	-388.0	-420.0	-485.7	529.6	-485.1	-437.6	-427.8
3.45	–389.3	-416.7	-477.2	-513.4	-469.6	-428.8	-422.0
3.50	-388.0	-411.4	-466.9	-496.5	-453.8	-418.9	-414.7
3.55	-384.5	-404.5	-455.3	-479.1	-437.9	-408.2	-406.2
3.60	-379.2	-396.4	-442.7	-461.6	-422.1	-397.0	-396.8
3.65	-372.7	-387.3	-429.4	-444.1	-406.6	-385.9	-386.8
3.70	-365.1	-377.6	-415.8	-426.8	-391.3	-373.8	-376.3
				ϕ=60°			
2.75	438.7	339.1	367.4	-204.0	-296.4	-91.4	-13.2
2.80	265.2	437.2	151.3	-329.5	-378.1	-184.6	-111.6
2.85	123.2	247.6	-19.9	-423.5	-439.1	-258.7	-191.7
2.90	6.4	93.8	-154.1	-491.8	-483.1	-317.0	-256.2
2.95	-88.6	-30.1	-257.9	-539.5	-513.2	-361.9	-307.3
3.00	-165.3	-129.3	-336.8	-570.7	-532.4	-395.7	-347.1
3.05	-226.2	-207.3	-395.2	-589.0	-542.3	-420.0	-377.5
3.10	-274.3	-268.4	-437.4	-596.6	-545.3	-437.0	-399.8
3.15	-311.3	-314.9	-466.2	-596.4	-542.9	-447.4	-415.5
3.20	-339.3	-349.8	-484.5	-596.4	-536.4	-452.8	-425.6

Table A5.2 continued.

3.25	-359.8	-375.1	-494.7	-590.2	-526.5	-453.9	-431.1
3.30	-374.0	-392.5	-497.4	-565.3	-514.2	-451.8	-432.9
3.35	-383.0	-403.5	-495.4	-545.7	-500.3	-446.9	-431.6
3.40	-388.0	-409.4	-489.4	-530.5	-485.1	-440.0	-427.8
3.45	–389.3	-410.9	-480.4	-511.5	-469.3	-431.5	-422.0
3.50	-388.0	-409.3	-469.2	-492.0	-453.0	-421.8	-414.7
3.55	-384.5	-405.0	-456.5	-472.7	-436.7	-411.2	-406.2
3.60	-379.2	-398.8	-442.8	-453.2	-420.5	-400.1	-396.8
3.65	-372.7	-391.1	-428.4	-434.2	-404.6	-388.2	-386.8
3.70	-365.1	-382.2	-413.7	-415.8	-389.1	-376.8	-376.3

Table A5.3 Interaction energies (μE_h) of Ne_2-NH_3 calculated at the CCSD(T) level for the planar geometry of NH_3 (>HNH=120.00°) at β=90°.

			ϕ=0°	
R / θ	0°	30°	60°	90°
2.75	271.9	56.6	-159.8	-201.6
2.80	136.5	-48.3	-253.8	-307.5
2.85	24.2	-134.4	-328.1	-390.4
2.90	-68.2	-204.3	-385.7	-453.7
2.95	-143.7	-283.6	-429.2	-500.8
3.00	-204.8	-304.5	-461.1	-534.2
3.05	-253.5	-338.6	-483.1	-556.4
3.10	-292.1	-364.3	-497.0	-569.4
3.15	-321.8	-382.9	-504.4	-574.8
3.20	-344.2	-395.8	-506.5	-574.3
3.25	-360.4	-403.9	-504.4	-568.8
3.30	-371.5	-408.0	-498.9	-559.9
3.35	-378.4	-409.0	-490.8	-548.0
3.40	-381.8	-407.1	-480.8	-534.0
3.45	-382.1	-403.1	-468.8	-518.5
3.50	-380.3	-397.3	-455.8	-502.0
3.55	-376.7	-390.3	-442.5	-484.9
3.60	-371.5	-382.3	-428.5	-467.4
3.65	-365.1	-373.5	-414.4	-450.0
3.70	-357.8	-364.2	-400.3	432.7
			ϕ=60°	
2.75	271.9	269.0	26.7	-142.4
2.80	136.5	118.7	-118.8	-283.4
2.85	24.2	-3.8	-232.2	-389.4

Table A5.3 continued.

2.90	-68.2	-102.8	-319.1	-467.2
2.95	-143.7	-182.1	-384.3	-422.3
3.00	-204.8	-245.1	-432.1	-559.2
3.05	-253.5	-294.1	-465.3	-581.7
3.10	-292.1	-331.5	-487.1	-592.7
3.15	-321.8	-359.7	-499.7	-595.1
3.20	-344.2	-379.8	-505.1	-590.7
3.25	-360.4	-392.4	-505.2	-581.5
3.30	-371.5	-401.7	-500.6	-568.1
3.35	-378.4	-405.7	-492.6	-552.3
3.40	-381.8	-406.2	-482.2	-534.5
3.45	-382.1	-404.0	-469.9	-515.8
3.50	-380.3	-399.5	-456.5	-496.3
3.55	-376.7	-393.4	-449.2	-476.9
3.60	-371.5	-85.9	-427.5	-457.4
3.65	-365.1	-377.4	-412.6	-437.9
3.70	-357.8	-368.3	397.8	-419.5

Table A5.4 Interaction energies (μE_h) of Ne_2-NH_3 calculated at the CCSD(T) level for the equilibrium geometry of NH_3 (>HNH=106.67°) at β=0°.

	ϕ=0°						
R / θ	0°	30°	60°	90°	120°	150°	180°
2.75	491.8	738.2	418.1	403.4	73.9	-157.6	-144.6
2.80	296.6	491.2	225.0	198.2	-80.5	-248.3	-226.6
2.85	136.5	288.4	66.1	31.6	-201.5	-319.3	-292.0
2.90	6.3	123.0	-63.3	-102.12	-295.2	-373.7	-343.4
2.95	-98.8	-10.9	-167.8	-208.3	-366.3	-414.7	-383.1
3.00	-182.8	-118.2	-251.0	-291.3	-418.9	-444.4	-412.8
3.05	-249.2	-203.4	-316.3	-354.9	-456.5	-464.8	-434.1
3.10	-301.0	-270.1	-366.5	-402.5	-481.7	-477.4	-448.6
3.15	-340.3	-321.4	-404.1	-436.9	-497.4	-483.7	-457.3
3.20	-369.6	-359.9	-431.3	-460.4	-505.2	-485.4	-461.3
3.25	-390.6	-388.0	-449.7	-475.0	-506.7	-483.4	-461.6
3.30	-404.5	-407.5	-461.1	-482.6	-503.4	-477.8	-458.6
3.35	-412.9	-419.9	-466.7	-484.6	-496.6	-470.2	-453.2
3.40	-416.7	-426.8	-467.7	-482.0	-487.0	-460.5	-445.7
3.45	-416.9	-429.1	-464.9	-475.9	-475.3	-449.5	-436.9
3.50	-414.1	-427.8	-459.1	-467.1	-462.2	-437.55	-427.0

Table A5.4 continued.

3.55	-409.1	-423.6	-451.1	-456.3	-448.1	-424.9	-416.1
3.60	-402.3	-417.2	-441.2	-444.3	-433.4	-411.8	-404.6
3.65	-394.2	-409.2	-430.1	-431.1	-418.5	-398.7	-392.9
3.70	-385.1	-399.9	-418.2	-417.4	-403.6	-385.5	-381.0
				ϕ=60°			
2.75	491.8	75.4	-160.6	-328.4	-400.2	-255.1	-144.6
2.80	296.6	-48.8	-256.6	-405.5	-457.1	-322.5	-226.6
2.85	136.5	-149.7	-332.0	-462.9	-498.5	-375.1	-292.0
2.90	6.3	-230.6	-390.1	-504.2	-526.9	-414.9	-343.4
2.95	-98.8	-294.5	-433.6	-532.5	-545.0	-444.3	-383.1
3.00	-182.8	-344.1	-465.2	-550.1	-554.4	-464.8	-412.8
3.05	-249.2	-382.1	-486.9	-558.9	-557.2	-478.1	-434.1
3.10	-301.0	-409.8	-500.3	-560.8	-554.6	-485.1	-448.6
3.15	-340.3	-429.4	-507.0	-557.4	-547.9	-487.3	-457.3
3.20	-369.6	-442.3	-508.5	-549.8	-537.9	-485.9	-461.3
3.25	-390.6	-449.6	-505.6	-538.8	-525.7	-481.3	-461.6
3.30	-404.5	-452.1	-499.2	-525.5	-511.5	-474.1	-458.6
3.35	-412.9	-451.0	-490.5	-510.8	-496.3	-465.2	-453.2
3.40	-416.7	-447.1	-479.6	-494.6	-480.3	-454.7	-445.7
3.45	-416.9	-440.9	-467.4	-477.8	-463.9	-443.1	-436.9
3.50	-414.1	-432.9	-454.0	-460.7	-447.5	-430.9	-427.0
3.55	-409.1	-423.5	-440.1	-443.5	-431.1	-418.1	-416.1
3.60	-402.3	-412.2	-425.8	-426.5	-414.9	-405.1	-404.6
3.65	-394.2	-402.2	-411.3	-409.7	-399.1	-392.0	-392.9
3.70	-385.1	-390.7	-397.0	-393.7	-383.7	-379.0	-381.0

Table A5.5 Interaction energies (μE_h) of Ne_2-NH_3 calculated at the CCSD(T) level for the intermediate geometry of NH_3 (>HNH=113.34°) at β=0°.

				ϕ=0°			
R / θ	0°	30°	60°	90°	120°	150°	180°
2.75	440.9	679.4	447.8	379.5	210.1	-12.2	-13.1
2.80	267.3	449.4	249.3	182.5	33.0	-125.3	-111.6
2.85	124.2	260.7	86.4	22.0	-107.7	-215.5	-191.7
2.90	6.9	106.8	-46.2	-107.3	-217.9	-286.5	-256.2
2.95	-88.3	-177.5	-153.0	-210.3	-303.2	-341.4	-307.3
3.00	165.1	-187.6	-237.9	-291.1	-367.8	-383.0	-347.1
3.05	-26.3	-197.1	-304.5	-353.3	-415.5	-413.5	-377.5
3.10	-274.6	-259.3	-355.7	-400.1	-449.3	-434.8	-399.9
3.15	-311.7	-307.3	-394.0	-434.0	-471.9	-448.8	-415.5

Table A5.5 continued.

3.20	-339.7	-343.6	-421.6	-457.4	-485.6	-457.0	-425.5
3.25	-360.3	-370.1	-440.5	-472.2	-492.2	-460.0	-431.1
3.30	-374.4	-388.5	-452.3	-479.9	-493.0	-459.2	-432.9
3.35	-383.5	-400.5	-458.1	-482.1	-489.4	-455.2	-434.4
3.40	-388.3	-407.3	-459.3	-479.2	-482.4	-448.7	-427.8
3.45	-389.7	-409.8	-456.7	-474.2	-472.9	-440.4	-422.0
3.50	-388.4	-408.9	-451.2	-465.9	-461.6	-430.7	-414.8
3.55	-384.9	-405.3	-443.4	-455.5	-449.1	-420.0	-406.3
3.60	-379.6	-399.7	-433.9	-443.7	-435.5	-408.5	-396.9
3.65	-373.0	-392.5	-423.1	-430.9	-421.2	-396.7	-386.9
3.70	-365.4	-384.1	-411.5	-417.5	-406.9	-384.5	-376.3
				ϕ=60°			
2.75	440.9	94.6	-164.1	-309.8	-337.5	-154.8	-13.1
2.80	267.3	-24.2	-255.0	-386.6	-403.3	-235.1	-111.6
2.85	124.2	-121.3	-326.6	-444.7	-452.6	-299.1	-191.7
2.90	6.9	-199.7	-381.7	-486.6	-487.8	-349.2	-256.2
2.95	-88.3	-261.9	-422.8	-515.9	-511.8	-387.3	-307.3
3.00	165.1	-310.8	-452.8	-534.4	-526.7	-415.8	-347.1
3.05	-226.3	-348.6	-473.3	-544.5	-533.8	-435.9	-377.5
3.10	-274.6	-376.9	-486.0	-547.4	-535.7	-449.2	-399.9
3.15	-311.7	-397.1	-482.2	-545.2	-531.8	-456.8	-415.5
3.20	-339.7	-411.0	-493.6	-538.6	-524.8	-460.1	-425.5
3.25	-360.3	-419.4	-490.9	528.6	-514.9	-459.5	-431.1
3.30	-374.4	-423.3	-484.8	-516.4	-502.9	-456.0	-432.9
3.35	-383.5	-423.8	-476.3	-502.6	-489.2	-450.1	-434.4
3.40	-388.3	-421.5	-466.0	-487.2	-475.1	-442.3	-427.8
3.45	-389.7	-416.8	-454.3	-471.2	-460.0	-433.1	-422.0
3.50	-388.4	-410.4	-441.5	-454.9	-444.5	-422.8	-414.8
3.55	-384.9	-402.6	-428.2	-438.3	-429.0	-411.8	-406.3
3.60	-379.6	-393.7	-414.5	-421.9	-413.5	-400.3	-396.9
3.65	-373.0	-384.1	-400.8	-405.9	-398.3	-388.5	-386.9
3.70	-365.4	-374.0	-387.1	-390.1	-383.5	-376.5	-376.3

Table A5.6 Interaction energies (μE_h) of Ne_2-NH_3 calculated at the CCSD(T) level for the planar geometry of NH_3 (>HNH=106.67°) at β=0°.

		ϕ=0°		
R / θ	0°	30°	60°	90°
2.75	272.5	376.8	427.5	330.9
2.80	137.0	203.3	222.9	146.7
2.85	24.6	61.9	57.1	-3.7
2.90	-68.1	-52.6	-76.0	-125.3
2.95	-143.7	-144.5	-181.8	-222.4
3.00	-204.8	-217.3	-264.8	-298.7
3.05	-253.7	-274.4	-328.3	-358.0
3.10	-292.2	-318.5	-376.6	-402.4
3.15	-321.9	-351.6	-411.8	-434.7
3.20	-344.3	-375.5	-436.2	-456.9
3.25	-360.6	-392.4	-452.1	-470.8
3.30	-371.7	-403.1	-460.9	-478.4
3.35	-378.6	-408.9	-464.3	-480.4
3.40	-381.9	-410.5	-463.1	-478.2
3.45	-382.4	-409.5	-458.6	-472.6
3.50	-380.6	-405.7	-451.3	-464.4
3.55	-376.9	-399.9	-442.0	-454.4
3.60	-371.7	-392.8	-431.4	-442.7
3.65	-365.3	-384.3	-419.6	-430.2
3.70	-358.0	-382.2	-407.2	-416.9
		ϕ=60°		
2.75	272.5	46.0	-207.0	-284.1
2.80	137.0	-59.3	-289.3	-361.5
2.85	24.6	-145.3	-353.1	-420.3
2.90	-68.1	-214.7	-402.2	-463.6
2.95	-143.7	-270.1	-437.9	-494.1
3.00	-204.8	-313.5	-463.1	-514.2
3.05	-253.7	-346.8	-479.8	-525.5
3.10	-292.2	-371.8	-489.0	-530.2
3.15	-321.9	-390.0	-492.7	-529.3
3.20	-344.3	-401.7	-491.6	-524.1
3.25	-360.6	-409.0	-487.2	-515.8
3.30	-371.7	-412.4	-479.7	-504.6
3.35	-378.6	-412.6	-470.4	-491.8
3.40	-381.9	-410.1	-459.2	-477.9
3.45	-382.4	-405.4	-447.0	-462.8
3.50	-380.6	-399.2	-434.0	-447.4
3.55	-376.9	-391.9	-420.5	-431.7
3.60	-371.7	-383.3	-406.9	-416.0
3.65	-365.3	-374.2	-393.2	-400.5
3.70	-358.0	-364.7	-379.5	-385.4

Table A5.7 Interaction energies (μE_h) of Ne_2-NH_3 calculated at the CCSD(T) level for the equilibrium geometry of NH_3 (>HNH=106.67°) at β=90° using the aug-cc-pVDZ basis set for Ne.

				ϕ=0°			
R / θ	0°	30°	60°	90°	120°	150°	180°
2.90					-547.9		
2.95					-560.7		
3.00					-567.1		
3.05				-544.4	-567.0	-492.9	
3.10				-553.7	-562.5	-497.8	-472.3
3.15				-556.9		-498.1	-478.6
3.20			-464.4	-554.8		-494.8	-480.3
3.25		-422.2	-475.7	-548.6		-488.6	-478.4
3.30		-430.2	-481.4				-473.5
3.35	-401.6	-43.8	-482.3				-466.4
3.40	-406.0	-433.7	-479.5				
3.45	-406.8	-430.6	-473.7				
3.50	-404.7						
3.55	-400.2						
				ϕ=60°			
2.90					-550.4		
2.95					-561.5		
3.00				-556.7	564.9		
3.05				-574.6	-562.6	-486.5	
3.10			-403.4	-582.5	-555.8	-493.7	-472.3
3.15			-440.8	-583.0		-495.8	-478.6
3.20			-466.2	-577.5		-494.0	-480.3
3.25			-481.9	-567.8		-488.9	-478.4
3.30			-489.8				-473.5
3.35	-401.6	-408.4	-491.7				-466.4
3.40	-406.0	-417.2	-488.4				
3.45	-406.8	-421.0	-481.6				
3.50	-404.7	-420.9					
3.55	-400.2	-417.5					

Table A5.8 Interaction energies (μE_h) of Ne_2-NH_3 calculated at the CCSD(T) level for the intermediate geometry of NH_3 (>HNH=113.34°) at β=90° using the aug-cc-pVDZ basis set for Ne.

				ϕ=0°			
R / θ	0°	30°	60°	90°	120°	150°	180°
3.00					-539.3		
3.05				-533.5	-545.0		
3.10				-546.5	-545.4	-459.3	
3.15				-552.5	-541.3	-465.1	
3.20			-462.5	-552.9	-534.1	-466.7	-441.9
3.25		-400.4	-471.6	-548.6		-464.8	-445.6
3.30		-407.9	-475.6	-540.9		-460.0	-445.6
3.35	-376.9	-411.4	-475.3				-442.7
3.40	-381.7	-411.6	-471.7				-437.5
3.45	-383.3	-409.0					
3.50	-382.1						
3.55	-378.8						
				ϕ=60°			
3.00				-546.1	-531.4		
3.05				-568.4	-542.0		
3.10				-579.6	-545.6		
3.15				-582.6	-543.6	-460.3	
3.20			-465.9	-578.9	-537.2	-464.1	-441.9
3.25			-478.5	-570.5		-463.9	-445.6
3.30			-484.2			-460.5	-445.6
3.35	-376.9	-394.4	-484.4			-454.5	-442.7
3.40	-381.7	-401.1	-480.2				-437.5
3.45	-383.3	-403.8	-473.0				
3.50	-382.1	-402.9					
3.55	-378.8	-399.3					

Table A5.9 Interaction energies (μE_h) of Ne_2-NH_3 calculated at the CCSD(T) level for the planar geometry of NH_3 (>HNH=120.00°) at β=90° using the aug-cc-pVDZ basis set for Ne.

		ϕ=0°		
R / θ	0°	30°	60°	90°
3.10			-478.3	-536.1
3.15			-487.8	-546.2
3.20			-492.0	-549.6
3.25		-406.0	-491.7	-547.7
3.30	-375.7	-409.3	-488.1	-541.4
3.35	-381.7	-409.6		
3.40	-384.4	-407.3		
3.45	-384.2	-403.2		
3.50	-381.7			
3.55	-377.5			
		ϕ=60°		
3.05				-558.8
3.10				-573.8
3.15			-489.4	-579.7
3.20			-496.6	-578.3
3.25			-497.9	-571.3
3.30	-375.7	-402.7	-494.6	
3.35	-381.7	-406.3	-487.9	
3.40	-384.4	-406.7		
3.45	-384.2	-404.1		
3.50	-381.7	-399.4		
3.55	-377.5			

APPENDIX 6

Tables of microwave transition frequencies measured for the Rg_3-NH_3 trimers

Table A6.1 Measured transition frequencies (MHz) for the $\Sigma 0_{0a}$ state of Ar_3-NH_3.

J'K'-J"K"	F'-F"	ν_{obs}	$\Delta\nu$[a]	J'K'-J"K"	F'-F"	ν_{obs}	$\Delta\nu$
2_0-1_0	1-1	4583.2552	-6.7	5_0-4_0	4-3	11455.6304	-1.0
	3-2	4583.3316	-3.2		5-4	11455.6304	0.8
	2-1	4583.3316	-0.1		6-5	11455.6304	1.5
	1-0	4583.3562	-15.1				
				5_3-4_3	6-5	11455.9577	11.9
3_0-2_0	3-2	6874.6156	0.1				
	4-3	6874.6156	1.9	6_0-5_0	5-4	13745.0521	-2.7
	2-1	6874.6310	8.3		6-5	13745.0521	-1.6
	3-3	6874.6621	-0.2		7-6	13745.0521	-1.1
4_0-3_0	3-2	9165.4349	-0.2	6_3-5_3	7-6	13745.4415	4.9
	4-3	9165.4349	2.9				
	5-4	9165.4349	4.0	7_0-6_0	6-5	16033.5433	-7.1
					7-6	16033.5433	-6.3
4_3-3_3	5-4	9165.6716	-7.6		8-7	16033.5433	-5.9
				7_3-6_3	8-7	16034.0019	3.8
				7_6-6_6			
					8-7	16035.3418	-3.1

[a] $\Delta\nu=\nu_{obs}-\nu_{calc}$ in kHz.

Table A6.2 Measured transition frequencies (MHz) for the $\Sigma 0_{0a}$ state of Ar_3-$^{15}NH_3$.

J'K'-J"K"	ν_{obs}	$\Delta\nu$[a]	J'K'-J"K"	ν_{obs}	$\Delta\nu$
2_0-1_0	4509.0795	-0.6	6_0-5_0	13522.5347	0.5
3_0-2_0	6763.2520	-0.4	6_3-5_3	13522.8499	-1.1
4_0-3_0	9016.9839	0.3	7_0-6_0	15774.0612	1.8
4_3-3_3	9017.1947	-0.1	7_3-6_3	15774.4262	-2.8
5_0-4_0	11270.1278	1.3	7_6-6_6	15775.5388	1.0
5_3-4_3	11270.3903	-0.3			

[a] $\Delta\nu=\nu_{obs}-\nu_{calc}$ in kHz.

Table A6.3 Measured transition frequencies (MHz) for the $\Sigma 0_0$ states of Ar_3-ND_3.

		$\Sigma 0_{0a}$		$\Sigma 0_{0a}$	
J'K'-J"K"	F-F"	ν_{obs}	$\Delta\nu$[a]	ν_{obs}	$\Delta\nu$
2_0-1_0	1-1	4354.0010	-6.5		
	2-1	4354.1618	-4.8	4354.0875	-7.5
	3-2	4354.1618	2.0	4354.0875	-0.7
	1-0	4354.2515	-10.6		
3_0-2_0	3-2	6530.9296	1.4	6530.8234	2.2
	4-3	6530.9296	5.2	6530.8234	6.1
4_0-3_0	3-2	8707.3046	-5.8	8707.1622	-6.2
	4-3	8707.3046	1.0	8707.1622	0.7
	5-4	8707.3046	3.4	8707.1622	3.1
4_3-3_3	5-4	8707.3410	0.3	8707.2013	2.9
5_0-4_0	4-3	10883.1717	9.1	10882.9849	-6.5
	5-4	10883.1717	7.4	10882.9849	3.1
	6-5	10883.1717	3.7	10882.9849	-1.0
5_3-4_3	6-5	10883.2293	3.0	10883.0484	-1.0
6_0-5_0	5-4	13058.3829	-0.1	13058.1737	0.6
	6-5	13058.3829	1.5	13058.1737	3.0
	7-6	13058.3829	2.7	13058.1737	4.3
6_3-5_3	7-6	13058.4638	0.5	13058.2515	-1.1
7_0-6_0	6-5	15232.8257	-2.2		
	7-6	15232.8257	-0.6		
	8-7	15232.8257	0.3		
7_3-6_3	8-7	15232.9222	-3.8		
7_6-6_6	8-7	15233.2280	0.3		

[a] $\Delta\nu = \nu_{obs} - \nu_{calc}$ in kHz.

Table A6.4 Measured transition frequencies (MHz) for the $\Sigma 0_{00}$ states of Ar_3-ND_2H.

		$\Sigma 0_{00a}$		$\Sigma 0_{00s}$	
J'K'-J"K"	F'-F"	ν_{obs}	$\Delta\nu$[a]	ν_{obs}	$\Delta\nu$
2_0-1_0	1-1	4425.7788	0.5	4425.8228	-0.2
	2-1	4425.9191	-4.9	4425.9612	-5.1
	3-2	4425.9191	1.4	4425.9612	1.0
3_0-2_0	3-2	6638.5351	1.4	6638.5955	-1.4
	4-3	6638.5351	4.9	6638.5955	2.0
4_0-3_0	3-2	8850.7219	-5.0	8850.8032	-7.3
	4-3	8850.7219	1.3	8850.8032	-1.2
	5-4	8850.7219	3.5	8850.8032	1.0
4_3-3_3	5-4	8850.8433	-1.8	8850.9314	2.7
5_0-4_0	4-3	11062.3469	-0.5	11062.4507	-0.4
	5-4	11062.3469	3.0	11062.4507	3.0
	6-5	11062.3469	4.6	11062.4507	4.5
5_3-4_3	6-5	11062.5098	-4.0	11062.6160	-1.2
6_0-5_0	5-4	13273.2654	0.7	13273.3866	-1.5
	6-5	13273.2654	2.9	13273.3866	0.7
	7-6	13273.2654	4.0	13273.3866	1.8
6_3-5_3	7-6	13273.4730	-0.3	13273.5957	-0.3
7_0-6_0	6-5	15483.3383	1.1	15483.4799	0.5
	7-6	15483.3383	2.6	15483.4799	2.1
	8-7	15483.3383	3.5	15483.4799	2.9
7_3-6_3	8-7	15483.5798	-5.5	15483.7238	-2.9
7_6-6_6	8-7	15484.3391	2.4	15484.4764	0.6

[a] $\Delta\nu = \nu_{obs} - \nu_{calc}$ in kHz.

Table A6.5 Measured transition frequencies (MHz) for the $\Sigma 0_{00}$ states of Ar_3-NDH_2.

		$\Sigma 0_{00s}$		$\Sigma 0_{00a}$	
J'K'-J"K"	F-F"	ν_{obs}	$\Delta\nu$[a]	ν_{obs}	$\Delta\nu$
2_0-1_0	1-1	4500.4642	-5.8	4500.8623	-6.5
	2-1	4500.5774	-1.6	4500.9750	-1.5
	3-2	4500.5774	3.1	4500.9750	3.1
	1-0	4500.6208	-12.7	4501.0167	-13.7
3_0-2_0	3-2	6750.4901	2.9	6751.0887	3.2
	4-3	6750.4901	5.5	6751.0887	5.7
4_0-3_0	3-2	8999.9473	-0.4	9000.7455	1.4
	4-3	8999.9473	4.3	9000.7455	6.0
	5-4	8999.9473	5.9	9000.7455	7.7
4_3-3_3	5-4	9000.1412	-5.8	9000.9432	-3.3
5_0-4_0	4-3	11248.7973	4.9	11249.7932	4.1
	5-4	11248.7973	7.5	11249.7932	6.6
	6-5	11248.7973	8.6	11249.7932	7.8
5_3-4_3	6-5	11249.0558	0.4	11250.0558	-0.1
6_0-5_0	5-4	13496.8785	-0.5	13498.0773	0.5
	6-5	13496.8785	1.2	13498.0773	2.1
	7-6	13496.8785	2.0	13498.0773	2.9
6_3-5_3	7-6	13497.2071	5.9	13498.4049	1.4
7_0-6_0	6-5	15744.0479	-6.9	15745.4516	-3.2
	7-6	15744.0479	-5.7	15745.4516	-2.1
	8-7	15744.0479	-5.1	15745.4516	-1.4
7_3-6_3	8-7	15744.4343	-0.1	15745.8362	-3.2
7_6-6_6	8-7	15745.5778	-0.5	15746.9996	1.0

[a] $\Delta\nu=\nu_{obs}-\nu_{calc}$ in kHz.

Table A6.6 Measured transition frequencies (MHz) for the $\Sigma 0_{0a}$ state of Ne_3-NH_3.

		$^{20}Ne_3$-NH_3		$^{22}Ne_3$-NH_3	
J'K'-J"K"	F'-F"	ν_{obs}	$\Delta\nu^a$	ν_{obs}	$\Delta\nu$
1_0-0_0	0-1	4148.3448	-3.3	3942.6028	-0.2
	2-1	4148.5157	-5.6	3942.7794	-3.9
	1-1	4148.6362	0.7	3942.9022	-1.3
2_0-1_0	1-1	8295.1726	-2.1		
	3-2	8295.3640	0.8	7884.0561	-3.1
	2-1	8295.3755	3.8	7884.0717	3.9
	1-0	8295.4664	-3.7		
	2-2	8295.4926	2.8		
3_0-2_0	3-2	12438.7833	6.5	11822.2552	0.7
	4-3	12438.7833	1.8	11822.2552	5.4
4_0-3_0	3-2	16577.0602	-8.4	15755.8250	-8.0
	4-3	16577.0602	0.0	15755.8250	0.6
	5-4	16577.0602	3.0	15755.8250	3.6

[a] $\Delta\nu=\nu_{obs}-\nu_{calc}$ in kHz.

Table A6.7 Measured transition frequencies (MHz) for the $\Sigma 0_{0a}$ state of Ne_3-$^{15}NH_3$.

	$^{20}Ne_3$-$^{15}NH_3$		$^{22}Ne_3$-$^{15}NH_3$	
J'K'-J"K"	ν_{obs}	$\Delta\nu^a$	ν_{obs}	$\Delta\nu$
1_0-0_0	3850.7429	-0.3	4050.8352	-1.4
2_0-1_0	7700.0513	0.3	8100.0730	-0.4
3_0-2_0	11546.4879	0.0	12146.1122	1.5
4_0-3_0	15388.6118	-0.5	16187.3483	-0.5

[a] $\Delta\nu=\nu_{obs}-\nu_{calc}$ in kHz.

Table A6.8 Measured transition frequencies (MHz) for the $\Sigma 0_0$ states of $^{20}Ne_3$-ND_3.

		$\Sigma 0_{0s}$		$\Sigma 0_{0a}$	
J'K'-J"K"	F'-F"	ν_{obs}	$\Delta\nu$[a]	ν_{obs}	$\Delta\nu$
1_0-0_0	0-1	3886.8947	-0.6		
	2-1	3887.2035	-4.2		
	1-1	3887.4137	-2.3		
2_0-1_0	1-1	7772.7623	-5.0		
	3-2	7773.0986	-1.0	7773.0858	5.0
	1-0	7773.2902	2.2		
3_0-2_0	2-2	11655.9401	6.9		
	4-3	11656.2370	-0.4	11656.2032	-6.0
	3-2	11656.2483	2.6		
	3-3	11656.4691	0.2		
4_0-3_0	4-3	15535.2587	-7.1	15535.2276	-0.6
	5-4	15535.2587	-1.8	15535.2276	4.6
	3-2	15535.2818	1.1		

[a] $\Delta\nu=\nu_{obs}-\nu_{calc}$ in kHz.

Table A6.9 Measured transition frequencies (MHz) for the $\Sigma 0_{00}$ states of $^{20}Ne_3$-ND_2H.

		$\Sigma 0_{00s}$		$\Sigma 0_{00a}$	
J'K'-J"K"	F'-F"	ν_{obs}	$\Delta\nu$[a]	ν_{obs}	$\Delta\nu$
1_0-0_0	2-1	3967.7700	-5.1	3967.9096	-7.6
	1-1	3967.9583	-8.3	3968.0959	-14.2
2_0-1_0	1-1	7933.7854	4.1	7934.3753	2.1
	3-2	7934.0799	-7.0	7934.5605	12.8
	1-0	7934.2749	14.7		
3_0-2_0	4-3	11897.3557	-4.0	11897.7919	-1.4
4_0-3_0	4-3	15856.0917	2.8	15856.6763	-3.4
	5-4	15856.0917	-2.0	15856.6763	1.5

[a] $\Delta\nu=\nu_{obs}-\nu_{calc}$ in kHz.

Table A6.10 Measured transition frequencies (MHz) for the $\Sigma 0_{00}$ states of $^{20}Ne_3$-NDH_2.

		$\Sigma 0_{00s}$		$\Sigma 0_{00a}$	
J'K'-J"K"	F'-F"	ν_{obs}	$\Delta\nu$[a]	ν_{obs}	$\Delta\nu$
1_0-0_0	0-1	4053.5496	1.7	4054.0273	1.4
	2-1	4053.7722	-5.1	4054.2487	-2.6
	1-1	4053.9211	-9.2	4054.3971	-4.4
2_0-1_0	1-1	8105.7110	1.6	8106.6609	-0.4
	3-2	8105.9478	-5.6	8106.8966	-4.3
	1-0	8106.1059	14.1	8107.0423	5.5
3_0-2_0	4-3	12154.8346	-2.6	12156.2625	3.2
4_0-3_0	4-3	16198.7965	2.0	16200.6930	-3.2
	5-4	16198.7965	-2.0	16200.6930	0.6

[a] $\Delta\nu=\nu_{obs}-\nu_{calc}$ in kHz.

Table A6.11 Measured transition frequencies (MHz) for the $\Sigma 0_{0a}$ state of $^{20}Ne_2{}^{22}Ne$-NH_3.

J'K_a'K_c'- J"K_a"K_c"	F'-F"	ν_{obs}	$\Delta\nu$[a]	J'K_a'K_c'- J"K_a"K_c"	F'-F"	ν_{obs}	$\Delta\nu$
1_{01}-0_{00}	0-1	4076.3953	29.8	3_{12}-2_{11}	2-1	12294.1999	0.0
	2-1	4076.5693	-4.7		4-3	12294.1999	8.7
	1-1	4076.6882	-24.7				
				3_{22}-2_{21}	3-3	12221.2639	16.5
1_{11}-0_{00}	1-1	4293.3034	29.7		4-3	12221.2639	16.5
	2-1	4293.3587	-16.2		3-2	12221.3784	-17.9
					2-2	12221.3784	-17.9
2_{02}-1_{01}	1-1	8143.1652	20.9				
	3-2	8143.3502	-10.4	3_{21}-2_{20}	3-3	12252.3754	17.3
	1-0	8143.4536	-38.1		4-3	12252.3754	-5.9
					3-2	12252.5021	12.8
2_{12}-1_{11}	1-0	8099.5212	37.0		2-2	12252.5021	-18.5
	3-2	8099.6463	-12.2				
				4_{04}-3_{03}	3-2	16218.0636	2.9
2_{11}-1_{10}	3-2	8202.6944	11.0		5-4	16218.0636	-12.0
	2-1	8202.8164	-13.1				
				4_{14}-3_{13}	3-2	16172.2340	-9.9
2_{02}-1_{11}	3-2	7926.5664	6.7		5-4	16172.2340	6.2
2_{12}-1_{01}	2-1	8316.3798	18.9	4_{13}-3_{12}	3-2	16372.7404	10.0
	3-2	8316.4348	-24.6		5-4	16372.7404	-0.4
3_{03}-2_{02}	3-2	12191.7466	-8.1	4_{23}-3_{22}	5-4	16280.9855	6.4
	4-3	12191.7466	0.0		4-3	16281.0312	-8.6
3_{13}-2_{12}	2-1	12140.7018	-9.6	4_{22}-3_{21}	5-4	16351.9352	-3.6
	4-3	12140.7018	4.8				

[a] $\Delta\nu=\nu_{obs}-\nu_{calc}$ in kHz.

Table A6.12 Measured transition frequencies (MHz) for the $\Sigma 0_{0a}$ state of $^{20}Ne_2{}^{22}Ne$-$^{15}NH_3$.

$J'K_a'K_c'$-$J''K_a''K_c''$	ν_{obs}	$\Delta\nu$[a]	$J'K_a'K_c'$-$J''K_a''K_c''$	ν_{obs}	$\Delta\nu$
1_{01}-0_{00}	3981.1013	-4.4	3_{12}-2_{11}	12006.4808	0.7
1_{11}-0_{00}	4246.4074	-5.1	3_{22}-2_{21}	11935.1642	9.4
2_{02}-1_{01}	7954.3439	-2.3	3_{21}-2_{20}	11959.5488	7.9
2_{12}-1_{11}	7910.8247	-3.2	4_{04}-3_{03}	15851.1352	8.3
2_{11}-1_{10}	8009.8015	-2.7	4_{14}-3_{13}	15798.3064	-5.7
2_{02}-1_{11}	7689.0357	-3.7	4_{13}-3_{12}	15992.5937	3.2
2_{12}-1_{01}	8176.1344	-0.3	4_{23}-3_{22}	15901.4611	-6.9
3_{03}-2_{02}	11912.5152	4.1	4_{22}-3_{21}	15958.6767	-6.0
3_{13}-2_{12}	11858.7411	-1.4			

[a] $\Delta\nu=\nu_{obs}-\nu_{calc}$ in kHz.

Table A6.13 Measured transition frequencies (MHz) for the $\Sigma 0_{0a}$ state of $^{20}Ne^{22}Ne_2$-NH_3.

$J'K_a'K_c'$-$J''K_a''K_c''$	F'-F''	ν_{obs}	$\Delta\nu$[a]	$J'K_a'K_c'$-$J''K_a''K_c''$	F'-F''	ν_{obs}	$\Delta\nu$
1_{01}-0_{00}	0-1	4008.4699	2.1	3_{22}-2_{21}	3-3	12017.5990	3.0
	2-1	4008.6406	-1.3		4-3	12017.5990	3.0
	1-1	4008.7598	1.8		3-2	12017.7234	3.0
					2-2	12017.7234	3.0
1_{10}-0_{00}	2-1	4246.1589	0.4				
				3_{21}-2_{20}	3-3	12060.3063	-6.7
2_{02}-1_{01}	3-2	8004.4282	0.5		4-3	12060.3063	-2.6
	1-0	8004.5383	4.5		3-2	12060.4340	-1.5
					2-2	12060.4340	4.0
2_{12}-1_{11}	3-2	7958.9581	0.6				
	2-1	7959.0730	-5.2	4_{04}-3_{03}	3-2	15925.4402	-8.2
					5-4	15925.4402	2.9
2_{11}-1_{10}	3-2	8071.8241	-3.1				
	2-1	8071.9471	0.0	4_{14}-3_{13}	3-2	15886.6234	0.7
					5-4	15886.6234	6.3
2_{11}-1_{01}	3-2	8309.3436	-0.2				
				4_{13}-3_{12}	3-2	16103.0244	-2.2
3_{03}-2_{02}	3-2	11977.1013	-2.0		5-4	16103.0244	2.7
	4-3	11977.1013	0.4				
				4_{23}-3_{22}	5-4	16006.9596	1.9
3_{13}-2_{12}	2-1	11928.0986	-1.7		4-3	16007.0055	-4.4
	4-3	11928.0986	0.2				
				4_{22}-3_{21}	5-4	16100.5828	1.2
3_{12}-2_{11}	2-1	12095.7100	0.3				
	4-3	12095.7100	0.3				

[a] $\Delta\nu=\nu_{obs}-\nu_{calc}$ in kHz.

Table A6.14 Measured transition frequencies (MHz) for the $\Sigma 0_{0a}$ state of $^{20}Ne^{22}Ne_2$-$^{15}NH_3$.

$J'K_a'K_c'$- $J''K_a''K_c''$	ν_{obs}	$\Delta\nu$[a]	$J'K_a'K_c'$- $J''K_a''K_c''$	ν_{obs}	$\Delta\nu$
1_{01}-0_{00}	3914.9019	-1.7	3_{12}-2_{11}	11812.9390	15.5
1_{10}-0_{00}	4197.8160	-7.8	3_{22}-2_{21}	11736.7321	11.7
2_{02}-1_{01}	7819.9325	0.0	3_{21}-2_{20}	11769.1881	11.8
2_{12}-1_{11}	7774.3310	-1.8	4_{04}-3_{03}	15570.7990	-3.3
2_{11}-1_{10}	7881.6607	0.7	4_{14}-3_{13}	15522.4574	-9.1
2_{11}-1_{01}	8164.5768	2.9	4_{13}-3_{12}	15731.4962	-2.2
3_{03}-2_{02}	11706.4680	0.0	4_{23}-3_{22}	15709.5643	-10.5
3_{13}-2_{12}	11652.9692	-3.6	4_{22}-3_{21}	15635.2920	-10.4

[a] $\Delta\nu=\nu_{obs}-\nu_{calc}$ in kHz.

APPENDIX 7

Tables of *ab initio* data for the Ne_3-NH_3 tetramer

Table A7.1 Interaction energies (μE_h) of Ne_3-NH_3 calculated at the CCSD(T) level for the equilibrium geometry of NH_3 (>HNH=106.67°).[a]

				ϕ=0°			
R / θ	0°	30°	60°	90°	120°	150°	180°
2.80					-975.1		
2.85							
2.90			-782.8	-970.9	-1016.3	-942.1	-905.8
2.95				-991.3	-1019.6	-952.5	-918.3
3.00	-692.8		-869.0	-1000.3	-1016.5	-954.5	-925.3
3.05				-1000.6	-1005.7	-951.8	-925.1
3.10	-769.4	-792.3	-905.8	-993.7	-992.6	-945.3	-924.1
3.15			-910.6				
3.20	-806.3	-830.2	-908.8	-964.6	-953.4	-918.9	-904.8
3.25	-813.3	-837.1	-901.8				
3.30	-814.5	-838.0	-890.7			-885.2	-876.6
3.35	-8115	-837.1					
3.40	-805.0	-826.5				-845.2	-841.8
3.45							
3.50	-784.2						
				ϕ=60°			
2.90				-859.8	-972.4	-954.1	-905.8
2.95					-981.2	-960.4	-918.3
3.00	-692.8			-917.3	-987.3	-959.0	-925.3
3.05				-930.3	-984.5	-954.0	-925.1
3.10	-769.4	-816.7	-877.8	-935.9	-975.5	-946.6	-924.1
3.15			-886.4	-934.8	-962.8		
3.20	-806.3	-838.4	-888.8	-928.7	-946.3	-917.4	-904.8
3.25	-813.3	-840.7	-885.8				
3.30	-814.5	-837.4	-879.3		-907.1	-882.9	-876.6
3.35	-8115						
3.40	-805.0	-821.9	-855.7			-842.5	-841.8
3.45							
3.50	-784.2						
3.55							

[a] An addition θ angle (105°) was included for ϕ=0°. The minimum energy at this orientation was -1026.9 μE_h at R=2.95 Å.

Table A7.2 Interaction energies (μE_h) of Ne_3-NH_3 calculated at the CCSD(T) level for the intermediate geometry of NH_3 (>HNH=113.34°).

				ϕ=0°			
R / θ	0°	30°	60°	90°	120°	150°	180°
2.90				-953.6	-976.5	-873.2	-824.1
2.95				-976.2	-988.1	-893.5	
3.00			-866.3	-987.1	-990.3	-906.8	-863.2
3.05				-989.1	-1004.4	-912.0	-876.2
3.10			-897.5	-983.5	-975.3	-910.3	-875.1
3.15			-900.7			-904.9	-877.2
3.20	-774.7	-808.0	-897.9			-894.9	-871.9
3.25	-781.6	-814.1	-889.8				
3.30	-783.0	-814.6	-878.5				-853.0
3.35	-780.9	-810.7					
3.40	-775.3	-803.5					-825.4
3.45							
3.50	-781.6						
				ϕ=60°			
2.90					-924.0	-890.0	-824.1
2.95						-905.6	
3.00		-743.4	-826.3	-906.8	-954.4	-913.5	-863.2
3.05				-921.4	-957.9	-915.3	-876.2
3.10		-793.1	-867.0	-928.7	-954.6	-912.2	-875.1
3.15			-875.2	-928.8			-877.2
3.20	-774.7	-812.5	-878.0	-923.8	-934.4		-871.9
3.25	-781.6	-815.3	-874.6				
3.30	-783.0	-812.8	-867.7				-853.0
3.35	-780.9						
3.40	-775.3	-798.2	-845.0				-825.4
3.45							
3.50	-781.6						

Table A7.3 Interaction energies (μE_h) of Ne_3-NH_3 calculated at the CCSD(T) level for the planar geometry of NH_3 (>HNH=120.00°).

		ϕ=0°		
R / θ	0°	30°	60°	90°
2.90				-932.7
2.95				
3.00			-910.8	-970.4
3.05			-920.0	-974.1
3.10	-765.8	-812.5	-921.7	-970.5
3.15		-822.4	-917.2	
3.20	-784.9	-826.2	-908.0	-947.4
3.25	-792.9	-825.1	-894.8	
3.30	-786.9	-819.9		
3.35	-783.0	-811.7		
3.40	-775.4	-800.9		
3.45				
3.50				
3.55				
		ϕ=60°		
3.00		-789.9	-865.1	
3.05		-808.2	-882.1	-912.7
3.10	-765.8	-818.5	-891.6	-920.6
3.15		-825.1	-869.0	-921.7
3.20	-784.9	-825.7	-891.5	-917.9
3.25	-792.9	-822.4	-884.6	
3.30	-786.9	-815.4	-874.2	-898.0
3.35	-783.0			
3.40	-775.4	-795.6		